Echoes of Extreme Rainfall: Radar Perspectives of Multiscale Precipitation Controls

By

Ian C. Cornejo

A dissertation submitted in partial fulfillment of
the requirements for the degree of

Doctor of Philosophy

(Atmospheric and Oceanic Sciences)

at the

UNIVERSITY OF WISCONSIN–MADISON

2026

Date of final oral examination: April 6th, 2026

The dissertation is approved by the following members of the Final Oral Committee:
- Angela K. Rowe, Associate Professor, Atmospheric and Oceanic Sciences (AOS)
- Jonathan E. Martin, Professor, AOS
- Tristan L'Ecuyer, Professor, AOS
- Daniel B. Wright, Associate Professor, Computer Sciences
- Ulrike Romatschke, GeoSphere Austria

Abstract

Extreme rainfall presents a major societal hazard through flooding and landslides. Rain can be viewed along a spectrum of rainfall intensity and duration governed by key environmental ingredients, including moisture availability, lifting mechanisms, and microphysical processes. Improving understanding of how these ingredients interact across scales is critical for advancing both observations and prediction of extreme rainfall. This dissertation investigates these processes using data collected during the 2022 Prediction of Rainfall Extremes Campaign in the Pacific (PRECIP), which took place over northern Taiwan during the warm-season. Leveraging Taiwan's dense observational network and multiple research radars, the work examines controls on extreme rainfall from radar measurement techniques to microphysical and mesoscale processes.

The first component of this research develops improved radar-based rainfall estimation approaches for regions of complex terrain. Specific attenuation-based rain rate retrievals and a blended radar rainfall estimator were evaluated using observations collected during PRECIP. Results demonstrate that attenuation-based retrievals can mitigate the impacts of partial beam blockage from terrain while maintaining high-resolution estimates of heavy rainfall, highlighting the benefits of combining multiple radar-based rain rate estimators to improve performance across rainfall intensities.

The second component investigates the microphysical processes associated with extreme rainfall using a radar-based drop size distribution (DSD) modeling framework constrained by surface disdrometer observations. The analysis reveals widespread signatures of collision coalescence in both stratiform and convective precipitation and identifies links between ice-phase processes aloft and enhanced surface rainfall through increases in drop size and concentration below the melting layer.

The final component connects mesoscale dynamics to microphysical processes using high-resolution numerical weather prediction simulations alongside multi-Doppler radar analyses and radar-derived DSD estimates. Results indicate that precipitation efficiency and the vertical redistribution of moisture play central roles in controlling rainfall intensity. Orographically influenced flow interactions provide additional lifting mechanisms alongside the Mei-Yu front, highlighting the importance of terrain in organizing extreme rainfall. Model simulations reproduce some aspects of these processes but exhibit biases in rain microphysics, particularly in representing the observed drop size distributions.

Collectively, these findings emphasize the interconnected roles of terrain, precipitation efficiency, and drop size distributions in governing extreme rainfall and highlight pathways for improving both observational analysis and model representation of extreme precipitation.

For my parents, who sacrificed so much and worked tirelessly to get me here

Acknowledgments

Though my name may be listed as the author of this dissertation, it is through the efforts of many people in my life that this work was made possible. This section serves to thank those who helped me reach this point.

My deepest thanks go to my advisor, Angela Rowe, someone for whom it is incredibly difficult to be succinct. I will always be grateful that she chose me as one of her first students here in Madison. Angela plucked me out of obscurity and, in just a few years, transformed me from a radar novice into an expert. Along the way, she opened doors I could never have imagined, from fieldwork in Taiwan to countless conferences across the country and beyond. With each presentation, paper, and experience, she refined my abilities as both a researcher and a science communicator. Every award and honor I have received over these six years reflects not only my own work, but also the guidance and wisdom she has shared with me.

Beyond the technical and professional skills I have gained, the most important lesson she has taught me is to lead with compassion. It is through this that her students have been able to thrive. She has worked tirelessly to support us and ensure we have the resources and opportunities we need, both in research and in the classroom, where I was fortunate to serve as her teaching assistant several times. The selflessness she brings to mentoring is not only a reflection of her character, but also a model of leadership within atmospheric science. Her genuine care for our physical, mental, and emotional well-being is something I will carry forward as a lasting part of her influence.

I thank the members of my committee for their continued guidance over the years. To Jon Martin, it has been an absolute joy to observe you as a professor. Within minutes of attending your Frontal Cyclone course, I knew you were put on this earth to teach synoptic meteorology. To Tristan L'Ecuyer, the leadership you've shown with CIMSS and PREFIRE is truly inspiring. To Daniel Wright, it's remarkable how often the hydrological concepts you've taught me shape my research and thinking. To Ulrike Romatschke, my time with you at NCAR was wonderful, and I've learned so much from you. Also, ECCO is far and away the algorithm I recommend most often.

None of this work could have been done without the efforts of the PRECIP, TAHOPE, T-PARC II, and KPOP teams. Through these campaigns, I've met many wonderful people who became teammates, colleagues, collaborators, and friends. I especially thank Michael Bell, who, through all the chaos of 2022, maintained steady, level-headed leadership in the face of adversity. To Ting-Yu Cha, thank you for taking care of me during my first field campaign and helping me navigate the ups and downs of using an automatic balloon launcher and operating S-Pol. To the members of the Orographic Group, it was a pleasure to work alongside others devoted to the same problems while approaching them from different perspectives. To the NCU Radar Lab, especially Wei-Yu Chang and Kao-Shen Chung, it has been incredibly rewarding to collaborate with people I can talk endlessly about radar with. To Mike Dixon, John Hubbert, and Wen-Chau Lee at NCAR, thank you for your help with S-Pol data and for guiding me through the radar landscape. Lastly, I am grateful to everyone who contributed to data collection during these campaigns.

To the entirety of the AOSS community, thank you. To the members of SSEC, CIMSS, and AOS, thank you for making this building lively and exciting. To the AOS staff, you are the foundation that enables students and researchers to do what we do. To the faculty, especially Greg Tripoli and Grant Petty, I've gained knowledge that I will carry with me throughout my career. To my friends in the department, I've loved learning about the wide range of work you all do and being able to relax together through the chaos. I especially want to thank Ally, who brings so much light, joy, and foolishness into my life. One of the most rewarding things I've witnessed is the growth of the Rowe Lab, from just Ben, Angela, and me into a small community. I thank Ben, Anthony, Giselle, Becca, Sarah, Sam, Tyler, Night, Marian, Xander, and Ivan for the memories, laughter, advice, and good vibes you've brought to the 9th floor. I couldn't have asked for a better lab to be a part of.

I would also like to thank the mentors from my alma mater. To Eric Snodgrass, without you, I would not be in this field fow which I am grateful for your encouragement. To Sonia Lasher-Trapp, thank you for introducing me to cloud physics and atmospheric science research and for setting me on this path. To Anna Nesbitt, thank you for helping me grow as a coder and for the guidance you've provided.

Lastly, I thank my family. Despite not always understanding my work, you have always supported me, and for that I am deeply grateful. To my dad, I hope you are looking down with pride. To my mom, I am eternally grateful for everything you have done to support me on your own. I could not have done this without you.

Thank you, all

Contents

List of Tables

List of Figures

Chapter 1

Introduction

Extreme rainfall during the warm season represents a major socioeconomic hazard with far-reaching consequences for communities, infrastructure, and public safety worldwide. In many regions, warm-season precipitation can be convective, capable of producing short-duration, high-intensity rainfall that triggers flash flooding in urban and small-basin environments (Doswell III 1993; Hapuarachchi et al. 2011; Maddox 1979; Schumacher 2017). In addition to convection, longer-duration or sequential events can progressively saturate soils, elevate river stages, and destabilize hillslopes (Dai and Lee 2001; Segoni et al. 2018). Thus, both rainfall intensity and duration are fundamental controls on hazard outcomes: intense bursts can overwhelm drainage capacity within minutes, whereas prolonged or repeated events degrade soil strength and promote landslides and widespread riverine flooding (Dai and Lee 2001; Doswell III 1993; Doswell III et al. 1996; Segoni et al. 2018; Wright 2018). The societal toll of these processes is substantial. Globally, floods affect hundreds of millions of people each decade and accounted for approximately 45% of weather-related disaster losses between 1970 and 2019 (United Nations Office for Disaster Risk Reduction 2025), while in the United States alone inland flooding associated with billion-dollar disasters has averaged approximately $4.5 billion in damages per year from 1980 to 2024 (National Centers for Environmental Information 2020). These impacts underscore the need to evaluate the ingredients leading to warm-season extreme precipitation through the perspective of both rainfall intensity and duration.

A useful conceptual lens for examining these rainfall phenomena is an ingredients-based framework (e.g., Doswell III et al. 1996), which emphasizes that extreme precipitation arises from the co-location and persistence of key environmental ingredients rather than from any single controlling factor. In this framework, rainfall intensity and duration reflect differing combinations of moisture availability, instability, lift, and storm structure, as well as the efficiency with which water vapor converts to precipitation. For short-duration, high-intensity events, large precipitable water amounts, strong moisture flux convergence, and processes that enhance warm-rain efficiency may dominate, whereas longer-duration or sequential events may depend more on sustained synoptic-scale ascent, persistent low-level jets, quasi-stationary boundaries, and terrain interactions that maintain rainfall over the same region for hours to days (Doswell III et al. 1996; Lin et al. 2001). This dichotomy of rainfall can be placed within a spectrum whereby intensity has strong ties to vertical forcing whereas duration is more strongly tethered to horizontal forcing (Fig. 1.1). Different types of storms often are the result of different combinations of these ingredients such as high intensity deep convective cores, high duration broad stratiform regions, and tropical cyclones which are both high intensity and duration. These ingredients are not static; their magnitude, vertical structure, and source regions can vary substantially across the intensity - duration spectrum and from case to case. Thus, by understanding how the individual ingredients alter rainfall holistically, common threads that lead to extreme rainfall can be identified.

1.1 Controls on Rainfall Intensity and Duration

Rainfall intensity at the surface is ultimately a manifestation of the drop size distribution (DSD) as the amount of water reaching the ground depends on how many drops are present at each size and how fast they fall. Therefore, to understand and predict rain rates, we must examine the DSD itself. A DSD describes the number concentration of raindrops as a function of diameter, often expressed as $N(D)$. Within the warm rain depth, between the surface and the melting layer, warm rain microphysical processes ultimately modify the DSD. These processes include collision coalescence, whereby larger, faster falling drops overtake and merge with smaller ones; evaporation, with smaller drops shrinking faster than larger ones due to the greater surface area relative to volume; and drop break up, either through surface tension not being able to support large enough drops or through collision (Rogers and Yau 1996). These processes can dramatically change the DSD and with it rain rate. While the DSD describes the spectrum of raindrop sizes, its practical relevance

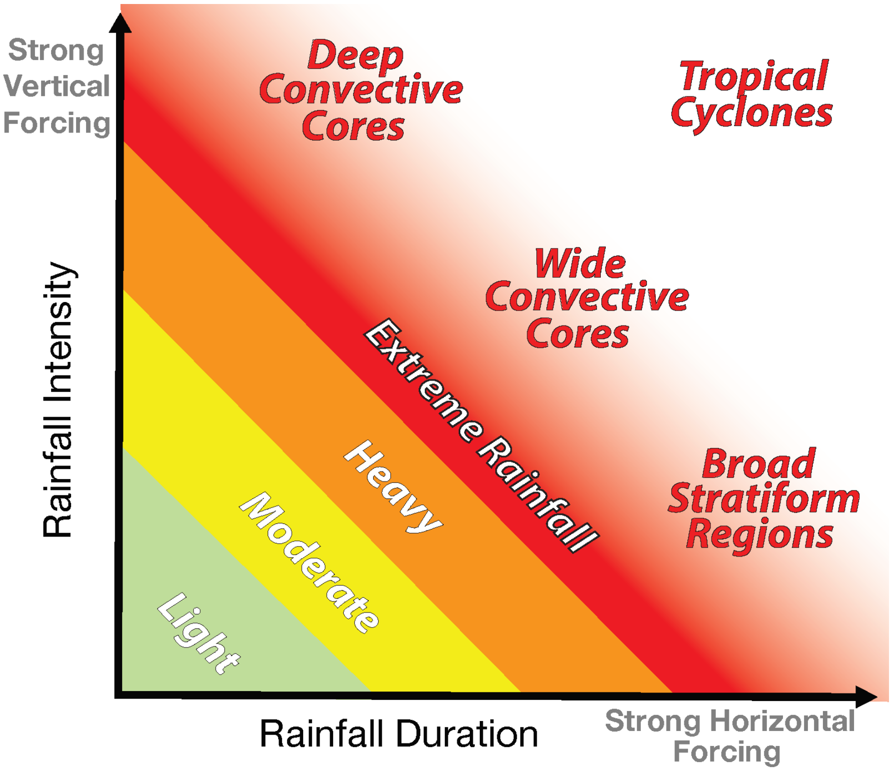

Figure 1.1: A conceptual diagram of the rainfall intensity-duration spectrum (PRECIP 2022).

arises from the moments of the distribution, statistical measures that summarize the bulk properties of the DSD, which can be defined as follows:

$$M_k[mm^k m^{-3}] = \int D^k N(D) dD \tag{1.1}$$

Where M_k is the moment value for moment order k. These moments can provide physical characteristics about the DSD such as M_0 being the number of drops within a volume or M_3 being proportional to liquid water content. Rain rate (R) is also closely related to moments, defined as:

$$R[mm\,hr^{-1}] = \frac{\pi \rho_w}{6} \int D^3 v(D) N(D) dD \tag{1.2}$$

Where ρ_w is the density of water and $v(D)$ is the drop terminal velocity, approximately making rain rate the 3.67th moment (Atlas et al. 1973). Therefore, by changing the DSD through warm rain processes, the moments and rain rate are changed. An example can be made using a simplistic view of the DSD, the exponential distribution, popularized by Marshall and Palmer (1948), defined as:

$$N(D)[mm^{-1}m^{-3}] = N_0 e^{-\Lambda D} \tag{1.3}$$

With N_0 being the intercept parameter and Λ being the slope parameter. While more complex distributions exist and real DSDs can not be represented using empirical fits, the exponential distribution can deliver key insights as to how microphysical processes can alter moments. Figure 1.2a shows an example of three exponential DSDs with varying N_0 and Λ values. When converted into the moment space (Fig. 1.2b), we find that multiple DSDs can result in similar moment values such as the red DSD having the same M_0 (M_6) value as the blue (black) DSD, but they do not match in other moment values. The black DSD having a higher N_0 value results in a greater number of overall drops, M_0, whereas the blue DSD, which has a lower Λ value, has a higher proportion of large drops, resulting in a larger M_6 value. Despite these two DSDs having different values on opposite sides of the moment space, they have similar M_3 values corresponding to equal liquid water content meaning they hold the same volume of water. These differences in low- and high-order moments can be traced back to microphysical processes such as drop break up causing large drops to break into numerous small drops, physically consistent with the similar M_3 values as liquid water content is not changing during this process. Even with the same M_3 values, however, the rain rate is higher in the blue DSD owing to larger drops falling faster than smaller drops. Therefore, even when information is available for lower-order moments (e.g., M_0), middle-order moments (e.g., M_3), or higher-order moments (e.g., M_6), ambiguity can remain in the inferred rain rate. This highlights the importance of understanding the underlying DSD and the processes that shape it.

The processes that modify the DSD, however, are not exclusively related to drop-to-drop interaction such as coalescence. The DSD can also be shaped by the dynamic and thermodynamic environment in which precipitation develops, particularly through variations in updraft strength and vertical moisture transport. These influences can be direct as in the case of size sorting, whereby small drops are kept lofted by updrafts while larger drops are able to continue falling to the surface (Kumjian and Ryzhkov 2012; Ulbrich and Atlas 1998). Other influences arise indirectly through changes to the moisture availability and

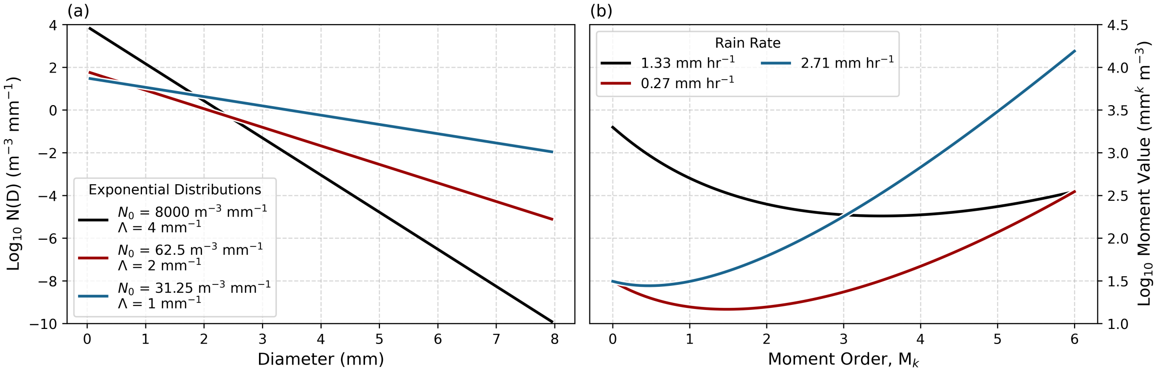

Figure 1.2: (a) Log_{10} $\mathrm{N(D)}$ for three example exponential DSDs with their N_0 and Λ values in the legend along with (b) corresponding Log_{10} moment values and rain rate calculated using the Brandes et al. (2002) drop velocity relationship in the legend.

distribution. Vertical moisture transport associated with moisture flux convergence can enhance condensation (Banacos and Schultz 2005; Holloway and Neelin 2009), increase the probability of collision coalescence (Ochs et al. 1995), reduce evaporation rates, and promote ice production aloft that subsequently melts into larger raindrops (Lasher-Trapp et al. 2018). Consequently, interpreting variability in the DSD, and ultimately rainfall intensity at the surface, requires understanding the vertical motions, moisture transport, and microphysical processes.

These processes are most strongly expressed in convective precipitation, where vigorous vertical motions and sustained moisture transport govern precipitation growth and organization. Greater rainfall intensity is therefore often associated with a greater propensity for convection compared to stratiform precipitation (Doswell III 1993; Doswell III et al. 1996; Schumacher and Houze 2003; Tokay and Short 1996). Therefore, understanding the mechanisms that initiate and sustain convection is critical for interpreting the controls on rainfall intensity. The lifting associated with convection can come from multiple sources such as lifting along fronts and boundaries, through convergence at the surface, or through orographic lift along topography. While lifting alone has implications for the DSD through controlling updraft intensity within the context of instability, it is when lifting is paired with moisture that more directly influences precipitation through condensation, freezing, evaporation, etc. Therefore, the ability to continually distribute moisture aloft is crucial for storm development, type, and longevity. More specifically, single cell convection lasts between 30 - 60 minutes due to precipitation overriding lift, cutting off critical supply of moisture to maintain updrafts and thus precipitation (Weisman and Klemp 1986). In contrast, mesoscale convective systems (MCS) are organized through increased vertical wind shear promoted by spatially separating the updraft from precipitation-driven downdrafts, allowing storms to persist and ultimately produce higher rain rates (Markowski and Richardson 2010; Weisman and Klemp 1984). However, by this example, storm organization produces both an increase in rainfall intensity as well as duration, implying that the two are connected and difficult to distinguish entirely Additional factors can also compound on both rainfall intensity and duration such as terrain. In the event of orographic precipitation when horizontal flow is forced upward by terrain, there is a constant vertical forcing mechanism as long as there are prevailing winds into the terrain. Thus, the limiting factor for both intensity and duration in this scenario is the moisture supply. Assuming that is available in the context of a lifting mechanism, high intensity rainfall can be sustained for long periods of time.

If rainfall intensity and duration are closely linked through storm organization and moisture supply, then both are also influenced by the microphysical processes governing precipitation growth. The rainfall and DSDs observed at the surface reflect a combination of warm rain processes and ice-phase processes operating within different precipitation regimes. Convective regions, characterized by strong updrafts and rapid hydrometeor growth, tend to favor collision coalescence and riming processes that produce larger drops and higher instantaneous rain rates. In contrast, stratiform regions often exhibit weaker vertical motions and longer hydrometeor residence times, allowing processes such as aggregation and melting to dominate, typically resulting in lower rain rates but longer duration precipitation (e.g., Schumacher and Houze 2003; Tokay and Short 1996). These microphysical pathways are not independent of the storm dynamics; for example, evaporation-driven cold pools can modify low-level convergence and tilt updrafts, influencing storm organization and the balance between convective and stratiform precipitation (Engerer et al. 2008; Rotunno et al. 1988; Weisman and Rotunno 2004).

Thus, rainfall intensity and duration emerge from the coupled interactions between dynamics, thermodynamics, and microphysics. In environments with abundant moisture and sustained lifting, these interactions can support both intense convective rainfall and prolonged stratiform precipitation within the same system. Understanding how these processes modulate DSD characteristics is therefore critical for interpreting rainfall extremes, particularly in regions where persistent forcing and high moisture availability promote both high rain rates and long-duration events.

1.2 Taiwan, a Natural Laboratory

Taiwan is an ideal location to study extreme rainfall (Chen 1992; Henny et al. 2021; Lin et al. 2001; Wu et al. 2019). Located within the Pacific Ocean in subtropical East Asia, Taiwan receives extreme rainfall as part of two separate warm seasons, the Mei-Yu season which runs from mid May to the end of June and the Typhoon season which starts in July and extends through September (Fig. 1.3; Henny et al. 2021). The Mei-Yu season is unique to East Asia and is linked to the East Asian summer monsoon (Chen 1992). During this season, moist southwesterly flow associated with the monsoon leads to heavy rainfall in Taiwan. This heavy rainfall is often in part due to the isolation of the island within the South China Sea and the steep topography of Taiwan (Chen and Chen 2003; Chen 1992). The island contains both the Snow Mountain Range (SMR) and the Central Mountain Range (CMR; peak elevation ≈ 4 km) leading to over two thirds of the island being covered in hills and mountains (Chen 1992). The nearly constant moisture supply during this season removes moisture as a limiting factor for studying extreme rainfall, with this moist southwest flow impinging on the steep topography providing a source of lift. During the Mei-Yu season, the primary rainfall producer is the Mei-Yu front, which is also influenced by Taiwan's steep topography.

The Mei-yu front is a quasi-stationary boundary that, near Taiwan, is more commonly characterized by a pronounced moisture gradient rather than a strong temperature gradient, although more substantial thermal contrasts can be present when the front is located over China (Chen 1992; Chen et al. 2007b). The front represents a boundary between the southwest monsoon and the northeast monsoon, the latter which is dominated by relatively drier and cold northeasterly flow originating from the Siberian high-pressure system (Jhun and Lee 2004). As the front moves over Taiwan, frontogenesis is dominated by convergence and deformation, while baroclinic contributions become weak or even frontolytic (Chen et al. 2007b). This convergence and deformation are associated with a low-level wind shift line extending from the surface to approximately 1 km along the leading edge of the front (Chen 1992; Chen and Hui 1990; Chen et al. 1989; Trier et al. 1990). With regards to precipitation, these frontal systems can produce prolonged high intensity rainfall as they are slow propagating, at times becoming quasi-stationary across portions of Taiwan. The frontal rainfall itself is often characterized by long-lasting stratiform rainfall and propagating MCSs along the front producing higher intensity rainfall, especially as they encounter the steep

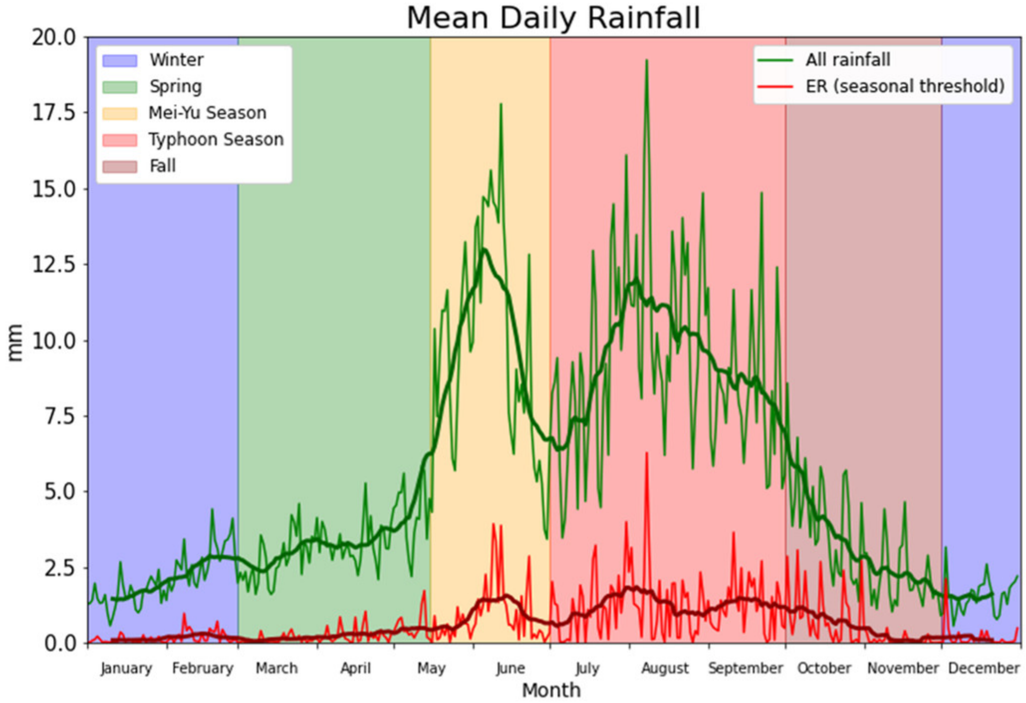

Figure 1.3: The mean total (green) and extreme (red) rainfall for each day of the year, with color-coded seasons between 1960 and 2015. The Taiwan Climate Change Projection Information and Adaptation Knowledge Platform rain data are averaged spatially. The thick lines denote 20-day running means. ER is defined based on a spatially and seasonally varying 99th-percentile threshold so as not to eliminate cold-season extreme events. From Henny et al. (2021).

terrain.

Many of the insights learned about Mei-Yu fronts were the result of two major observational field campaigns based in Taiwan: the 1987 Taiwan Area Mesoscale Experiment (TAMEX; Kuo and Chen 1990) and the 2008 Southwest Monsoon Experiment and Terrain-Influenced Monsoon Rainfall Experiment (SoWMEX/TiMREX; Jou et al. 2011). TAMEX, focused on northern Taiwan, established the fundamental dynamical framework for Mei-Yu rainfall (Li et al. 1997), demonstrating the critical roles of low-level jets (Zhang 1989), frontal convergence (Ray et al. 1991), and Taiwan's CMR in organizing and enhancing convection (Chen et al. 1991). Observations showed that rainfall extremes frequently arise from sustained moisture transport interacting with complex terrain, leading to back-building convection and mesoscale organization rather than isolated, short-lived cells (Akaeda et al. 1995; Jou and Deng 1992). Two decades later, SoWMEX/TiMREX expanded upon these findings using increased observations in southwestern Taiwan and improved numerical modeling (Jou et al. 2011). These experiments clarified the multiscale coupling between synoptic monsoon flow (Lai et al. 2011), mesoscale convective systems (Davis and Lee 2012), and orographic lifting (Xu and Zipser 2015), and highlighted the importance of moisture flux convergence (Feng et al. 2021), terrain-blocked flow (Ruppert et al. 2013), and microphysical processes in modulating rainfall intensity and duration (Chang et al. 2015). Collectively, these field campaigns established Taiwan as a natural laboratory for studying terrain-monsoon-convection interactions. A key component of these observational efforts was the deployment of ground-based weather radar, which provided unprecedented insight into the internal structure of precipitating systems and the evolution of convective organization within the Mei-Yu environment.

1.3 Radar Insights on Microphysics and Dynamics

Understanding the influences on and evolution of DSDs aloft can be difficult because the instruments commonly used to measure drop size distributions, such as disdrometers, are typically limited to surface observations. Weather radar provides a powerful tool for overcoming this limitation by remotely sensing precipitation structure throughout the depth of the atmosphere. Radars remotely sense the atmosphere by transmitting electromagnetic waves, often horizontally polarized, and measuring the portion of the scattered energy that returns to the antenna. When the scattering is within the Rayleigh regime, where the scattering targets are much smaller than the wavelength of the transmitted wave, the power return, P_r, becomes proportional to the squared volume of the scatterer:

$$P_r \propto (D^3)^2 = D^6 \tag{1.4}$$

Thus, the returned power is proportional to the 6^{th} moment of the DSD. This 6^{th} moment is designated as the radar reflectivity, $Z_h = 10\mathrm{Log}_{10}(M_6)$, providing a useful link between the returned power from the radar and the DSD. For decades, radar meteorologists have and continue to use this crucial insight into the DSD for the purposes of remotely sensing rain rates (e.g., Alfieri et al. 2010; Bournas and Baltas 2022; Fulton et al. 1998; Gunn and East 1954; Jorgensen and Willis 1982; Marshall and Palmer 1948; Rao et al. 2001; Stout and Mueller 1968; Zawadzki 1975). However, while this approach has lasted for multiple decades,

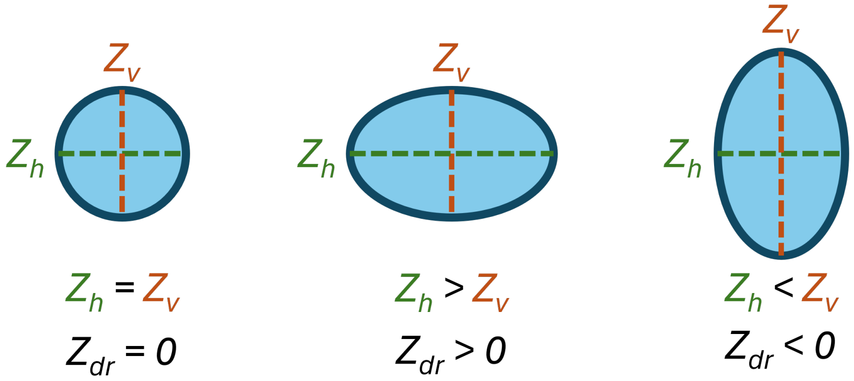

Figure 1.4: Conceptual image of Z_h, Z_v, and Z_{dr} for three different drops, a spherical drop, an oblate drop, and an elongated drop.

the variable is not optimal for rainfall estimation. As in the case of Figure 1.2, the red and black distributions have similar M_6 values and yet, they differ in rain rates owing to the differences in moment orders between M_6 and $M_{3.67}$. Beyond the microphysics, Z_h can struggle due to the limitations of radar beam propagation. For example, beam blockage, the obstruction of radar beams by terrain or buildings (Villarini and Krajewski 2010), and attenuation, loss of power through absorption or scattering outside of the Rayleigh regime (Hitschfield and Bordan 1954), can reduce overall returned power and reduce retrieved rain rates. Therefore, additional insights into the DSD are required to more accurately measure rain rates from radars.

Innovation came by way of Seliga and Bringi (1976) with the advent of dual-polarization. Z_h, horizontally polarized reflectivity, was often used as drops grow in width as they grow larger. However, the growth in the vertical is not at a similar rate as drops tend to become more oblate the larger they grow due to aerodynamic drag (Pruppacher and Beard 1970). Therefore, Seliga and Bringi (1976) theorized that by comparing the ratios of Z_h and vertically polarized reflectivity, Z_v, greater information regarding the drop characteristics within the DSD could be gained. This ratio, termed differential reflectivity, $Z_{dr} = 10\mathrm{Log}_{10}(Z_h/Z_v)$, was slowly but overwhelmingly accepted within the radar community. To conceptualize this relationship, Figure 1.4 shows three drops, each indicating how Z_h and Z_v would differ for each and the resulting Z_{dr}.

A few years after Seliga and Bringi (1976), a further application of dual-polarization was made apparent in Seliga and Bringi (1978) through the use of differential phase shift,

ϕ_{dp}. As the horizontally and vertically polarized waves transmit through large drops, the horizontally polarized wave encounters a greater refractive index due to the larger horizontal axis of oblate drops. This larger refractive index slows the propagation of the horizontal wave more than that of the vertical wave, thus once they transmit through to the other side of the drop, the two waves are out of phase and the phase has shifted. When integrated over a specified range, the specific differential phase shift, K_{dp}, is computed. K_{dp} has several advantages over Z_h with regards to rain rate estimation. Whereas Z_h is related to M_6, K_{dp} is approximately between $M_{4.24}$ and $M_{5.6}$ depending on the underlying DSD, thus more closely representative of rain rate at approximately $M_{3.67}$ (Brandes et al. 2001; Ryzhkov and Zrnić 1996; Sachidananda and Zrnić 1987; Zrnić and Ryzhkov 1996). In addition to the advantages in rain rate estimation, as K_{dp} relies on the phase of the waves as opposed to the power, K_{dp} is able to bypass partial beam blockage and attenuation allowing for precipitation estimation beyond some terrain and buildings (Zrnić and Ryzhkov 1996).

The use of dual-polarization has allowed for greater flexibility in viewing the underlying DSD of rainfall beyond just Z_h. In more recent applications, rain rate estimation is often a blend of different rain rate estimators, incorporating information from Z_h, Z_{dr}, and K_{dp} depending on when they are most useful (e.g., Bringi et al. 2009; Chang et al. 2021; Dixon et al. 2015; Zhang et al. 2020). Additionally, these dual-polarization fields respond differently depending on the hydrometeors they encounter, thus allowing for hydrometeor inference which can more accurately determine which rain rate estimator is best suited for a given radar volume (e.g., Dolan and Rutledge 2009; Dolan et al. 2013; Vivekanandan et al. 1999). With regards to the underlying processes modifying the DSD, dual-polarization radar can also be used to infer warm rain processes. By differencing Z_h, Z_{dr}, and occasionally K_{dp} within a vertical column, inferences in warm rain processes can be made using so-called microphysical fingerprints (Kumjian and Prat 2014; Kumjian et al. 2022). An example of their use would be with size sorting whereby small drops are separated from larger drops, thus Z_h decreases due to less drops overall, but Z_{dr} increases given the average drop being more oblate. Thus, in many ways, dual-polarization radar has allowed for greater microphysical understanding of DSDs aloft and the processes that influence it.

Despite the great innovations with which weather radar has advanced our understanding of rainfall, the tool and its applications still have limitations in their application. Dual-polarization fields themselves have drawbacks such as Z_{dr} being inherently noisier than Z_h given the compounding of noise in both Z_h and Z_v (Sachidananda and Zrnić 1985). K_{dp}

is also limited as it requires smoothing of the ϕ_{dp} resulting in the peakedness of extreme rainfall to not be well represented (Wang and Chandrasekar 2009). While K_{dp} can bypass partial beam blockage and attenuation, Z_{dr} and Z_h cannot, further explaining why advanced rain rate estimation algorithms pick and choose different polarization fields. However, while attenuation can be a drawback for power-based fields, it also presents itself as an opportunity for rain rate estimation as well. Recent work has shown that attenuation of pure rainfall can approximately be equated to $M_{3.67}$, the same moment as rain rate (Ryzhkov et al. 2014). At S-band frequencies (10 - 11 cm), the same frequencies at which the Next Generation Weather Radar program in the United States operates at, attenuation is minimal and not attributed to absorption by the atmosphere, thus it is assumed that all attenuation is produced by precipitation lending itself naturally to being the optimal rain rate estimator assuming its measured properly. However, ultimately, all rain rate estimators are only as capable as the assumptions of the underlying DSD. DSDs themselves are modified by different processes, but both the processes and the DSDs also vary based on climate (Dolan et al. 2018; Sauvageot and Lacaux 1995). For example, within the tropics where moisture is abundant, there is a tendency for more drops overall compared to midlatitude regions such as the continental United States due to greater amounts of condensation (e.g., Rivelli Zea et al. 2021; Ryu et al. 2021). Therefore, to understand these underlying controls on the DSD within a region and subsequently better estimate rainfall from radars, analysis must be scaled out to understand the mesoscale controls on the DSD.

While radar observations have proven invaluable for inferring precipitation and the evolution of drop size distributions, their utility extends well beyond microphysical interpretation. Doppler weather radar measures the motion of particles along the radar beam by detecting frequency shifts in the returned electromagnetic signal caused by moving scatterers. These radial velocity measurements provide information on the airflow within precipitating systems. When two or more Doppler radars observe the same storm, dual-Doppler techniques can be applied to combine their radial velocity measurements and reconstruct the three-dimensional wind field within the storm (Ray and Wagner 1976; Ray et al. 1980). Such analyses have played a central role in developing modern understanding of convective dynamics, including the structure of supercells (Brandes 1977; Lemon and Doswell 1979) and mesoscale convective systems (Biggerstaff and Houze 1991; Gamache and Houze 1982). Researchers during TAMEX leveraged dual-Doppler observations as a means to study frontal dynamics in northern Taiwan (Ray et al. 1991; Wang et al. 1990).

This approach was further expanded upon during SoWMEX/TiMREX by merging insights from both dual-Doppler synthesis and dual-polarization inferences of hydrometeors (Chang et al. 2015). Consequently, radar observations provide a powerful framework for examining both the microphysical and dynamical processes that control precipitation intensity and structure.

1.4 Prediction of Rainfall Extremes Campaign in the Pacific

The insights gained from TAMEX and SoWMEX/TiMREX highlighted the power of advanced radar observations for diagnosing both microphysical and dynamical processes in extreme rainfall events. However, these campaigns were limited in spatial and temporal coverage, and many aspects of the full spectrum of rainfall intensity and duration, particularly during the Mei-Yu and Typhoon periods, remained under-sampled. Building on this foundation, the 2022 National Science Foundation-funded Prediction of Rainfall Extremes Campaign in the Pacific (PRECIP) was conducted in northern Taiwan between late May and early August to more comprehensively investigate the ingredients of extreme rainfall. Like TAMEX, PRECIP focused on northern Taiwan with the intent of understanding extreme rainfall processes across a wide range of intensities and durations. Unlike TAMEX, PRECIP benefited from multiple modern research radars, disdrometers, and many more in-situ measurements (Fig. 1.5). Expanding on SoWMEX/TiMREX, which was held in southern Taiwan, the shift to the north with a longer observation period was meant to capture both the Mei-Yu and Typhoon periods, with emphasis on Mei-Yu fronts, afternoon thunderstorms, and typhoons as they span different parts of the rainfall intensity-duration spectrum. In addition to the expansive observation network provided by the Taiwanese Central Weather Administration (CWA) and the research equipment deployed for the field campaign, PRECIP also incorporated an extensive modeling component with real-time numerical weather prediction (NWP) ensembles to better determine the ingredients leading to extreme rainfall. With this combination of observations and modeling, PRECIP was uniquely positioned to diagnose the processes leading to extreme rainfall, identify shortcomings in state-of-the-art NWP models, and improve predictive understanding of dynamics, thermodynamics, and microphysics.

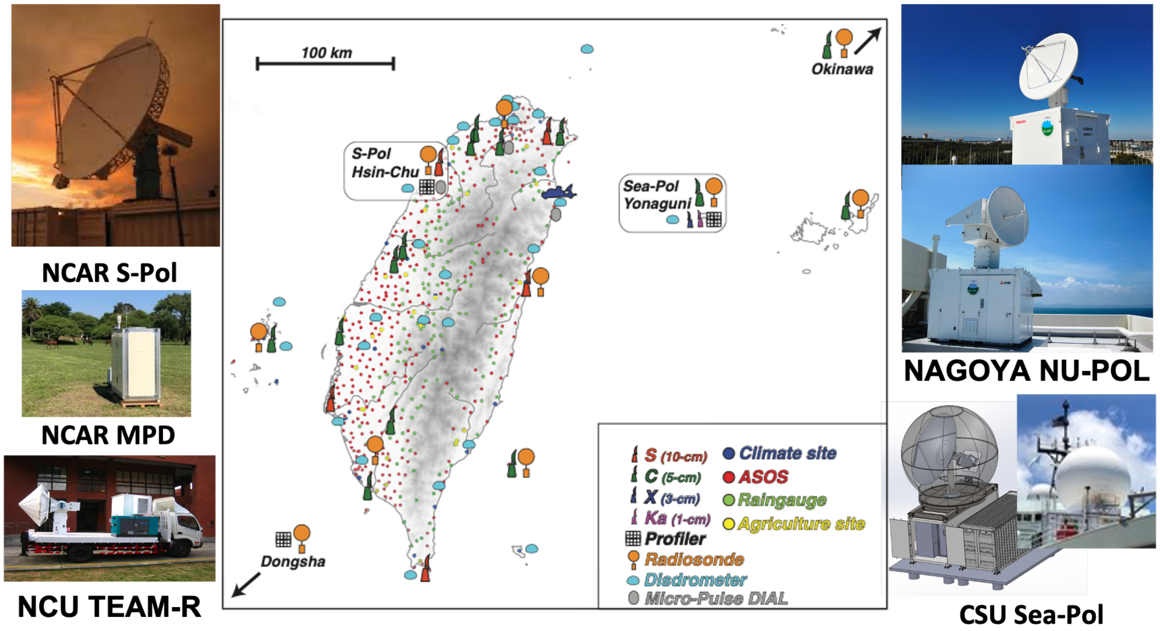

Figure 1.5: Instrumentation map for PRECIP 2022 (PRECIP 2022).

Despite there being a wealth of knowledge depicting all these interactions with regards to rainfall intensity and duration, there are still challenges in predicting these extreme rainfall events. Having determined that these events are often the result of interwoven dynamics, thermodynamics, and microphysics, the complexities which need to be accounted for in prediction are substantial. When predicting these rainfall events, NWP models are often tasked with nowcasting eminent rainfall to issue warnings (Lawson et al. 2018). The microphysical processes inherent to even the finest resolution NWP models cannot be resolved leading to parameterization. These microphysical parameterization schemes, often referred to as microphysics schemes, try to directly predict changes to the DSD within an environment without explicitly modeling how each drop evolves. The most common microphysics schemes characterize the DSD using simple distributions such as the exponential distribution as single moment schemes (e.g., allow Λ to vary) or double moment schemes (e.g., allow N_0 and Λ to vary). While this introduces flexibility in how we represent the DSD, most DSDs do not follow the exponential distribution. Similarly, the skill of a microphysics scheme is dependent on the dataset it was developed on and where it is applied. As previously mentioned, the common DSDs found in the tropics may not be similar to those found in the midlatitudes, thus microphysics schemes developed in the midlatitudes may not perform well within the tropics. There have been many intercomparisons of microphysics schemes compared against observations for heavy rain events and rarely do all microphysics schemes perform well, suggesting that improvement is necessary in either making microphysics schemes more applicable for more regions or the underlying microphysical assumptions require updating (e.g., Chen et al. 2022a; Chung et al. 2020; Tao et al. 2011; Wang et al. 2023).

In the mesoscale, these events are also complex and can be difficult to predict. To create a more probabilistic forecast, often models are run as an ensemble. By running multiple of the same model in tandem with slight perturbations in each, convergence in results can point to a stronger forecast. However, convergence is not guaranteed and when it does not converge, this can point to the difficulties in predicting these dynamics-thermodynamics-microphysics interactions. Just as there have been many studies pointing to the difficulties in microphysics schemes representing precipitation faithfully, there are also countless ensemble modeling studies where convergence of results leads to misrepresentations of rainfall intensity, duration, and accumulation in Taiwan (e.g., Chien and Chiu 2023; Ho et al. 2022; Hsiao et al. 2013; Lee et al. 2019; Yang et al. 2004). Model spread can indicate mismatches in how microphysics responds to dynamics and thermodynamics, or vice versa, emphasizing the need for improved observational constraints.

One of the most effective ways to enhance NWP model skill is through additional observations. Through collection of disdrometer data, there is more training data available to improve DSD representation. Similarly, by collecting more radar data, there is greater understanding of the processes inherent to rainfall as well as the utility of rainfall estimation for the purposes of model comparison. Not only can they serve to better our NWP models, radars are vital tools in nowcasting extreme precipitation. However, as previously mentioned, disdrometers and radars are limited in their capabilities. Disdrometers act as point source measurements of the DSD and can rarely measure DSDs above the surface. Radars can be overcome by attenuation, beam blockage, and still require some a priori knowledge of the DSD, often collected by a disdrometer at the surface. As both disdrometers and radars are costly instruments as well, dense networks of observations are hard to come by. This challenge is particularly pronounced in regions of complex terrain, where logistical constraints, limited accessibility, and radar beam blockage make the deployment and maintenance of dense observational networks difficult. Therefore, locations with dense, high-quality observations and consistent rainfall offer prime opportunities to study microphysical, dynamical, and thermodynamic processes and to improve NWP model predictions.

The PRECIP field campaign provides such an opportunity. While TAMEX and SoWMEX/-TiMREX were groundbreaking studies that improved much of our understanding of extreme rainfall, they were either limited in their technological capacity as in the case of TAMEX or limited in the types of cases observed as in SoWMEX/TiMREX, capturing only a subset of the full rainfall intensity-duration spectrum. As such, this dissertation seeks to investigate extreme rainfall across different scales contextualized through the rainfall intensity-duration spectrum during PRECIP 2022. This work investigates the fundamental processes governing extreme rainfall while advancing new observational and modeling approaches, including radar-based retrievals, disdrometer analyses, and numerical weather prediction applications. The broader objective of this research is to identify where extreme rainfall occurs during PRECIP, identify the microphysical processes aloft that influence that rainfall, and then determine what occurs dynamically and thermodynamically to promote or deter these microphysical processes, ultimately linking dynamics, thermodynamics, and microphysics to more holistically explain controls on rainfall intensity and duration.

1.5 Science Objectives and Dissertation Structure

This dissertation is structured into three sequential chapters, each scaling outward with regards to extreme rainfall development. Chapter 2 compares the innovative attenuation-based rain rate retrieval against traditional rain rate estimators across the PRECIP field campaign. The particular attenuation-based rain rate seeks to leverage the strengths of both power-based rain rate estimators in their resolution as well as phase-based rain rate estimators in their ability to overcome partial beam blockage. In addition to comparisons made across rain rate estimators, modifications and improvements to the attenuation-based rain rate are made to better account for terrain, clutter-induced noise, and by localizing the parameters of the retrieval to Taiwan using the extensive disdrometer network (Cornejo et al. 2025).

Having produced a method by which extreme rainfall could be located and quantified, Chapter 3 expands on the previous chapter by investigating the changes in the DSD aloft that result in extreme rainfall. Using a novel methodology, making use of the attenuation retrieval in Chapter 2, in which the DSD can be modeled using different dual-polarimetric radar fields, microphysical fingerprints of warm rain processes have their corresponding changes in the DSD finally quantified. Additionally, particle identification is applied to further determine how graupel aloft can modify the DSD aloft as well as rain rate near the surface (Cornejo et al. 2026).

Chapter 4 scales out further by comparing a high resolution NWP ensemble among one another as well as with observations including rain rate retrievals from Chapter 2, modeled DSDs from Chapter 3, and multi-Doppler syntheses of 3-dimensional winds. The intent of this chapter is to have a multifaceted approach in which model representation of dynamics, thermodynamics, and microphysics ultimately impacts rainfall intensity and duration. This analysis highlights key mesoscale (e.g., vorticity, divergence, lift) and microphysical factors (e.g., warm rain processes and DSD shape) that lead to or deter extreme rainfall. Chapter 5 integrates the major findings of this work, explores their broader implications, and outlines avenues for future research.

Chapter 2

Specific Attenuation-Based Rain-Rate Applicability to Varying Rainfall Intensity in Complex Terrain

2.1 Introduction

Ground-based radar remains one of the most powerful tools for estimating rainfall accumulation. With its ability to remotely sense precipitation at long distances, radars are often used to fill the gaps in regions of sparsely populated ground measurements such as in regions of complex terrain and over bodies of water. While radar reflectivity factor, Z_{h}, is commonly used to describe precipitation intensity, the advent of dual-polarization radar has allowed for increased accuracy and skill in estimating rainfall (Goddard and Cherry 1984; Ryzhkov and Zrnić 1995; Sachidananda and Zrnić 1987). Differential reflectivity (Z_{dr}) helps to account for variability in drop size distributions (DSDs), while specific differential phase (K_{dp}) is immune to radar calibration and signal loss owing to attenuation (Ryzhkov et al. 2022). A combination of these polarimetric variables is therefore used in radar-based rain estimation, taking into account their relative strengths and weaknesses for a range of rainfall intensities (e.g., Cifelli et al. 2011). However, practical issues remain in applying these hybrid dual-polarization algorithms to a variety of climate regimes owing to the remaining

---

The following Chapter is a reformatted reprint of Cornejo, I. C., Rowe, A. K., Dixon, M., and Romatschke, U. (2025); Journal of Atmospheric and Oceanic Technology; DOI: 10.1175/JTECH-D-24-0094.1.

sensitivity to DSD variability and challenges in regions of partial beam blockage. A newer approach, presented in Ryzhkov et al. (2014), has shown that the utilization of specific attenuation, A_h, can outperform reflectivity- and more traditional dual-polarization-based rain estimates in a broad array of scenarios.

The loss of radar power over a specified distance (A_h) has been historically thought of as a problem to be corrected from the Z_h (Hitschfield and Bordan 1954). Past studies have shown, however, that A_h is directly related to liquid water content and rain rate (Atlas and Ulbrich 1977; Matrosov 2005). In a comparison study using disdrometer-simulated rain rate estimates, $R(A_h)$ has been shown to outperform $R(Z_h)$, $R(Z_h, Z_{dr})$, and $R(K_{dp})$ at minimizing error at S-Band frequencies (Ryzhkov et al. 2022). Despite this known advantage of $R(A_h)$, a challenge is how to accurately measure A_h. A method that has been popularized by Ryzhkov et al. (2014) is to use a modified form of the ZPHI method, named for its requirements of only Z_h and differential phase shift (ϕ_{dp}; Bringi et al. 1990; Meneghini and Nakamura 1990; Testud et al. 2000). This method of calculating A_h proves to have many benefits over other rain rate products owing to its abilities to mitigate the effects of partial beam blockage, radar miscalibration, and wet radome. Additionally, $R(A_h)$ has been shown to be DSD invariant at S-Band frequencies (Ryzhkov et al. 2014, 2022). For these reasons, $R(A_h)$ has entered operational radar usage in the US and Taiwan (Chang et al. 2021; Cocks et al. 2019; Wang et al. 2019; Zhang et al. 2020).

While there are many advantages to using ZPHI for measuring A_h, practical limitations remain in applying this method to radars in different geographical and climate regions. In applying $R(A_h)$ to C-band radars in the mountainous areas of Taiwan, $R(A_h)$ improved rain estimates overall in both a 12-h typhoon rainy period and a 12-h stratiform-convective event, but required the use of higher elevation angles in completely blocked regions (Wang et al. 2014). This approach required assumptions about the vertical profile of Z_h using these two cases and avoided mixed-phase regions. Mixed-phase precipitation has also been shown to create an artificial increase in A_h while also decreasing A_h in other regions along the ray (Wang et al. 2019). Studies have found that segmenting the rays before and after the mixed-phase precipitation can fix this problem, but segmentation can also cause the A_h calculation to become unreliable in regions of low phase shift or weak precipitation (Ryzhkov et al. 2014; Wang et al. 2019) and is sensitive to the choice of filter of phase shift along the ray (Dufton 2016). Additionally, while $R(A_h)$ is invariant to DSD, the ZPHI method is sensitive to DSD through conversion of ϕ_{dp} into path-integrated attenuation

(PIA) (i.e., the α parameter) that varies in continental versus tropical regimes (Ryzhkov et al. 2014; Wang et al. 2014, 2019; Wolff et al. 2019). Therefore, implementing the ZPHI method requires a series of automated procedures to account for these sensitivities to local terrain, ray segmentation, and rain type. These procedures have been tested for select case studies in the aforementioned literature, but questions remain about the contribution of each of these sensitivities to rainfall estimation across a broader array of rain intensities.

As shown in Ryzhkov et al. (2022) for select simulated cases over Oklahoma, $R(A_h)$ should perform well in both high and moderate intensity rainfall, but $R(A_h)$ may not be well suited for low intensities owing to a weak attenuation signal (Zhang et al. 2020). Furthermore, small errors within $R(A_h)$ owing to data quality, filtering choices, and assumptions made within the ZPHI method may compound to reduce accuracy over longer duration (i.e., $>$ 24 hr) rain events. This study takes advantage of the multi-month deployment of an S-band radar in mountainous Taiwan to quantify the benefits of $R(A_h)$ across a range of rain intensities and durations. The National Science Foundation (NSF) National Center for Atmospheric Research (NCAR) S-band dual-polarization Doppler (S-Pol) radar was deployed in northwestern Taiwan from 25 May 2022 to 10 August 2022 as part of the Prediction of Rainfall Extremes Campaign in the Pacific (PRECIP) to capture both high intensity and high duration rainfall (Fig. 2.1a). S-Pol was situated in close proximity to the mountains of Taiwan allowing for processes leading to orographic enhancement of rainfall to be explored while also presenting challenges for radar-based rain estimation owing to partial and complete beam blockage. (Fig. 2.1b).

Within the campaign, 11 Intensive Observation Periods (IOPs) added additional sounding operations, while S-Pol ran nearly continuously during this 77-day period, capturing various heavy rainfall events from short-duration, intense afternoon thunderstorms to long-duration convective and stratiform precipitation associated with Mei-yu fronts. These slow-moving moisture-driven fronts produce a large portion of the rainfall in Taiwan, often last several days, and span across large portions of east Asia (e.g., Chen 1992; Henny et al. 2021). An advantage of evaluating radar-based rain estimation in Taiwan is the dense surface network of rain gauges and disdrometers operated by the Central Weather Administration (CWA) of Taiwan (Fig. 2.1a). Maximum 24-hour rainfall accumulations observed by rain gauges within 100 km of S-Pol reached values of 300+ mm during PRECIP (Fig. 2.2a). As a proxy for intensity, the maximum 1-hour rainfall accumulations showed upwards of 100 mm on the western slopes of the mountains within 150 km of S-Pol, suggesting periods of orographic

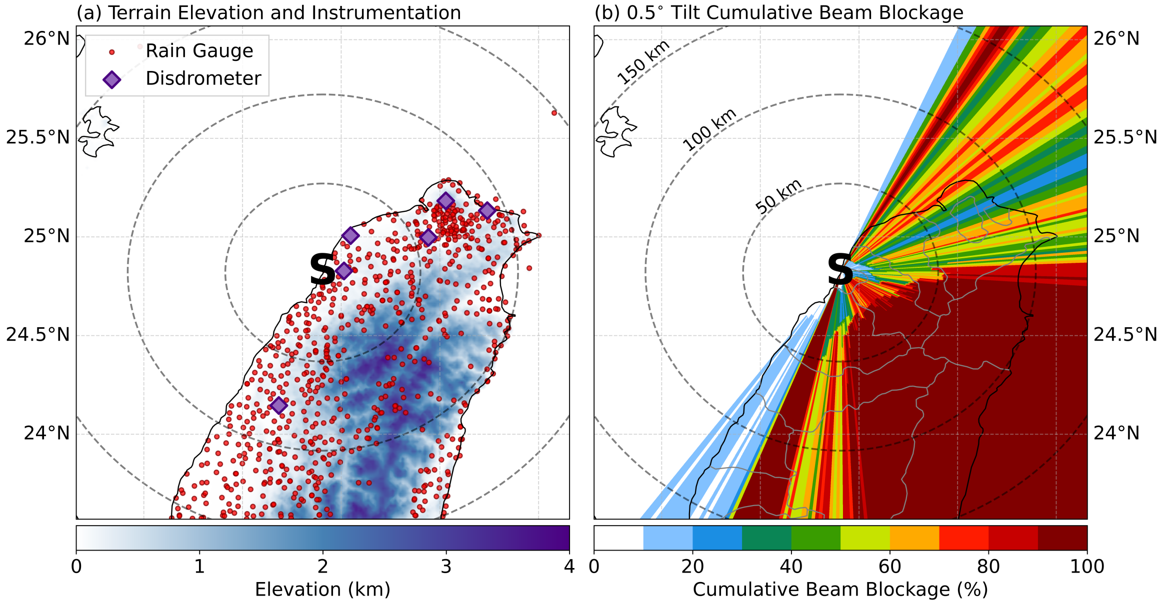

Figure 2.1: (a) Map of Taiwan with elevation (fill) and markers for rain gauges (red circles) and disdrometers (purple diamonds). (b) Cumulative beam blockage at 0.5° tilt for S-Pol. The S-Pol radar is situated at the "S" marker with dashed range rings every 50 km.

enhancement of precipitation (Fig. 2.2b). At the start of PRECIP, IOP 1 included rainfall totals greater than 300 mm within S-Pol's range over a 48-hour period with those peak rain accumulations falling along the coastline and additionally high amounts to the northeast over the populous Taipei Basin (Fig. 2.2c).

A key framework of PRECIP is that extreme rainfall can be characterized by high intensity and high duration, or a combination of both (e.g., Doswell III et al. 1996). With the steep topography and wide ranges of rainfall intensities and durations observed by S-Pol during PRECIP, $\mathrm{R}(A_h)$ should be ideal in mitigating the effects of partial beam blockage and should excel at observing various rain rates. For these reasons, Taiwan's CWA has already begun to implement $\mathrm{R}(A_h)$ in their operational dual-polarization, S-band radars (Chang et al. 2021; Tang et al. 2024).

To address research questions related to the understanding and predictability of heavy rainfall in this region, accurate radar-based estimates of rainfall across a range of intensities and durations are required, including in regions of steep topography where gauge data is limited. This S-Pol dataset serves as an ideal testbed for evaluating $\mathrm{R}(A_h)$ performance, with a variety of events composed of convective and stratiform precipitation, short periods

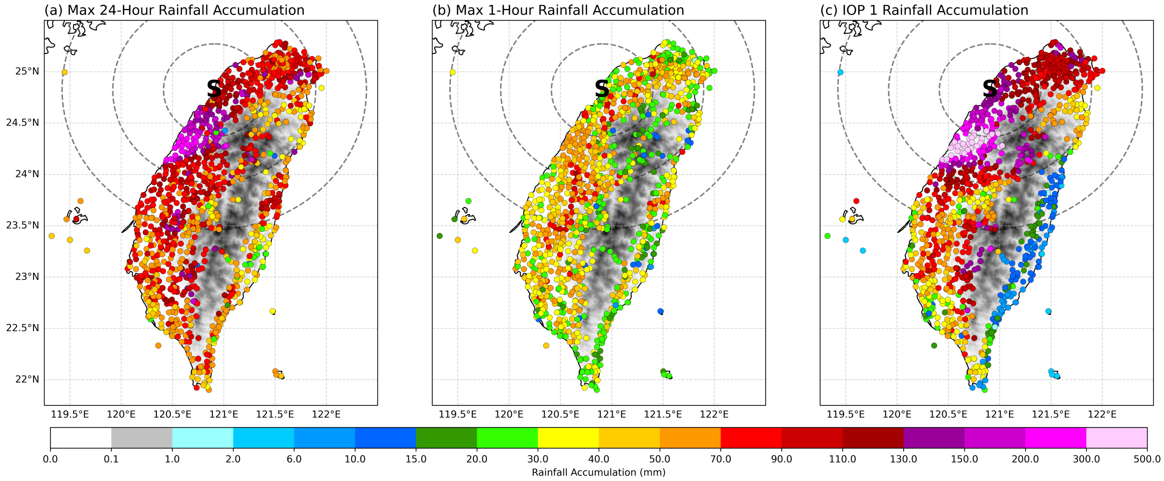

Figure 2.2: Maximum rainfall accumulation (mm) from gauges within (a) 24 hours and (b) 1 hour. (c) Rainfall accumulation for IOP 1 (0000 UTC 26 May 2022 - 0000 UTC 28 May 2022). Dashed circles represent the 50, 100, and 150 km range rings from S-Pol (marked by an S).

of high intensity rainfall, long durations of low intensity rainfall, and steep terrain in close proximity to the radar. The purpose of this study is therefore to quantify the performance of $R(A_h)$ from S-Pol throughout the PRECIP field campaign and to evaluate sensitivities in $R(A_h)$ performance to the variety of automated procedures required to estimate varying intensities of rainfall from attenuation in regions of complex terrain. More specifically, the ZPHI method will be modified to address reported issues of low skill in highly blocked regions and low rain rates in $R(A_h)$. The NSF NCAR Hybrid dual-polarization-based radar rain rate algorithm will be utilized as a comparison dataset owing to its ability to choose specific rain rate estimators when they are most applicable (Dixon et al. 2015).

2.2 Data and Quality Control Methods

2.2.1 NSF NCAR S-Pol

The NSF NCAR S-Pol radar is a ground-based S-band (10-cm wavelength) dual-polarization, Doppler radar that operated during PRECIP nearly continuously from 25 May 2022 to 11 August 2022. The radar was deployed to the northwestern coast of Taiwan (24.81° N, 120.91° E) to capture precipitation over the South China Sea, the coastline, and inland toward the steep mountains (Fig. 2.1). The radar operated in a 12-minute scan cycle with two surveillance volume scans with varying elevation angles (SUR1 and SUR2), as well as multiple Range Height Indicator (RHI) scans. SUR1 operated with 10 elevation angles ranging from 0.5° to 11°, and SUR2 operated with 4 elevation angles ranging from 0.5° to 2.0°. For the purposes of rain rate estimation, data from SUR1 is used in this study owing to its higher, unblocked elevation angles than SUR2 and greater spatial coverage than the RHI sectors. Additional details on S-Pol's operations during PRECIP are shown in Table 2.1.

Table 2.1: S-Pol radar characteristics

Wavelength	10.557 cm
Minimum detectable dBZ	-42.4 dBZ at 1 km; -0.24 dBZ at 100 km
Polarization	H-V simultaneous
Beamwidth	0.92°
SUR scan rate	$10.5^\circ\ s^{-1}$
Max range	300 km
Gate spacing	150 m
SUR1 elevation angles	0.5, 1.0, 1.5, 2.0, 3.0, 4.0, 5.0, 7.0, 9.0, 11.0
Antenna height	10 m MSL

This study uses the S-Pol V1 quality controlled dataset (NCAR/EOL S-Pol Team 2023) that includes clutter mitigation. First, a baseline clutter time series is determined using clutter power monitoring, with most clutter persistent over the mountains and urban areas. To mitigate the clutter, gates are censored in the instance of both normalized coherent power < 0.2 and signal-to-noise ratio (SNR) < 0.0 dB. Additional engineering calibrations and post-processing steps were performed to mitigate unstable transmit power and decreased H-channel receiver gain that led to low biased Z_h and Z_{dr}. While those corrections helped reduce the effects of clutter, some clutter still remains in the dataset. Additional details on the quality control of V1 are described in Dixon et al. (2023).

The S-Pol dataset is analyzed in this study using the NSF-supported Lidar Radar Open Software Environment - "Topaz" (LROSE; Bell 2022) and the Python ARM Radar Toolkit (Py-ART; Helmus and Collis 2016). LROSE is a valuable tool for implementing radar-based rainfall estimation as it calculates rain rates using dual-polarization variables, determines the lowest elevation angle in which rain rate retrievals are reliable, and converts those rain rates into a Cartesian-gridded rainfall accumulation. An additional goal of this work is to implement an $R(A_h)$ framework into LROSE that can be applied to a variety of radars and regions. Py-ART was used for radar data visualization and development of the $R(A_h)$ algorithm used in this study.

2.2.2 Operational Rain Gauge Network

Several Taiwanese agencies operate a combined network of 1000+ tipping-bucket rain gauges with an average density of 1 gauge per 40 km^2 (Chang et al. 2021), with 522 of them within 100 km of S-Pol (Fig. 2.1). These rain gauges output 10-minute rainfall accumulations every 10 minutes. For most of this study, 24-hour rainfall accumulations are used for comparison with radar-based estimates of rainfall. To ensure erroneous data is not used (e.g., suspiciously high rain rates, no recorded rainfall), rain gauge data is compared with the Quantitative Precipitation and Segregation Using Multiple Sensors (QPESUMS) system operated by the CWA (Chang et al. 2021). The QPESUMS rain estimates include input from the operational radar network and the gauge network, with a process that incorporates spatial context for a given grid box's rain estimate. Therefore, it serves as a reliable check for the gauge estimates. Using daily rainfall accumulations for comparison, gauge data is removed if the following criteria is met:

$$|P_{gauge} - P_{QPESUMS}| > 0.5P_{QPESUMS} + 10mm \tag{2.1}$$

where P is the 24-hour rainfall accumulation in mm. When applied to rain gauges within 100 km of S-Pol, this quality control procedure removes 1.57% of daily rainfall data on average throughout the campaign. Therefore, sufficient and reliable data remains for comparison with the S-Pol-derived rain accumulations in this study.

2.2.3 Operational OTT Particle Size Velocity Disdrometer (Parsivel^2)

The CWA operated a network of 23 Parsivel disdrometers during PRECIP used to measure hydrometeor size and fall velocity. These laser disdrometers have a ~50 cm^2 sampling area and classify particles into 32 diameter bins and 32 fall velocity bins. The disdrometers observe minimum and maximum diameters of 0.06 mm and 24.5 mm, respectively, and minimum and maximum velocities of 0.05 m s^{-1} and 20.8 m s^{-1}, respectively. In this study, 6 of the 23 disdrometers were used for simulation of polarimetric variables (Fig. 2.1), chosen based on their close proximity to S-Pol and low bias when comparing 10-minute rainfall accumulation to collocated rain gauges throughout the field campaign (not shown).

Parsivel disdrometers are known to collect erroneous data when compared to impact and video disdrometers (Raupach and Berne 2015; Tokay et al. 2014). Many of these errors arise owing to the effects of strong winds, splashing, and hydrometeors falling on the edges of the sampling area (Friedrich et al. 2013a,b). As such, a quality control procedure has been implemented to correct erroneous data from the disdrometers. The procedure follows a methodology similar to the process CWA implements in their internal quality control process (Lu et al. 2020). As this procedure was applied to one of the PRECIP-specific disdrometers, further details on the quality control procedure can be found in Cornejo et al. (2023).

Once quality controlled, the disdrometer data is used to produce a corrected rain rate (Friedrich et al. 2013b) and simulate Z_h, Z_{dr}, A_h, and K_{dp} using PyDSD (Hardin and Guy 2017) and PyTMatrix (Leinonen 2014). The scattering frequency of 2.81 GHz was chosen to match the antenna frequency of S-Pol. The scattering temperature of 20°C was chosen based on recent studies using operational disdrometers in Taiwan (Wang et al. 2014). Raindrops were simulated with a mean canting angle of 0° and a canting angle standard deviation of 7.5° (Bringi et al. 2008). The drop aspect ratio follows the Thurai and Bringi (2005) drop model.

2.3 Rainfall Overview of IOP 1

While campaign statistics will determine the effectiveness of a rain rate estimator over various types of events, the ability to accurately estimate rainfall from an extreme event is crucial for testing the limits of each estimator. For that reason, PRECIP IOP 1 will be used to assess the sensitivity of $R(A_h)$ to individual automated procedures that go into the rain estimation method. IOP 1 occurred on 26-28 May 2022 starting and ending at 0000 UTC, where rainfall was associated primarily with a Mei-yu front. This quasi-stationary front moved onshore over northern Taiwan a day prior to the start of the IOP before becoming stationary just south of S-Pol. Much of this stationary rainfall to the south of S-Pol is collocated with the 24-hour rainfall maximums over the campaign pointing to this event being one of the most extreme rainfall events during PRECIP (Figs. 2.2a, c).

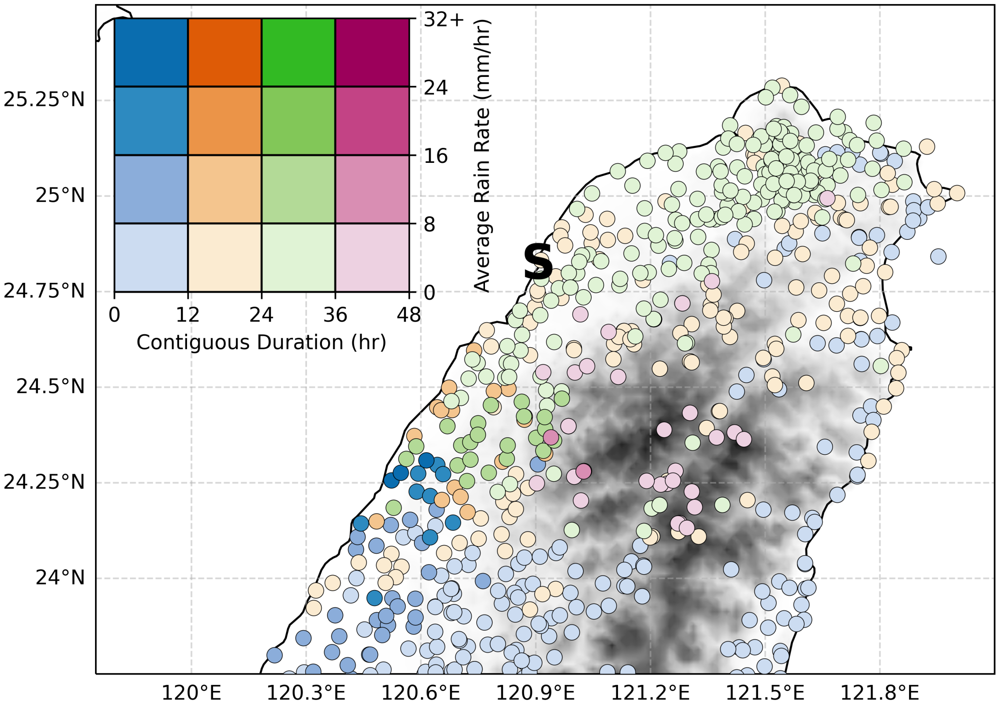

Figure 2.3: Bivariate choropleth of rain period rainfall rate and duration for IOP 1 using rain gauges. An inset color matrix is used as a reference for the intensity and duration based on the period of maximum rainfall accumulation for each gauge.

In terms of the intensity and duration of the rainfall during IOP 1, we define rain periods for each rain gauge as periods of continuous rainfall with allowance for 1-hour gaps in rainfall (Cornejo et al. 2024). Each period has a contiguous duration and an average rain rate acting as proxies for rainfall duration and intensity, respectively. For each rain gauge, duration and average rain rate of the rain period with the highest rainfall accumulation is mapped spatially to form a bivariate choropleth (Fig. 2.3). For much of northwestern Taiwan, IOP 1 was a low intensity, high duration event with rainfall durations between 24-36 hours over Taipei (~25° N, 121.5° E). Rainfall intensity increases southward from S-Pol and maximum duration increases from the coastline inland to the mountains where rainfall durations are between 36-48 hours. Within close proximity to S-Pol, there is a wide range of rainfall intensities and durations making this a suitable event for further examination of the radar-based rain rate estimators.

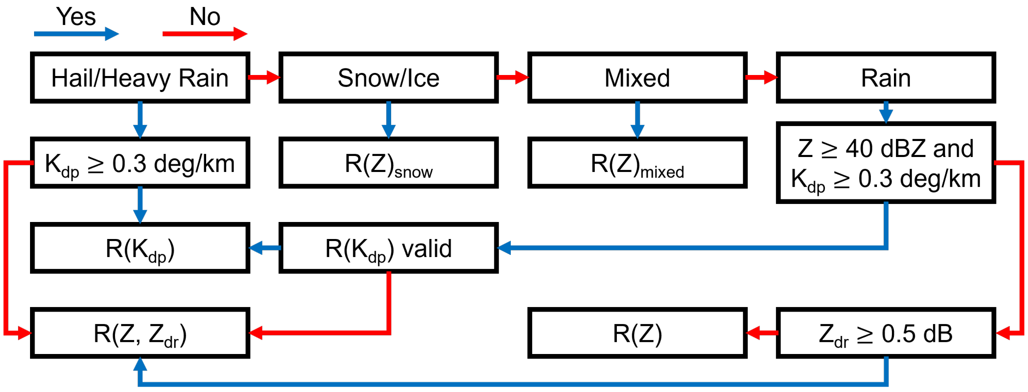

Figure 2.4: The NCAR hybrid rain rate algorithm flow chart. Blue arrows indicate if a condition is met. Red arrows indicate if a condition is not met.

2.4 $R(Hybrid)$ tuning and application to PRECIP

As a comparison to the $R(A_h)$ rain rate, the NSF NCAR hybrid rain rate algorithm, hereafter $R(Hybrid)$, is applied to the S-Pol dataset (Dixon et al. 2015). $R(Hybrid)$ takes elements of Bringi et al. (2009)'s hybrid rain rate algorithm as well as the NSF NCAR fuzzy logic Particle Identification (PID) algorithm (Vivekanandan et al. 1999) to determine which radar-based rain estimator to use for a given hydrometeor type (Fig. 2.4). More specifically, $R(Hybrid)$ decides the appropriate rain rate estimator among $R(Z_h)$, $R(Z_h)_{snow}$, $R(Z_h)_{mixed}$, $R(K_{dp})$, and $R(Z_h, Z_{dr})$ based on the PID of the individual radar gate and user-defined thresholds of dual-polarization variables to take into account relative strengths and weaknesses of individual estimators. The forms of each rain rate estimator is as follows:

$$R(Z_h) = aZ_h^b \tag{2.2}$$

$$R(Z_h)_{snow} = cZ_h^d \tag{2.3}$$

$$R(Z_h)_{mixed} = R(Z_h - 10dBZ) \tag{2.4}$$

$$R(K_{dp}) = sgn(K_{dp}) \cdot e|K_{dp}|^f \tag{2.5}$$

$$R(Z_h, Z_{dr}) = gZ_h^h Z_{dr}^i \tag{2.6}$$

In a previous deployment of the S-Pol radar during the Plains Elevated Convection at Night field campaign, $R(Hybrid)$ was shown to outperform the standard $R(Z_h)$ relationship as well as the NSF NCAR weighted-PID algorithm in both stratiform and convective rainfall (Dixon et al. 2015). However, the coefficients of the individual rain estimators must be determined for a specific rainfall regime owing to the aforementioned DSD-dependence on many dual-polarization radar variables. Using the simulated polarimetric variables and rain rates from the disdrometers, coefficients for $R(Z_h)$, $R(Z_h, Z_{dr})$, and $R(K_{dp})$ are derived for the PRECIP S-Pol observational period. This process requires a minimum number of drops to be observed by the disdrometer, therefore, 1-minute time steps of measurable precipitation ($R > 0.05$ mm hr^{-1}) and large concentration of drops ($N_{drops} > 100$) were used for this analysis. Orthogonal linear regression was used to derive coefficients for $R(Z_h)$ and $R(K_{dp})$ to minimize uncertainty in the rain rate estimates and the simulated polarimetric variables. $R(K_{dp})$ had an additional constraint of using time steps with simulated $R(K_{dp})$ greater than 0.3 deg km^{-1} to be consistent with how it would be used in $R(Hybrid)$. A multiple linear regression was performed for $R(Z_h, Z_{dr})$ due to its multiparameter power law. The sample size for $R(Z_h)$ and $R(Z_h, Z_{dr})$ was 37,401 1-minute time steps and the sample size for $R(K_{dp})$ was 2037 1-minute time steps, both using the entirety of the PRECIP period.

To apply these coefficients to S-Pol, Z_h and Z_{dr} first undergo a 5-gate median filter to smooth out erroneously high or low values. K_{dp} is computed for S-Pol using the LROSE method which is an updated version of the technique developed by Hubbert and Bringi (1995). For the derivation of K_{dp}, ϕ_{dp} is first unfolded and smoothed over two iterations of a 10-gate finite impulse response filter. Phase shift on backscatter is then removed by going backwards in range and trimming peaks in ϕ_{dp}. Valid regions of increasing phase shift are located using a 9-gate range over which the standard deviation, mean, and range of ϕ_{dp} is checked in addition to a cross-correlation coefficient (ρ_{hv}) > 0.95 criteria. Once validated, K_{dp} is derived by taking the slope of the differential phase divided by two. Smoothing may result in broadening of higher K_{dp} values over non-precipitating regions; therefore, for regions with $K_{dp} > 0.25$ deg km^{-1}, a self-consistency method similar to that used in Giangrande et al. (2013) is employed. A synthetic K_{dp} is derived using Z_h and Z_{dr}, but scaled to give the same phase shift as the smoothed observed ϕ_{dp}. This scaled synthetic K_{dp} is used to replace K_{dp} computed from the smoothed ϕ_{dp}, acting to redistribute K_{dp} in high phase shift regions.

Once rain rate is estimated at each radar range gate following the $R(Hybrid)$ flow chart (Fig. 2.4), the three-dimensional (3D) $R(Hybrid)$ field is collapsed down to two dimensions

(2D) by finding the lowest elevation angle, starting at 0.5°, in which the rain rate estimates are still valid. Validity is determined based on the following criteria: clutter-free gates as defined by PID, altitudes below 4.5 km (approximately the melting layer during PRECIP), SNR greater than 3 dB, and cumulative beam blockage fraction less than 25%. The cumulative beam blockage fraction is derived using data from the Shuttle Radar Topography Mission (Syl 2001). Additionally, rain rates are capped at 250 mm hr^{-1} and rain rates below 0.25 mm hr^{-1} are set to 0 mm hr^{-1}. These 2D rain rate fields are then integrated throughout each day, starting and ending at 0000 UTC to produce daily rainfall accumulations.

Each estimator, $R(Hybrid)$, and forthcoming iterations of $R(A_h)$ are compared with the nearest rain gauge using mean absolute error (MAE), Pearson correlation coefficient (CC), and mean bias ratio (MBR) as defined by:

$$MAE = \frac{\sum_{i=1}^{n} |RR_i - RG_i|}{n} \tag{2.7}$$

$$CC = \frac{\sum_{i=1}^{n} (RG_i - \bar{RG})(RR_i - \bar{RR})}{\sqrt{\sum_{i=1}^{n} (RG_i - \bar{RG})^2 (RR_i - \bar{RR})^2}} \tag{2.8}$$

$$MBR = \frac{\bar{RR}}{\bar{RG}} \tag{2.9}$$

with RR and RG as the daily accumulation from the rain rate estimators and the nearest rain gauge, respectively. MAE is used to measure the accuracy and error in the radar rain rates relative to the rain gauges. CC is used to determine precision between radar rain rates and rain gauges. MBR is used to determine how much the rain rate estimators overestimate or underestimate rainfall compared to rain gauges. The rain rate bias correction method developed by Steiner et al. (1999) was then used to further tune $R(Hybrid)$ by comparing a power-law rain rate estimator with gauges for all of PRECIP. The multiplier term of the power-law rain rate estimator is then divided by the campaign-wide MBR. This bias correction is only applied to $R(Z_h)$ and $R(Z_h, Z_{dr})$, now with "BC" subscripts to denote bias correction. Given that $R(K_{dp})$ and $R(Z_h)_{snow}$ are used in less frequent heavy rainfall and snow scenarios, respectively, obtaining reliable MBR statistics for these relationships over the entire campaign is difficult. Therefore, these estimators are not bias corrected. The more commonly used $R(Z_h)$ and $R(Z_h, Z_{dr})$ produced MBR values of 0.878 and 0.782 over the entire campaign, leading to multiplier corrections of 1.13 and 1.28, respectively. The final coefficients for the individual rain rate estimators are as follows:

$$R(Z_h)_{BC} = 0.052 Z_h^{0.631} \tag{2.10}$$

$$R(Z_h)_{snow} = 0.0365 Z_h^{0.625} \tag{2.11}$$

$$R(K_{dp}) = sgn(K_{dp}) \cdot 48.4 |K_{dp}|^{0.831} \tag{2.12}$$

$$R(Z_h, Z_{dr})_{BC} = 0.011 Z_h^{0.904} Z_{dr}^{-3.914} \tag{2.13}$$

$R(Hybrid)_{BC}$ will be used to indicate the $R(Hybrid)$ algorithm using bias corrected coefficients.

When compared to rain gauges, broad rainfall underestimation in $R(Hybrid)_{BC}$ is observed during IOP 1 (Fig. 2.5a) regardless of measurement height relative to the terrain as well as the terrain height (Fig. 2.6a). Much of the range of the $R(Hybrid)_{BC}$ is limited by the elevation angle selection which is predominantly determined by terrain blockage. This issue is most apparent to the south-southwest of the radar where a line of low rainfall accumulation ends closely to the radar as a result of buildings near the radar in the SRTM dataset. Overall, $R(Hybrid)_{BC}$ does well in placing rainfall in the correct locations but is still lacking as a result of beam blockage and highly tuned, DSD-dependent coefficients within the $R(Hybrid)$ algorithm. Therefore, given $R(A_h)$'s noted benefit of DSD invariability and ZPHI's noted benefit of relative immunity to beam blockage, we expect $R(A_h)$ to outperform $R(Hybrid)_{BC}$.

2.5 Results of applying $R(A_h)$ to IOP 1

2.5.1 $R(A_h)$ V1: Optimizing the ZPHI Method

The ZPHI method of estimating A_h requires only Z_h and the PIA, the latter derived by taking $\Delta\phi_{dp}$ between ranges r_1 and r_2 (e.g., Ryzhkov et al. 2014; Testud et al. 2000). The equations needed to calculate A_h using the ZPHI method are as follows:

$$A_h(r) = \frac{[Z_a(r)]^{\beta} C(\beta, PIA)}{I(r_1, r_2) + C(\beta, PIA) I(r, r_2)} \tag{2.14}$$

where

$$I(r|r_1, r_2) = 0.46\beta \int_{r|r_1}^{r_2} [Z_a(s)]^b ds \tag{2.15}$$

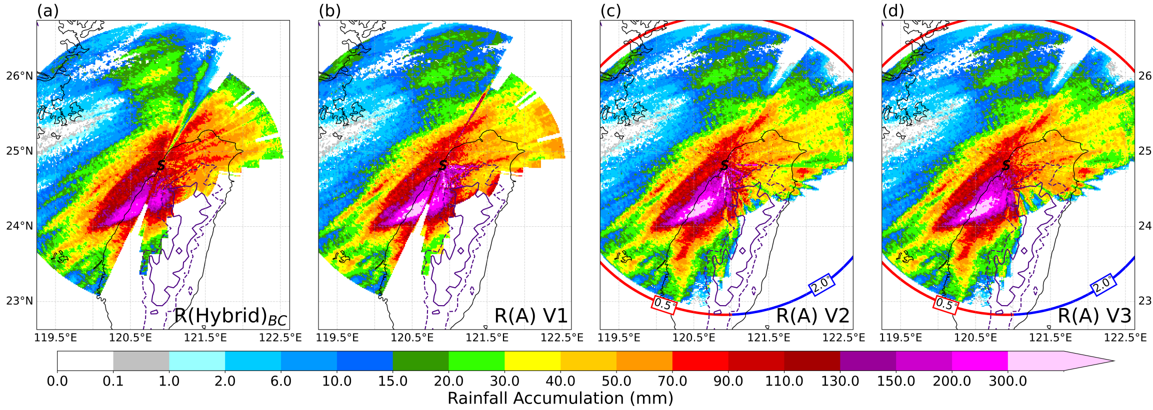

Figure 2.5: Rainfall accumulation (mm) for IOP 1 with contours (purple) of terrain height (dashed for 1 km; solid for 2 km) for (a) $R(Hybrid)_{BC}$, (b) $R(A_h)$ V1, (c) $R(A_h)$ V2, and (d) $R(A_h)$ V3. The outer ring in (c) and (d) represent the starting elevation angles for a given azimuth: 0.5° (red) and 2.0° (blue).

$$C(\beta, PIA) = exp(0.23\beta PIA) - 1 \tag{2.16}$$

$$PIA(r_1, r_2) = \alpha[\phi_{dp}(r_2) - \phi_{dp}(r_1)] = \alpha\Delta\phi_{dp} \tag{2.17}$$

The constant β is set here to 0.62 as a typical value at S-band wavelengths (Ryzhkov et al. 2014). While these equations are consistent throughout the literature, several studies since the initial Ryzhkov et al. (2014) study have found methods of optimizing these equations and improving $R(A_h)$. The first version of $R(A_h)$ for this study, V1, implements the initial ZPHI method of Ryzhkov et al. (2014) including optimizations and interpretations of methods provided by subsequent studies (e.g., Dufton 2016; Seo et al. 2020; Tang et al. 2024; Wang et al. 2019; Zhang et al. 2021, 2020).

A_h is calculated along each ray from gates r_1 to r_2, indicating the start and end, respectively, of liquid precipitation along the ray. If poorly placed, noisy ϕ_{dp} at the start or end of the ray can cause over or underestimations in PIA (Dufton 2016). To address this concern, several methods of filtering and smoothing are applied when estimating A_h. Gates with $\rho_{h\nu} < 0.8$ (from Zhang et al. 2021), SNR < 3 dB (similar to Zhang et al. 2021), temperature $< 6°$ C, and $Z_h > 53$ dBZ (from Seo et al. 2020) are removed prior to selecting r_1 and r_2 to avoid ice and mixed-phase precipitation as well as clutter and noise. The starting gate r_1 is set beyond 5 km from the radar to limit ground clutter, and there must be 10 continuous gates of precipitation after r_1 and before r_2 to further limit noise (Dufton 2016). The mean

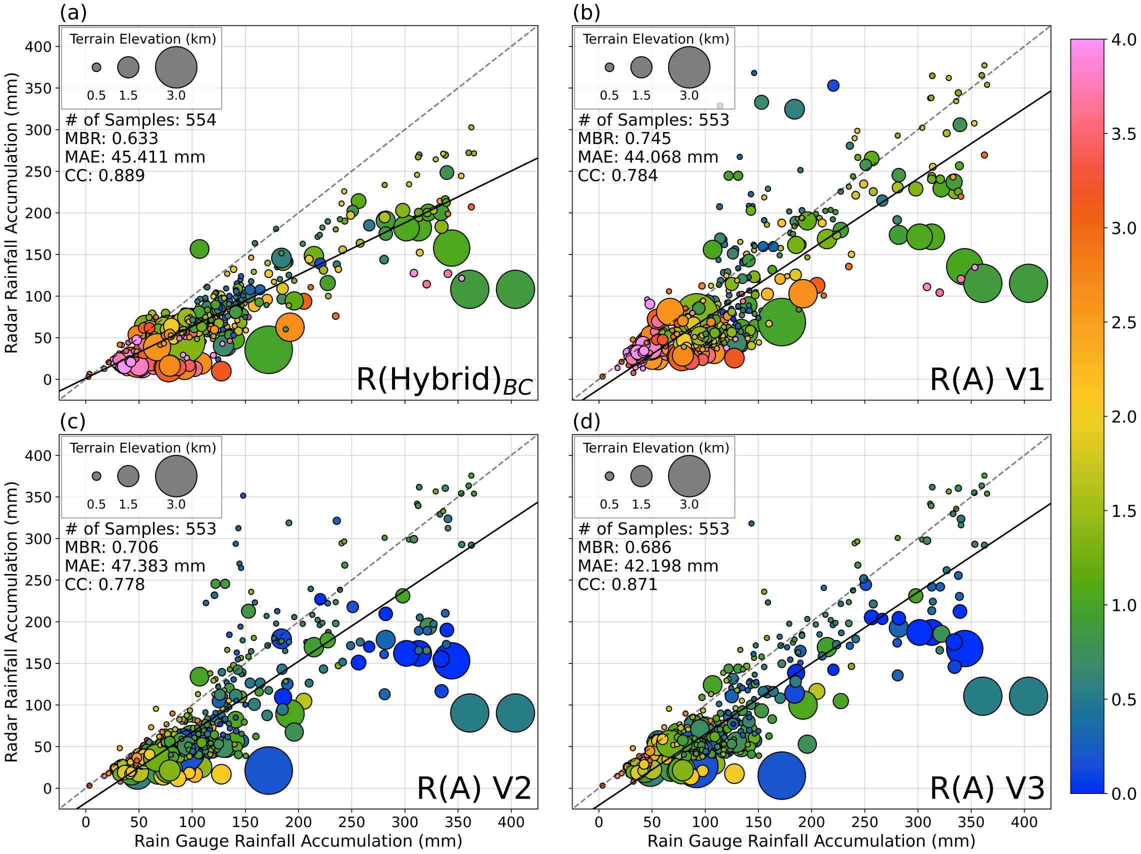

Figure 2.6: Rain gauge rainfall accumulation (mm) compared with rainfall accumulation for IOP 1 from (a) $\mathrm{R(Hybrid)_{BC}}$, (b) $R(A_h)$ V1, (c) $R(A_h)$ V2, and (d) $R(A_h)$ V3. The color of each marker represents the average height of the radar measurement relative to the ground (km AGL) and the size of each marker represents the elevation of the terrain (km). The dashed line represents the 1:1 parity line and the solid line represents the linear regression.

of the unfolded ϕ_{dp} within those 10 continuous gates is used in the PIA calculation to limit spurious end and start of ray noise. Furthermore, PIA must be positive. Negative PIA is only found in the presence of noise (Dufton 2016).

Prior studies have also advised segmenting the ray multiple times if a hail signature is found as it can alter A_h in regions with no hail due to the integrative nature of ZPHI. However, we have opted to not choose that approach since hail was seldomly found during PRECIP and in Taiwan (Chen and Tang 2004). Caution is often advised in segmenting rays as there is a risk of lowering ϕ_{dp} within segments which can hinder ZPHI's accuracy (Zhang et al. 2020).

A commonly modified variable in the calculation of PIA is α, a measure of the net ratio of A_h to K_{dp}. This parameter is highly variable with changing temperatures as well as DSD variability. Therefore, while $R(A_h)$ is DSD invariant, the α component of ZPHI is not, implying some localization may be required (Huang et al. 2020; Seo et al. 2020; Tang et al. 2024). To estimate α for the PRECIP dataset, the "Z_{dr} slope" method is applied whereby a sufficiently large number of Z_h-Z_{dr} samples (e.g., 3000 in Seo et al. 2020) is used to simulate the DSD of a volume in real-time. The methodology for finding the "Z_{dr} slope", K, follows that of Wang et al. (2019), but with sampling up to the 2.0° elevation angle to increase sample size. To limit the effects of non-rain precipitation and clutter on this calculation, similar filtering of samples as those used to limit r_1 and r_2 are applied, but with a stricter ρ_{hv} threshold of 0.98 and a $|Z_{dr}| < 4$ dB criteria (Wang et al. 2019). A slight modification to their "Z_{dr} slope" method is made here to reduce the impacts of undersampling in heavy rainfall. Specifically, if the number of Z_h-Z_{dr} samples within the uppermost reflectivity bin (e.g., centered at 50 dBZ initially) is less than 100, the uppermost bin is shifted down by 2 dBZ until the bin sample size is above 100 or the center reaches 36 dBZ as 35 dBZ is often set as the delineation between convective and stratiform precipitation (Steiner et al. 1995).

The α-K relationship was determined for the PRECIP dataset using simulated polarimetric variables from the ground-based disdrometers (Fig. 2.1). Given the quadratic nature of the α-K relationship (Seo et al. 2020), convective and stratiform limits are imposed to prevent α increasing with increasing K in convective rainfall or becoming unrealistically large with decreasing K in stratiform precipitation. The Bringi et al. (2009) convective-stratiform partitioning method is used to classify all PRECIP disdrometer data into either convective, stratiform, or other. The resulting derived relationship for the PRECIP campaign is as follows:

$$\alpha = \begin{cases} 14.929K^2 - 1.86K + 0.071, & \text{if } 0.0287 \leqslant K \leqslant 0.0541 \\ 0.0304, & \text{if } K < 0.0287 \\ 0.0145, & \text{if } K > 0.0541 \end{cases} \tag{2.18}$$

Outside of the stratiform partition, the relationship bears striking resemblance to that of the original Wang et al. (2019) relationship which was formulated using data from Oklahoma (Fig. 2.7). This is somewhat surprising given the differences in climate between Taiwan and Oklahoma. Between the PRECIP-derived statiform and convective partitions, relationships

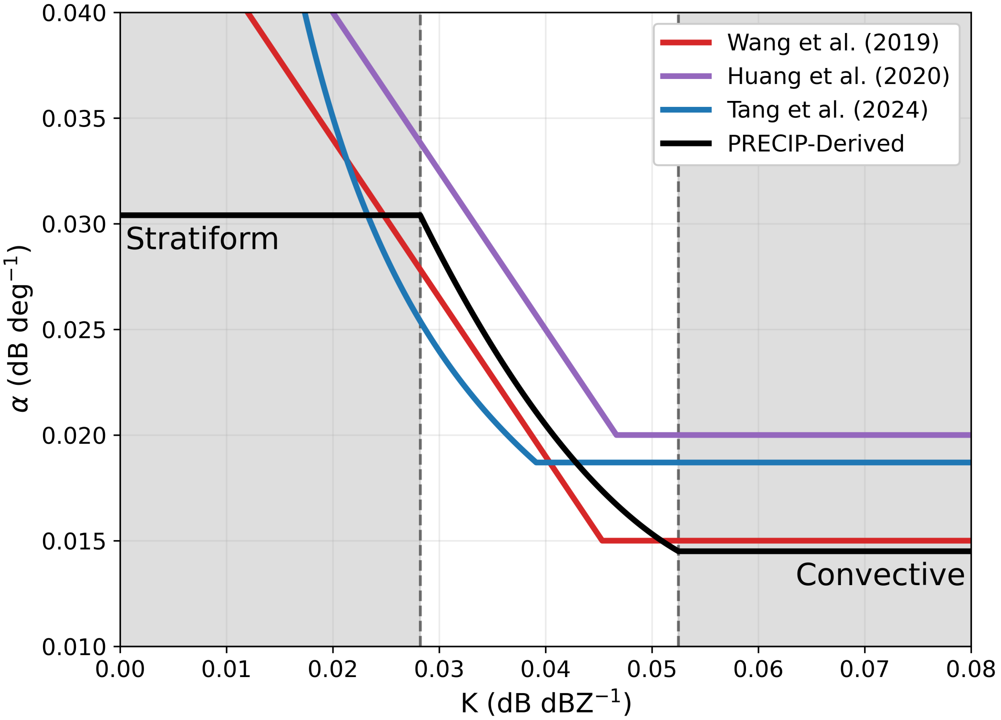

Figure 2.7: The “Z_{dr}-Slope” relationships from Wang et al. (2019) in red, Huang et al. (2026) in purple, Tang et al. (2024) in blue, and the relationship derived for PRECIP in black. The gray regions indicate the stratiform and convective cut off regions for the PRECIP-derived relationship.

developed for all-season northern Taiwan operations (e.g., Tang et al. 2024) and warm-season convection in southern China (e.g., Huang et al. 2020) lie on opposite sides of the Wang et al. (2019) and PRECIP-derived relationships for $K < 0.4$ dB dBZ^{-1}. Additionally, placement of the convective limit differs in each relationship, highlighting the importance of the disdrometer dataset used. Differences in rainfall estimation performance when using the Wang et al. (2019) relationship and the PRECIP-derived relationship were minimal, but slightly favored the PRECIP-derived relationship (not shown) which will therefore be used for this study.

Once A_h is calculated for each radar gate given the aforementioned modifications, the precipitation rate is estimated from A_h at tilts $\leqslant 2.0°$ with $Z_h < 53$ dBZ using:

$$R(A_h) = c_1(T)c_2(\lambda)A_h^{1.03} \tag{2.19}$$

where

$$c_1(T) = (2.23 + 0.078T + 0.00085T^2)10^3 \tag{2.20}$$

$$c_2(\lambda) = 1 - 0.26(11.0 - \lambda) \tag{2.21}$$

with T as temperature in °C and λ as the wavelength in cm (Ryzhkov et al. 2014). A general consensus has not been met as to the maximum elevation angle at which ZPHI can be applied, with most studies opting for the lowest elevation angles (Wang et al. 2019; Zhang et al. 2020). A 2.0° maximum is applied in this study because of the high levels of beam blockage that can render low elevation angles useless, as well as making this approach applicable for both SUR1 and SUR2 scans. When applied at S-Pol's wavelength (10.53 cm) for a constant temperature of 20° C, the rain rate relationship becomes:

$$R(A_h) = 3654A_h^{1.03} \tag{2.22}$$

In the calculation of A_h, if a gate is not valid, $R(A_h)$ falls back to $R(Z_h)_{BC}$ for $Z_h < 53$ dBZ and $R(K_{dp})$ for $Z_h > 53$ dBZ with 53 dBZ as a differentiator between hail and non-hail precipitation (Seo et al. 2020). To retrieve rainfall accumulations, the same procedure as in $R(Hybrid)$ is used for elevation angle selection and integration.

Qualitatively, $R(A_h)$ V1 produces higher rainfall totals to the south of S-Pol when compared to $R(Hybrid)_{BC}$ during IOP 1 (Fig. 2.5b). Toward the mountains, there are clutter signatures still present in the Z_h and ϕ_{dp} fields, as high rainfall accumulations (> 300 mm) are seen along some radials as well as unrealistic decreases in rainfall totals beyond the 1-km terrain height contour. Over northern Taiwan, there is broad underestimation similar to $R(Hybrid)_{BC}$ that could be explained by the lower skill in $R(A_h)$ for low $\Delta\phi_{dp}$ (lower intensity) rainfall (Fig. 2.3; Ryzhkov et al. 2022). When compared to gauges, we find generally good correlation, but spread is large once rainfall totals go above 100 mm (Fig. 2.6b). Despite the better performance in capturing the rainfall maximum in the south, $R(A_h)$ still underestimates rainfall by approximately 25% based on MBR. This error in bias seems to correspond to rainfall measurements in the high terrain as underestimates greater than 200 mm are observed. There seems to be no trend in error with the height of the radar measurements relative to the surface (Fig. 2.6b). The following subsections will step through modifications made to $R(A_h)$ in an effort to reduce this error and bias, as well as increase correlation through the lens of IOP 1.

2.5.2 $R(A_h)$ V2 and V3: Circumventing Effects of Clutter and Blockage

The clutter and blockage specific to S-Pol's deployment during PRECIP presents unique challenges in implementing $R(A_h)$. The tall, sloping terrain brings clutter closer to the radar's lowest elevation angles. When viewing a single scan of S-Pol at the 0.5° tilt, the effects of clutter are highly prevalent in the Z_h and unfolded ϕ_{dp} fields with much of it in the same azimuths as those with high cumulative beam blockage along the ray (Fig. 2.8). Clutter has two effects on Z_h during this deployment within 15 km of the radar: unrealistic peaks or removal of echo as seen by the $<$ 5 dBZ echo between 45° and 135° azimuths (Fig. 2.8b).

In $R(A_h)$ V1, a blockage, SNR, and PID check were in place to try and reduce these effects. If one of the criteria failed, the next highest elevation angle would be used; however, ground clutter would often circumvent these checks in regions of most blockage and reduce the performance of $R(A_h)$ (e.g., 90°-180° azimuthal sector in Figs. 5a, b).

To reduce these impacts, modifications were made to how the lowest valid elevation angles were found. The first change is in regions of severe blockage to the southeast of the radar. Zhang et al. (2020) and Ryzhkov et al. (2022) have implemented a 90% maximum beam blockage criteria to determine when blockage is too severe for $R(A_h)$. Therefore for $R(A_h)$ V2, between the first and last azimuth with maximum cumulative beam blockage $>$ 90% (91.5° and 177°), the starting elevation angle is raised from 0.5° to 2.0° as much of the effects of the terrain are mitigated at this elevation angle (Fig. 2.8a). Additionally, between 25° and 32.5° azimuth, the starting elevation angle is also 2.0° due to a nearby building casting reflections. One region that does not change its starting elevation angle is near 200° azimuth despite high calculated blockage (Fig. 2.8a). Z_h and unfolded ϕ_{dp} appears relatively unphased (Figs. 2.8b, c), meaning there has been a potential change in elevation since the SRTM dataset has been produced. Therefore, the 25% cumulative beam blockage check that was in place in $R(A_h)$ V1 has been been removed and has been replaced with a $\rho_{hv} > 0.9$ check when determining to use a higher elevation angle.

Qualitatively, this change increases the range in which $R(A_h)$ can be calculated over northeastern Taiwan during IOP 1 (Fig. 2.5c). Additionally, azimuths over which a building was present has reduced in their noisiness. While some of the overestimated rainfall amounts between 90° and 180° azimuth have been removed by this process, several overestimations

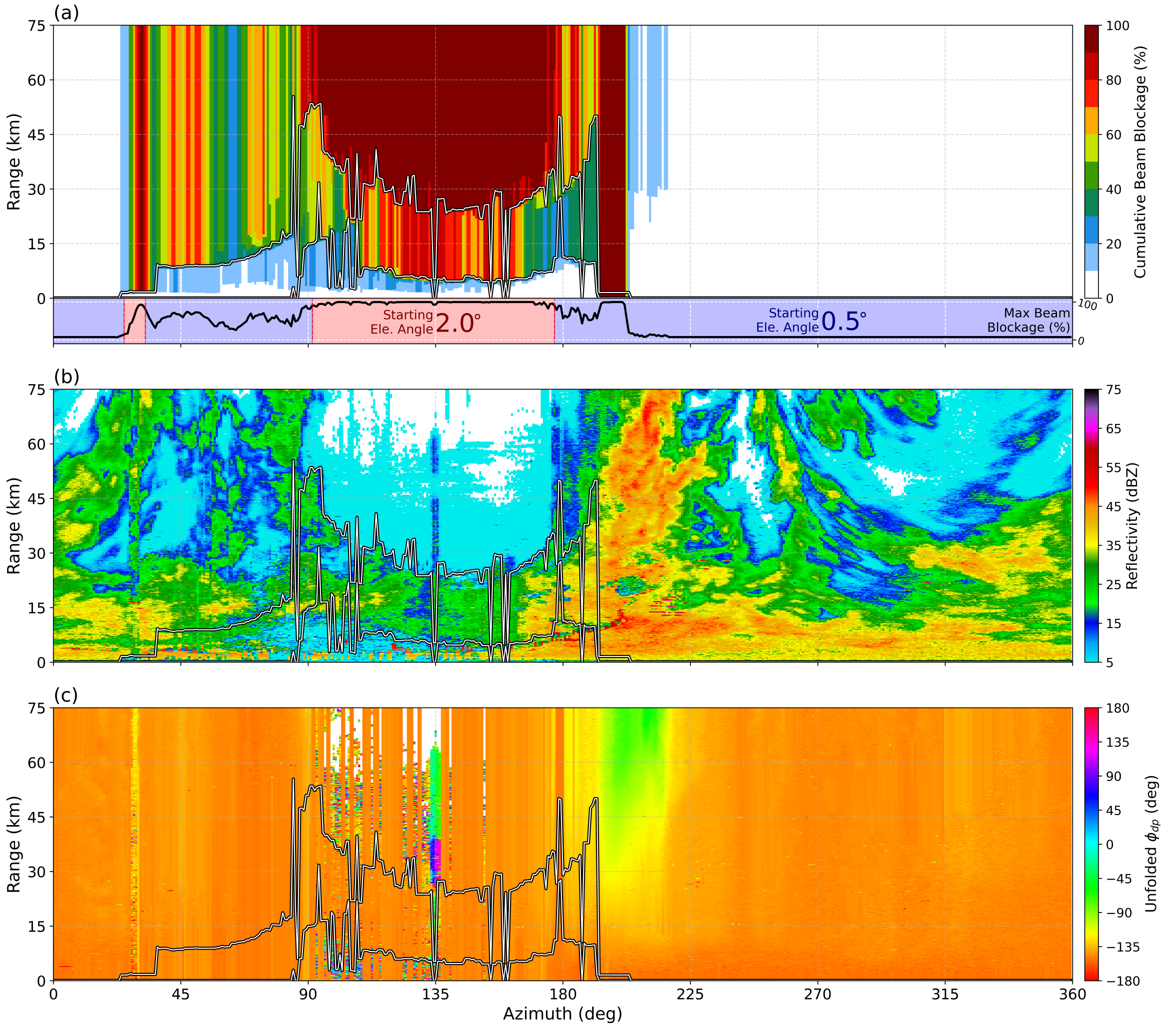

Figure 2.8: Azimuth by range diagrams of (a) cumulative beam blockage in percentage, (b) Z_h, and (c) unfolded ϕ_{dp} for the 0.5° elevation angle of the 0848 UTC 26 May 2022 S-Pol SUR1 scan. The white lines represent where beam segmentation takes place with $R(A_h)$ V3 calculated within each segment. The added line plot in (a) represents the maximum cumulative beam blockage along the azimuth and the default starting elevation angles implemented in $R(A_h)$ V2.

along radials between the radar and the terrain south of the radar appear owing to the removal of the beam blockage criteria for moving to a higher elevation angle. While the added range is a benefit, to ensure that quantitative comparisons are over the same regions, further statistical analysis will be confined to the same area as that of $R(Hybrid)$ and $R(A_h)$ V1(Fig. 2.5a, b). Quantitatively, this process does not yield any improvements with all metrics performing worse than $R(A_h)$ V1 (Fig. 2.6c). By changing the starting elevation angle, most high terrain elevation measurements are shifted toward underestimation and lower terrain elevation measurements toward overestimation.

While there are qualitative benefits, the quantitative drawbacks are numerous. The drawbacks stem from two regions in particular: 1) the south of the radar where terrain slopes and blockage is high but not high enough to meet 90% and 2) the high terrain, regions with terrain elevation above 1.5 km due to the removal of the beam blockage criteria for looking higher. While the issues in the high terrain cannot be fixed without significant subjectivity in implementing an azimuth-by-azimuth beam blockage criteria, the issues to the south can be mitigated through ray segmentation by beam blockage.

The integrative nature of Eq. (2.15) assumes a reduction in Z_h beyond some stepwise increase in blockage, ideally near the radar, but in the case of sloping terrain where multiple stepwise increases in blockage may occur, ZPHI may become faulty. To the south of the radar (~180° azimuth), two stepwise increases in blockage occur which can lead to two segments of the ray with reduced Z_h (Fig. 2.8a, b). With the highest relative Z_h occurring near the radar, ZPHI will assume that much of the phase shift and attenuation is occurring upstream of the blockage, close to the radar, leading to the peaks in rainfall accumulation in Figure 2.5c.

To try and mitigate this effect, the rays can be segmented by beam blockage similar to how ZPHI would be segmented for hail. This process has been performed previously in Tang et al. (2024), but due to the longer climatology of their study, the same process cannot be reproduced in this study. To avoid subjectively deciding where segments are placed, a method of segmenting rays has been developed for this deployment of S-Pol and is implemented within R(A) V3. For each azimuth, the largest 10-gate (1.5 km) increase in cumulative beam blockage is found, and if larger than 10%, the ray is segmented at the end of those 10 gates. If the second largest increase is at least 100 gates (15 km) away from the first, the ray is segmented again. Within these segments, the entire ZPHI method is completed with r_1 and r_2 contained within the segments. This process and the choices made were subjective and based on trial and error. Having a longer climatology of how noise persists in the Z_h and ϕ_{dp} fields and manually placing the ray segments would be ideal, but given S-Pol's relatively short deployment, that cannot be done. A caveat to this ray segmentation is that this lowers the PIA within the segments and can reduce the ϕ_{dp} below what is reliable for $R(A_h)$.

An inadvertent benefit of this ray segmentation is that stepwise increases in beam blockage tend to also be collocated with noise and clutter. Segmenting a ray can isolate those clutter and noise signatures to a single segment and not contaminate the rest of the ray. An example of this impact is found in Figure 2.8. Each white line delineates the endpoints of the ray segmentation using the method as described previously. Between 90° and 200°, three segments exist: one closest to the radar with either noisier ϕ_{dp} or an artificial peak in Z_h, a middle segment with relatively smoother ϕ_{dp} and Z_h, and a third segment in near complete blockage with $<$ 5 dBZ echo and noisy ϕ_{dp}. If left unsegmented, the region containing this middle segment would be exposed to the noise and clutter of the other regions in this instance when applying Eq. (2.15).

When applied to IOP 1, there is near complete removal of the erroneous peaks in rainfall accumulation to the south of S-Pol in addition to some reduced rainfall amounts near the radar to the southeast (Fig. 2.5d). Statistically, this ray segmentation approach improves on prior versions of $R(A_h)$ in many ways (Fig. 2.6d). CC and MAE improve when compared to $R(A_h)$ V1 and V2. The MBR decreases from V2, but mostly through reducing much of the overestimation at low terrain elevations. Not shown is that both the modifications to the elevation angle selection process and the ray segmentation is required to receive this outcome in that the ray segmentation benefits are only realized after the implementation of elevation angle selection implemented in V2. If we were to skip modifying the elevation angle selection process, the benefits of adding ray segmentation would not be as prevalent.

2.5.3 $R(A_h)$ V4: Adaptive Clutter Filtering

Many of the steps in the prior subsection aimed to mitigate the detrimental impacts of remaining clutter on the ZPHI method. Therefore, for this final iteration of $R(A_h)$, a more advanced adaptive clutter filter is implemented to see if remaining error and bias in the S-Pol $R(A_h)$ estimation can be improved. Details about the clutter filter changes are found in the S-Pol V2 quality controlled dataset documentation (NCAR/EOL S-Pol Team 2024) and briefly summarized here:

1. ρ_{hv} is used to augment the clutter mitigation decision tool as previously used in $R(A_h)$ V1 - V3. If clutter is present, ρ_{hv} should increase after application of the clutter filter. Therefore, significant increases to ρ_{hv} after filtering may indicate high prevalence of clutter and the clutter mitigation tool now flags that gate for filtering. Further detail can be found in Ellis et al. (2018).
2. Reduction in the spectral noise floor to the measured noise values.
3. The clutter model width, the typical width of a clutter target given a radar's antenna scan rate, was expanded. Further details of the clutter model can be found in Passarelli (1981).

When this new clutter filter is applied for IOP 1, there is a slight improvement in performance over regions of complex terrain with the best results to the southeast of the radar up until the 1-km terrain line where terrain is steepest (dashed purple line in Fig. 2.9a). Statistically, the implementation of the adaptive clutter filter presents improvements to MAE and MBR in comparison to $R(A_h)$ V3 (Fig. 2.10a). While this is another iterative improvement, there tends to be a low bias in rainfall in northern Taiwan that may be the result of more systemic issues with S-Pol's deployment or the clutter environment in that region (Fig. 2.9a). For example, significant urban clutter over northern Taiwan may be forcing the use of higher elevation angles which can lower the rainfall amounts.

2.6 Results from the Full PRECIP Dataset

2.6.1 $R(A_h)$ Full Campaign Statistics

To evaluate the performance of $R(A_h)$ over the full campaign, three additional statistical metrics are introduced: True Positive Rate (TPR), False Positive Rate (FPR), and the Cross Over (CO), with TPR and FPR defined as follows:

$$\mathrm{TPR} = 100 \times \frac{\mathrm{TP}}{\mathrm{TP}+\mathrm{FN}} \tag{2.23}$$

$$\mathrm{FPR} = 100 \times \frac{\mathrm{FP}}{\mathrm{TN}+\mathrm{FP}} \tag{2.24}$$

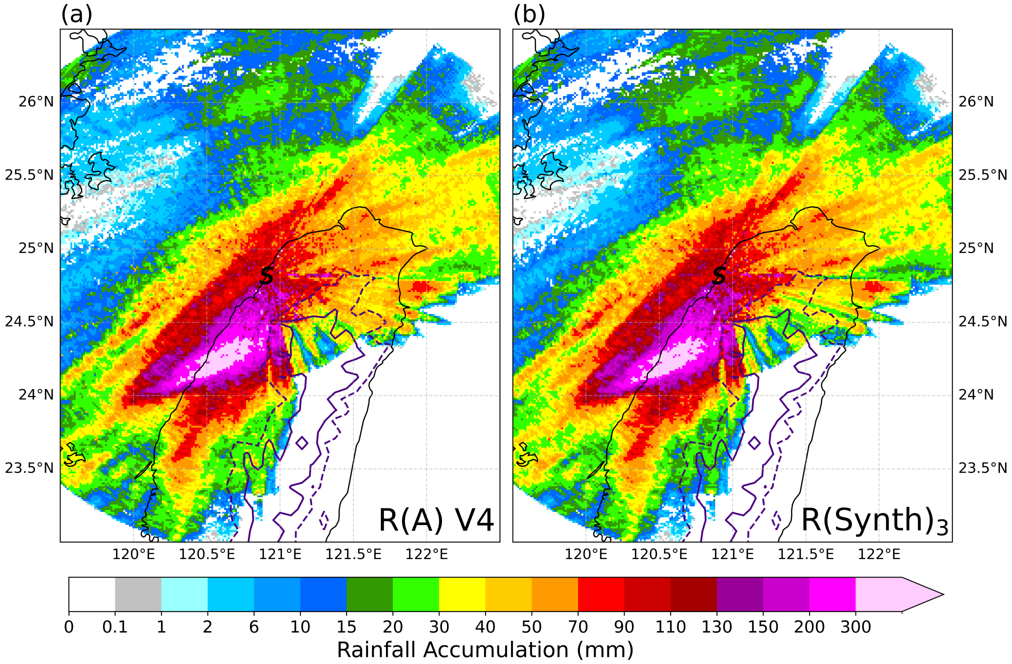

Figure 2.9: Same as Figure 2.5, but for (a) $R(A_h)$ V4 and (b) $R(Synth)_3$.

TPR and FPR both utilize the confusion matrix, a method of evaluating model performance. The true positive (TP) and true negative (TN) is the number of times a model correctly estimates a positive or negative outcome, respectively. The false positive (FP) and false negative (FN) is the number of times a model incorrectly estimates positive or negative outcomes, respectively. For campaign statistics, the outcome is an evaluation of $R(A_h)$ for rainfall greater than 5 mm per day. For example, if a rain gauge measures no rainfall for a day, but the radar estimates $>$ 5 mm of rainfall, the FPR would increase. Therefore, the TPR corresponds to how often the radar estimates rainfall when there is rainfall, with FPR noting where the radar estimates rainfall when none is reported by gauges. CO is a metric quantifying where a linear regression between daily gauge and radar rainfall totals cross the 1:1 ratio line. When evaluated for over the entirety of PRECIP, all rain rate estimators had the tendency for overestimation of rainfall at daily gauge accumulations below the CO. Therefore, the greater the amount of overestimation at low gauge amounts, the larger the CO. Both FPR and CO are metrics for determining overestimation at low gauge accumulations with FPR detailing the frequency of overestimation and CO detailing the magnitude.

Using ~22,000 radar-gauge comparisons during PRECIP, each metric can be found in

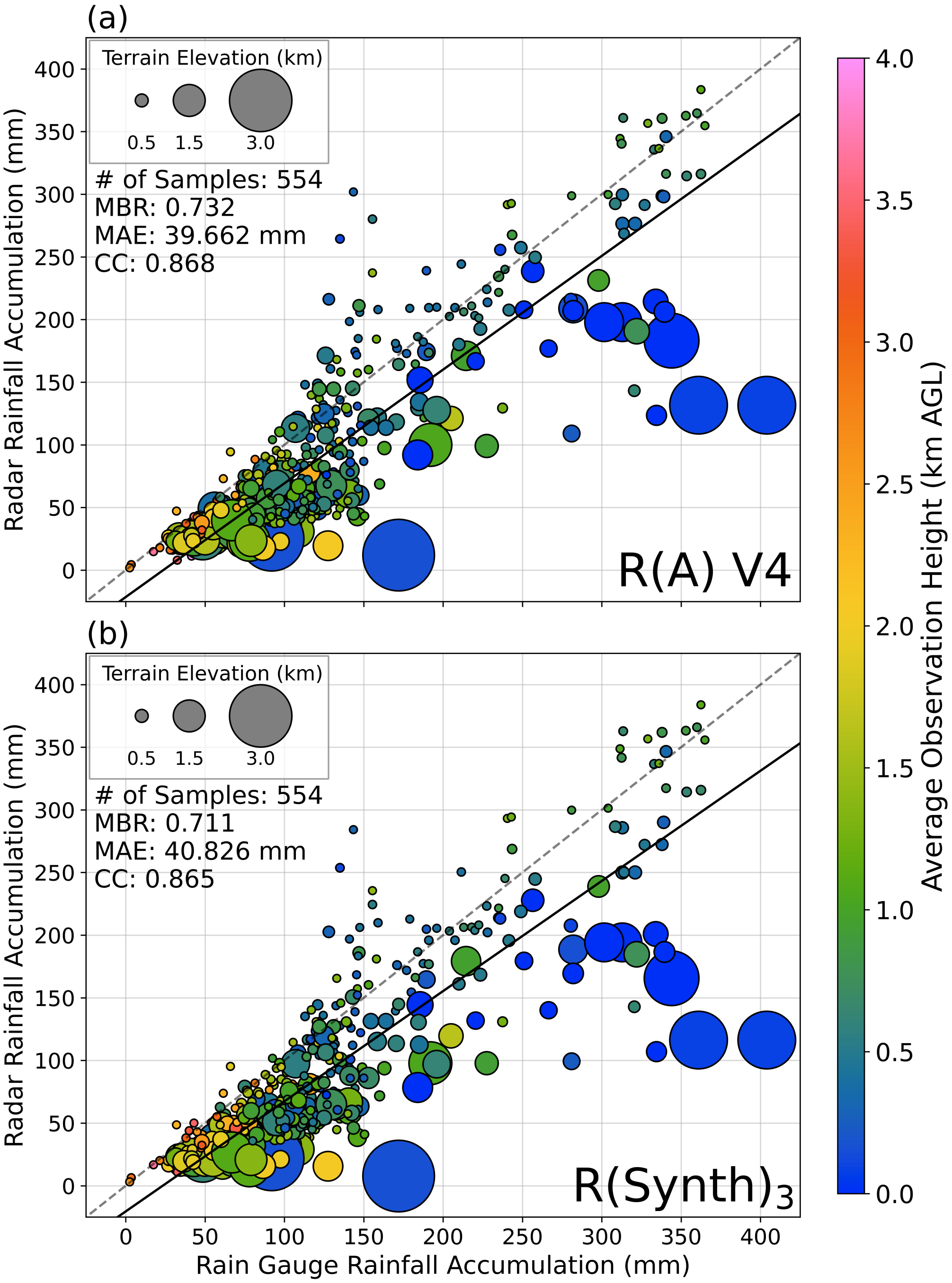

Figure 2.10: As in Figure 2.6, but for (a) $R(A_h)$ V4 and (b) $R(Synth)_3$.

Table 2.2 for all rain rate estimators. $\mathsf{R(Hybrid)_{BC}}$ performs well in limiting error, spread, and bias in daily rainfall. However, in the $\mathsf{R(Hybrid)_{BC}}$ flow chart (Figure 2.4), recall that incorrect PID, such as that present within regions of beam blockage, would direct toward rain estimators other than $\mathsf{R(Z_h)_{BC}}$ and $\mathsf{R(Z_h, Z_{dr})_{BC}}$ thus contributing to $\mathsf{R(Hybrid)_{BC}}$'s bias. Therefore, $\mathsf{R(Hybrid)_{BC}}$ bias will not reach parity.

Table 2.2: Campaign statistics of $\mathsf{R(Hybrid)_{BC}}$, $\mathsf{R(A_h)}$ V4, and $\mathsf{R(Synth)_3}$ using rain gauges as truth.

	MBR	CC	MAE (mm)	TPR (>5 mm; %)	FPR (>5 mm; %)	CO (mm)
$\mathsf{R(Hybrid)_{BC}}$	0.925	0.904	5.606	92	16	10.81
$\mathsf{R(A_h)}$ V4	1.142	0.831	7.659	91	27	25.67
$\mathsf{R(Synth)_3}$	0.978	0.853	7.276	88	19	14.05

Underestimation at higher gauge accumulations is implicit given the MBR less than one and can be explained through multiple ways. All rain rate estimators will produce too much rainfall when trace amounts are observed by the gauges as can be explained by the FPR. This result may be a sign that clutter contamination remains in the radar data as clutter echoes would still produce a rainfall amount if erroneously categorized as precipitation in the PID. This overestimation at low rainfall totals dampens any corrective efforts when bias correction is applied. Additionally, $\mathsf{R(Hybrid)_{BC}}$ uses $\mathsf{R(K_{dp})}$ in the presence of intense rainfall, but because that relationship is also tuned using disdrometers, undersampling of intense storms by the disdrometers can result in rainfall underestimation. This highlights a few of the downsides to using $\mathsf{R(Hybrid)_{BC}}$ as it requires appropriate tuning of all its component rain rate estimators. The reliance on PID may also cause $\mathsf{R(Hybrid)_{BC}}$ to occasionally switch from a more tuned estimator like $\mathsf{R(Z_h, Z_{dr})_{BC}}$ to a less tuned estimator like $\mathsf{R(Z_h)}_{snow}$.

$\mathsf{R(A_h)}$ V4 performed better than $\mathsf{R(Hybrid)_{BC}}$ over IOP 1, but performed worse over the entirety of the campaign with higher bias, lower correlation and greater error. A potential source of this worse performance may be the non-local nature of $\mathsf{R(A_h)}$. Should clutter or erroneous $\mathsf{Z_h}$ or ϕ_{dp} be found along a ray, error is spread along the entire ray for $\mathsf{R(A_h)}$, whereas error in the individual rain rate estimators of R(Hybrid) is localized or removed via smoothing. Another possible reason is a tendency for overestimation at trace or small amounts of rainfall. Both $\mathsf{R(Hybrid)_{BC}}$ and $\mathsf{R(A_h)}$ V4 have similar TPR indicating similar ability to produce rainfall, but $\mathsf{R(A_h)}$ V4 has a much larger FPR and CO meaning not only is

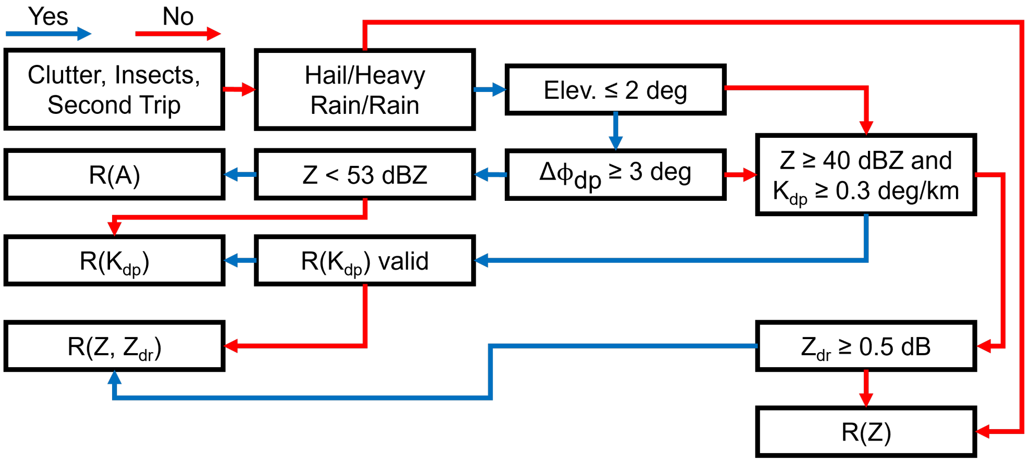

Figure 2.11: Same as Figure 2.4, but for the $\mathrm{R(Synth)}$ algorithm.

$\mathrm{R}(A_h)$ V4 producing rainfall when it is not actually being observed, but it is producing large amounts, owing to either clutter or through low phase shift, a commonly cited cause of error for $\mathrm{R}(A_h)$ (e.g., Diederich et al. 2015; Ryzhkov et al. 2022; Zhang et al. 2016). Despite this overestimation, $\mathrm{R}(A_h)$ V4 performs best in higher gauge rainfall amounts as seen in IOP 1. Therefore, there is likely benefit in incorporating strengths of both $\mathrm{R(Hybrid)_{BC}}$ and $\mathrm{R}(A_h)$ to optimize rain estimates across this broad range of observed intensities and durations.

2.6.2 Introduction of the $\mathrm{R(Synth)}$ Algorithm

A new algorithm, $\mathrm{R(Synth)}$, is developed to take components of $\mathrm{R(Hybrid)_{BC}}$ and work in $\mathrm{R}(A_h)$ when it is most optimal (Fig. 2.11). As in $\mathrm{R(Hybrid)}$, an initial PID check begins the flowchart to reduce impacts of non-meteorological echo (i.e., clutter, insects, and second trip echoes) and the melting layer; the latter which defaults to $\mathrm{R}(Z_h)$. Otherwise, several steps are made to ensure that $\mathrm{R}(A_h)$ is optimally used. Elevation angle is considered to limit the presence of ice and mixed-phase precipitation specifically for $\mathrm{R}(A_h)$ as it would lower its performance. A minimum change in phase shift along the ray segment is also considered to limit the poor performance of $\mathrm{R}(A_h)$ in low phase shift. The final check is if Z_h is too high indicating hail, using 53 dBZ from Seo et al. (2020). If those conditions are not met, the algorithm reverts back to the rain/heavy rain path in the $\mathrm{R(Hybrid)}$ algorithm.

The choice of a 3 degree phase shift was decided based on multiple tests of the $\mathrm{R(Synth)}$

algorithm not shown in this study. Across prior studies, there has yet to be a consensus as to how much phase shift is required for $R(A_h)$ to be applicable. These values can range from 3 degrees in Ryzhkov et al. (2022) to 5 degrees in Tang et al. (2024). $R(Synth)$ was tested with minimum phase shifts between 3 and 6 degrees. Across both IOP 1 and PRECIP, the use of a 3 degree minimum performed best though only slightly outperforming higher phase shift minimums. Therefore, 3 degrees was determined as the minimum for this deployment of S-Pol and $R(Synth)_3$ will be used to discuss this version of $R(Synth)$.

When applied to IOP 1, $R(Synth)_3$ does not actually improve on $R(A_h)$ V4 across any metric though their results are quite similar (Fig. 2.10b). Qualitatively, differences between $R(A_h)$ V4 and $R(Synth)_3$ are minimal (Fig. 2.9b). When comparing across IOP 1, there was little expectation of improvement as $R(A_h)$ V4 already performed well in capturing the case. $R(Synth)_3$ would likely use $R(A_h)$ more frequently as this case was extreme leading to high amounts of phase shift, a scenario in which $R(A_h)$ performs best. For this reason, any instance where the pathways to $R(A_h)$ V4 are not optimal, $R(Synth)_3$ reverts back to $R(Hybrid)_{BC}$ terms and may explain why it does not perform as well as $R(A_h)$ V4.

The largest improvements in rain estimation are seen when $R(Synth)_3$ is applied across the entire PRECIP campaign. $R(Synth)_3$ produces MBR closest to 1 when compared to $R(Hybrid)_{BC}$ and $R(A_h)$ V4 and improves on MAE and CC when compared to $R(A_h)$ V4 (Table 2.2). Much of the overestimation at low gauge amounts as evidenced by the high FPR and crossover in $R(A_h)$ V4 is drastically reduced leading to the improved MBR. It is important to note, however, that each rain rate estimator, $R(Hybrid)_{BC}$, $R(A_h)$ V4, and $R(Synth)_3$, overestimate rainfall at low gauge amounts (Fig. 2.12). This overestimation in $R(A_h)$ V4 and subsequently, $R(Synth)_3$, is likely attributable in part to remaining clutter. The influence of clutter is inferred from a reduction in overestimation found in $R(Synth)_3$ when compared to $R(A_h)$ V4, where the R(Synth) algorithm incorporates an initial PID-based check to attempt to reduce the impact of clutter, leading to performance fairly close to $R(Hybrid)_{BC}$ in this rain category. $R(A_h)$ V4 performs better when rainfall totals exceed 20 mm with $R(Hybrid)_{BC}$. $R(Hybrid)_{BC}$ and $R(Synth)_3$ perform similarly beyond this range, but at the most extreme rainfall totals (e.g., $>$ 50 mm), $R(Hybrid)_{BC}$ performs noticeably worse than $R(Synth)_3$. In the context of error, $R(Hybrid)_{BC}$ excels at every rainfall accumulation category with $R(Synth)_3$ outperforming $R(A_h)$ V4 at low rainfall accumulations and vice versa at high rainfall accumulations (Fig. 2.12b).

The remaining challenges in $R(Synth)_3$, via incorporating $R(A_h)$, are likely still owing

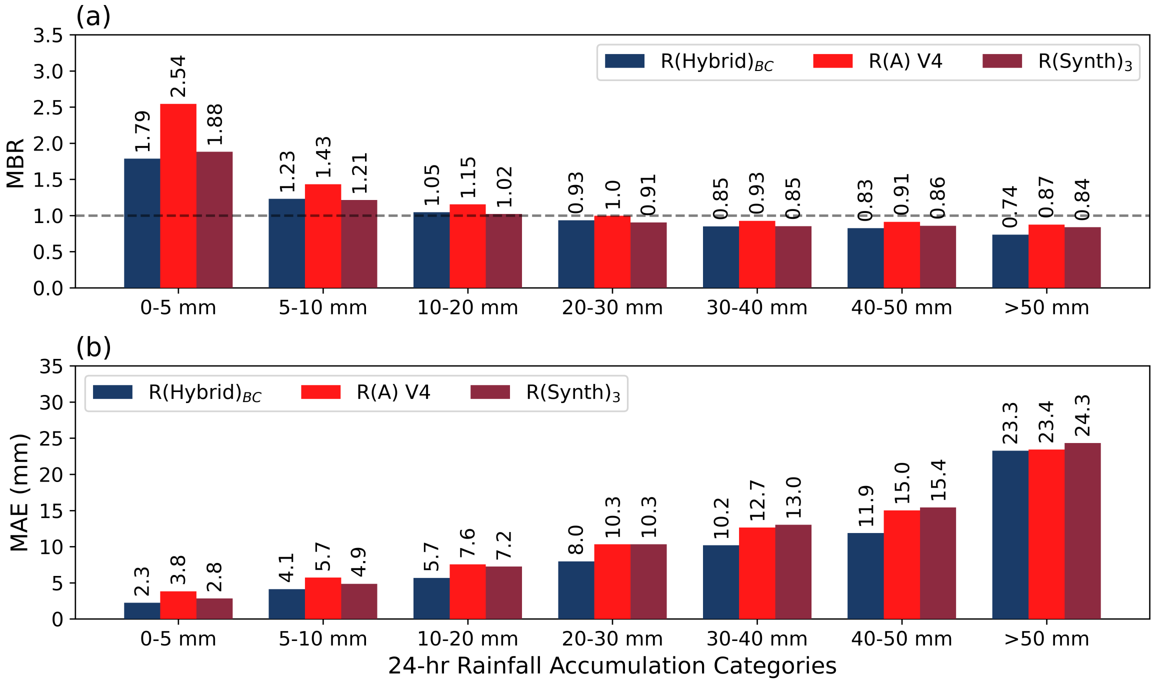

Figure 2.12: Rain gauge and radar rainfall retrieval comparisons of (a) MBR and (b) MAE for $\mathrm{R(Hybrid)_{BC}}$, $\mathrm{R(A_h)}$ V4, and $\mathrm{R(Synth)_3}$ categorized by rain gauge daily rainfall accumulations (mm).The dashed line in (a) represents the 1.0 MBR line.

to clutter producing erroneous rain rates, which would be expected to be cumulatively problematic downstream of remaining ground clutter given the path integration required for the ZPHI method. Therefore, the 50th, 75th, and 90th quantiles of 1-hr rain gauge rainfall accumulation and radar rain rate in units of mm hr^{-1} are compared spatially across the S-Pol domain (Fig. 2.13). From this spatial, intensity viewpoint, $\mathrm{R(Hybrid)_{BC}}$ underestimates at each quantile with no clear spatial trend (Fig. 2.13a-c), up until the 90th quantile in which there are points of overestimation in the high terrain. $\mathrm{R(A_h)}$ V4 and $\mathrm{R(Synth)_3}$ show similar trends to each other in the 50th and 75th quantiles with comparatively better bias compared to $\mathrm{R(Hybrid)_{BC}}$, but far greater variability in which locations over- and underestimate rainfall away from and near the radar, respectively (Fig. 2.13d, e, g, h). Overestimation becomes most prevalent at the highest quantile (i.e., highest rain intensities) with some locations estimating double or more than that of the gauges within an hour (Fig. 2.13f, i). This overestimation occurs predominantly near the radar, but not exclusively in the directions of the mountains; suggesting that remaining near-surface ground clutter is degrading the performance of $\mathsf{R}(\mathsf{A_h})$ V4 and thus $\mathsf{R}(\mathsf{Synth})_3$.

2.7 Discussion

With the steep topography and wide ranges of rainfall intensities and durations observed by S-Pol during PRECIP, it was thought that $\mathsf{R}(\mathsf{A_h})$ would mitigate the effects of partial beam blockage and excel at estimating high rain rates. Within the context of IOP 1, with both high intensity rainfall and long duration of light precipitation, $\mathsf{R}(\mathsf{A_h})$ was found to provide improved rain estimates compared to $\mathsf{R}(\mathsf{Hybrid})_{BC}$. However, when incorporating data over the entire campaign, $\mathsf{R}(\mathsf{Hybrid})_{BC}$ overall performed better, warranting the creation of $\mathsf{R}(\mathsf{Synth})$ to incorporate the strengths of both $\mathsf{R}(\mathsf{A_h})$ V4 and $\mathsf{R}(\mathsf{Hybrid})_{BC}$. While $\mathsf{R}(\mathsf{Synth})_3$ produced better MBR than $\mathsf{R}(\mathsf{Hybrid})_{BC}$ over the campaign, it still uses $\mathsf{R}(\mathsf{A_h})$ under non-optimal conditions, particularly in regions of remaining clutter.

Prior studies addressed challenges in applying $\mathsf{R}(\mathsf{A_h})$ and ZPHI, including minimum phase shift requirements (e.g., Diederich et al. 2015; Ryzhkov et al. 2022; Zhang et al. 2016), sensitivity to ice and mixed-phase precipitation (e.g., Ryzhkov et al. 2014; Wang et al. 2019; Zhang et al. 2020), sensitivity to ϕ_{dp} processing (e.g., Dufton 2016), and the variance of α with local DSDs (e.g., Seo et al. 2020; Tang et al. 2024; Wang et al. 2019; Zhang et al. 2020). Many of the previous studies applied these methods to operational radars with longstanding clutter climatologies that can be used to greatly mitigate the effects of clutter. S-Pol's deployment during PRECIP was comparatively brief and thus this study uniquely quantified the sensitivity of ZPHI to clutter, highlighting the need for advanced clutter mitigation strategies when applying $\mathsf{R}(\mathsf{A_h})$ to these shorter-term radar deployments.

The remaining clutter in S-Pol's dataset hindered $\mathsf{R}(\mathsf{A_h})$'s performance in a few different ways. As ZPHI requires only Z_h and ϕ_{dp}, the most direct impacts were to these two fields. The largest impact was on ϕ_{dp} as clutter changes the end points, r_1 to r_2, for ZPHI. Clutter near the end points introduces noise that shortens the r_1 to r_2 window which may limit how much phase shift is occurring along the ray. If the clutter is persistent across multiple gates, ϕ_{dp} may be artificially raised or lowered at the ends and impact the PIA. Some of the impacts of clutter on Z_h when applied to ZPHI are similar to impacts of hail on ZPHI (e.g., Ryzhkov et al. 2014). Artificial increases in Z_h not associated with pure liquid rain create both a local and non-local increase in rain rate. Because the ZPHI method requires integration of Z_h along the ray, clutter anywhere along the ray will severely impact rainfall

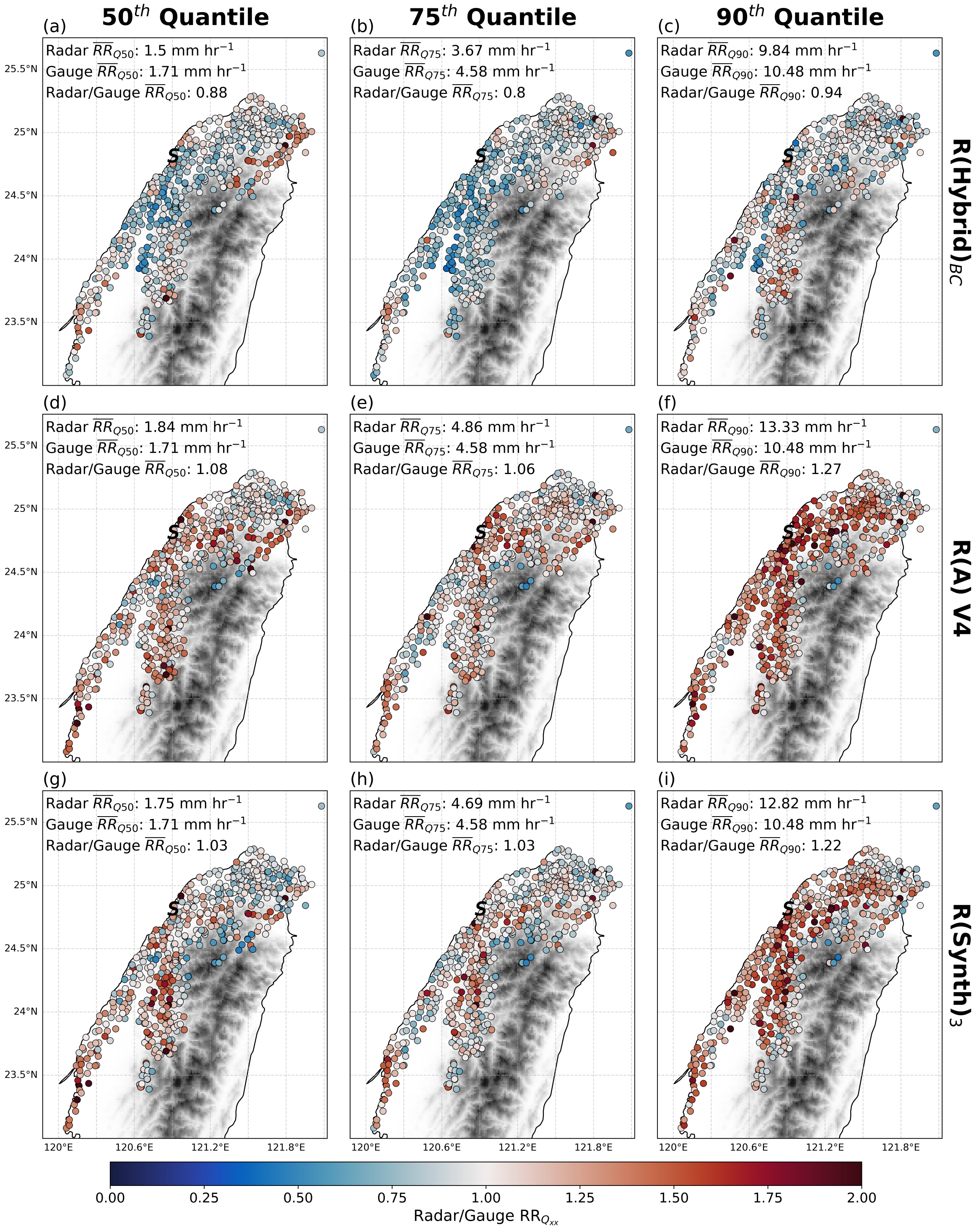

Figure 2.13: Comparisons of 1-hour rainfall accumulation from rain gauges and radar rain rate in units of mm hr^{-1} for (a-c) $\mathrm{R(Hybrid)_{BC}}$, (d-f) $\mathrm{R(A_h)}$ V4, and (g-i) $\mathrm{R(Synth)_3}$ at the (a, d, g) 50th quantile, (b, e, h) 75th quantile, and (c, f, i) 90th quantile. Rainfall accumulation and rain rate quantiles are averaged across all gauge locations and added to the top left corner of each quantile and rain rate estimator.

elsewhere in that same ray. This is why ray segmentation by beam blockage (i.e., $R(A_h)$ V3) inadvertently reduced much of the overestimation near the mountains (e.g., Tang et al. 2024). The segmentation, however, also kept clutter signatures within a smaller portion along the ray.

If clutter was treated like hail through introducing a segment when Z_h increases above 45-55 dBZ (e.g., Ryzhkov et al. 2014), too much segmentation would be introduced. More specifically, there is rarely less than one clutter signature along a ray for S-Pol as it scans over the mountains. Clutter segmentation could therefore introduce 3 or 4 different segments within a short horizontal distance, which would introduce lower phase shift differences within each segment leading to lower skill in $R(A_h)$ (Diederich et al. 2015; Ryzhkov et al. 2022; Tang et al. 2024; Zhang et al. 2020). Therefore, the easiest solution would be to look higher in the atmosphere to reduce the effects of clutter. However, the greater the height above ground, the shorter the path between r_1 and r_2 owing to needing to remain below the melting layer. Shorter endpoints potentially lead to lower phase shift differences along the ray. Furthermore, rain rate retrievals higher above ground may not be representative of the rainfall near the surface. This issue may be leading to underestimation in northern Taiwan as significant clutter may increase the lowest valid elevation angle. This issue has been corrected in operational radars through use of vertical columns of rainfall (e.g., Wang et al. 2014) but requires more of a climatology than S-Pol's PRECIP deployment offers.

Overall, a key outcome of this work is emphasizing the caution required when determining which radar rain rate estimator to apply in a clutter heavy dataset with widely varying rainfall intensities and durations. For the high intensity rain rates as seen in IOP 1, $R(A_h)$ V4 and $R(Synth)_3$ excel regardless of clutter. However, in a full campaign dataset with frequent periods of low intensity rainfall, $R(A_h)$'s performance is reliant on the duration of the event and the type of precipitation present. For low intensity, high duration cases dominated by persistent broad stratiform (i.e., IOP 1 during PRECIP), it is possible to achieve significant enough cumulative phase shift to make $R(A_h)$ applicable. However, for this long-lasting, low-intensity precipitation, such as that which is orographically forced to the southeast of S-Pol, errors can accrue, leading to overestimations from $R(A_h)$ and $R(Synth)$ for the lowest rainfall quantiles. Overall, this issue of remaining clutter in short-term deployments, especially in complex terrain, poses a significant challenge in the applicability of A_h for field campaigns. It remains to be determined what the maximum amount of blockage or blockage slope is in which clutter becomes a limiting factor. Therefore, despite that $R(A_h)$

should perform well when compared to other rain rate estimators (e.g., Ryzhkov et al. 2022), in practice $R(A_h)$'s broader applicability is limited by a myriad of caveats in using ZPHI.

While this study carefully details methods in which to improve $R(A_h)$ performance, from regionally optimizing to ray segmentation, a question still remains in what maximum elevation angle can be applied to ZPHI. Operationally, it is common to stop at 0.5° (Ryzhkov et al. 2022). When tested in this paper, results were improved upon utilizing $R(A_h)$ up to 2.0° accounting for the steep terrain, but performance started to vary above that elevation angle (not shown). Furthermore, one of the implicit assumptions of the ZPHI method is that blockage increases instantaneously as would be common in a building intersecting a radar beam. The challenge, however, is $R(A_h)$'s performance in constantly increasing beam blockage, such as in sloping terrain. If blockage is constantly increasing, a constant Z_h profile would be perceived as monotonically decreasing along the path of a radar beam. In the case of S-Pol's deployment, blockage tended to occur in several small increments along a radial which proved to create problems in $R(A_h)$. Ray segmentation by blockage was one approach to handling this issue, but a more objective method of addressing sloping terrain should be addressed in the future. A component of ZPHI that is more recently being modified is the use of the net α for an entire volume. It can be seen as an oversight to assume the DSD does not change across the radar domain. A proposed method of overcoming this issue is through an azimuthally varying α that depends on Z_h and Z_{dr} along the radial (Ryzhkov et al. 2022), but the method is rather new and requires more testing.

Introduced in this study is the $R(Synth)$ algorithm which would benefit from further enhancement to the $R(A_h)$ algorithm. However, portions of the $R(Synth)$ algorithm and coincidentally, the $R(Hybrid)$ algorithm, could be improved by improving the skill of the traditional rain rate estimators such as R(K_{dp}). At S-band frequencies, the skill of R(K_{dp}) has been shown to slightly outperform $R(A_h)$ in the highest rain rates (e.g., $>$ 60 mm hr^{-1}; Ryzhkov et al. 2022). These rain rate values would exceed those observed in the 90th percentile of PRECIP and may account for the underestimation in that percentile for $R(Hybrid)_{BC}$, thereby necessitating further $R(K_{dp})$ improvement (Fig. 2.13c). More recent work has been performed in enhancing $R(K_{dp})$'s performance in modifying the multiplying term, "e" in Eq. (2.5), including using a large value (e.g., $>$ 70; Li et al. 2023) or scaling it by α (Ryzhkov et al. 2022) which could be considered in future improvements to $R(Hybrid)$ and $R(Synth)$ in a variety of rain intensities.

2.8 Conclusions

In this study, a nearly 3-month dataset of the NSF NCAR S-Pol radar's deployment during PRECIP 2022 was utilized to quantify the performance of $\mathtt{R}(\mathtt{A}_\mathtt{h})$ and its sensitivities for varying intensities of rainfall in a region of complex terrain. A summary of the findings are as follows:

1. $\mathtt{R}(\mathtt{A}_\mathtt{h})$ performed better than $\mathtt{R}(\mathtt{Hybrid})$ in all metrics for an extreme rainfall event, IOP 1, but required multiple modifications including a localized term and ray segmentation by blockage to accomplish this better performance.
2. Over the entirety of the PRECIP field campaign, $\mathtt{R}(\mathtt{A}_\mathtt{h})$ performed worse than $\mathtt{R}(\mathtt{Hybrid})$ across all metrics owing to high overestimation in low intensity rainfall and challenges in rainfall estimates owing to remaining clutter.
3. Development of a novel $\mathtt{R}(\mathtt{Synth})$ algorithm, incorporating strengths of $\mathtt{R}(\mathtt{Hybrid})$ and $\mathtt{R}(\mathtt{A}_\mathtt{h})$, improved on $\mathtt{R}(\mathtt{A}_\mathtt{h})$ across all metrics throughout the campaign, but produced higher error due to using $\mathtt{R}(\mathtt{A}_\mathtt{h})$ when it is not optimal (e.g., clutter).
4. In high intensity rainfall, $\mathtt{R}(\mathtt{A}_\mathtt{h})$ and $\mathtt{R}(\mathtt{Synth})$ are recommended whereas high duration, low intensity rainfall requires greater scrutiny in which rain rate estimator to apply.

Despite remaining challenges in applying $\mathtt{R}(\mathtt{A}_\mathtt{h})$ and ZPHI across the wide range of rainfall intensities and durations sampled during PRECIP, there are still clear advantages over other rain rate estimators, including some DSD invariability and partial immunity to beam blockage. This study highlights areas to explore for future improvement in applying $\mathtt{R}(\mathtt{A}_\mathtt{h})$ in a broader range of scenarios, specifically in finding the limits of ZPHI with regards to elevation angle, sloping terrain, and heavy clutter regions. If these issues can be addressed, $\mathtt{R}(\mathtt{A}_\mathtt{h})$ would become much more accessible for shorter term deployments of radars without long climatologies of clutter analyses.

For this particular deployment, $\mathtt{R}(\mathtt{Synth})$ is the favored outcome for estimating rain rates during PRECIP. The addition of $\mathtt{R}(\mathtt{A}_\mathtt{h})$ to the traditional $\mathtt{R}(\mathtt{Hybrid})$ method highlights the benefits in better estimating high intensity rain rates, which is a key focus of the scientific goals of the PRECIP campaign. If exclusively looking at extreme cases such as

IOP 1, utilization of $R(A_h)$ alone would suffice. Future iterations of the S-Pol dataset will try implementing a regression-based clutter filter (Hubbert et al. 2021) in an attempt to further reduce the impacts of clutter and thus improve rain estimations. In addition to using this $R(Synth)$ rain estimation output for further scientific studies, future work will also use the measurements of A_h for its microphysical inferences. Similar to K_{dp}, A_h is highly proportional to liquid water content, but can be measured without the smoothing of K_{dp} measurements. Therefore, microphysical processes in which the liquid water content changes would be observed through A_h, showing further applications of the efforts of this paper for not only estimating rain rates, but determining the processes leading to those high intensity and long duration extreme events.

Chapter 3

Modeling Rainfall Drop Size Distribution Moments using an S-Band Polarimetric Radar in Complex Terrain

3.1 Introduction

Rainfall observed at the surface is the result of many microphysical processes aloft. Deciphering those processes improves understanding of how extreme rainfall forms, the controls on its intensity and duration, and the impact it has at the surface. The use of ground-based weather radar has been critical in exploring these processes through inferences of microphysical processes and drop size distributions (DSDs; Kumjian et al. 2022; Lee et al. 2023). A continuing challenge, however, is applying these techniques in regions of complex terrain where ground-based disdrometers are uncommon and radar measurements are hindered by beam blockage (Chang et al. 2021; Germann et al. 2022). Understanding the microphysical processes within and upstream of these regions of topography is crucial given the enhancements to rainfall often found near mountains (Lin et al. 2001; Roe 2005).

Radar-inferred DSDs rely on statistical methods applied to moments of the DSDs. The k^{th} order moment, M_k, is described as:

The following Chapter is a reformatted version of Cornejo, I. C., Rowe, A. K., Bell, M. M., and Chang, W.-Y. (2026); Quarterly Journal of the Royal Meteorological Society; (In Revision)

$$M_k[\mathrm{mm}^k \mathrm{m}^{-3}] = \int_0^\infty N(D) D^k dD \tag{3.1}$$

where $N(D)$ is the number concentration in units of mm^{-1} m^{-3} and D is the diameter of drops in units of mm. A reliable method to recreate the DSD is through double moment normalization, which uses two DSD moments (Lee et al. 2023, 2004). The strength of this approach is in its proposed invariance across various DSDs when a generalized gamma (GG) distribution is assumed, as well as its minimization of measurement noise (Lee et al. 2023, 2004).

Given the relationship between moments and drop diameter, the representation of different drop sizes within the DSD can strongly impact moment values. Higher order moments (e.g., M_6, or radar reflectivity) tend to be skewed by larger drops, lower order moments (e.g., M_0, or number of drops) by small drops, and middle order moments (e.g., M_3, proportional to liquid water content, and $M_{3.67}$, approximately proportional to rain rate) by both small and large drops. Therefore, for better representation of the full DSD, both the drizzle mode ($D \leqslant 0.5$ mm) and the precipitation mode ($D > 0.5$ mm) need to be captured (Bringi et al. 2020; Lim et al. 2026; Raupach et al. 2019; Thurai et al. 2019, 2022, 2017, 2025). It is difficult for a single disdrometer to measure both modes, but by combining multiple instruments, the full DSD could be measured and utilized for DSD modeling with GG fitted double moment normalization (Bringi et al. 2020; Lim et al. 2026; Raupach et al. 2019; Thurai et al. 2025). Therefore, in order to best model microphysical processes that pertain to drop multiplication, subtraction, growth, and shrinking, the ability to represent the drizzle mode is paramount.

Although double moment normalization has been shown to be invariant across regions and climates (e.g., Bringi et al. 2020; Lee et al. 2004; Raupach et al. 2019), the use of this model has predominantly been in midlatitude regions. Therefore, ambiguity remains on its applicability to a more subtropical climate such as Taiwan. Taiwan frequently experiences extreme rainfall owing to steep topography, monsoon moisture flux, and the prevalence of the Mei-Yu front; an east Asian, quasi-stationary frontal system known to bring heavy rainfall in the late spring and early summer (Chen and Chen 2003; Chen et al. 2007b; Cornejo et al. 2025, 2024; Henny et al. 2021). The National Science Foundation (NSF)-funded 2022 Prediction of Rainfall Extremes Campaign in the Pacific (PRECIP) was conducted in northern Taiwan as a natural laboratory for studying the ingredients and processes leading to heavy

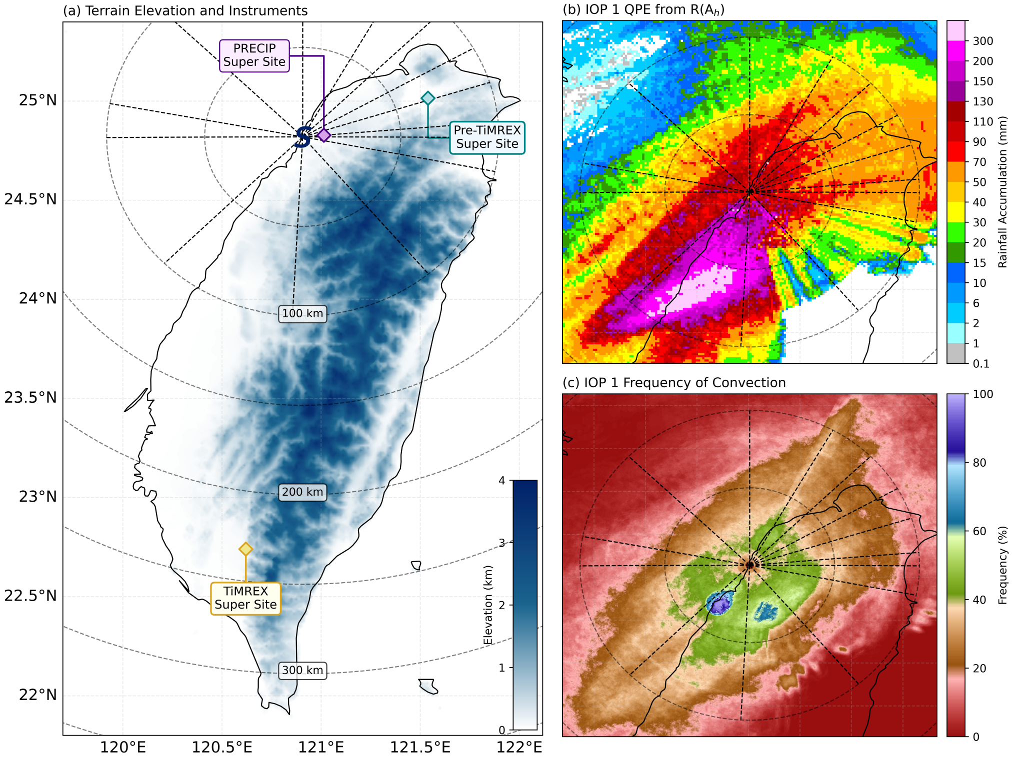

Figure 3.1: Maps of (a) Terrain elevation in km (shaded) with locations of instrument super sites (diamonds) and S-Pol ("S"), (b) rainfall accumulation for IOP 1 from S-Pol using $R(A_h)$, and (c) the unconditional frequency of convection during IOP 1. 50 km range rings and IOP 1 RHI azimuths are included (dashed).

rainfall. One of the instruments operating throughout the campaign on the northwest coast of Taiwan was the NSF National Center for Atmospheric Research (NCAR) S-Pol radar ("S" in Fig. 3.1a), a dual-polarization, S-band (10.557 cm) research radar capable of measuring high spatial and temporal evolution of precipitation over a wide range of intensities. During the 48-hr period of PRECIP's first intensive observation period (IOP 1; 26-28 May 2022; Fig. 3.1b), a Mei-Yu front produced widespread rainfall across S-Pol's domain and a high intensity rainfall maximum to the south of the radar with rainfall totals exceeding 300 mm (Cornejo et al. 2025). Given the close proximity of S-Pol and the high precipitation associated with this IOP, including variability with terrain elevation, the case serves as a suitable candidate for better understanding rain microphysical processes in proximity to topography. Additionally, the breadth of echo types within the case (Fig. 3.1c) allows for a comparison of microphysical processes from stratiform to convective echo.

The Particle Size Velocity disdrometers (Parsivel^2) operated during PRECIP but truncate at small drop diameters, so they are not an ideal input for the double moment normalization model (e.g., Raupach et al. 2019). Therefore, for this study, disdrometer data collected before and during the 2008 Terrain-influenced Monsoon Rainfall Experiment (TiMREX; Chang et al. 2020; Jou et al. 2011) in Taiwan are used for their combined ability to represent the full DSD during a similar season and region (Teal and Yellow diamonds in Fig. 3.1a). More specifically, a 2D Video Disdrometer (2DVD) and a Micro Rain Radar (MRR) that were collocated during both the Pre-TiMREX and TiMREX periods are used. Similar to the methodology of Raupach et al. (2019), the 2DVD serves to represent the precipitation mode whereas the MRR can represent the drizzle mode taking the place of the Meteorological Particle Spectrometer, or MPS, used in Raupach et al. (2019). These combined datasets allow for observations of the complete DSD in a subtropical environment toward localizing the double moment normalization shape parameters for S-Pol's deployment. Then, the complete DSD will be used to create a moment retrieval algorithm for S-Pol to supply the normalization moments necessary for the DSD model.

By modeling the DSD from S-Pol, there is an opportunity to compare traditional inferences of the DSD to the modeled changes within the DSD. More specifically, microphysical fingerprinting is a common application of dual-polarization variables (Kumjian and Prat 2014; Kumjian et al. 2022). By differencing both reflectivity, Z_h, and differential reflectivity, Z_{dr}, between two levels of a vertical column, dominant microphysical processes, or fingerprints, can be inferred. For example, inferred collision coalescence can be linked to increasing Z_h and Z_{dr} towards the surface owing to the increasing size of drops. Although these are qualitative analyses of microphysical processes, there is a burgeoning effort to quantify the changes to the DSD underlying the microphysical fingerprints (Kumjian et al. 2022). By comparing these fingerprints to the double moment normalized DSD model tuned for S-Pol's deployment, this study will explore topographic-dependent microphysical processes within a heavy rainfall event and how these processes impact the DSD.

To address this overarching goal, the objectives of this study are as follows:

1. Recreate the full DSD to produce local shape parameters for a double moment normalized DSD model.
2. Produce a moment retrieval for S-Pol using the disdrometer-derived full DSDs as inputs.

3. Link dominant microphysical processes inferred from fingerprinting to S-Pol retrieved DSDs across varying terrain and echo types.
4. Explore potential impacts of precipitation-sized ice aloft on the near-surface DSDs.

Section 3.2 details the novel methodology required to model and analyze DSDs from S-Pol. Section 3.3 will discuss results of these retrievals as applied to echo types frequency, warm rain fingerprint analysis, and cold rain inferences from IOP 1. Section 3.4 will discuss and contextualize these results. Section 3.5 will conclude with main takeaways and future work.

3.2 Data and Methods

The process to get from the radar polarimetric variables (e.g., Z_{h}, Z_{dr}, etc.) to radar-modeled DSD moments requires a variety of datasets as input to multiple steps, summarized in figure 3.2. Key to this process is that a DSD model must be trained on a disdrometer dataset that represents the region's DSD and captures both the precipitation and drizzle modes of the DSD. The following section will step through this process required to obtain a double moment normalized DSD model with an underlying GG shape, known for its skill in reproducing low-order moments (Bringi et al. 2020; Lee et al. 2023; Lee and Zawadzki 2005; Lee et al. 2004; Maur 2001; Raupach and Berne 2017; Raupach et al. 2019; Thurai et al. 2019; Thurai and Bringi 2018).

3.2.1 Combining DSDs

To obtain the full DSD, multiple instruments are required to observe the drizzle and precipitation modes (Thurai et al. 2017). With a 2DVD operating during the Pre-TiMREX and TiMREX periods, the precipitation mode is well represented. The 2DVD uses two high-speed cameras at orthogonal angles to capture projections of hydrometeors as they fall through the sampling volume (Kruger and Krajewski 2002). These projections and their coincident fall speeds are recorded into 1-minute temporal resolution DSDs with 0.1 mm equivolume diameter class widths, maximum drop size of 10 mm, and quality control (QC) procedures following Chang et al. (2020). As the 2DVD has a tendency to under-represent small drops (e.g., < 0.6 mm via Tokay et al. 2001), it is only implemented for the precipitation mode.

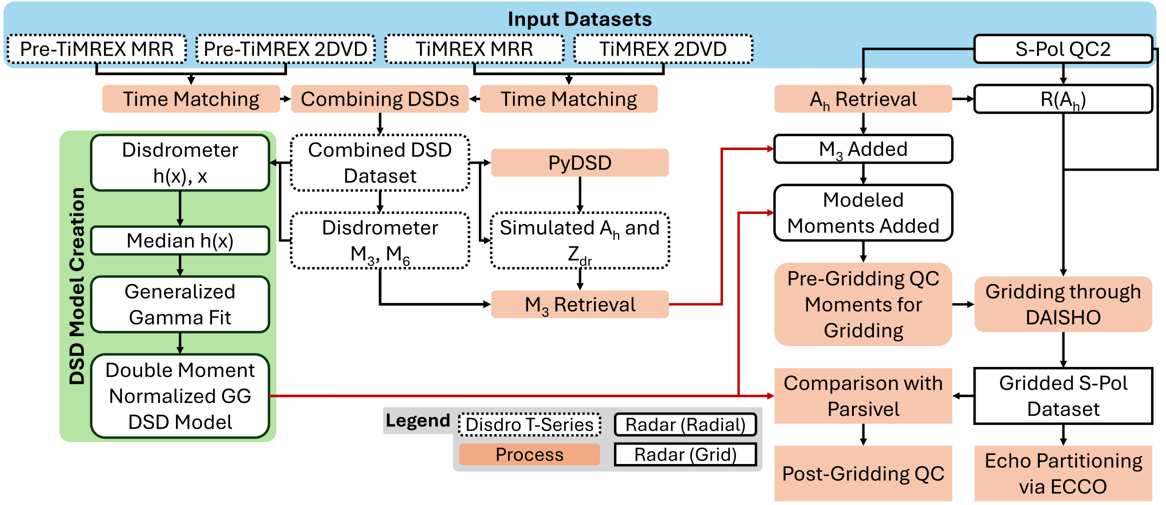

Figure 3.2: Flow chart highlighting the steps taken to get from the input datasets to gridded S-Pol moments and echo partitioning.

An MRR collocated with the 2DVD in both the Pre-TiMREX and TiMREX periods (“M5” in Chang et al. 2020) is utilized to observe the drizzle mode. The MRR is a vertically pointing, frequency modulated continuous wave Doppler radar (Löffler-Mang et al. 1999) operating at 12.5 mm (24 GHz), providing vertical profiles of reflectivity and mean Doppler velocity with a 3-dB beamwidth of 3°. The vertical and temporal resolution of the MRR is 10 m and 1 min, respectively. The DSD is obtained using the Doppler power spectrum at 30 m above the MRR to avoid ground clutter contamination with fixed intervals of 0.2 m s^{-1} between 0.7 m s^{-1} and 9.7 m s^{-1}. An altitude correction is factored into the fall velocity-diameter relationship as described by Chang et al. (2020). The collocated 2DVD is utilized to correct biases in the MRR’s $N(D)$ measurements after a time-lag correction was applied (“Time Matching” in Fig. 3.2), both described in Chang et al. (2020). The direct inversion of the vertical Doppler power spectrum allows for high sensitivity to small drops (Chang et al. 2020). That being said, the MRR is used only to represent small drops as attenuation by large drops at this wavelength prohibits reliable estimates of the precipitation mode. While the instrument has a higher measurable minimum diameter compared to an MPS used in Raupach et al. (2019) (0.23 mm vs. 0.05 mm), the MRR is capable of capturing drizzle mode, including no truncation at small drop sizes and a “shoulder”, or the transition between drizzle and precipitation (Chang et al. 2020). Both the 2DVD and MRR operated between 18 April - 8 May 2008 (Pre-TiMREX) and 16 May - 30 June 2008 (TiMREX) providing 19,851 minutes of data with measurable rain rates (> 0.0 mm hr^{-1}) to appropriately capture the DSD.

The average DSD for each disdrometer and an example 1-min DSD is shown in figure 3.3a and 3.3b, respectively. When averaged, there is good agreement between MRR and 2DVD across most diameters except in the smallest drops (< 1.0 mm) and largest drops (> 4.0 mm). While a single diameter transition between the two disdrometers could be applied as in the case of Raupach et al. (2019), this may produce an unphysical gradient in $N(D)$ as would be in the case of the example DSD (Fig. 3.3b). To alleviate this gradient, a linearly scaling crossover is applied between the two disdrometers, following a process similar to that of Lim et al. (2026). The relative bias of $N(D)$ at linearly interpolated diameter intervals between the two time-matched disdrometers was found to be minimized between 0.7 and 1.2 mm (not shown). Therefore, to combine the two DSDs, $N(D)$ is linearly interpolated between these diameter intervals, with MRR representing diameters 0.7 mm and 2DVD representing diameters 1.2 mm (dotted lines in Fig. 3.3a, 3.3b). This combined DSD dataset will hereafter be labeled as MRR+2DVD. The combined MRR+2DVD retains both the high M_0 values from the MRR and the high M_6 values from the 2DVD with middle moment order values (i.e., M_2 - M_4) larger than both separate disdrometers in the example DSD (Fig. 3.3c).

3.2.2 DSD Model Creation

With this combined DSD dataset, the DSD model can now be created (“DSD Model Creation” in Fig. 3.2). Double moment normalization allows the representation of the DSD by a combination of two of its moments and a unitless, double moment normalized DSD function $h(x)$ that describes the distribution shape (Lee et al. 2004). The DSD is written as (Lee et al. 2004):

$$N(D) = M_i^{\frac{j+1}{j-i}} M_j^{\frac{i+1}{i-j}} h(x) \tag{3.2}$$

$$x = D M_i^{\frac{1}{j-i}} M_j^{\frac{-1}{j-i}} \tag{3.3}$$

with i and j as the two normalization moment orders and x as the double moment normalized diameter.

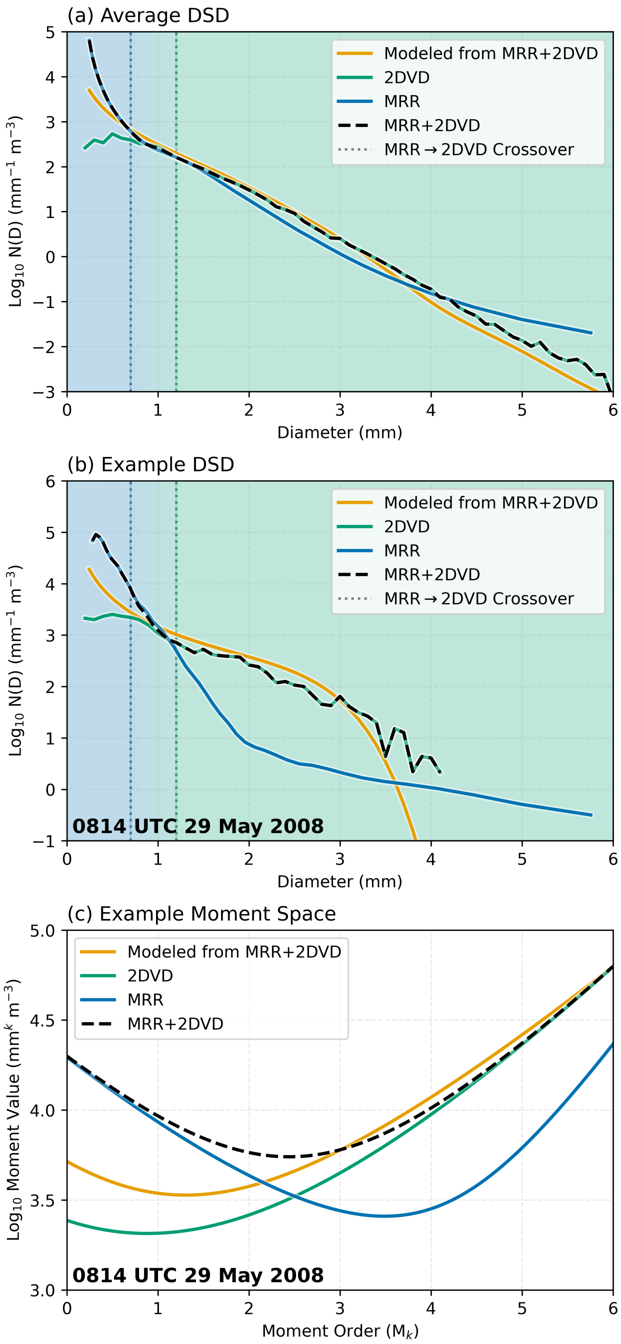

Figure 3.3: The (a) average DSD, (b) an example DSD, and (c) a corresponding example moment space from the 2DVD (green), MRR (blue), combined MRR+2DVD (black dashed), and modeled DSD using the MRR+2DVD (yellow). The background fill and dotted lines in (a, b) indicate the crossover between the MRR and 2DVD when combining disdrometers.

The function $h(x)$ is determined from individual observed DSDs. When modeled under an assumed shape, it takes the form of $\hat{h}(x)$. The shape of $\hat{h}(x)$ used within this study will be the generalized-gamma function, as suggested in Lee et al. (2004) for its flexibility in representing a wide variety of DSDs. Additionally, it has since been shown to better fit DSDs that include a drizzle mode as opposed to the standard gamma model when the shape parameter is allowed to be negative (Thurai and Bringi 2018). The GG $\hat{h}(x)$ function can be written as:

$$\hat{h}(x) = c\Gamma_i^{\frac{j+c\mu}{i-j}} \Gamma_j^{\frac{-i-c\mu}{i-j}} x^{c\mu-1} e^{-(\Gamma_i/\Gamma_j)^{\frac{c}{i-j}} x^c} \tag{3.4}$$

where c (unitless) and μ (unitless) are shape parameters and Γ is the gamma function expressed as $\Gamma_{i|j} = \Gamma(\mu + (i|j)/c)$ (Lee et al. 2004). Therefore, for a given double moment normalization pairing, one only needs to find c and μ to describe the underlying shape of the DSD. For this study, we will use the 3^{rd} and 6^{th} moments for normalization owing to their close relationships to polarimetric variables available at S-band frequencies, prior utilization in radar DSD retrievals, and the spacing between moment orders that provides greater information of the full DSD compared to moment order pairings that are too close (Lee et al. 2004; Raupach et al. 2019; Shin et al. 2023).

To determine the shape parameters used for our model, the MRR+2DVD dataset is subset using two conditions: (1) include 1-min DSDs that have MRR and 2DVD rain rates > 0.1 mm hr^{-1} (following Raupach et al. 2019) and (2) 1-min DSDs must have peaks in $N(D)$ at diameters < 0.5 mm. The second condition is used to remove DSDs where the MRR does not result in a drizzle mode owing to instrument noise. Of the 19,851 minutes of MRR+2DVD DSDs with rain rates > 0.0 mm hr^{-1}, the first condition removes 8201 minutes and the second condition removes 707 minutes resulting in 10,943 minutes of DSDs.

The $h(x)$ function and x are calculated from these combined (i.e., full) DSDs using their 3^{rd} and 6^{th} moments and plotted as a 2-D histogram (Fig. 3.4). The median $h(x)$ is calculated for dx = 0.05 intervals as described by Raupach et al. (2019) (black curve in Fig. 3.4). The shape parameters to the generalized gamma function are then found using a least squared regression on the median $h(x)$ values (values shown in Fig. 3.4). Median $h(x)$ values that are 0 are not included in the curve fitting (e.g., Lee et al. 2004). The shape of the median curve compared to the generalized gamma function derived in Raupach et al. (2019), as well as their respective shape parameters, shows remarkable resemblance. This highlights

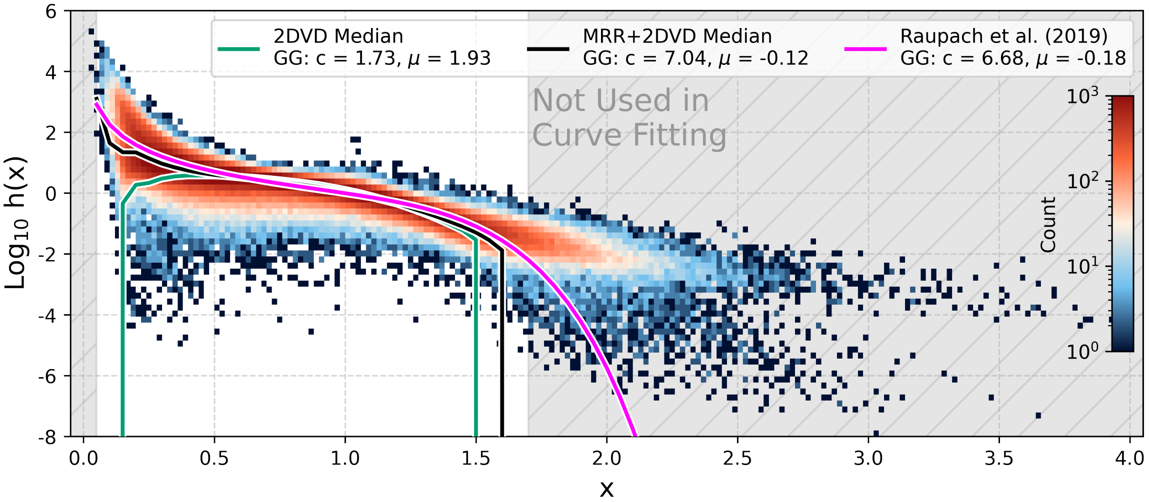

Figure 3.4: 2-D histogram of x and $\mathrm{Log}_{10}\ h(x)$ calculated from the subset MRR+2DVD dataset using M_3 and M_6. Lines represent the 2DVD median fit (green), MRR+2DVD median fit (black), and the Raupach et al. (2019) fit (pink). Each contains the corresponding generalized gamma shape parameters in the legend. Regions that aren't used in the curve fitting process are shaded in grey.

the invariance of the double moment normalized generalized gamma DSD model across different climates (e.g., Taiwan and continental US). Additionally, when the results of the 2DVD alone are included, we find that the MRR is necessary for capturing the drizzle mode (approximately $x < 0.5$). With these steps, the "DSD Model Creation" portion of the process (Fig. 3.2) has been completed.

The model is applied to M_3 and M_6 of MRR+2DVD to evaluate its performance by comparing model-derived moments to the actual ones of MRR+2DVD (Table 3.1). This works on the assumption that the radar we apply this model to will have the capacity to retrieve M_3 and M_6 accurately, therefore anticipating errors in retrieved moments by the radar once applied. The statistical metrics used are correlation coefficient (CC), root mean square error (RMSE), and mean bias ratio (MBR) as defined by:

$$CC = \frac{\sum_{i=1}^{n}(Y_i - \overline{Y})(X_i - \overline{X})}{\sqrt{\sum_{i=1}^{n}(Y_i - \overline{Y})^2 (X_i - \overline{X})^2}} \tag{3.5}$$

$$\mathrm{RMSE} = \sqrt{\sum_{i=1}^{n} \frac{(Y_i - X_i)^2}{n}} \tag{3.6}$$

$$\mathrm{MBR} = \frac{\overline{X}}{\overline{Y}} \tag{3.7}$$

with X and Y being Log_{10} moment values from the modeled DSDs and directly from the MRR+2DVD, respectively. We find that while the model is highly correlated with the MRR+2DVD in M_3 and greater, there is still reduced skill at low order moments. This result is similar to RMSE in that there is the most error in M_0. That being said, the amount of error will tend to be about 0.39 dB of error of underprediction as noted by the MBR. These results can somewhat be explained in the average and example DSD in figure 3.3. While the average and example modeled DSD produces a peak in $N(D)$ at small drop sizes, the average and modeled DSDs do not achieve as high of a magnitude as the MRR+2DVD. When converted into the moment space, the model will result in underproduced M_0, however skill improves near the normalization moments, M_3 and M_6. Decreasing skill in modeling moments furthest from the normalization moments is a known drawback to the double moment normalized DSD model (Lee et al. 2004; Raupach et al. 2019). As the intended purpose of this analysis is vertical evolution of the DSD, we have found that errors and biases will tend to cancel out.

Table 3.1: Statistics on Log_{10} DSD moment values using 2DVD+MRR as truth and modeled DSDs using 2DVD+MRR's M_3 and M_6 as the test.

	M_0	M_1	M_2	M_3	M_4	M_5	M_6
CC	0.840	0.924	0.985	1.000	0.999	0.999	1.0
RMSE	0.394	0.255	0.111	0.013	0.041	0.032	0.001
MBR	0.989	0.980	0.985	0.996	1.002	1.003	1.000

3.2.3 M_3 Retrieval for S-Pol

For the DSD model to be applied to S-Pol data, S-Pol must be able to retrieve the two normalization moments, and M_6. M_6 is more straightforward to implement as Z_h in linear units is directly proportional to M_6 at S-band frequencies. An M_3 retrieval for S-Pol's frequency is developed using A_h and Z_{dr} similar to Bringi et al. (2020). A_h is proportional to liquid water content (LWC) and M_3 at S-band frequencies (Ryzhkov et al. 2014), and Z_{dr} provides information about the underlying DSD shape inherent to M_3 (Raupach and Berne 2017). To create an $M_3(A_h, Z_{dr})$ relationship for S-Pol (i.e., "M_3 Retrieval" in Fig. 3.2), PyDSD and PyTmatrix were implemented to simulate polarimetric variables from the MRR+2DVD dataset (Hardin and Guy 2017; Leinonen 2014). The simulation setup is similar to that of Cornejo et al. (2025) in representing characteristics of S-Pol and Taiwan.

The S-Pol retrieval of M_3 streamlines the methodology of Bringi et al. (2020). M_3 directly computed from MRR+2DVD was used to test against retrieved M_3 values computed from A_h and Z_{dr}. Whereas Bringi et al. (2020) followed a multi-step procedure relating A_h and Z_{dr} to mass-weighted diameter and rain water content to reduce parameterization error, this study uses the final form of their M_3 retrieval ($M_3 \propto A_h/f(Z_{dr})$) as a starting point. Multiple forms of rational and polynomial functions are tested with coefficients determined by least squared regression of the retrieved M_3 against the MRR+2DVD M_3. After trial and error, the following relationship is determined:

$$M_3 = \frac{2.277 \times 10^6 A_h^{0.999}}{5.858 + 1.997 Z_{dr}} \approx \frac{1.14 \times 10^6 A_h}{2.93 + Z_{dr}} \tag{3.8}$$

The retrieved Log_{10} M_3 shows high skill when compared to the MRR+2DVD Log_{10} M_3 with a CC of 0.999, RMSE of 0.009 dBmm^3 m^{-3} and MBR of 0.996. Therefore, there is confidence in applying this M_3 retrieval on S-Pol.

3.2.4 Gridding and Modeled DSD Performance from S-Pol

With an M_3 retrieval and a tuned DSD model developed (i.e., "M_3 Retrieval" and "DSD Model Creation" in Fig. 3.2), the final step is application of both into S-Pol. S-Pol operated during PRECIP using a 12-min scan cycle which contained two separate surveillance scans (SUR1 and SUR2) and range height indicator scans (RHI) at the following azimuthal angles during IOP 1: 0, 29, 45, 60, 72, 85, 90, 101, 140, 183, 225, 270, 281, and 315° (dashed in Fig. 3.1). RHIs are primarily used for this study owing to their higher vertical resolution, which operated with a 0.92° beamwidth, 6° s^{-1} scan rate, and 150-m gate spacing.

This study uses the S-Pol V2 quality-controlled dataset (NCAR/EOL S-Pol Team 2024) that includes an adaptive clutter filter. Details on the quality control procedures in the V1 version of the dataset can be found in Dixon et al. (2023) and a summary of the enhancements made in V2 can be found in Cornejo et al. (2025). The S-Pol dataset is analyzed in this study using the NSF-supported Lidar Radar Open Software Environment (LROSE) - “Colette” (DeHart et al. 2025) to grid and accumulate the SUR scan rain rates (i.e., Fig. 3.1b, c) and the Python ARM Radar Toolkit (Py-ART; Helmus and Collis 2016) for data visualization.

For this study, A_h is retrieved using a modified form of the self-consistent ZPHI method (Cornejo et al. 2025; Ryzhkov et al. 2014, 2022; Testud et al. 2000; Zhang et al. 2020). Specific modifications made to the ZPHI method for this deployment of S-Pol include localization of the term and segmented calculation of A_h by terrain blockage. For more details on the A_h retrieval implemented to S-Pol, see Cornejo et al. (2025). A_h has been applied for the purposes of rain rate retrieval (SUR and RHI scans) and DSD retrieval (RHI only). A_h and the rain rate retrieval, $R(A_h)$, are calculated for all elevation angles as opposed to the 2° used in Cornejo et al. (2025). The resulting rain rate relationship used by S-Pol is as follows (Cornejo et al. 2025):

$$R(A_h) = 3654A_h^{1.03} \tag{3.9}$$

In addition to the many QC checks implemented in Cornejo et al. (2025), several more QC procedures were implemented to the RHIs before gridding to reduce contamination of the gridded output (“Pre-Gridding QC Moments for Gridding” in Fig. 3.2). The first condition is that the differential phase shift within each segment as described in Cornejo et al. (2025) must be greater than 1 deg as the ZPHI method has been shown to become less reliable when phase shift is low for S-band frequencies (Cornejo et al. 2025; Ryzhkov et al. 2014, 2022; Zhang et al. 2020). The second condition is that gates are removed where:

$$|10\mathrm{Log}_{10}(M_6) - Z_h| \geqslant 10\mathrm{dBZ} \tag{3.10}$$

This condition is used to ensure that the DSD modeled Z_h does not vary too greatly from the observed Z_h.

For each RHI azimuth angle, the base polarimetric moments and DSD moments 0 through 6 are gridded using the Daisho.jl open source software package (`https://github.com/csu-tropical/Daisho.jl`). The interpolation uses a beam power weighting that is designed to more accurately represent the volume of each radar measurement compared to linear or distance weighting used in prior gridding techniques. The weighting assumes a Gaussian beam shape with an increasing radius of influence with range, such that the weight given to any radar gate for a grid point exponentially decays from the beam center to the grid point location using spherical geometry. A linear weight is used in the range direction with a fixed radius of influence. The weighting closely matches the power distribution of the radar beam, allowing for finer detail closer to the radar and coarser detail at longer range similar to the radar volume itself. Z_h and Z_{dr} are interpolated using their linear equivalents. To infer hydrometeor type as well as distinguish non-meteorological echo, the NSF NCAR fuzzy logic particle identification (PID) algorithm is gridded using the nearest gate rather than beam weighting (Vivekanandan et al. 1999). Each gridded RHI had a grid spacing of 250-m in both range and altitude above the radar antenna.

To qualitatively assess S-Pol's retrieval of M_3 and other modeled moments, a subset of the RHI data collected at the 85° azimuth is compared with the Parsivel disdrometer at the PRECIP super site located approximately 10 km away from the radar along the azimuth (purple diamond in Fig. 3.1a; "Comparison with Parsivel" in Fig. 3.2). This Parsivel, operated by Taiwan's Central Weather Administration, is a laser disdrometer classifying particles into 32 diameter bins with a minimum and maximum observable diameter of 0.06 and 24.5 mm, respectively. A QC procedure similar to that of Lu et al. (2020) was applied with further details found in Cornejo et al. (2023). The gridded radar measurements are taken at 250-m above sea level (ASL) at the range closest to the Parsivel. Due to spatial offsets and truncation of the Parsivel DSD at small drop sizes (Bringi et al. 2020; Raupach et al. 2019), statistical metrics are not used to assess the skill of the retrievals and models. The objective of this comparison is to ensure the radar captures similar magnitudes of moment values near the correct times and to inform subsequent QC procedures. To better understand how the model represents lower order and middle order moments, comparisons are made between M_0 (Fig. 3.5b) and the mass-weighted diameter, D_m, defined as M_4/M_3 (Fig. 3.5c).

For the M_3 retrieval, there is good agreement between S-Pol and the Parsivel, noting that the peak near 0430 UTC is well captured along with the subsequent drop near 0500 UTC (Fig. 3.5a). Then, between 0700 UTC and 0930 UTC, the retrieval is able to capture similar variability as the Parsivel, not only at this one grid point, but in the surrounding grid points as well (shading). Despite these periods of similarity, there are also periods such as 0600 UTC and the period beyond 0930 UTC where the radar deviates from the disdrometer. In assessing the cause of this deviation, it was determined that these were periods of extensive low-level clutter and noise as inferred by PID, as well as in noisy or negative Z_{dr} (not shown). The lack of negative Z_{dr} data in the simulated MRR+2DVD dataset explains the lack of skill in retrieving M_3 in these periods.

(a) M_3 Time Series

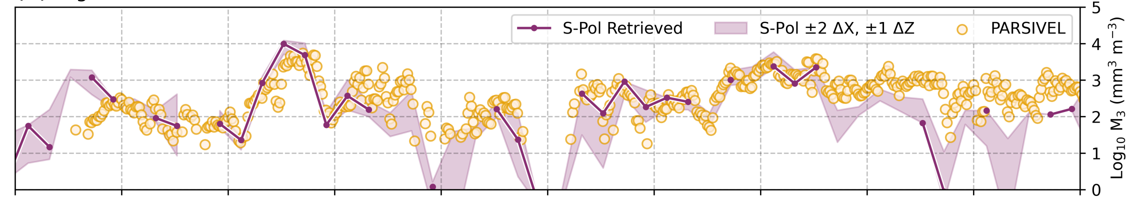

(b) M_0 Time Series

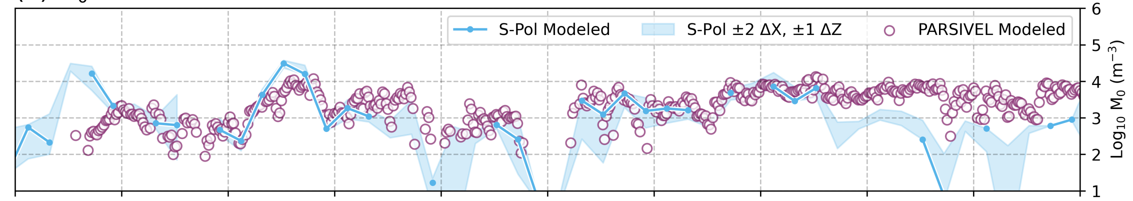

(c) D_m (M_4/M_3) Time Series

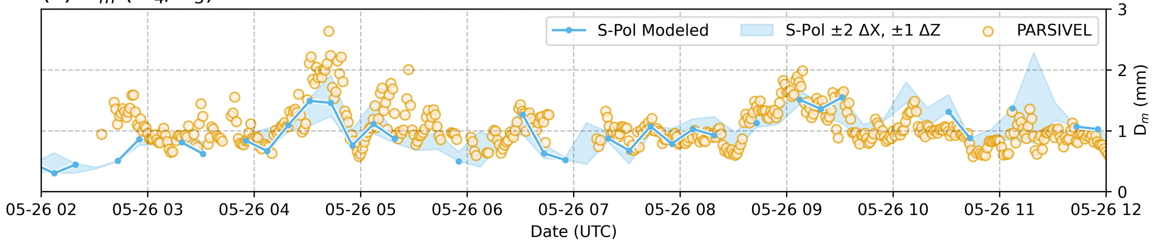

Figure 3.5: Time series comparisons between S-Pol gridded output at 250-m ASL (line), the surrounding grid points (shading), and the PRECIP super site Parsivel (markers). The time series compared (a) S-Pol retrieved M_3, (b) S-Pol modeled M_0, and (c) S-Pol modeled D_m. The Parsivel M_0 output is modeled due to small drop truncation.

A challenge in comparing low order moments such as M_0 is the inability of the Parsivel to resolve small drops resulting in a truncation of the DSD. To compare these low-order moments, M_3 and M_6 from the Parsivel were used as normalization moments in the same DSD model to output an M_0 that includes a drizzle mode (Fig. 3.5b). While this does raise a dilemma in comparing modeled moments from both a radar and a disdrometer, modeling full DSDs from incomplete Parsivel DSDs has been found to be a reasonable correction technique for Parsivel disdrometers (Raupach et al. 2019). For both M_0 (Fig. 3.5b) and D_m (Fig. 3.5c), similarities and deviations between the radar modeled moments and the Parsivel are found in the same periods that the M_3 retrieval performs well and poorly, respectively. This highlights that M_3 is crucial for representing lower and middle order moments within the framework of this double moment normalization.

Informed by this time series analysis as well as a visual assessment of where RHI data is suspect (not shown), additional QC procedures were implemented after gridding to better ensure data quality for analysis ("Post-Gridding QC" in Fig. 3.2). To remove the effects of noise and clutter, grid cells with non-meteorological echo as inferred by PID are removed. Additionally, grid cells with negative Z_{dr} are removed. What is not captured explicitly in the time series are the effects of non-uniform beam filling, partial beam blockage, and beam curvature. To highlight some of these effects and to visualize the post-gridding QC procedures, an example of D_m from an RHI is shown in radial format prior to pre-gridding QC in figure 3.6a and after post-gridding QC in figure 3.6b.

Prior to pre-gridding QC, we find that while there is a coherent structure in D_m, it is marred by inconsistencies between elevation angles and unrealistically high values indicative of near-radar noise (Fig. 3.6a). After pre-gridding QC, gridding, and post-gridding QC efforts, the vertical structure is clearer, and features that previously looked erroneous are removed (e.g., 12.5 km away at 3 km altitude; Fig. 3.6b). The near-radar noise was consistent across many azimuths and is suspected to be a result of issues with the ZPHI method of retrieving Ah in near-vertical radar paths. Therefore, the 5 km closest to the radar are omitted from analysis. In a similar vein, non-uniform beam filling degrades the quality of all radar data with range; therefore, the maximum range for analysis is set at 100 km. Taiwan's mountainous terrain introduces both increased ground clutter as well as partial beam blockage. Elevation data from the Shuttle Radar Topography Mission (van Zyl 2001) is used to omit grid points whose lower edges intersect with the terrain. Similarly, grid points with lower edges that intersect a 0° elevation angle beam are also omitted to reduce near-surface effects. To limit the effects of partial beam blockage, data beyond the highest terrain peak within 100 km of each RHI that is above the 0° elevation angle beam is also omitted. An example of this is found in figure 3.6c whereby the greatest terrain peak is found at 53 km away from the radar, but beyond that, reduced low-level Z_h is observed, indicative of partial beam blockage. While all these procedures do not ensure perfect data quality, they were found to reduce much of the erroneous data and give greater confidence in the analysis of the radar-modeled DSD moments.

3.2.5 Echo Partitioning via ECCO

To assess how DSD moments evolve across different echo types, the Echo Classification from COnvectivity (ECCO) algorithm was applied to the gridded S-Pol reflectivity field ("Echo

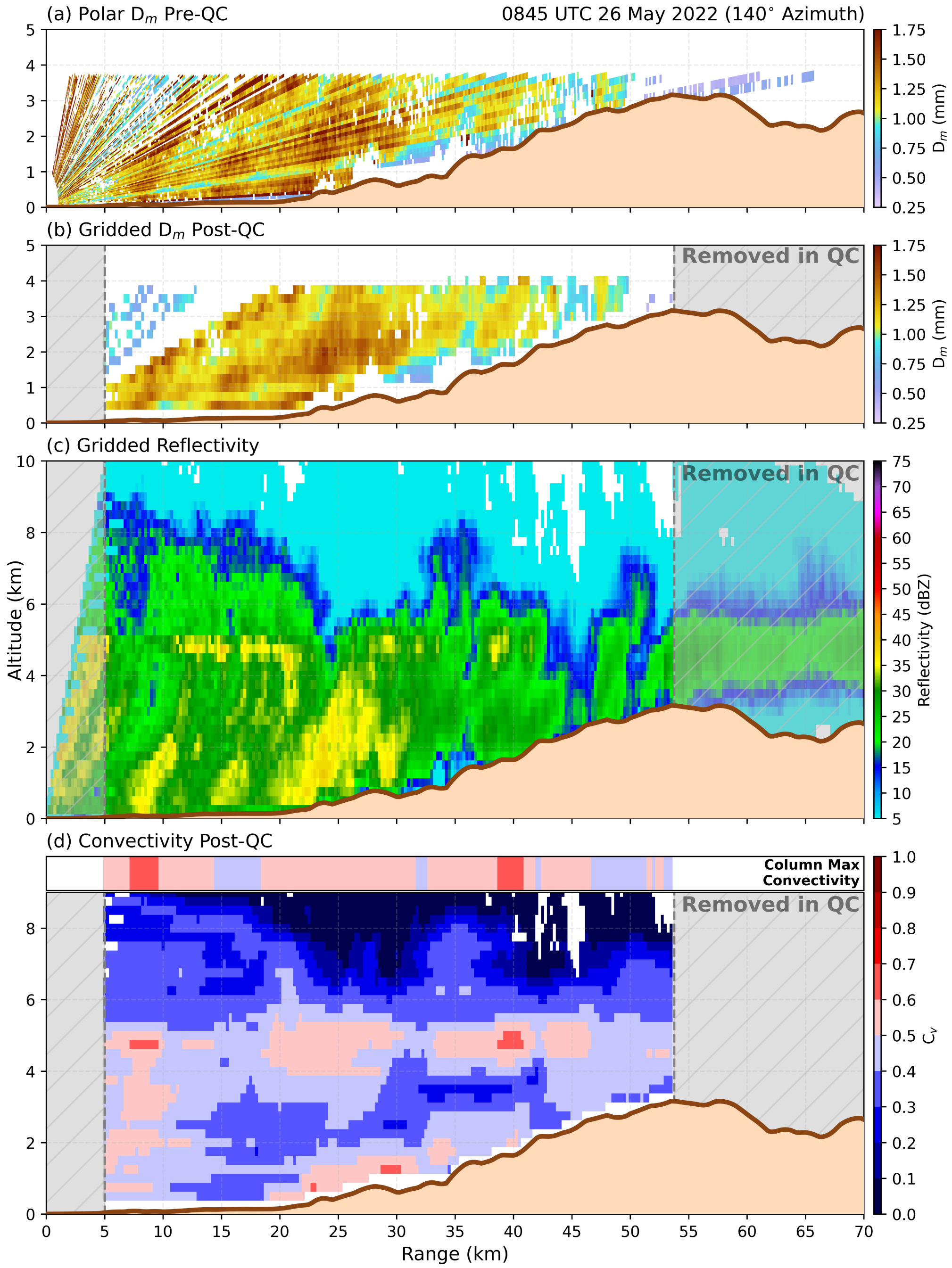

Figure 3.6: An RHI scan from 0845 UTC 26 May 2022 at the 140° azimuth showing (a) D_m prior to preprocessing in radial format, (b) D_m after postprocessing in gridded format, (c) gridded Z_h, and (d) convectivity and column maximum convectivity. For each, the terrain profile has been added.

Partitioning via ECCO" in Fig. 3.2; Dixon and Romatschke 2022; Romatschke and Dixon 2022). The 3-D variant of ECCO is applied to the SUR scans using the default parameters for the purposes of spatial context of echo types relative to the RHI azimuth angles to produce Fig. 3.1c (Dixon and Romatschke 2022). The vertical variant (ECCO-V) is applied to the RHI scans to classify columns as stratiform, mixed, or convective (Romatschke and Dixon 2022). Therefore, the 3-D ECCO is only used on SUR scans to contextualize the RHIs, whereas all echo classification analysis is done using RHI scans and ECCO-V. As echo classification is a somewhat subjective process, parameters for ECCO-V were based on visual assessment as well as prior context for stratiform and convective echo. An example of this assessment would be tweaking parameters to ensure that a weak embedded convective cell within a stratiform band was identified given its local maximum in reflectivity. Simplistically, the ECCO algorithm employs a moving horizontal window in which Z_h texture is calculated based on the homogeneity of Z_h within the window and is then converted to convectivity, C_v, a quantitative measure of how convective a grid point is. The window size used for the gridded S-Pol output is 19 grid points or 2.25 km. To classify echo, C_v was used directly with $C_v = (0.0, 0.4]$ being stratiform, $C_v = (0.4, 0.5)$ being mixed, and $C_v = [0.5, 1.0)$ being convective (e.g., Fig. 3.6d).

For the purposes of this study, echo classification at the individual grid level was not as important as defining the echo classification for the entire column. Therefore, a method was developed to determine the column echo classification. For each column, the maximum C_v is found, but if that value happens to be the first valid value closest to the surface, the next maximum C_v value is found. This step is to avoid erroneous C_v values that can sometimes be found near terrain or at the surface where artificial peaks in Z_h are observed. The max C_v (or second max C_v) is then used to represent the entire column (e.g., Fig. 3.6d).

3.3 Results

3.3.1 Echo Distributions during IOP 1

With the processes represented in the flowchart (Fig. 3.2) complete, a gridded S-Pol dataset of echo classification, rain rate, Z_h, Z_{dr}, PID, and modeled moments is available to address the research objectives through PRECIP IOP 1. As with most Mei-Yu fronts, a combination of broad stratiform regions with embedded convection are evident in this IOP (Cornejo et al. 2024). Specifically, convection is observed upwards of 40% of the 48-hr period for SUR scans (Fig. 3.1c). South-southeast of S-Pol, this frequency exceeds 60% (noting the 80% values to the southwest are contaminated by ground clutter). While the RHIs missed the rainfall maximum to the southwest of the radar, they captured a representative range of rain accumulations, echo types, and terrain elevations in context of the SUR scans during IOP 1 (Fig. 3.1). With the greater vertical resolution of these RHIs, we then can infer the microphysical processes leading to these ranges of rain rates with terrain, including our radar-modeled DSDs. To explore microphysical characteristics as a function of elevation, three elevation groups are defined: ocean (0 km), coast (0 - 0.5 km), and terrain ($>$ 0.5 km). Table 3.2 shows that each elevation group contains $>$ 30% of both stratiform and convective echo with mixed echo making up $<$ 30%. The higher proportion of convection in the coast is linked to the rainfall maximum over the central west coast of Taiwan (Fig. 3.1b). Note that the highest terrain bin ($>$ 0.5 km) primarily covers RHIs at 140° and 183° azimuth (Figure 3.1a), while still capturing a mix of echo classifications.

Table 3.2: Number of gridded RHI columns across the three elevation groups with partitioning for stratiform, mixed, and convective echo classification. Convection is further partitioned into columns with and without graupel observed aloft. Percentages under each partition are relative to the total for the respective elevation group.

	Total	Stratiform	Mixed	Convective	Convective (No Graupel Aloft)	Convective (Graupel Aloft)
Ocean	352091	164388 (46.7%)	70924 (20.1%)	116779 (33.2%)	111866 (31.8%)	4913 (1.4%)
Coast	254222	87370 (34.4%)	52576 (20.7%)	114276 (44.9%)	109785 (43.2%)	4401 (1.7%)
Terrain	73734	25922 (35.2%)	20441 (27.7%)	27371 (37.1%)	25575 (34.7%)	1796 (2.4%)

Separating vertical profiles of Z_h and Z_{dr} for each echo type and elevation group show that the terrain group exhibits a 5-10 dBZ increase in median Z_h at all altitudes relative to the other elevation groups (Fig. 3.7a-c). These observations hint towards an amplification of precipitation near higher terrain. The greatest difference between median Z_h profiles can be found in mixed precipitation, suggesting that the mechanisms that produce mixed echo in the terrain may be different or enhanced compared to lower elevations. In each echo type and elevation group, there is an evident bright band effect with a vertically localized

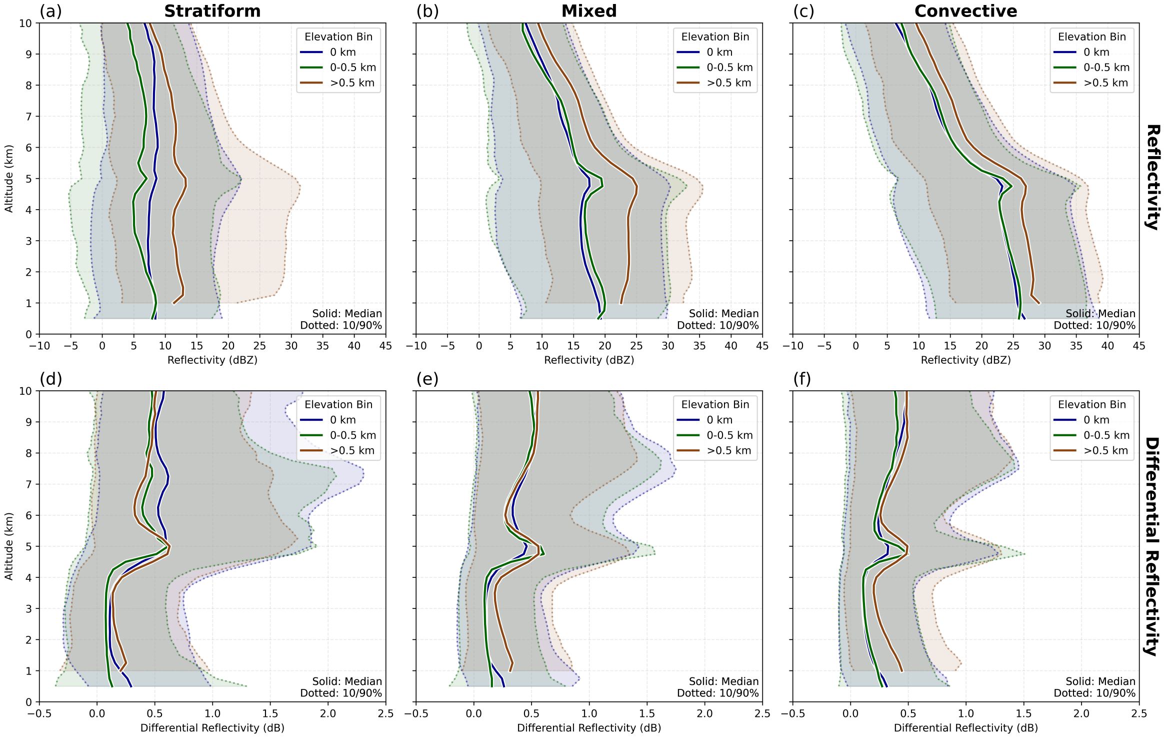

Figure 3.7: Vertical distributions of (a, b, c) Z_h and (d, e, f) Z_{dr} for (a, d) Stratiform, (b, e) Mixed, and (c, f) Convective columns. Solid lines indicate the median at each level while dotted lines indicate the $10^{th}/90^{th}$ percentiles for the ocean (blue), coast (green), and terrain (brown) elevation groups.

increase in reflectivity near 5 km inferring that melting ice occurs in all echo types.

Similar trends emerge in vertical profiles of Z_{dr}, but not throughout the whole column (Fig. 3.7d,e,f). Above the bright band height, median Z_{dr} is similar across all elevation groups for each respective echo type with the greatest differences in stratiform precipitation. However, below the bright band, there is increased Z_{dr} in the terrain relative to the ocean and coast with this being least pronounced in the stratiform echo. This points towards liquid precipitation being more oblate in the terrain relative to the other regions.

Within all echo types and elevation groups, there is a change in both Z_h and Z_{dr} with altitude implying that there is an inherent change to the DSD within the column attributed to a microphysical process. In mixed echo precipitation, there appears to be no change in median Z_h just below the melting layer (~3.5 km) to the middle of the warm rain depth (~2.0 km; Fig. 3.7b), but Z_{dr} increases in this layer for the terrain group (Fig. 3.7e). Below this level, down to 1 km height, Z_h increases towards the surface for the ocean and coast, but decreases for the terrain (Fig. 3.7b). Therefore, different processes are likely occurring within different portions of the warm rain depth (1.0 - 3.5 km). Therefore, the use of microphysical fingerprinting and DSD retrievals will reveal more about the potential differing processes with elevation. Despite the mixed echo having distinct vertical profiles that fall between convective and stratiform echo (Fig. 3.7b, e), further analysis will not include it as there is ambiguity in interpreting microphysical processes within the mixed category as it can consist of echo on the edges of convective cells and/or growth or decaying stages in convection.

3.3.2 Warm Rain Processes

One of the traditional approaches to infer microphysical processes is through their fingerprints, as determined by differencing polarimetric radar variables with altitude (Kumjian and Prat 2014; Kumjian et al. 2022). The most common application is through the ΔZ_h, ΔZ_{dr} phase space for warm rain processes, an example of which can be found in Figure 3.8 whereby Z_h and Z_{dr} are differenced between 1.0 km and 3.5 km ASL and normalized by depth for all convective columns. This depth acts as our total warm rain depth, mitigating data quality issues below 1.0 km and ensuring the A_h retrieval is not compromised by melting hydrometeors above 3.5 km as determined by bright band signatures in Figure 3.7. Each quadrant in this phase space indicates an inferred microphysical process such as collision coalescence when Z_h and Z_{dr} both increase towards the surface, drop break up when Z_h and Z_{dr} both decrease, or a balance of the two when Z_h increases but Z_{dr} decreases. The top left quadrant where Z_h decreases while Z_{dr} increases towards the surface indicates either size sorting or evaporation as large drops remain and small drops are removed from the DSD. Discriminating between the two processes is an ongoing area of study and is a known limitation of fingerprints (Kumjian et al. 2022). Knowledge of the storm structure as well as the environmental thermodynamics are often necessary as in the case of Tam et al. (2022) whereby graupel concentrations aloft, updraft depths and intensities, and warm rain depth all contributed to size sorting magnitudes. Another limitation is that these fingerprints infer the most dominant process meaning there are likely multiple processes occurring within a single volume with inferred changes to the DSD being ambiguous.

To address the ambiguity in the changes to the DSD, modeled DSD moments are added to the analysis (e.g., shaded normalized change in $\mathrm{Log}_{10}M_0$ in Fig. 3.8) to directly compare

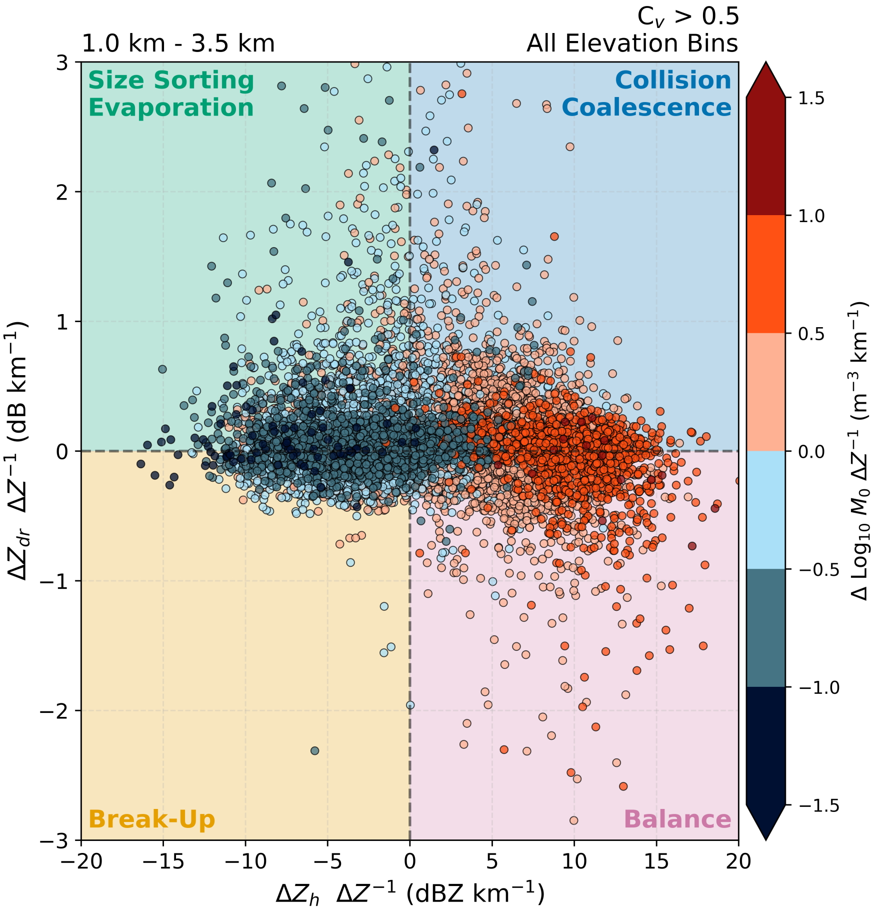

Figure 3.8: ΔZ_h / ΔZ_{dr} phase space for all convective columns normalized by depth with differencing between 1.0 km and 3.5 km ASL. Shading represents the normalized change in $\mathrm{Log}_{10}M_0$ for the same depth. Associated fingerprint names are labeled in each quadrant's corner.

with fingerprints. In adding the information from this modeled moment, there is a notable increase in drops associated with both collision coalescence and balance whereas drops tend to be removed in size sorting/evaporation and break up, contradicting the expected changes to the DSD with these dominant processes (Kumjian et al. 2022). Noting the overlap in points in Fig. 3.8, the phase space is transformed into distributions of normalized ΔM_0 for each fingerprint to better convey the changes in the DSD, and its potential variability, within each process (Fig. 3.9). Furthermore, the analysis is separated into convective and stratiform echo (columns) and elevation groups (rows) as Figure 3.7 showed that Z_h and Z_{dr} profiles vary across echo type and elevation, suggesting different processes. The difference in features noted at different levels of the warm rain depth in Figure 3.7 motivates splitting analysis to two levels, the top of the warm rain depth at 2.0 - 3.5 km and the bottom at 1.0 - 2.0 km (Fig. 3.9, 3.10). In making these changes, we can see that fingerprints are not solely dominated by increases or decreases in M_0, but by a spectrum of change.

In the upper warm rain depth (i.e., 3.5 to 2 km), collision coalescence is the most frequently observed convective fingerprint (Fig. 3.9b, d, f) while balance is the most frequent in stratiform echo (Fig. 3.9a, c) with the exception of the terrain bin where collision coalescence is also the most frequent in stratiform echo (Fig. 3.9f). All collision coalescence inferences are associated with a median increase in M_0 with that increase being amplified when transitioning from stratiform to convective echo. Additionally, the frequency of balance and size sorting/evaporation decreases between stratiform and convective echo, with each fingerprint contributing median increases and decreases in M_0, respectively. With increasing elevation, the changes to M_0 are relatively similar across fingerprints, but the frequency of those fingerprints are different. More specifically, the frequency of collision coalescence increases in stratiform echo with elevation while balance decreases in frequency (Fig. 3.9a, c, e). Additionally, size sorting/evaporation inferences have their greatest frequency in the terrain group for both echo types (Fig. 3.9e, f). Despite collision coalescence and balance making up over 50% of all fingerprints across all echo types and elevation groups, each with median increases to M_0, the net median change to M_0 (grey rows) is near zero suggesting that there is a greater decrease in M_0 from breakup and size sorting/evaporation than there is an increase from collision coalescence and balance.

With little change in M_0 at the top of the warm rain depth and greater changes in the polarimetric profiles at the bottom of the warm rain depth (Fig. 3.7), the lower portion of the warm rain depth is investigated in a similar manner as the upper portion (Fig. 3.10). For this analysis, the terrain group is omitted due to the elevation intersecting with the altitude. Now near the surface, collision coalescence becomes the most frequently occurring fingerprint for both the coast and ocean elevation groups and for both echo types, again with greater increases in M_0 for convection. While collision coalescence and balance still make up over 50% of the convective fingerprints near the surface (Fig. 3.10b, d), the proportion of break up and size sorting/evaporation has increased as compared to aloft (Fig. 3.9b, d) indicating greater variability of processes near the surface. Additionally, there is greater variability in the M_0 outcome for all fingerprints across the different echo types and elevation groups near the surface as noted by the widened interquartile range and 10/90th percentiles when

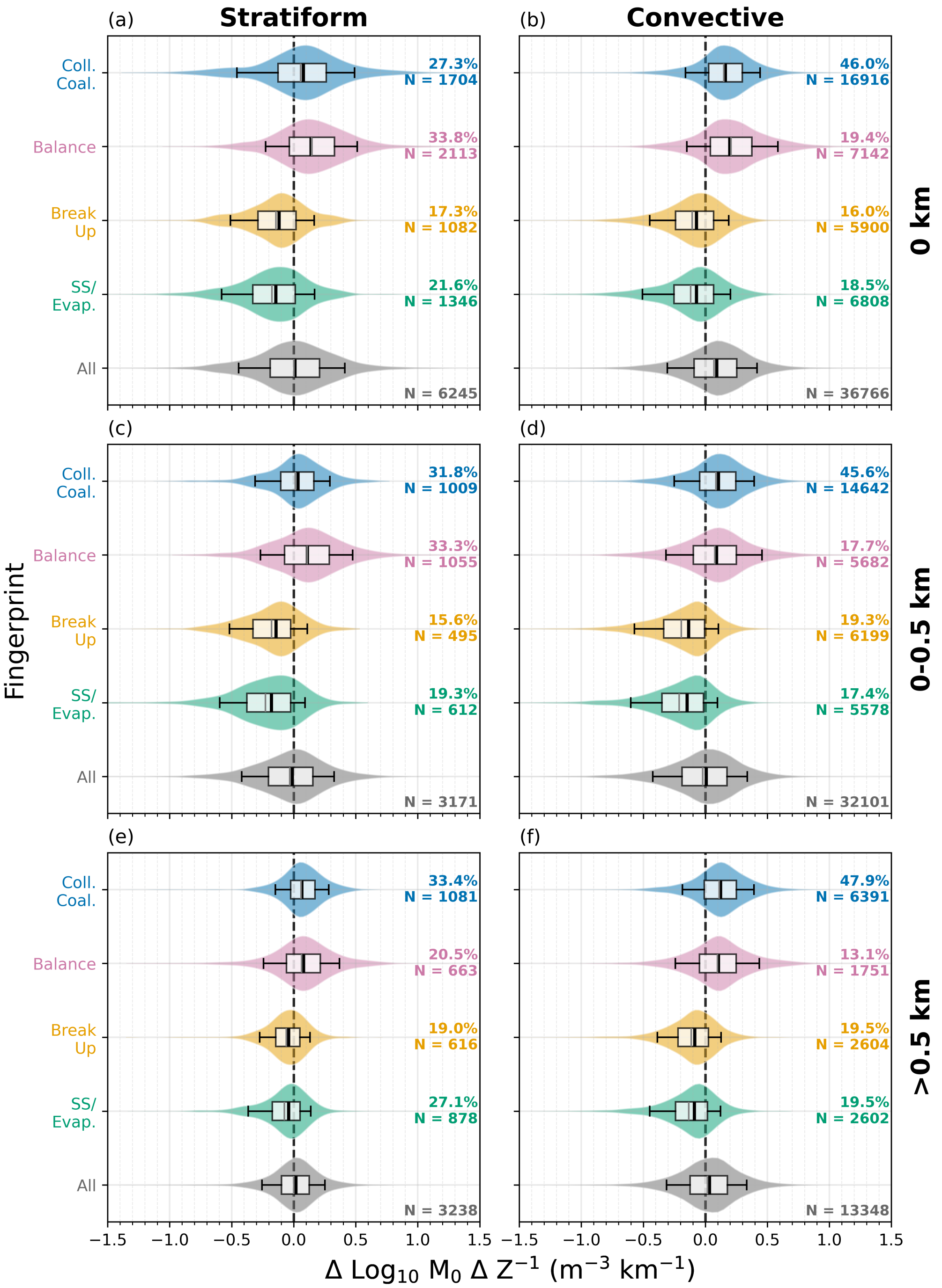

Figure 3.9: Violin plots with embedded boxplots for $\text{Log}_{10}\ \Delta M_0$ between 2.0 km and 3.5 km ASL for each fingerprint in (a, c, e) stratiform and (b, d, f) convective echo. Further categorization by elevation is shown for (a, b) ocean, (c, d) coast, and (e, f) terrain. In the embedded boxplots, whiskers represent $10^{\text{th}}/90^{\text{th}}$ percentiles, boxes represent interquartile range, and the black (grey) lines represent the median (mean). For each fingerprint, the number of columns and their frequency within the respective echo types and elevation group are labeled.

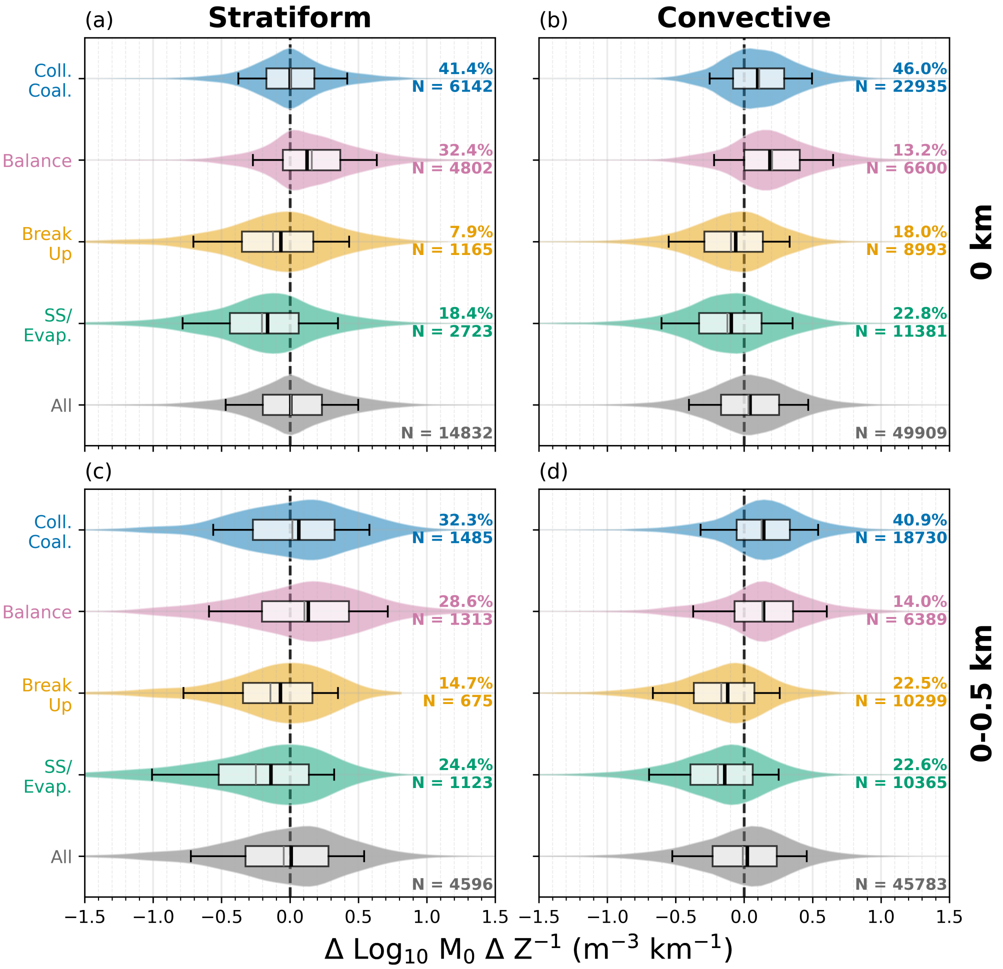

Figure 3.10: As in Fig. 3.9, but between 1.0 km and 2.0 km ASL. The terrain bin is excluded.

comparing Figures 3.9 and 3.10. Similar to the upper warm rain depth, increasing elevation does not produce noticeable changes in M_0 for the same fingerprints, but the frequency of occurrence changes with collision coalescence becoming less prevalent and break up more frequent for the coast compared to over ocean. When looking at the net changes to M_0 near the surface, there is a median increase in M_0 in convective echo (Fig. 3.10b, d) that is not observed in stratiform echo (Fig. 3.10a, c), indicating that the number of drops tend to increase in convective echo and at the bottom of the warm rain depth.

Warm rain fingerprints infer the changes to both the concentration and characteristic size of rain drops within a volume. Therefore, to add to the above analysis of M_0, D_m is utilized to characterize the change in drop size coincident with the fingerprints. When viewed in the upper warm rain depth, there is a net median increase in D_m across all echo types and elevation groups driven by collision coalescence and balance (Fig. 3.11). The median increases in D_m from collision coalescence and drop break up increase for convection compared to stratiform, inferring, as expected, that convective rainfall grows larger drops through the same depth as stratiform rainfall. Also of note is that break up and evaporation/size sorting do not contribute any drop growth or shrinking in the stratiform median for the ocean and coast group (Fig. 3.11a, c), but in the terrain, they tend to shrink drops (Fig. 3.11e).

When applied to the lower rain depth, rather than convective echo producing larger net median increases in D_m when compared to stratiform echo as in Figure 3.11, it is the stratiform echo that has slightly larger net median increases in D_m (Fig. 3.12). This result would imply that stratiform rainfall grows drops closer to the surface whereas convective rainfall grows drops throughout the top of the warm rain depth. Note though that the 10^{th} and 90^{th} percentiles are wider for convective rainfall near the surface (Fig. 3.12b, d) when compared to stratiform rainfall (Fig. 3.12a, c), meaning there is potential for larger near-surface growth in convective precipitation. Whereas median drop growth appeared uniform across collision coalescence and balance in the upper warm rain depth for all elevation groups and echo types (Fig. 3.11), it is clearer near the surface that collision coalescence results in larger median drop growth compared to balance in all but the stratiform coast (Fig. 3.12a, b, d). When elevation increases, there is also a larger decrease in drop size attributed to drop break up for both stratiform and convective echo (Fig. 3.12c, d). For both upper and lower warm rain depth, there is either a net increase or constant change in M_0 with descension, but with a net increase in D_m. This implies that there is both drop generation with concurrent drop growth for this event, regardless of echo type or elevation bin.

What the prior analysis does not show is changes in M_0 and D_m near the surface in the terrain group, the impact these processes and DSD changes have on the resulting rain rate at the surface, and the importance of the magnitudes of M_0 and D_m as opposed to the changes to them. To better understand the relationships between M_0, D_m, and rain rate, Figure 3.13 shows two RHIs containing convection, one over the 183° azimuth where there is high terrain at 0320 UTC 27 May 2022 (Fig. 3.13a, c, e, g) and another over the 225° azimuth over the ocean at 1756 UTC 26 May 2022 (Fig. 3.13b, d, f, h). The two RHIs were chosen for their similar number of convective columns and similar polarimetric characteristics (e.g., Z_h values, PID profiles, inferred fingerprints). Two regions of interest stand out with similar

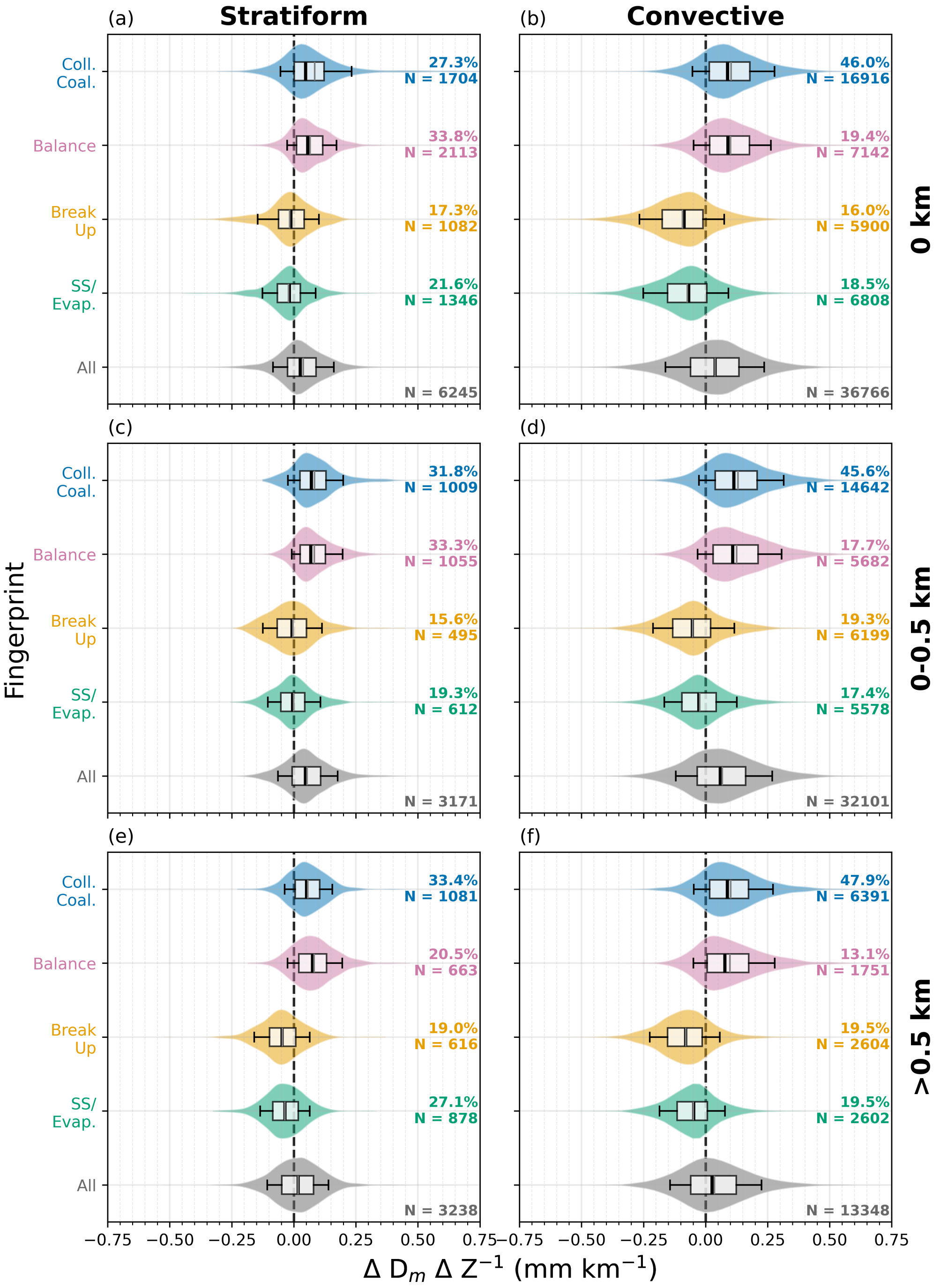

Figure 3.11: As in Fig. 3.9, but for ΔD_m.

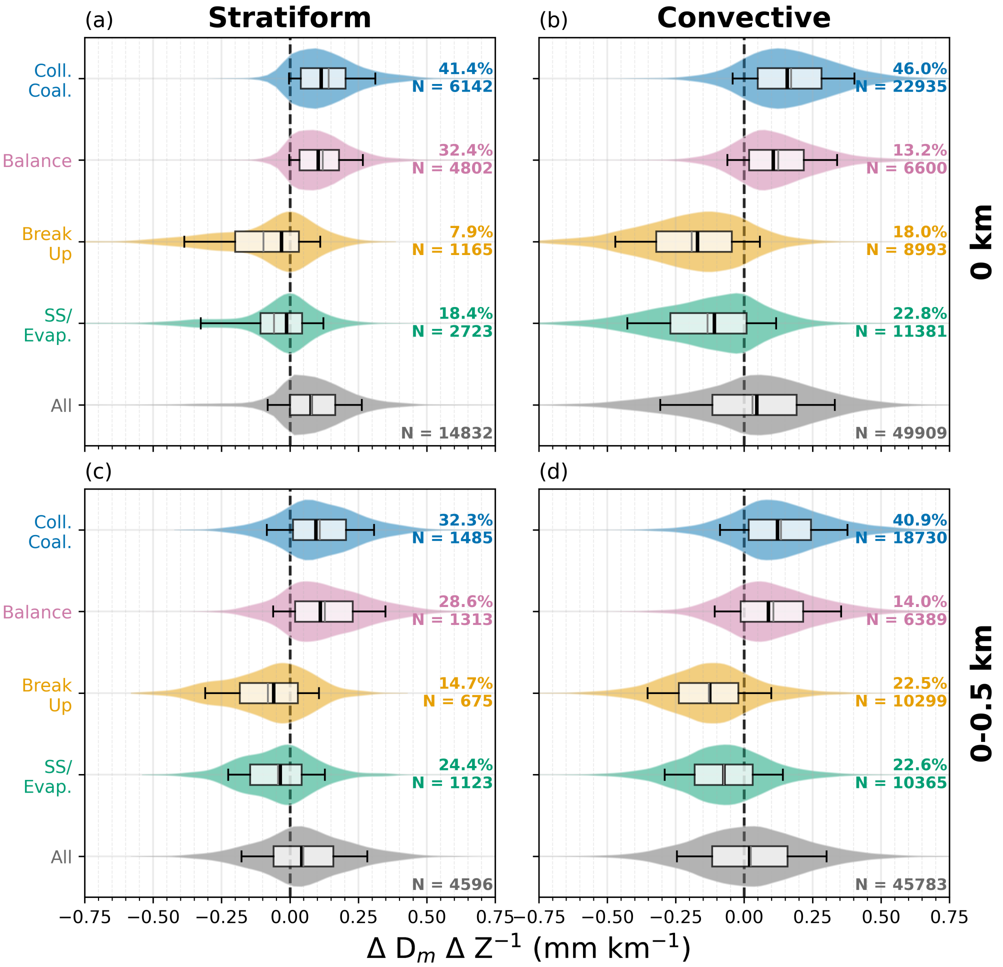

Figure 3.12: As in Figure 3.10, but for ΔD_m.

characteristics: 58 km range in the 183° azimuth and 90 km range in the 225° azimuth. Both show signatures of inferred collision coalescence in the column with increasing Z_h and Z_{dr} towards the surface, with similar magnitudes of Z_h and Z_{dr} (Fig. 3.13a, b). In the PID, both RHIs show similar inferred processes: graupel melting into moderate rain which intensifies into heavy rain (Fig. 3.13c, d). Despite these similarities, the resulting attenuation-based rain rate, $R(A_h)$, is 20-40 mm hr^{-1} higher in the 183 azimuth (Fig. 3.13e, f). This difference is further explored through the changes in the modeled DSD (Fig. 3.13g, h). At the top of the warm rain depth, both RHIs have similar M_0 values (4 dB m^{-3}), but D_m is 0.25 mm higher in the 225° azimuth. With decreasing height toward the surface, M_0 increases in the 183° azimuth with D_m remaining constant. Within the 225° azimuth, both M_0 and D_m do

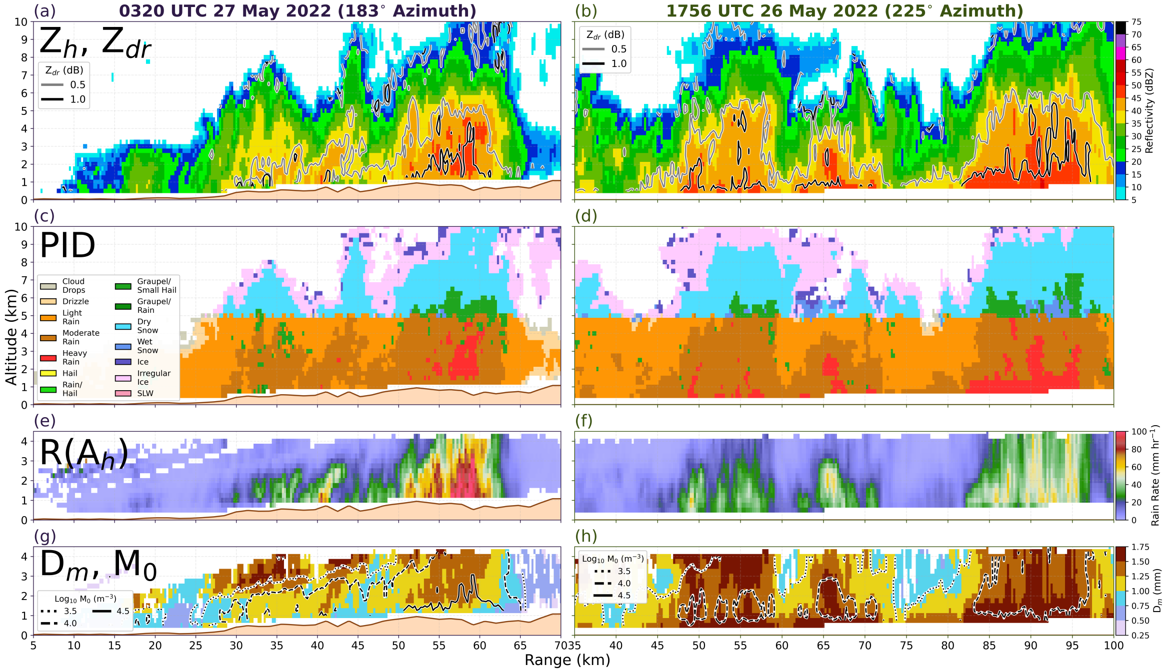

Figure 3.13: Gridded RHIs of (a, b) Z_h shaded with contoured Z_{dr}, (c, d) PID, (e, f) $R(A_h)$, and (g, h) D_m shaded with contoured $\mathrm{Log}_{10}\, M_0$ for (a, c, e, g) 0320 UTC 27 May 2022 at 183° azimuth and (b, d, f, h) 1756 UTC 26 May 2022 at 225° azimuth. Brown contours represent terrain.

not increase, though the surrounding regions show increasing D_m.

These changes within the DSDs or lack thereof then provide potential explanations for why the convective echo in the 183° azimuth over higher elevations produces higher rain rates compared to the convective echo at 225° over the ocean despite similar Z_h, Z_{dr}, and PID characteristics. First, drop concentrations increasing as D_m is relatively constant implies drop growth via collision coalescence also occurring with drop break up (i.e., a “balanced” scenario) and/or could be explained through advection of small drops into the bottom of the column. Additionally, these results suggest that DSD characteristics at the top of the warm rain depth layer likely influence the outcome below. More specifically, M_0 was similar below the melting layer for each RHI, but D_m differed. Exploring the advection of small drops is outside the scope of this study as analysis would need to expand towards the mesoscale forcing behind the precipitation observed. The characteristics of the DSD just below the melting layer, however, can be analyzed through cold rain inferences, or specifically the inferred melting of ice hydrometeors.

3.3.3 Cold Rain Processes

The example RHIs in Figure 3.13 hint towards ice hydrometeors above the melting layer dictating the characteristics of the DSD beneath. More specifically, graupel as it is often attributed for producing heavier rainfall (Lasher-Trapp et al. 2018). As graupel is commonly found in convective rainfall through extensive riming in prolonged updrafts, the analysis will pertain to convective echo (Lasher-Trapp et al. 2018). The PID can not inform characteristics of graupel such as concentration or shape, but can infer if graupel is present. To this end, convective columns will be designated as containing graupel aloft if PID infers graupel at at least two levels (to mitigate erroneous single graupel points) above 4-km (i.e., just below the bright band; Fig. 3.7). These criteria result in 1.4% - 2.4% of all convective columns containing graupel with the greatest proportion being found in the terrain group (Table 3.2). As more graupel aloft is found with increasing elevation, this may explain the shift towards relatively more frequent upper warm rain depth drop break up as melted graupel produced larger drops which would eventually break up (Fig. 3.9, 3.11). Consequently, the prevalence of graupel in terrain may also be linked to the increase in near surface rain rate observed in the terrain example of Figure 3.13.

To expand upon this inference from one example RHI, we employ a near surface rain rate using A_h with “near surface” starting at 1 km ASL to avoid ground clutter and moving up in altitude only if there is blockage present. For convective columns, both the ocean and coast display similar distributions of near surface rain rate with 90^{th} percentiles matching just above 10 mm hr^{-1} (Fig. 3.14a). Despite having a similarly shaped distribution, however, the 90^{th} percentile of terrain profiles is approximately 10 mm hr^{-1} higher implying that higher elevation promotes higher rain rates. As $>$ 90% of convective columns do not contain graupel aloft, the similarities and differences in the distributions of near surface rain rate are the same with only columns without graupel are considered (Fig. 3.14b). However, when only columns with graupel aloft are considered, 90^{th} percentile near surface rain rates increase dramatically, between a 30 mm hr^{-1} increase in the ocean up to a 40 mm hr^{-1} increase in the terrain (Fig. 3.14c). Additionally, convective columns with graupel aloft are found most frequently in the terrain (Fig. 3.14c). The instability in rain rates greater than 50 mm hr^{-1} for the terrain distribution are the result of limited sample size as opposed to deficiencies in the $R(A_h)$ algorithm. Rain rate distributions with and without graupel aloft are compared across all elevation bins using a Kolmogorov-Smirnov test and a

Mann-Whitney U test, which assesses whether the distributions are drawn from the same underlying population and whether graupel-aloft conditions tend to produce stochastically higher rain rates, respectively. Both tests indicate that the difference is statistically significant at the 99% confidence level across all elevation bins, with rain rates associated with graupel aloft being stochastically higher than those without. These results imply that not only is graupel more frequently occurring in the terrain, but graupel also enhances rainfall more in the terrain.

To quantify the effects of graupel presence on the DSD below, the convective mid-level (2-km) M_0/D_m phase space is explored across different elevation groups with and without graupel (Fig. 3.15). The near surface rain rate is shaded with median M_0/D_m ("x") and density contours are added for both low rain rates (0 - 10 mm hr^{-1}) and higher rain rates ($>$ 10 mm hr^{-1}). For both low and high rain rates as well as all elevation groups, graupel aloft has a tendency to increase both M_0 and D_m. Despite this result, elevation does not seem to have a noticeable impact on drop concentration or median drop size regardless of if graupel is present or not aloft. With regards to ranges in M_0 and D_m, it appears that the terrain does not produce DSDs with $D_m < 0.5$ mm. For profiles with graupel aloft, there is also an approximate minimum M_0 of 2.5 dB m^{-3} and D_m of 0.75 mm based on where the 50% density contours end. Therefore, it can be expected that if graupel is inferred aloft, there will be $>$ 100 drops in the mid-level with median drops sizes $>$ 0.75 mm.

3.4 Discussion

By combining the MRR and 2DVD, the full DSD was resolved similar to that of Thurai et al. (2017), giving credibility to the MRR's ability to capture the drizzle mode. While this gives future research flexibility in capturing the drizzle mode beyond using an MPS, there remains some ambiguity towards the MRR's performance that requires further comparison with an MPS. The MRR, in comparison to the MPS, has a larger minimum diameter, can become attenuated in heavy rainfall, and requires significant QC (as mentioned in 3.2.1). Despite these challenges, the results of the double moment normalized DSD model boast similar results to that of Raupach et al. (2019), showing that the differences between the MRR and MPS may only be slight (Fig. 3.4). Additionally, this adds to Lee et al. (2004)'s notion of double moment normalization invariance across climates, in this case subtropical Taiwan. Not only are the double moment normalization shape parameters derived in TiMREX valid

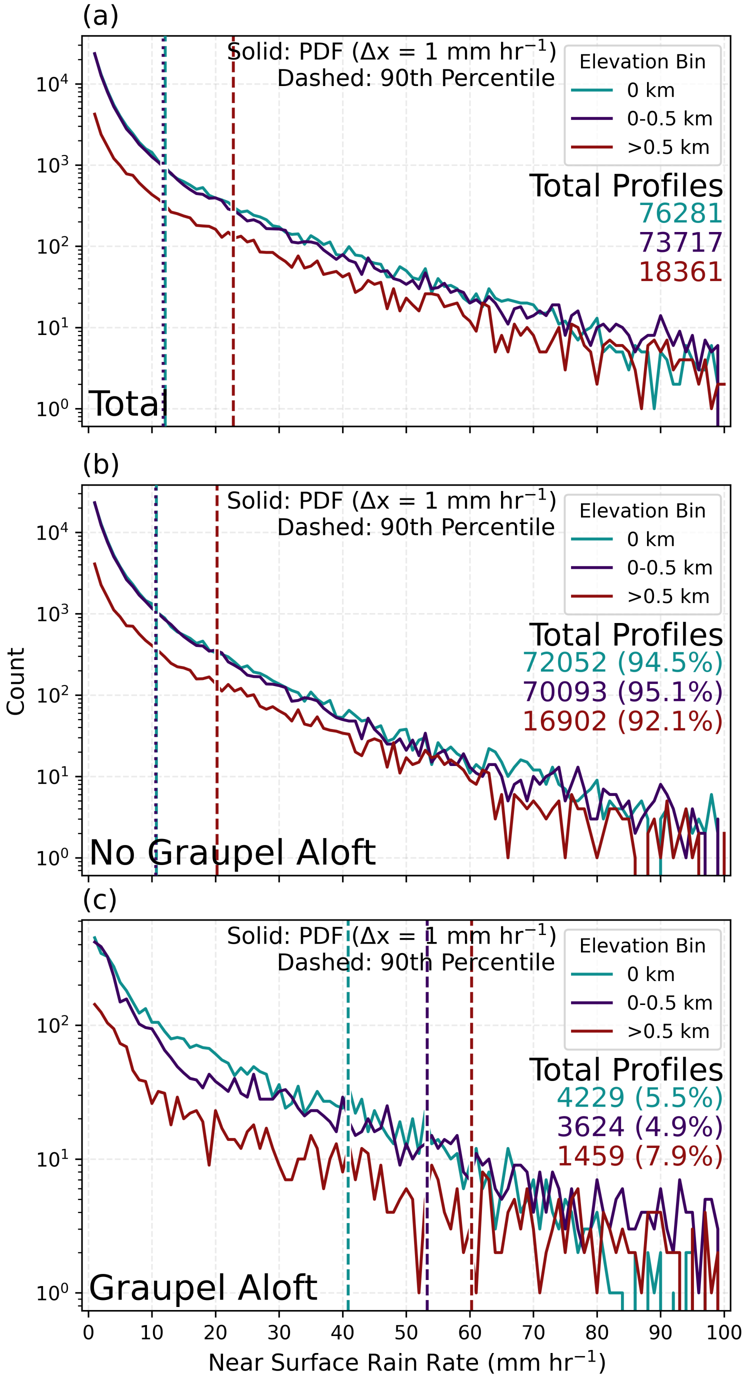

Figure 3.14: Distributions of near surface rain rate (a) all convective columns, (b), convective columns without graupel aloft, and (c) convective columns with graupel aloft. Distributions start at 1 mm hr^{-1} with 1 mm hr^{-1} width. Teal, purple, and red correspond to ocean, coast, and terrain bins with dashed lines corresponding to their respective 90$^{\text{th}}$ percentile.

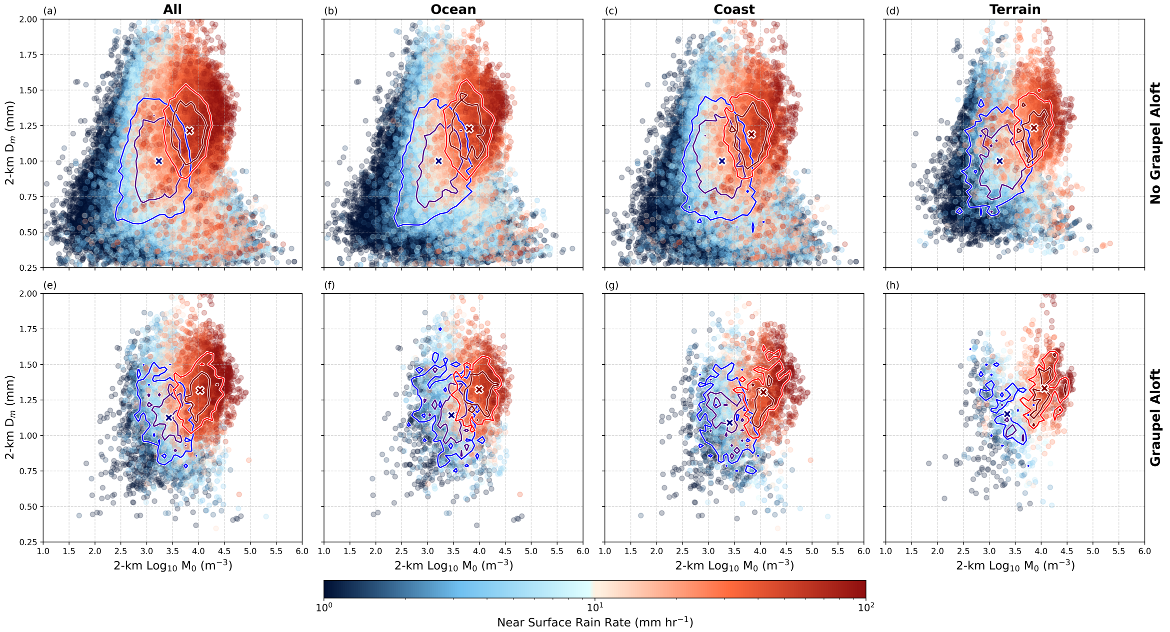

Figure 3.15: 2-km Log_{10} M_0 / D_m phase space with shaded near surface rain rate for (a, e) all, (b, f) ocean, (c, g) coast, and (d, h) terrain columns (a-d) without graupel aloft and (e-h) with graupel aloft. For rain rates below (blue) and above (red) 10 mm hr^{-1}, contours of 25/50% density and medians as "x" are added.

for PRECIP (e.g., Fig. 3.5), but the distribution of $h(x)$ in Figure 3.4 is remarkably similar to the $\hat{h}(x)$ derived in Raupach et al. (2019) for datasets obtained in the continental U.S. (i.e., Colorado and Alabama). Slight deviations may lie in large normalized drop sizes (i.e., $x > 1.5$ in Fig. 3.4) as the $h(x)$ values in TiMREX appear larger than that of the Raupach $\hat{h}(x)$. Additionally, different $h(x)$ trends appear when separating the Pre-TiMREX and TiMREX datasets, although these both differ from the Raupach $\hat{h}(x)$ and don't produce a significantly different $\hat{h}(x)$ for Taiwan (not shown).

In application to S-Pol, the combined MRR+2DVD dataset also proves effective in creating an M_3 retrieval based on A_h and Z_{dr}. While the new method within this study is based on Bringi et al. (2020)'s X-band retrieval of M_3, the process is much simpler at S-band given the reduction in biases in A_h at this wavelength (Bringi et al. 2020; Ryzhkov et al. 2022). Given A_h, LWC, and M_3 are so closely related, A_h tends to dominate the M_3 retrieval at S-band with Z_{dr} being used for drop size characteristics, giving greater application of A_h beyond rain rate and Z_h correction (Eq. 3.8). Despite the initial improvements made within Cornejo et al. (2025) in retrieving A_h in a mountainous, clutter-rich environment, subsequent quality control checks were needed in this study's application. Despite these efforts, suspect data can still remain, such as at 30 - 35 km range in Figure 3.13g whereby a slight erroneous increase in A_h aloft along the radial (as seen in Fig. 3.13e) produces drastically increased D_m along the radial. Nevertheless, examples like these are few and far between as evidenced by the comparisons made with the Parsivel in Figure 3.5. Should this type of retrieval and modeling be applied in a different radar deployment, considerable care should be taken in ensuring radar clutter is avoided, partial beam blockage is mitigated, and significant checks on data quality are made.

Application of this method to PRECIP IOP 1 adds valuable detail to radar fingerprinting approaches in inferring microphysical processes leading to heavy rainfall. The fingerprint analysis highlighted the dominance of collision coalescence fingerprints in both stratiform and convective rainfall, similar to the findings of Yang et al. (2025) and Miao et al. (2025) in a similar region. However, the anticipated changes to the DSD are not as would be expected. In both the upper and lower portions of the warm rain depth, collision coalescence is often coincident with median increases to both the number of drops as well as that expected for D_m. The two underlying assumptions of the fingerprints are that the inferred processes are the most dominant and not the only process occurring and that the inferred processes are based on the expected changes in the DSD due to changes in polarimetric variables. The first assumption has started to be challenged by Kumjian et al. (2022) whereby simulated process rates indicate that break up and evaporation/size sorting fingerprints can sometimes be the result of underlying dominant collision coalescence. Additionally, the second assumption has been challenged by Xie et al. (2016), Kumjian et al. (2022), and Smith et al. (2025) whereby expected DSD outcomes for a given fingerprint has exceptions. In particular, Xie et al. (2016) has found that in radar volumes of large mean diameters and broad DSDs, evaporation can be coincident with increasing Z_{dr} towards the surface. Based on the changes in median M_0 and D_m in this study, none of the fingerprints achieve their expected DSD changes.

This challenge in inferring DSD changes from fingerprinting in subtropical and tropical climates may also be linked to large number concentrations of small drops (e.g., Fig. 3.13a, b), which tend to produce relatively small Z_{dr} values. When displayed in the phase space for the full warm rain depth (Fig. 3.8), many of the columns straddle the ΔZ_{dr} = 0 dB line, indicative of minimal change to Z_{dr}. In such regimes, differencing near-zero values of Z_{dr} can be caused by instrument noise rather than hydrometeors, making the differentiation between evaporation/size sorting and break up difficult, as noted in Kumjian et al. (2022).

This ambiguity may help explain why the changes in M_0 and D_m are more closely aligned with changes in Z_h than with Z_{dr}. Therefore, directly modeling the changes to the moments may prove to be more beneficial than inferring DSD changes from fingerprints. Additionally, fingerprints inherently describe only the most dominant processes inferred from Z_h and Z_{dr} and may not capture concurrent background warm rain processes such as drop break up. Improved characterization of smaller drops, beyond the constraints of Z_h and Z_{dr}, may therefore provide more complete insight into the underlying microphysical evolution. In theory, K_{dp} can be used in addition to Z_h and Z_{dr} for fingerprints (e.g., Kumjian et al. 2022), but often in the same role as Z_h for warm rain processes. Therefore, K_{dp} would not enhance our understanding of fingerprints as the near zero Z_{dr} changes are what causes much of the fingerprint ambiguity. Potential future updates in fingerprinting may be in using specific differential attenuation as an alternative to Z_{dr}.

In addition to challenges in the underlying assumptions made in fingerprinting, ice processes are even more difficult to infer. Within this study, individual ice processes are not assessed, but rather the influence of graupel and its subsequent melt on the DSD below. Prior literature in the region has shown that the presence of graupel can lead to enhanced rain rates within the region (Chen et al. 2019; Miao et al. 2025; Yang et al. 2025), however, this study expands on this through the added complexity of topography and DSD modeling. Whereas the ocean, coast, and terrain all exhibit increased rain rate with graupel aloft, the increase is even greater with increasing elevation (Fig. 3.14). This result aligns with the findings of 3.14 whereby decreasing elevation induces less intense rainfall in terrain as opposed to flatter terrain. In prior studies, melting graupel was attributed to larger drop sizes aloft (e.g., Chen et al. 2019; Miao et al. 2025; Yang et al. 2025); however, within this study, there is also a coincident increase in the number of drops at 2-km ASL (Fig. 3.15). The implication being that large drops originate below the melting layer and undergo drop break up as they descend in the upper warm rain depth. Ideally, to better determine the impacts of graupel on the resulting DSD, modeling of the DSD just below the melting layer is preferential over modeling at 2-km. However, graupel can intrude and degrade the quality of the modeled DSDs and thus should be a topic of improvement for DSD modeling.

3.5 Conclusions

In this study, a double moment normalized generalized gamma distribution DSD model was localized to Taiwan and applied to the NSF NCAR S-band polarimetric (S-Pol) radar during IOP 1 of the 2022 NSF-funded PRECIP field campaign for the purposes of studying terrain-dependent microphysical processes leading to heavy rainfall. A summary of the key results are as follows:

1. The use of an MRR and 2DVD can resolve the full DSD (i.e., both drizzle and precipitation modes) and therefore is used to produce shape parameters for a double moment normalized DSD model with an underlying generalized gamma distribution. These shape parameters resemble those used in prior midlatitude studies further supporting the invariance of this model.
2. As an input to the DSD model, S-Pol can accurately retrieve M_3 through a novel retrieval utilizing A_h and Z_{dr} which compares well with disdrometers.
3. In warm rain, collision coalescence is the most frequently occurring microphysical radar fingerprint with the DSD model finding coincident increases in both median drop concentrations and drop size. As elevation increases, the frequency of break up fingerprints near the surface increases resulting in median decreases in both drop concentrations and drop size.
4. The presence of graupel above the melting layer influences the DSD below by increasing rain rate, drop concentrations, and median drop size. The amount that graupel increases the rain rate is amplified by the terrain elevation.

Despite the analysis only pertaining to a single case study, the utility of the radar-modeled DSD paired with conventional radar methods such as microphysical fingerprints and PID proves to be an effective method for analyzing microphysical processes. In extending these results, future work will apply this analysis to the remainder of the 3-month PRECIP field campaign where an even wider array of rainfall intensities and durations (Cornejo et al. 2025) and types of events (e.g., Mei-Yu front, afternoon thunderstorms, moisture flux from a tropical storm). Toward linking the microphysical processes to the environmental conditions of these different types of cases, future work will examine these microphysical processes in context of their thermodynamics (e.g., horizontal and vertical moisture distributions) and dynamics (e.g., advection, synoptic-scale, mesoscale, and terrain-induced lift) using additional PRECIP observations within the S-Pol domain and convection-permitting numerical weather prediction models.

This work also highlights new potential for observational analysis of DSDs for use in model parameterization as well as interpretation of microphysical fingerprints. As noted in Kumjian et al. (2022), quantification of DSD impacts inherent to fingerprints is still a burgeoning field of study and by linking these fingerprints to DSDs, there is great potential for improvement in microphysical parameterization schemes. In utilizing the techniques within this study, there should be great care in quality controlling the disdrometer and radar data. Given the many steps required in producing radar-modeled DSDs (Fig. 3.2), minor data quality issues can amplify into larger issues throughout the process. While shape parameters have been shown to be universal across climates, this study provides ample instruction on a method in which DSDs can be modeled from S-band radars.

Chapter 4

Leveraging Observations and Ensemble Member Skill to Identify Drivers of Extreme Mei-Yu Rainfall

4.1 Introduction

Extreme rainfall events are often highly impactful and can produce great socioeconomic cost through downstream impacts such as floods and landslides. The prediction of these events is often limited by the abilities of our numerical weather prediction (NWP) models to correctly predict precipitation intensity and duration. Intensity and duration can be assessed through an ingredients-based framework (i.e., Doswell III et al. 1996) through quantifying factors pertaining to intensity such as precipitation efficiency or to duration such as the spatiotemporal scales of storms. Determining how ingredients affect intensity and duration is often difficult due to the interplay between dynamics and thermodynamics and ultimately, the microphysics behind the precipitation produced. This challenge can become even more difficult when considering regions of complex terrain whereby dynamics, thermodynamics, and microphysics are all impacted.

A region of complex terrain commonly studied for its extreme rainfall is Taiwan. One of the main drivers of precipitation in the region is the interaction of monsoonal southwest

---

The following Chapter is in preparation for submission with authors: Cornejo, I. C., Rowe, A. K., DeHart, J. C., Yang, S.-K., Chung, K.-S.

flow upon the steep topography that covers most of the island (e.g., Chen and Chen 2003). In addition to the moist, monsoonal flow, Taiwan frequently receives extreme rainfall through phenomena such as typhoons and Mei-Yu fronts, the latter which are East Asian quasi-stationary fronts often characterized not by strong temperature gradients, but rather, strong moisture gradients (e.g., Chen 1992; Cho and Chen 1995; Cornejo et al. 2024). These quasi-stationary fronts often produce high duration precipitation through broad stratiform rainbands and high intensity rainfall through embedded convective cells. This rainfall can be exacerbated through their interactions with terrain whereby a Mei-Yu front encounters Taiwan's steep topography, impacting propagation of the front and prolonging rainfall duration (e.g., Cornejo et al. 2024).

When modeling Mei-Yu front events using an ensemble, there is often a broad spread in rainfall distribution leading to varying degrees of rainfall intensity and duration (Ke et al. 2025; Wang et al. 2021; Zhang et al. 2023). For models that are faithfully able to represent rainfall intensity or duration, the underlying mechanisms may not reflect the truth. An example can be found in Cornejo et al. (2024) whereby a Mei-Yu front event was modeled with well-represented intensity and duration, but ice microphysical representation was far exaggerated compared to reality resulting in a misplacement for the root causes in rainfall intensity. Additionally, Mei-Yu fronts are often dynamically complex, especially near topography (e.g., Cornejo et al. 2026, 2025, 2024; Huang et al. 2026; Ke et al. 2025). The many low-level jets present during the Mei-Yu season, including the orographically induced barrier jet, often interact with the front through enhanced convergence, increased moisture, or altering the frontal propagation speed (Chen et al. 2022b; Cornejo et al. 2024; Huang et al. 2026; Tu et al. 2022; Wang et al. 2021) thereby modifying frontal rainfall. The fronts themselves can also be influenced directly by the topography as in Cornejo et al. (2024) whereby orographic deformation of winds induced additional frontal convergence which may contribute to differences in rainfall intensity. With these complexities each contributing to changes in rainfall intensity and duration, models allow for nuanced investigations into the physical mechanisms inherent to these events. However, these models need to be grounded in reality.

One of the key objectives of the 2022 Prediction of Rainfall Extremes Campaign in the Pacific (PRECIP) was to study extreme rainfall through the lens of intensity and duration both through extensive modeling and intensive observation. It is through these observations that the physical processes within models can be thoroughly investigated. The campaign was

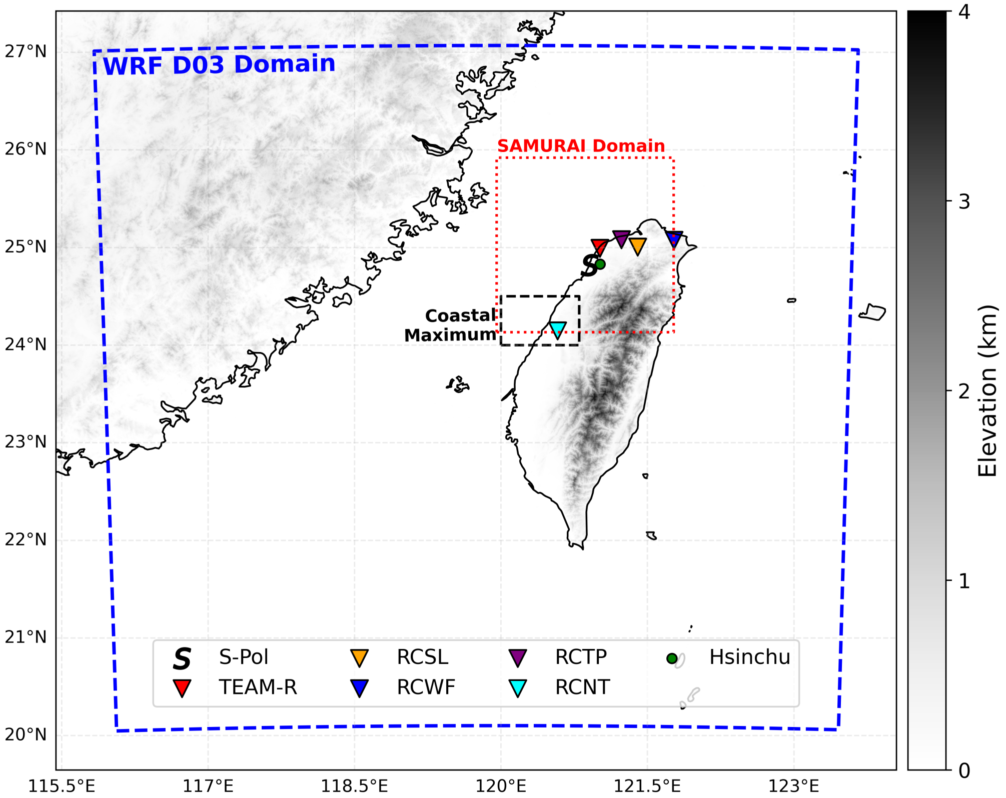

Figure 4.1: Elevation map of Taiwan. Triangle markers indicate operational radars from CWA, "S" indicates S-Pol, and the green dot indicates the Hsinchu sounding site. The blue dashed box indicates the WRF D03 domain, the red dotted box indicates the SAMURAI analysis domain, and the black dashed line indicates the coastal maximum region.

conducted in northern Taiwan between late May and early August. During this campaign, two Mei-Yu front events, intensive observation periods (IOPs) 1 and 3, were well observed by the dense network of observations including radars operated by the Taiwanese Central Weather Administration (CWA; RCSL, RCNT, RCTP, and RCWF in Fig. 4.1) and those deployed for the field campaign: the National Central University (NCU) TEAM-R radar, and the National Science Foundation (NSF) National Center for Atmospheric Research's (NCAR) S-band, dual polarimetric Doppler radar, S-Pol (Cornejo et al. 2026, 2025; DeHart and Bell 2025).

These observations have already allowed for key insights on Mei-Yu dynamics and on model interpretation of Mei-Yu fronts. For example, an improvement in rainfall representation was found in Yang et al. (2024) by assimilating radar data when modeling the IOP

3 Mei-Yu front, highlighting the importance of correct placement and timing of mesovortices along the Mei-Yu front. This link between greater vorticity and greater rainfall was highlighted in the DeHart and Bell (2025) analysis of IOPs 1 and 3 through multi-Doppler syntheses using the radars in Figure 4.1. More specifically, higher rain rates were found to be collocated with greater vorticity throughout the column, convergence below 5 km above sea level (ASL), and updrafts increasing with altitude. These studies highlight the important link between dynamic pathways and rainfall intensity and duration but gaps in understanding remain. Timing of these physical features (e.g., mesovortices, convergence) relative to peak rainfall seems to be a key factor, but has not yet been explored more comprehensively across models and observations. Additionally, there remains some ambiguity on the key sources of lifting along the front. DeHart and Bell (2025) indicate convergence and vorticity; however, the controls on those two can be complex as their study was focused over the ocean without consideration of low-level jets and terrain, which prior Taiwan studies have shown can enhance convergence and provide key moisture for sustaining rainfall (Chen et al. 2005, 2022b; Cornejo et al. 2024; Huang et al. 2026). While moisture gradients across the front, measured by equivalent potential temperature (θ_e), are a defining trait of Mei-Yu fronts, there remains ambiguity as to their role in frontal lifting (Chen et al. 2022c; Huang et al. 2026; Tu et al. 2022; Wang et al. 2021). Therefore, through a more detailed investigation of these cases, these complexities can be tackled through assessing what models do best representing rainfall and why.

PRECIP's IOP 1 provides an ideal opportunity to investigate these processes as during this Mei-Yu event, upwards of 300 mm of rainfall between 26 - 28 May 2022 (Cornejo et al. 2026, 2025), with the greatest rainfall amounts observed within the 8 hour span between 0700 - 1500 UTC 26 May 2022 along the northwest coast of Taiwan (black dashed box in Fig. 4.1; 120° - 120.8° E and 24 - 24.5° N). This event was well observed by the surrounding radars and other observations as well as simulated through high-resolution ensemble modeling. With these observations and modeling runs combined, the factors pertaining to rainfall intensity and duration can be explored through a model grounded in reality by observations. The ability to correctly place the rainfall maximum is representative of the model's ability to place the Mei-Yu front in the correct location as the rainfall predominantly falls in the frontal convergence region (Chen 1992). This relationship is in large part due to the frontal placement dictating low-level wind directions relative to terrain and thus rainfall duration (Cornejo et al. 2024). Therefore, members will be selected based on their ability to correctly place rainfall maximums. This approach allows for greater scrutiny for the controls on Mei-Yu rainfall intensity and duration, ultimately giving the ability to compare what makes some ensemble members perform better than others in producing rainfall.

This study will expand on these prior studies to better understand the multiscale controls on extreme Mei-Yu front rainfall using IOP 1 of the PRECIP 2022 field campaign. To address the broader goal, the specific scientific objectives are as follows:

1. Compare model representation of extreme rainfall against observations.
2. Determine the dynamic, thermodynamic, and microphysical processes leading up to and during extreme rainfall associated with a Mei-Yu front.

Section 4.2 will explain the data and methods utilized during this study. Section 4.3 will compare observations and model members and examine thermodynamical dynamical and microphysical relationships across model members. Section 4.4 will discuss and contextualize these results with prior literature. Section 4.5 will conclude with main takeaways from this study and future work.

4.2 Data and Methods

4.2.1 Ground-based Radars

This study uses several radars for their ability to remotely sense precipitation structures of the Mei-Yu front, as well as being used in unison for multi-Doppler synthesis. The primary radar within this study is the NSF NCAR S-Pol radar, a dual-polarization, S-band radar operating at 10.557 cm ("S" in Fig. 4.1). S-Pol operated on a 12-min scan cycle during PRECIP including a full-volume surveillance scans sequence, SUR1, used in this study that scanned 10 elevation angles with 150-m gate resolution, a 10.5° s^{-1} scan rate, and a 0.92° beamwidth. This study uses the S-Pol V2 quality-controlled dataset (NCAR/EOL S-Pol Team 2024) that includes an adaptive clutter filter. Further details on the quality control procedures in the V1 version of the dataset can be found in Dixon et al. (2023), and a summary of the improvements in V2 can be found in Cornejo et al. (2025). For microphysical inference, the NSF NCAR fuzzy logic particle identification algorithm (PID; Vivekanandan et al. 1999) and drop size distribution (DSD) modeling from Cornejo et al. (2026) are applied to all SUR1 V2 data from IOP 1. Additionally, the $\mathsf{R(Synth)}$ rain rate product produced in Cornejo et al. (2025) is used for its ability to accurately quantify high intensity rain rates during IOP 1. The S-Pol data is gridded using the NSF-supported Lidar Radar Open Software Environment (LROSE) - "Colette" (DeHart et al. 2025) at a horizontal and vertical resolution of 0.5 km. Additional analysis and data visualization is performed using the Python ARM Radar Toolkit (Py-ART; Helmus and Collis 2016). As rainfall intensity and duration are often associated with the degree of convection within an environment, the Echo Classification from COnvectivity (ECCO) tool from LROSE is applied to S-Pol for its ability to classify convection and stratiform echo. This tool leverages the peakedness of radar reflectivity values in a horizontal plane to produce a scaling parameter for convection known as convectivity (C_v; Dixon and Romatschke 2022). C_v scales from 0 to 1 with values between 0 - 0.4 being stratiform, 0.4 - 0.5 being mixed, and 0.5 - 1 being convective.

The dense Doppler radar observations are used to connect the microphysical and convective properties of the echo to the surrounding kinematics comparisons. In a previous study by DeHart and Bell (2025), several radars were utilized to produce a multi-Doppler analysis using the Spline Analysis at Mesoscale Utilizing Radar and Aircraft Instrumentation (SAMURAI; Bell et al. 2012) during IOP 1 to retrieve 3-dimensional (3-D) winds at high resolution. This study will also utilize their multi-Doppler synthesis to provide real world context behind the winds in the models. These syntheses ingest radial velocity data from S-Pol, four CWA operational radars (RCSL, RCTP, RCNT, and RCWF in Fig. 4.1) and the NCU TEAM-R radar (TEAM-R in Fig. 4.1). RCWF operates at S-band, TEAM-R operates at X-band, and the remaining operational radars operate at C-band. Further detail on quality control for these radars including velocity unfolding and dealiasing can be found in DeHart and Bell (2025). Once quality controlled, the six radars are used to produce a multi-Doppler synthesis using SAMURAI to solve for 3-D winds. This study uses SAMURAI given its ability to solve for surface boundary conditions allowing for more accurate retrievals of winds near complex terrain (Cha and Bell 2023). All SAMURAI analyses are spatially anchored by S-Pol (red dotted box in Fig. 4.1) with a resolution of 1 km horizontally and 0.5 km vertically. To avoid temporal aliasing, data is used from the other radars within 8 minutes of S-Pol's scan cycle, resulting in 33 analyses between 0600 and 1500 UTC during this case. To reduce noise and remove poor data, a Gaussian spatial filtering is applied and grid points with condition number, a metric for beam geometry, greater than 10 are removed. For further details on the SAMURAI process, refer to DeHart and Bell (2025).

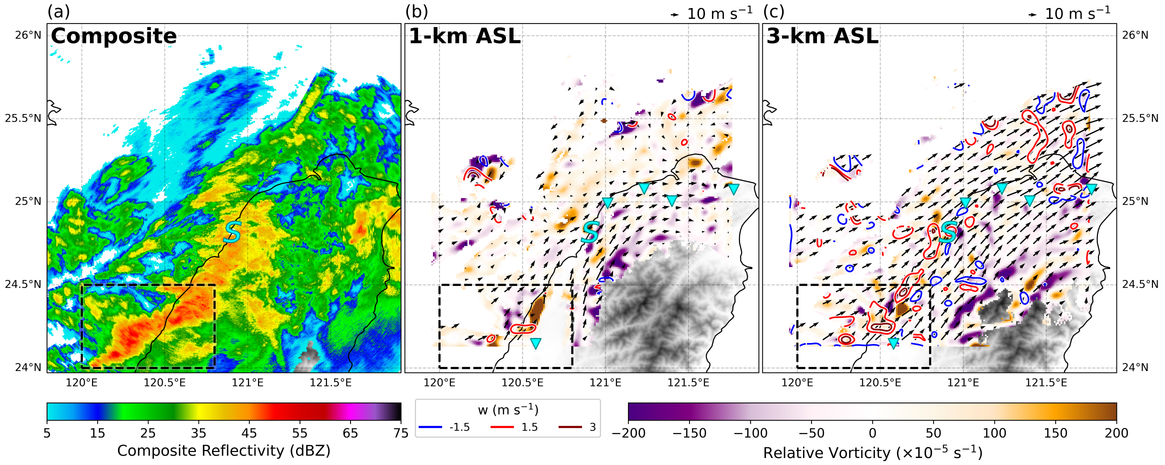

Figure 4.2: Spatial maps at 0848 UTC 26 May 2022 of (a) column maximum composite radar reflectivity in dBZ from S-Pol and SAMURAI multi-Doppler synthesis at (b) 1-km ASL and (c) 3-km ASL. Within these syntheses, quivers indicate horizontal winds, the background fill is relative vorticity, and the contours are vertical velocity. Each shows the coastal maximum region as a black dashed box, topography shaded, and locations of radars used; "S" for S-Pol and triangles for additional SAMURAI radars.

Figure 4.2 shows an example column-maximum composite of radar reflectivity from S-Pol as well as two multi-Doppler syntheses from different altitudes, 1- and 3-km ASL. The time chosen corresponds to when the Mei-Yu front produces the maximum rain rate for S-Pol within the coastal maximum region (dashed line in Fig. 4.2). The first consideration for these syntheses is that SAMURAI does not produce output for the entire coastal maximum domain due to the RCNT radar being located within that region (the southernmost triangle in Fig. 4.2). The second consideration is the prevalence of a baseline, the inability to resolve multi-Doppler winds owing to the path between radars. This issue is most prevalent between the RCNT radar and S-Pol at 1-km ASL where wind retrievals are not shown (Fig. 4.2b). However, with increasing altitude, coverage from surrounding radars allows for that baseline to be filled (Fig. 4.2c). The final consideration is that wind retrievals are only possible once radar echo becomes detectable. In the case of SAMURAI, the minimum sensitivity is -20 dBZ. Therefore, any comparisons with ensemble members will follow the same -20 dBZ thresholding.

While these are notable considerations, we find the SAMURAI syntheses are able to produce high quality 3-D winds, especially at altitudes where baseline issues disappear (e.g., 3-km). Within the example, areas where winds are rotating clockwise distinctly around the topography are associated with physically consistent negative vorticity providing confidence of SAMURAI appropriately accounting for terrain boundary conditions (Cha and Bell 2023). Additionally, lifting is properly placed as in the vorticity couplet at 120.6° E and 24.4° N in Fig. 4.2c. A negative and positive vorticity couplet would produce an updraft to the north due to the convergence of counter rotating winds, and then to the south, additional lifting is found when the combined northeast winds of the couplet converge with the mean southwest flow. In the lack of that strong couplet at 1-km, the lifting is logically only observed to the south of the positive vorticity (Fig. 4.2b). Thus, there is confidence in SAMURAI's overall ability to represent the 3-D winds.

4.2.2 Quantitative Precipitation Estimation and Segregation Using Multiple Sensors

While the coastal maximum is the primary concern for this study, the spatial context surrounding this region is important as well as that can inform influences of nearby topography and frontal rainfall outside of the coastal maximum. $\mathtt{R(Synth)}$ has been shown to produce reliable rainfall estimates over the coastal maximum region as part of Cornejo et al. (2025); however, in the surrounding regions, remaining challenges in data quality produce adverse results. Therefore, the Quantitative Precipitation Estimation and Segregation Using Multiple Sensors (QPESUMS; Chang et al. 2021) will be used to supplement S-Pol's rain rate product for selecting model members. The QPESUMS product uses 10 operational radars and over 1000 rain gauges to provide precipitation estimates every hour at 0.0125° x 0.0125° (~1.3 km^2) resolution, coarser than S-Pol that contributes to underestimation of the highest intensity rainfall compared to S-Pol. Therefore, QPESUMS will be used to evaluate overall spatial trends in modeled rainfall whereas S-Pol will be used to compare to model member analysis of peak rainfall intensities.

4.2.3 Radiosondes

Moisture data recorded by radiosondes launched at Hsinchu (green dot in Fig. 4.1) are used in this study as a comparison for the WRF members. This data is quality controlled in a two step procedure, initially using the Vaisala Digicora software then further quality control using the NSF NCAR ASPEN software (Bell and Yu 2023). Data from the 0600 and 1200 UTC

26 May 2022 launches are used and processed using MetPy (May et al. 2022).

4.2.4 Weather Research and Forecasting Model Ensemble

To address the research objectives, the Advanced Research Weather Research & Forecasting (WRF) v4.3 model (Skamarock et al. 2019) is used with an ensemble approach following Ke et al. (2025). Initial and boundary conditions are from the European Centre for Medium-Range Weather Forecasts Reanalysis v5 (ERA5; Hersbach et al. 2020) for three, two-way nested domains with horizontal resolution scaling from 15 km in the outermost domain (D01) to 1 km in the innermost domain and 52 vertical levels (D03; blue dashed line in Fig. 4.1). All three domains initialized at 0000 UTC 26 May 2022 and ran until 0000 UTC 27 May 2022 with D03 having output every 30 minutes. To account for model spin-up time (approximately the first 5 hours as in Ke et al. 2025) and with peak rainfall occurring between 0700 - 1500 UTC 26 May 2022, only WRF D03 data between 0600 - 1500 UTC 26 May 2022 is used for this analysis. The 0600 UTC hour is included to examine conditions prior to peak rainfall to allow for comparison with a 0600 UTC radiosonde launch.

Random physical state perturbations are introduced in D03 using WRFDA CV3 to produce 128 ensemble members. Perturbations are made in control variables such as the stream function, unbalanced velocity potential, unbalanced temperature, mixing ratio, and unbalanced surface pressure. The perturbations emphasize the dynamic and thermodynamic features on the synoptic scale compared with the convective scale. Since all members use the same D01 and D02 domains, the synoptic scale state of the atmosphere is intended to be similar across all D03 members to enforce differences across members are predominantly differences on the mesoscale. Each member utilizes the same model parameterization as seen in Table 4.1. The choice of each parameterization was based on what is used operationally and commonly used in research in the same region (e.g., Chung et al. 2020; Ke et al. 2025). Analysis of D03 was performed using WRF-Python (Ladwig 2017) and Metpy (May et al. 2022).

From the 128 WRF ensemble members, two rounds of subsetting were performed to isolate members that produce rainfall maximums within the same coastal maximum region as observations. As determined by Cornejo et al. (2024), frontal placement and the heavy rainfall produced by it strongly dictates rainfall duration. Thus, by limiting analysis to members producing rainfall maximums in nearly the same location, more nuance regarding

Table 4.1: Parameterization schemes used in WRF Model.

Microphysics	Goddard 4ICE (Tao et al. 2016, 1989)
Longwave Radiation	Rapid Radiative Transfer Model (Mlawer et al. 1997)
Shortwave Radiation	Dudhia Scheme (Dudhia 1989)
Planetary Boundary Layer	Yonsei University Scheme (Hong et al. 2006)

extreme rainfall controls can be analyzed beyond if the front was in the right location. The initial procedure was through a K-means clustering approach following Ke et al. (2025). Simplistically, the K-means clustering approach seeks to cluster members with similarities while also maximizing the differences across different clusters. In that way, each cluster is distinct from one another, but similar within their own members. Through this approach, the 128 members are grouped into 5 clusters based on the spatial distribution of rainfall between 0700 - 1500 UTC. When viewing cluster average rainfall accumulation, one 29-member cluster mean stood out as producing a coastal rainfall maximum similar to QPESUMS and S-Pol.

While the initial procedure is meant to group members with similar rainfall maximum locations , individual members within that group may vary. Therefore, to further isolate members that most resembled reality in regard to the coastal maximum, these 29 members were compared with QPESUMS for the same 0700 - 1500 UTC time period (Fig. 4.3). While QPESUMS does not produce as much rainfall compared to $\mathtt{R}(\mathtt{Synth})$, QPESUMS better details the spatial distribution of rainfall during this event, thus it is better suited for spatial comparison with the ensemble members. During this time, QPESUMS estimated a domain maximum rainfall accumulation within the boxed region between 120° - 120.8° E and 24 - 24.5° N, hereafter $\mathtt{R}_{\mathtt{8hr}}$, of 248 mm (Fig. 4.3a). Of the 29 members remaining after K-means clustering, members that had their $\mathtt{R}_{\mathtt{8hr}}$ within the same boxed region were 24, 65, 77, 104, 127, and 128 (hereafter, M24, M65, etc.).

4.3 Results

4.3.1 Comparisons of Member Intensity and Duration

Across the 6 members, $\mathtt{R}_{\mathtt{8hr}}$ magnitudes varies greatly with the largest values being from M24 and M128 (244 and 227 mm; Fig. 4.3b, g) and the lowest value from M77 (110 mm; Fig.

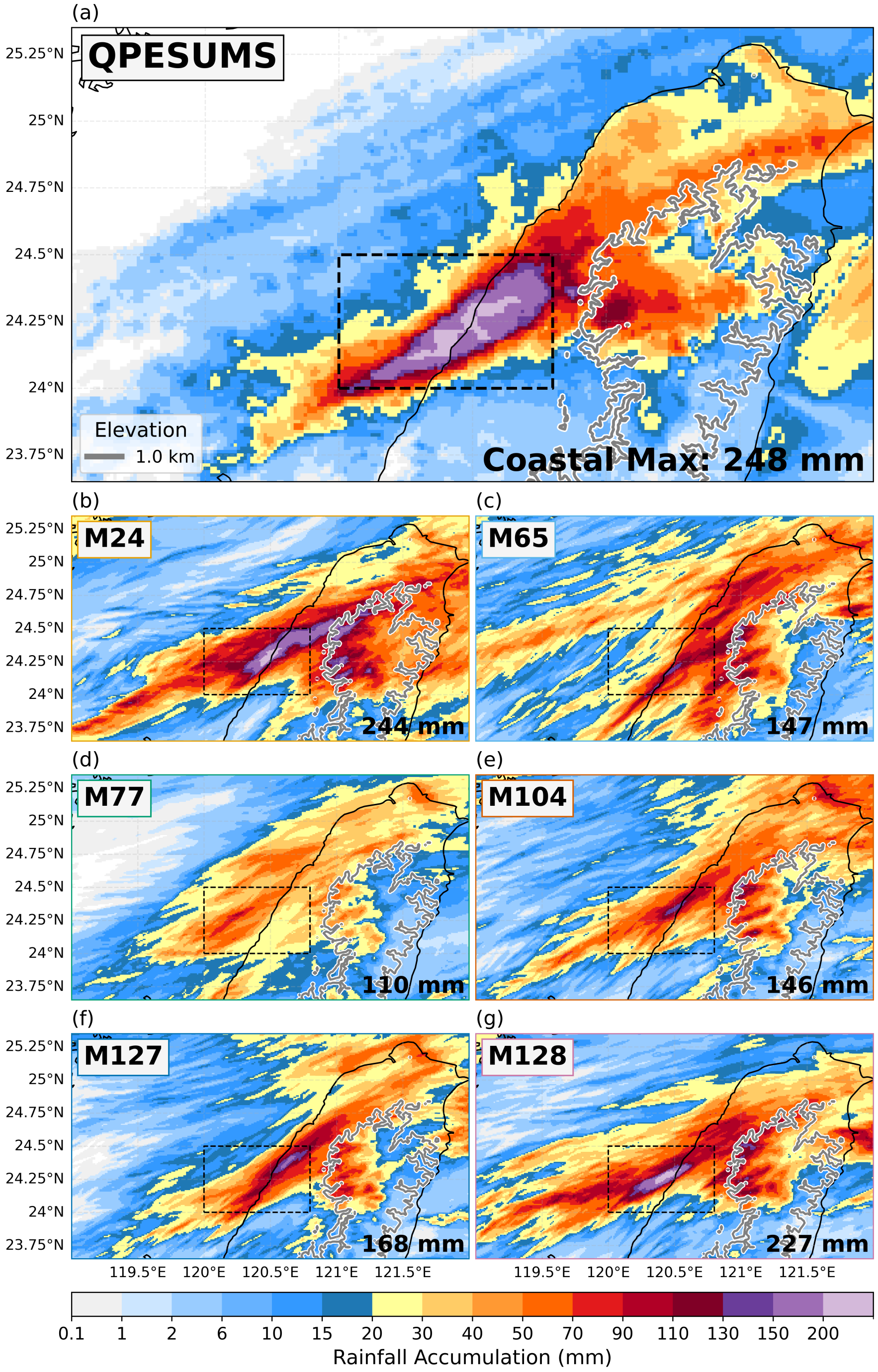

Figure 4.3: Rainfall accumulation between 0700 - 1500 UTC 26 May 2022 for (a) QPESUMS, (b) M24, (c) M65, (d) M77, (e) M104, (f) M127, and (g) M128. The black dashed line indicates the coastal maximum region. The grey contour outlines 1-km elevation. In the bottom right corner of each subplot is the $\mathrm{R}_{8\mathrm{hr}}$ value for the respective rainfall estimator.

4.3d). While M24 reaches very close to QPESUMS' R_{8hr} value, within 5 mm, no member captures the same area of > 200 mm rainfall, suggesting that intense rainfall from the models was not very widespread compared to reality. To explore this relationship between rainfall accumulations, intensity, and duration, each of the 5 selected model members is compared with QPESUMS further through a bivariate choropleth. Similar to Cornejo et al. (2024) and Cornejo et al. (2025), rain periods are defined for each grid point as periods of continuous rainfall with allowance for 1-hr gaps in rainfall between 0700 - 1500 UTC. Each period has a contiguous duration and an average rain rate acting as proxies for rainfall duration and intensity. The duration and average rain rate of the rain period with the highest rainfall accumulation are mapped spatially to form bivariate choropleths (Fig. 4.4). QPESUMS indicates that rainfall duration is maximized throughout the 8-hr period, not only for the coastal maximum, but over the entirety of northern Taiwan (Fig. 4.4a). However, it is within the coastal maximum whereby intensity is also maximized, with the highest rainfall intensities (> 24 mm hr^{-1}; Fig. 4.4a) observed in the same locations where rainfall accumulation is maximized (> 200 mm; Fig. 4.3a). All members are able to produce high duration rainfall (6-8 hr) within the coastal maximum. Thus, many of the differences in rainfall accumulation between members observed in Figure 4.3 are attributed to differences in rainfall intensity. M24 and M128, having had the largest R_{8hr}, produced some of the most intense rainfall ($\geqslant 24$ mm hr^{-1}) whereas M77, which had the lowest R_{8hr}, produced lower intensity rainfall (< 12 mm hr^{-1}).

The bivariate choropleth provides the average intensity for the entire rain period, but does not provide the maximum intensity, which is needed for finding the timing relative to peak rainfall in each member. For that purpose, we use the maximum 1-hr rainfall accumulation from S-Pol within the coastal maximum, hereafter referred to as R_{1hr}. Figure 4.5a shows the same 8-hr rainfall accumulation as in Figure 4.3a, but using S-Pol's $R(Synth)$ product to show that it captures the same coastal maximum as in QPESUMS but with a notably higher R_{8hr}, 298 mm. Maximum 1-hr rainfall from S-Pol is 155 mm, higher than M65, M77, and M104's R_{8hr} values.

The differences in rainfall intensity may be attributed to differences in contributions to rainfall from convective versus stratiform echo within the region. When viewing the unconditional frequencies of S-Pol ECCO $C_v > 0.5$ within a vertical column, the regions with the highest 8-hr rainfall accumulation are found to be predominantly associated with a narrow band which bisects the coastal maximum region (Fig. 4.5c), indicating that the

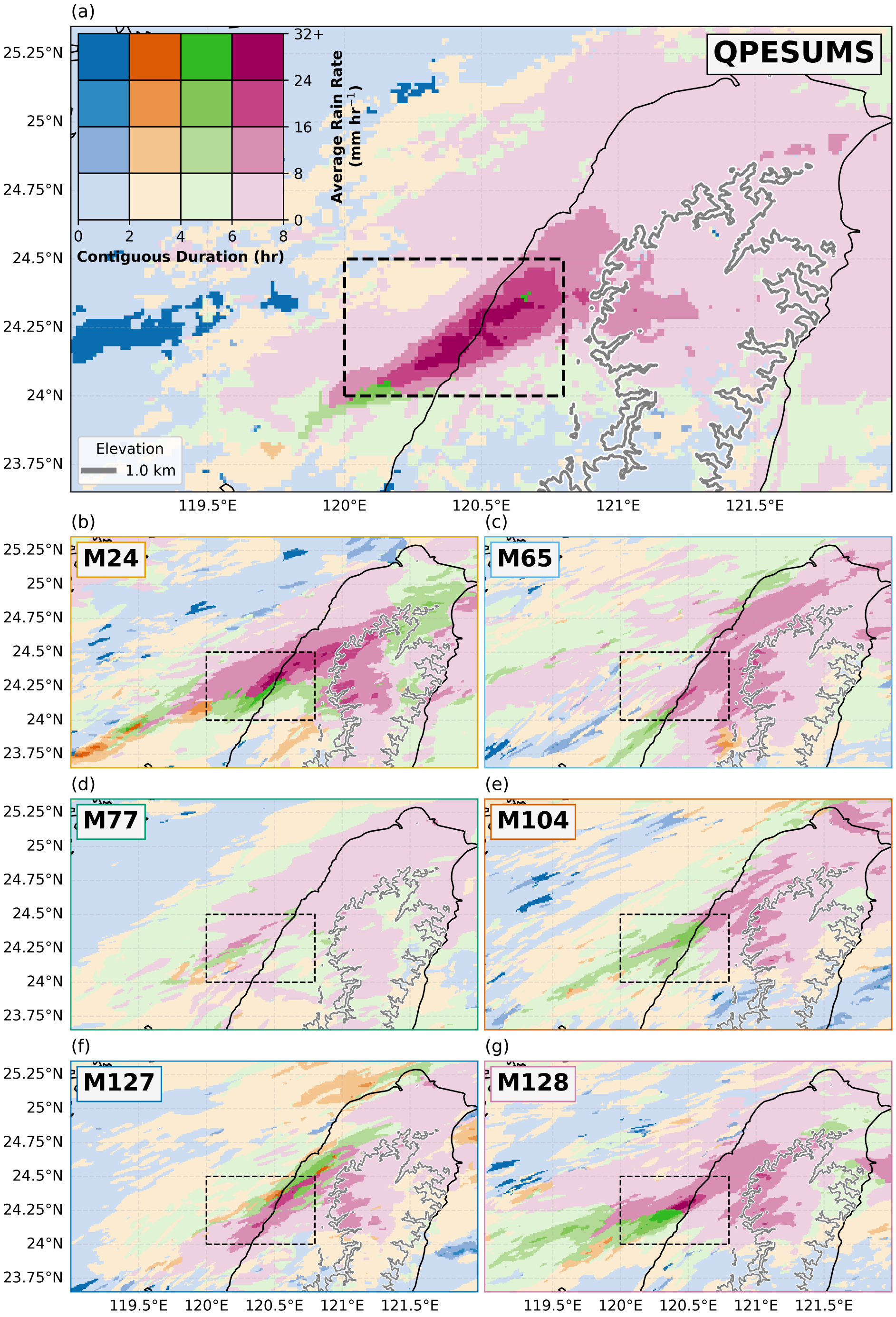

Figure 4.4: Bivariate choropleth average rainfall rate and duration between 0700 - 1500 UTC 26 May 2022 for (a) QPESUMS, (b) M24, (c) M65, (d) M77, (e) M104, (f) M127, and (g) M128. A color matrix is used as a reference for the intensity and duration based on the period of maximum rainfall accumulation gridpoint inset within (a). The coastal maximum is indicated by the black dashed box along with a 1-km elevation reference contour in grey.

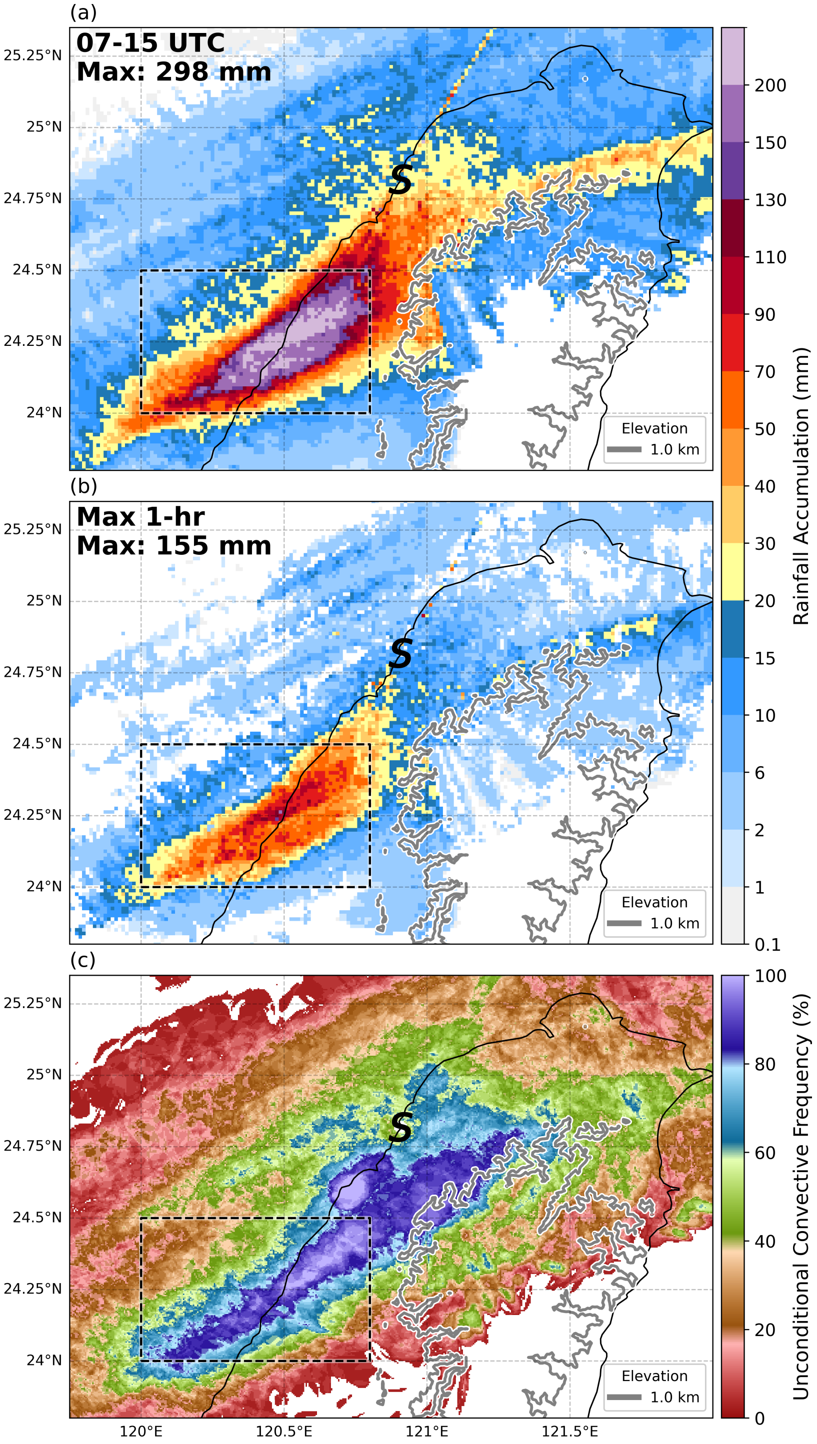

Figure 4.5: Spatial maps using S-Pol for (a) 0700 - 1500 UTC rainfall accumulation using $\mathtt{R(Synth)}$, (b) maximum 1-hr rainfall accumulation using $\mathtt{R(Synth)}$ between 0700 - 1500 UTC, and (c) unconditional frequency of convection. For each, the black dashed box indicates the coastal maximum and the grey contour outlines the 1-km elevation line.

highest intensity and duration rainfall is most frequently associated with convection.

To assess the echo distribution with height and recognizing that peak rainfall may occur at different times within the model members, Figure 4.6 shows a time series of the median C_v conditional on when there is non-zero C_v within the coastal maximum region for all height levels from S-Pol (Fig. 4.6a) and the 6 ensemble members (Fig. 4.6b-g). In addition, the maximum rainfall within the next hour for the coastal maximum is also overlaid on the time series. S-Pol predominantly shows domain median convection below 5-km, the melting layer for this case (Cornejo et al. 2025), highlighting the predominance of warm-rain convection in this region. All ensemble members overall replicate this trend, but the duration of convection varies across members. The members that most closely produced S-Pol's R_{8hr} values, M24 and M128, have more short-lived convection, less than four hours. That being said, greater rainfall intensity in WRF does not seem to be primarily associated with highest C_v values (i.e., the starts of R_{1hr} periods as triangle markers in Fig. 4.6 not being in M24 and M77). Likewise, members such as M65 and M104 have a tendency to produce convection for a longer time period compared to reality, indicating that the impact of convection on rainfall accumulation is not being well represented in the models.

As rainfall accumulation is commonly linked with greater moisture content (e.g., Chen et al. 2005, 2022b; Doswell III et al. 1996; Huang et al. 2026), differences in R_{1hr} and frequency of convection across ensemble members may be a result of differences in moisture content. Precipitable water (PW) is compared across all members in Figure 4.7 for the coastal box and against quality controlled soundings in Hsinchu (green dot in Fig. 4.1; Fig. 4.7a) where ensemble member PW values are spatially interpolated to match the coordinates of the Hsinchu sondes released at 0600 and 1200 UTC. Each member is within 10% of PW values for both the 0600 and 1200 UTC sondes giving confidence that each member can produce realistic PW values. For each member, the distributions of PW measurements at every grid point within the coastal maximum box for all times between 0600 - 1500 UTC are shown in Figure 4.7b. Generally, the members that most closely captured R_{8hr}, M24 and M128, exhibit higher median and 90^{th} percentile PW measurements compared to other members. With M77 showing the lowest intensity from Figure 4.4, it would be expected to have the lowest PW; however, the lowest median PW is given by M127. In addition to the distributions are the maximum PW values within the domain leading up to, during, and after R_{1hr} occurs (triangles in Fig. 4.7b). Through this comparison, M77 is revealed to have the lowest PW leading up to and before the peak rainfall period. With the exception of M77 and M128, all

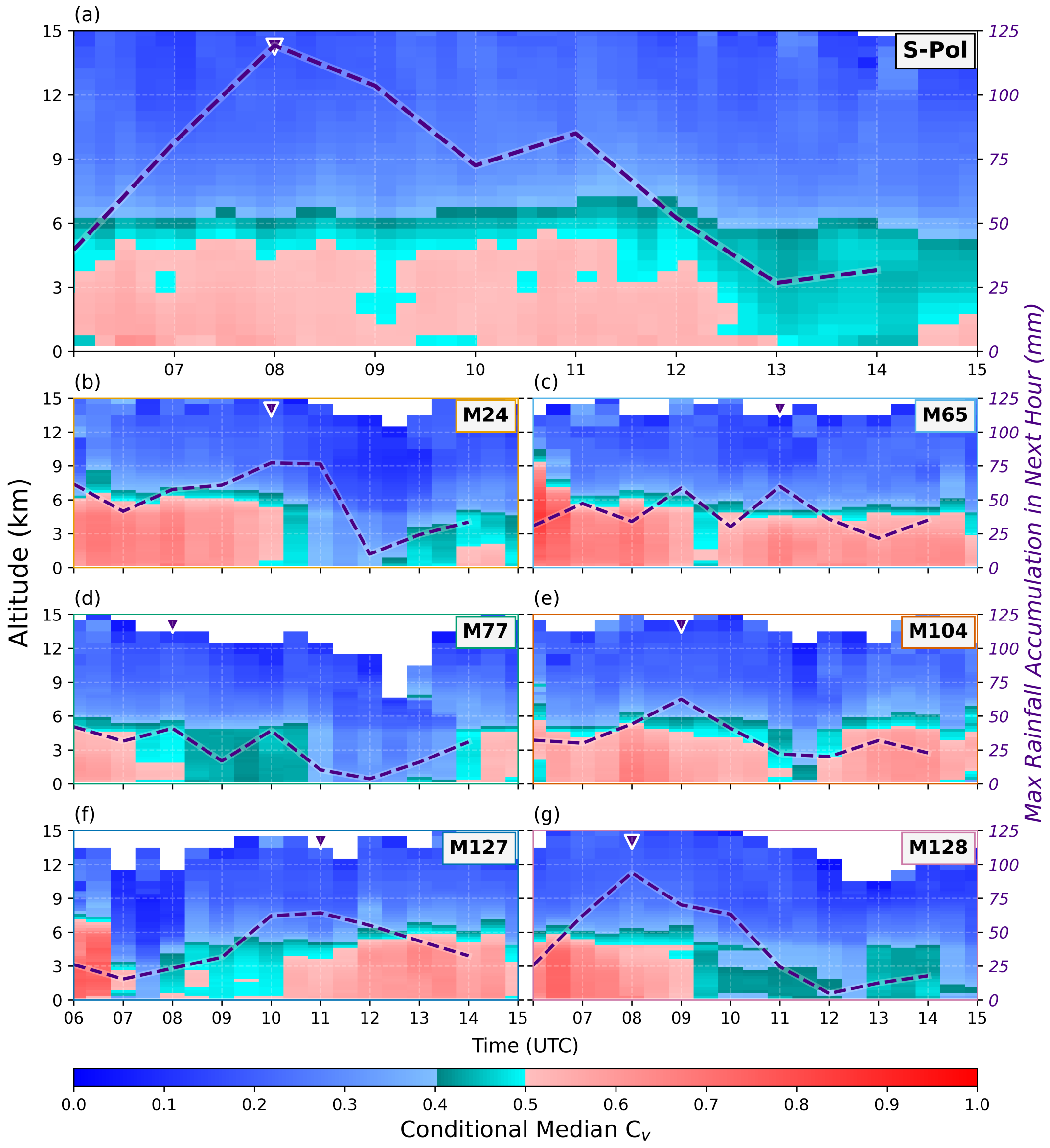

Figure 4.6: Time-height series of conditional median C_v for the coastal maximum region between 0600 - 1500 UTC 26 May 2022 for (a) S-Pol, (b) M24, (c) M65, (d) M77, (e) M104, (f) M127, and (g) M128. Additionally overlaid is a time series of maximum rainfall accumulation in the next hour for the coastal maximum region as the dashed purple lines using (a) R(Synth) and (b-g) WRF output. Triangle markers indicate starting periods for R_{1hr}.

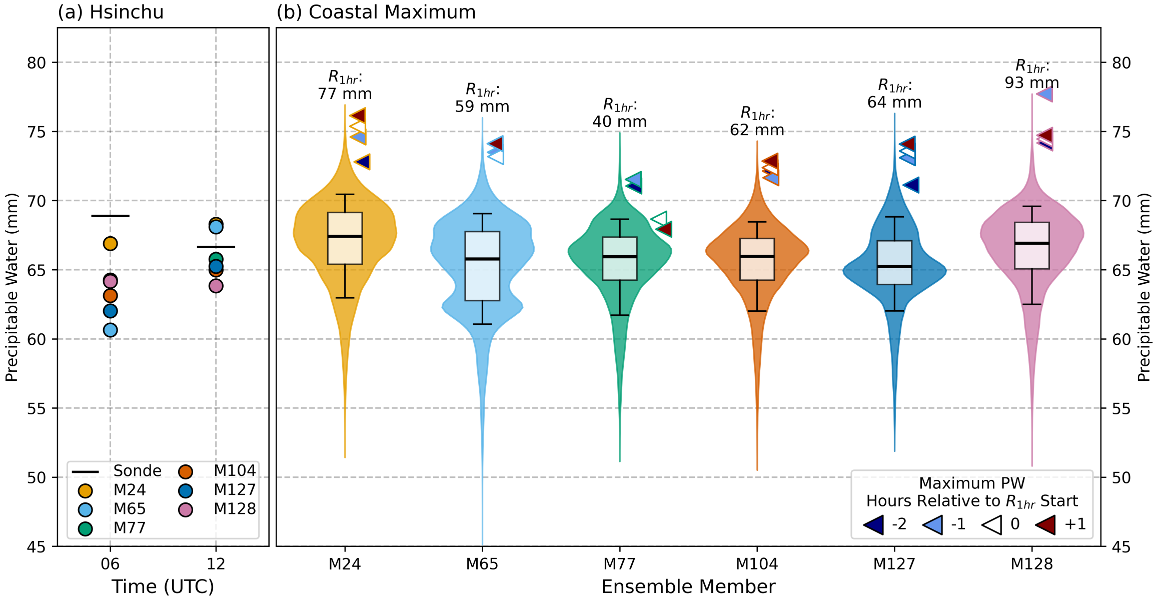

Figure 4.7: (a) Hsinchu PW and (b) coastal maximum PW distributions. Radiosonde PW and spatially interpolated ensemble member values are shown in (a). Coastal PW distributions in (b) are depicted using violin plots with embedded box plots ($10^{\text{th}}/90^{\text{th}}$ percentile whiskers, interquartile range boxes, and median lines). Triangle markers denote the timing of maximum PW relative to $\mathrm{R}_{1\mathrm{hr}}$ onset (markers in Fig. 4.6), with corresponding $\mathrm{R}_{1\mathrm{hr}}$ values labeled.

members tend to increase in maximum PW as time moves forward supporting the notion that enhanced moisture leads to increased rainfall.

In such a moisture-rich environment, the limiting factor for extreme rainfall is unlikely to be total moisture content, as all members exhibit median PW values within 5 mm of one another. Instead, differences in rainfall production are more likely tied to the efficiency with which moisture is converted into precipitation. Here, efficiency is considered at the column scale by comparing the temporal and spatial maximum column PW within the coastal maximum box to $\mathrm{R}_{1\mathrm{hr}}$ values. For an isolated column with no external moisture supply, this efficiency is physically bounded by 100%, such that $\mathrm{R}_{1\mathrm{hr}}$ cannot exceed the available PW, consistent with the traditional definitions of precipitation efficiency (e.g., Doswell III et al. 1996). When $\mathrm{R}_{1\mathrm{hr}}$ exceeds the maximum PW, it indicates that precipitation production cannot be sustained by local moisture alone and instead requires resupply from the surrounding environment. This resupply may occur through horizontal moisture advection into the column and/or vertical transport that continuously replenishes condensate within the precipitating layer, meaning values exceeding 100% reflect the combined effects of microphysical conversion and dynamical moisture resupply rather than true local efficiency. Using this framework, S-Pol observations ($R_{1hr} > 150$ mm) imply substantial external moisture resupply, as PW values exceeding 100 mm are not realistic (Guan et al. 2019). Among the model members, only M24 and M128 reach or exceed this 100% threshold, consistent with their ability to produce $R_{8hr} > 200$ mm. The remaining members fall below this threshold, indicating that despite similarly high moisture availability, they are less effective at either converting moisture into precipitation or dynamically resupplying moisture to the column.

4.3.2 Dynamical Controls on Rainfall

A common tool in diagnosing the strength, depth, positioning, and lifting of Mei-Yu fronts is relative vorticity at low levels (e.g., Chen et al. 2006, 2003, 2022c; Wang et al. 2016). As such, differences across members and reality may be due to differences in relative vorticity. Figure 4.8 shows a time-height series of median relative vorticity within the coastal maximum region using SAMURAI and the six WRF members. Additionally, as lifting is expected along the front, the 90th percentile updrafts within the domain are also added as contours. Using SAMURAI, the onset of R_{1hr} is coincident with a large increase of relative vorticity ($> 30 \times 10^{-5}$ s^{-1}) to a depth of 1.5-km, similar to the depths of Mei-Yu fronts observed during the 1987 Taiwan Area Mesoscale Experiment (Chen 1992). Only a few members show an increase in low-level relative vorticity, but none produce a magnitude or depth as high as SAMURAI. If low-level relative vorticity peaks are found, they predominantly occur within the lowest 500-m ASL as in M24, M104, and M128. Some members such as M77 and M127 produce near zero relative vorticity implying the front may not even be in the region or if it is, it has weak rotation associated with it. However, the lack of low-level rotation does not seem to deter lifting as M127 produces 90th percentile updrafts greater than 1.5 m s^{-1} during R_{1hr}. These periods of high vertical velocity also seem to correspond to when convection is present for all members (Fig. 4.6). When comparing against SAMURAI, members generally produce updrafts of similar magnitudes at the same altitudes (e.g., 2-km ASL minimum for 1.5 m s^{-1} and approximately 5-km ASL for 3 m s^{-1}); however, the differences lie in how sustained lifting is throughout the entire period even in periods without strong low-level rotation.

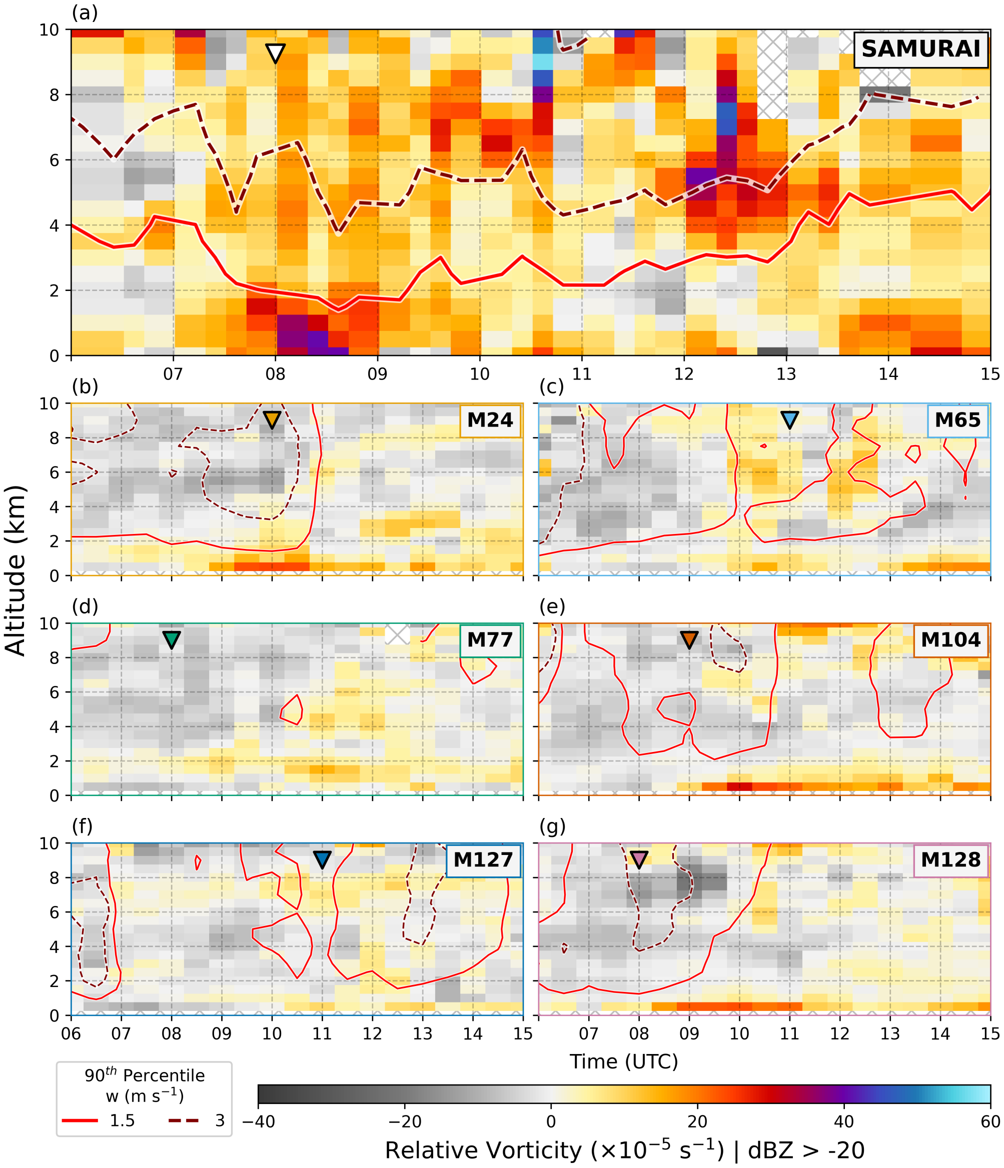

Figure 4.8: Time-height series of median relative vorticity within the coastal maximum region between 0600 - 1500 UTC 22 May 2022 using (a) SAMURAI, (b) M24, (c) M65, (d) M77, (e) M104, (f) M127, and (g) M128. Contours represent 90th percentile updrafts within the coastal maximum region. Values are only considered in the median and 90th percentile if they are collocated with radar reflectivity > -20 dBZ. Triangle markers indicate starting periods for R_{1hr}.

Lifting is often found at the leading edge of the front, yet the Figure 4.8 shows there is evidence of lift without coincident low-level vorticity in SAMURAI and most ensemble members. As such, there may be an external source of lifting such as low-level convergence not associated with the front, thus warranting an examination of the evolution of divergence (Fig. 4.9). For SAMURAI, the onset of $\mathrm{R_{1hr}}$ is associated with an increase in convergence at a depth up to 4-km (Fig. 4.9a), approximately just below the 3 m s^{-1} 90^{th} percentile contour in Figure 4.8. Unlike the relative vorticity, this enhanced convergence persists for several hours after $\mathrm{R_{1hr}}$, implying that convergence and lifting in the region are occurring regardless of frontal placement. As with relative vorticity, no member matches the same depth of convergence as SAMURAI, but M24 and M128 are able to come close in terms of magnitude ($<$ -10 $\times$ 10^{-5} s^{-1}; Fig. 4.9b, g). The difference between the two, however, is that M24 has peak convergence prior to the onset of $\mathrm{R_{1hr}}$ and M128 has the peak convergence during M128 consistent to when convection ends for each in Fig. 4.6. Across all members, unlike relative vorticity, low-level convergence is nearly persistent in all members, but it does not seem linked to vertical velocity in timing and magnitude compared to SAMURAI. For example, M77 has low-level convergence from 0-2 km ASL between 0600 - 1100 UTC, but 90^{th} percentile updrafts rarely rise above 1.5 m s^{-1} (Fig. 4.9d, 4.8d); the implication being lifting from convergence in M77 is substantially weaker than in SAMURAI. That being said, peak rainfall is found within this time period implying that there must be enough lifting of moisture to produce rainfall.

With relative vorticity and convergence maximums occurring at depths that are relatively shallow compared to SAMURAI, the altitude at which moisture is able to be lifted may be a determining factor as to why some members produce more rainfall than others. Therefore, median vertical moisture advection, $w\mathrm{q}$, is assessed similar to Figures 4.8 and 4.9, but only across WRF members (Fig. 4.10). Across all members, the highest $w\mathrm{q}$ values are found below 4-km, just below the melting layer. This result implies that this moisture is predominantly being used to form condensate. That being said, most members are able to vertically advect moisture above the melting layer during $\mathrm{R_{1hr}}$ implying a link to cold rain processes enhancing peak rainfall. In fact, the members with the largest and most prominent positive $w\mathrm{q}$ are M24 and M128, the members with the highest $\mathrm{R_{8hr}}$ values. Additionally, as previously noted with convergence, both M24 and M128 have the greatest column-wide $w\mathrm{q}$ values tied to when domain median convection ends as in Fig. 4.6 (Fig. 4.10a, f). Therefore, convergence and lifting of moisture may be more intimately related to convection as opposed

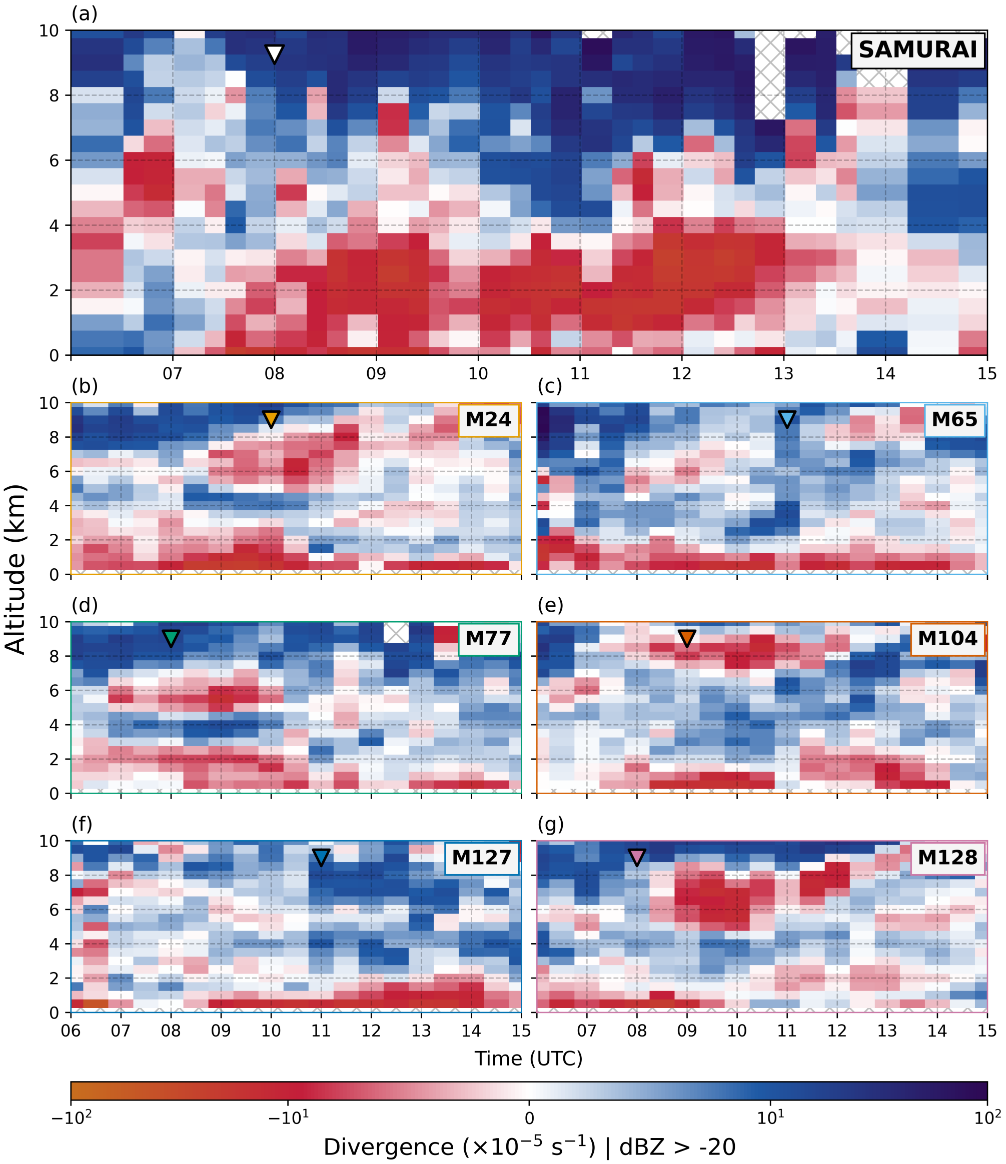

Figure 4.9: As in Fig. 4.8, but for median divergence without updraft contours.

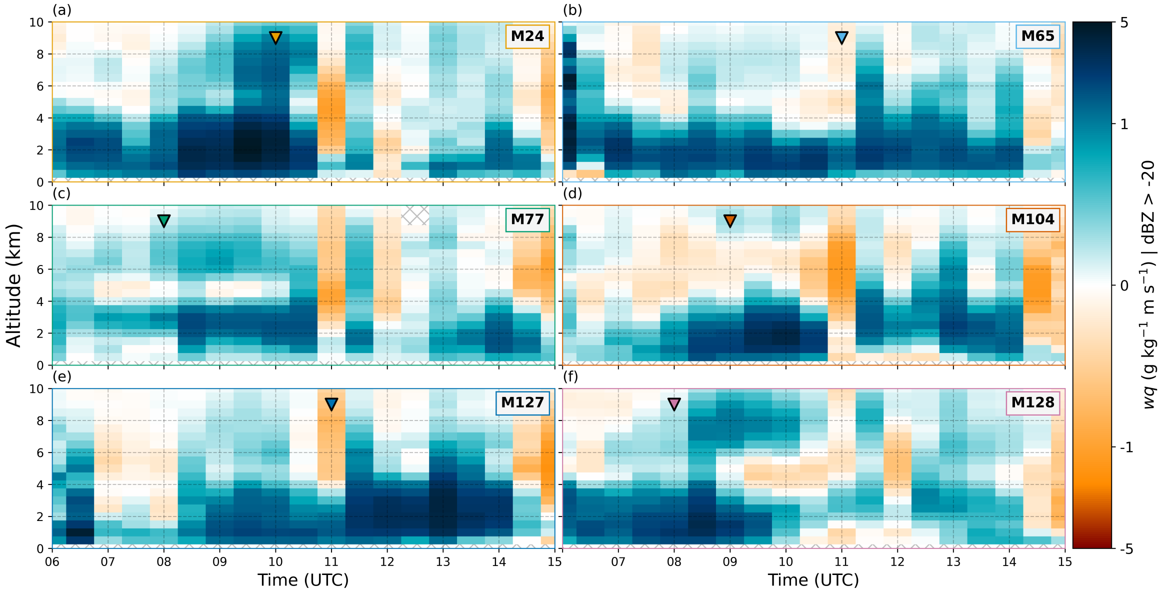

Figure 4.10: Time-height series of median wq within the coastal maximum region between 0600 - 1500 UTC 22 May 2022 for (a) M24, (b) M65, (c) M77, (d) M104, (e) M127, and (f) M128. Values are only considered in the median and 90th percentile if they are collocated with radar reflectivity > -20 dBZ. Triangle markers indicate starting periods for $\mathrm{R}_{1\mathrm{hr}}$.

to peak rainfall. An outlier in terms of lifting of moisture above the melting layer is M77. Similar to M128, M77 begins $\mathrm{R}_{1\mathrm{hr}}$ at 0800 UTC and lifts moisture throughout the column. However, the two members have a difference of 117 mm in $\mathrm{R}_{8\mathrm{hr}}$ values. With differences in low-level vorticity values (Fig. 4.8d, g) and differences in low-level convergence depth (Fig. 4.9d, g), understanding the root causes of these dynamic differences beyond the coastal maximum may point towards the resulting differences in rainfall intensity and accumulation.

4.3.3 Controls on Precipitation across Scales

Common features that interact with the Mei-Yu front in Taiwan are the low–level jets that often form on the southern side of the front. These jets include the synoptic low-level jet, often induced by a deepening of the Mei-Yu vortex that the front extends from, the marine-boundary layer low-level jet, an indication of the strengthening monsoonal flow, and the barrier jet, a more localized jet to Taiwan that is a result of a pressure gradient induced by orographic blocking (Chen et al. 2022b). The weakening or strengthening of these jets have profound effects on Mei-Yu front strength, convergence, vorticity, and rainfall produced (Chen 1992; Chen and Yu 1988; Chen et al. 2022b; Kuo and Chen 1990). The barrier jet in particular often produces the greatest effect to the Mei-Yu front when over Taiwan (e.g., Cornejo et al. 2024; Huang et al. 2026; Ke et al. 2019; Tu et al. 2022; Yeh et al. 2002). As frontal rotation was not observed in M77, but convergence and vertical moisture advection were present, the barrier jet may play a role in producing rainfall even when a well-defined front is absent, similar to the case described by Huang et al. (2026), where a Mei-Yu front's progression was halted by a strong barrier jet but precipitation persisted. SAMURAI analyses indicate periods in which lifting and convergence occurred both with and without a coherent frontal rotation. Similar behavior is reproduced across the ensemble, with some members exhibiting a rotating frontal structure and others showing primarily convergent lifting. M77 and M128 are therefore examined as representative examples of these two regimes: M77 exhibits sustained convergence and lifting without clear frontal rotation, whereas M128 retains a rotating frontal structure under otherwise similar conditions. As such, the height at which a barrier jet is commonly observed, 1 km ASL (Chen et al. 2022b), will be compared between M77 and M128 (Fig. 4.11).

As both members have the same R_{1hr} onset time, 0800 UTC, conditions before and after are assessed to better determine key environmental factors leading to peak rainfall as well as factors that ended peak rainfall. Prior to the start of the R_{1hr}, a few key differences can be observed between M77 and M128 (Fig. 4.11a, d). Primarily, the anomalous low pressure to the northeast of Taiwan is stronger in M128 and extends further into northwest Taiwan. This mesolow is a common feature for Mei-Yu fronts as the monsoonal southwest winds rise over the terrain and adiabatically cool to the northeast, forming leeside troughing (Cornejo et al. 2024; Wang and Chen 2002). This leeside troughing often has strong connection to the strength of windward winds as well as the stability upstream of Taiwan's topography (Wang and Chen 2002). With a stronger mesolow formed, the northeast winds in the postfrontal (northern) region of the front being 5 m s^{-1} stronger in M128 compared to M77. In the prefrontal (southern) region of the front, winds are relatively similar, both exhibiting maximum wind speeds upwards of 15 m s^{-1}, reaching the criteria for a synoptic low level jet (Chen et al. 2022b). Whereas M128 has a stronger high pressure anomaly on the western slopes of Taiwan, M77's high pressure anomaly and subsequent barrier jet extends further north, potentially explaining why the frontal wind shift line is extended to 25.75° N.

At the onset of R_{1hr} mesolows to the northeast have deepened for each member (denoted by the average pressure levels in Fig. 4.11b, e), however, the M128 mesolow is more

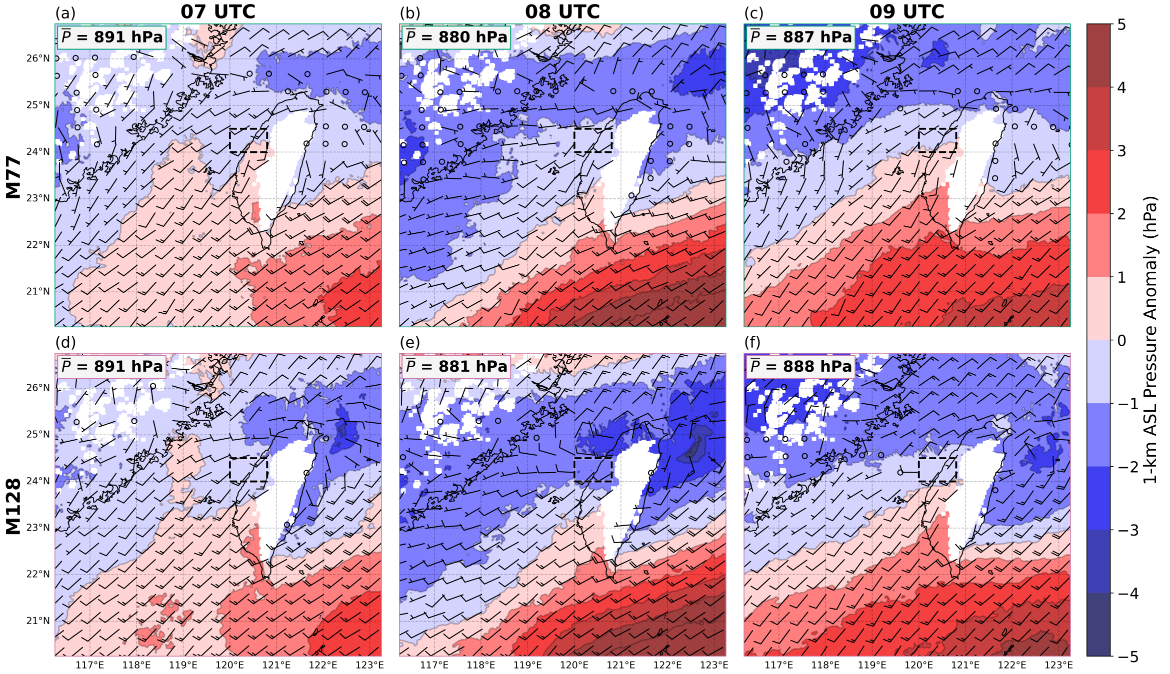

Figure 4.11: 1-km ASL pressure anomalies relative to the domain mean and wind barbs in m s^{-1} for (a, b, c) M77 and (d, e, f) M128 at (a, d) 0700 UTC, (b, e) 0800 UTC, and (c, f) 0900 UTC 26 May 2022. The coastal maximum region is outlined using a black dashed box and domain mean pressure values for each are noted in the top left.

anomalous relative to the surroundings. Thus, the postfrontal northeasterly winds remain 5 m s^{-1} stronger than in M77. Additionally, this mesolow in M128 seems to intensify the north-south pressure gradient on the western side of Taiwan. While this could also be an intensification of the barrier jet, it does not appear so in M128 as the prefrontal winds on the western slopes do not turn to southerly winds as in M77. In fact, the prefrontal winds in M77 drop to 10 m s^{-1}, outside of the range for a synoptic low-level jet. As the R_{1hr} period ends, the northeastern mesolows have filled as in M77 or have begun to weaken as in M128 (Fig. 4.11c, f). Despite this, M128 still has convergent winds > 15 m s^{-1} on both sides of the front within the coastal maximum region which partially explains why M128 maintains relatively high rainfall amounts after R_{1hr} compared to M77 (Fig. 4.6).

What is challenging however, is the lack of the wind shift line for M77 throughout this 3 hour span despite containing its R_{1hr} period. To more closely observe frontal characteristics, 500-m ASL winds, convergence, and θ_e are assessed (Fig. 4.12). This height is chosen given the presence or lack thereof in relative vorticity for M128 and M77, respectively (Fig. 4.8d,

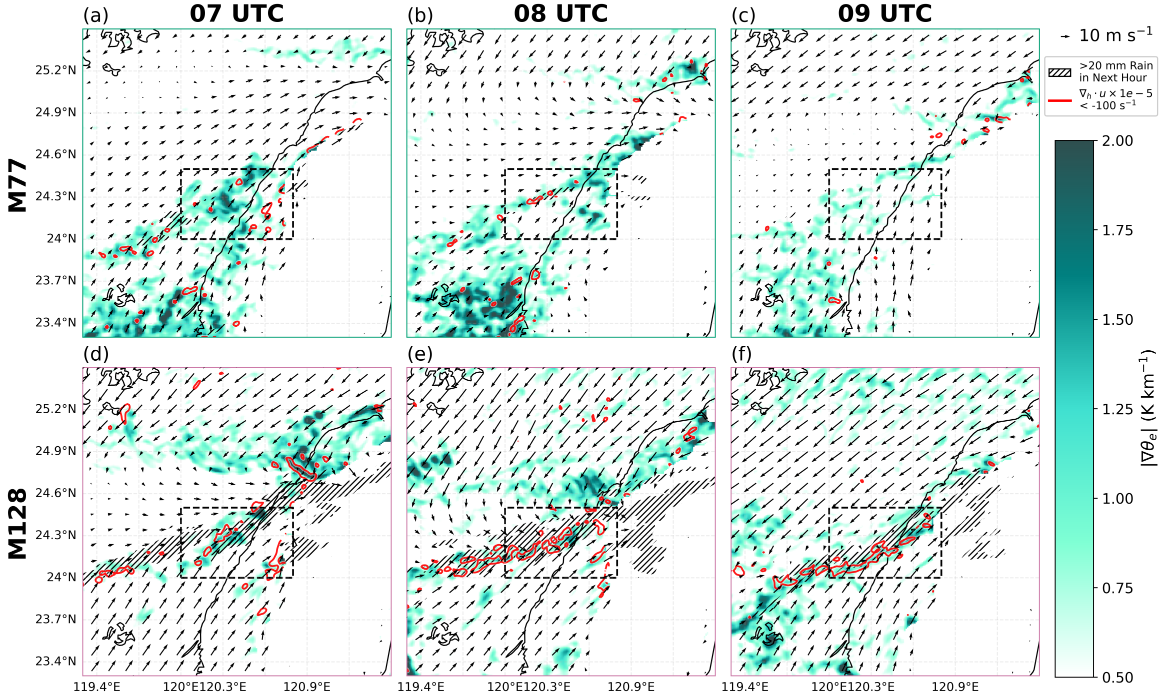

Figure 4.12: Spatial maps of 500-m ASL horizontal winds (quivers), $|\theta_e|$ (fill), divergence (red contour), and rain within the next hour (hatched contour) for (a, b, c) M77 and (d, e, f) M128 at (a, d) 0700 UTC, (b, e) 0800 UTC, and (c, f) 0900 UTC 26 May 2022. The coastal maximum region is outlined by the black dashed box.

g). As in Figure 4.11a, M77 does not exhibit a wind shift line near the coastal maximum region throughout the 3 hour period (Fig. 4.12a-c). What is apparent for M77 is a θ_e gradient oriented southwest to northeast at 0700 and 0800 UTC (Fig. 4.12a, b). Convergence aligns with this θ_e gradient at 0800 UTC producing substantial rainfall ($>$ 20 mm) in the next hour (Fig. 4.12b). After that period, the θ_e gradient weakens, winds become more southerly indicative of stronger orographic blocking in the south, and convergence dissipates.

M128 differs in that two bands of high θ_e gradients are prevalent at 0700 UTC and converge between 0800 and 0900 UTC (Fig. 4.12 d-f). Additionally, convergence and substantial rainfall are constant throughout the period in the coastal maximum region and aligned with the southern most θ_e gradient. This convergence can be associated with the larger magnitude winds on both sides of the moisture gradient, but also due to a visible wind shift starting at 0800 UTC, the start of R_{1hr} (Fig. 4.12e). The prefrontal southwesterly winds are also strong enough that they do not become blocked by the terrain, indicated by

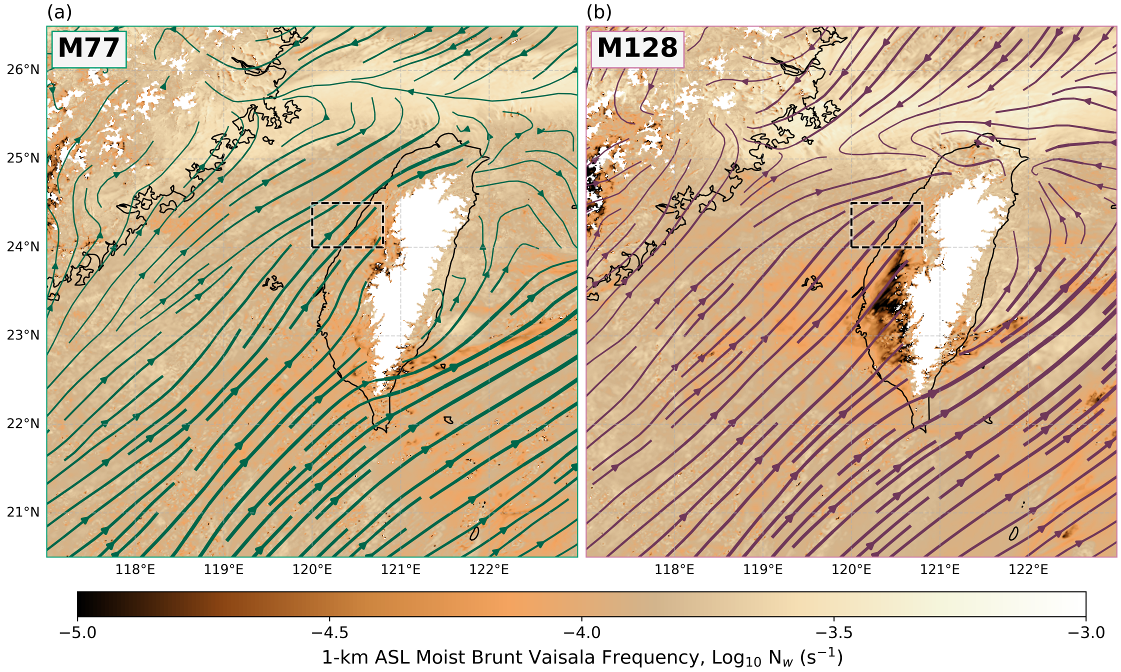

Figure 4.13: Maps of 1-km ASL Moist Brunt-Väisälä frequency with horizontal winds as streamlines at 0700 UTC 26 May 2022 for (a) M77 and (b) M128. The coastal maximum region is outlined by the black dashed box.

convergence in the eastern portion of the coastal maximum and the rainfall downstream of it in the mountains. Therefore, M128 does not show a strong prefrontal southerly flow indicative of blocking which could have shifted the front north as in Huang et al. (2026). The degree of orographic blocking is linked to the stability of the atmosphere (Chen et al. 2008b); thus Figure 4.13 shows the 1-km unsaturated, moist Brunt-Väisälä frequency (N_w) at 0700 UTC for both members. This form of the Brunt-Väisälä frequency is used as opposed to the dry form as it accounts for the changes in density associated with vapor through virtual potential temperature and is commonly used in this region (e.g, Chen et al. 2008b; Chu and Lin 2000). Prior to R_{1hr}, M128 shows substantially lower N_w relative to M77 confined near the topography between 23° and 24° N consistent with stronger stability in M77. It is through this stability that we find air flow into the topography and then diverted north indicative of stronger blocking (Fig. 4.13a). The weaker blocking in M128 also explains why the mesolow to the northeast is stronger given the stronger southwest winds and weaker stability when compared to M77.

The most striking difference between the two members is the rainfall intensity and spatial extent along the coast, with M77 producing more isolated precipitation while M128 produces broader and stronger rainfall (Fig. 4.12). These differences are consistent with higher magnitude low-level convergence and upward motion in M128 (Fig. 4.9, 4.10), but also with the widespread convection observed through S-Pol (Fig. 4.5). Stronger, moist ascent can enhance condensational growth and promote the production of frozen hydrometeors aloft, motivating further examination of microphysical differences between the two simulations. To assess these differences, hydrometeor mixing ratios of ice, snow, and graupel are averaged within the coastal rainfall maximum region and compared with the maximum rain mixing ratio produced between 0600 - 1500 UTC (Fig. 4.14). Averaging the frozen hydrometeor fields provides a measure of the broader microphysical environment supporting precipitation production, while the maximum rain mixing ratio reflects the intensity of the most efficient rainfall-producing cells. Consistent with the differences in rainfall intensity, M128 produces a larger maximum rainwater mixing ratio during $\mathrm{R_{1hr}}$ compared to M77 and also exhibits greater average mixing ratios of ice, snow, and graupel, with substantially deeper snow and graupel layers, suggesting that enhanced production and vertical transport of frozen hydrometeors contributes to the higher rainfall intensities in M128.

Across the two members, M128 consistently produces larger mixing ratios of ice, snow, and particularly graupel compared to M77, with graupel exhibiting both greater magnitude and vertical depth. These differences are consistent with the stronger ascent identified earlier in M128 and help explain its larger rain mixing ratios and higher rainfall intensities relative to M77. Despite this enhanced production of snow and graupel, however, both members still produce lower $\mathrm{R_{1hr}}$ and $\mathrm{R_{8hr}}$ values than observed by S-Pol during the event. This discrepancy suggests that even in M128, where graupel production is relatively strong, the simulated microphysical processes may not fully reproduce the hydrometeor evolution occurring in reality. In particular, limitations within the bulk microphysical scheme may be a limiting factor in producing more intense rainfall.

4.3.4 Model Representation of Microphysics

S-Pol cannot directly measure hydrometeor mixing ratios; however, PID can be used to infer dominant hydrometeor types. This algorithm is applied to the entirety of S-Pol's coverage of the coastal maximum to assess the relative evolution of hydrometeors (Fig. 4.15). Figure 4.15a shows the altitude relative percentage of the different PID classifications between 0600

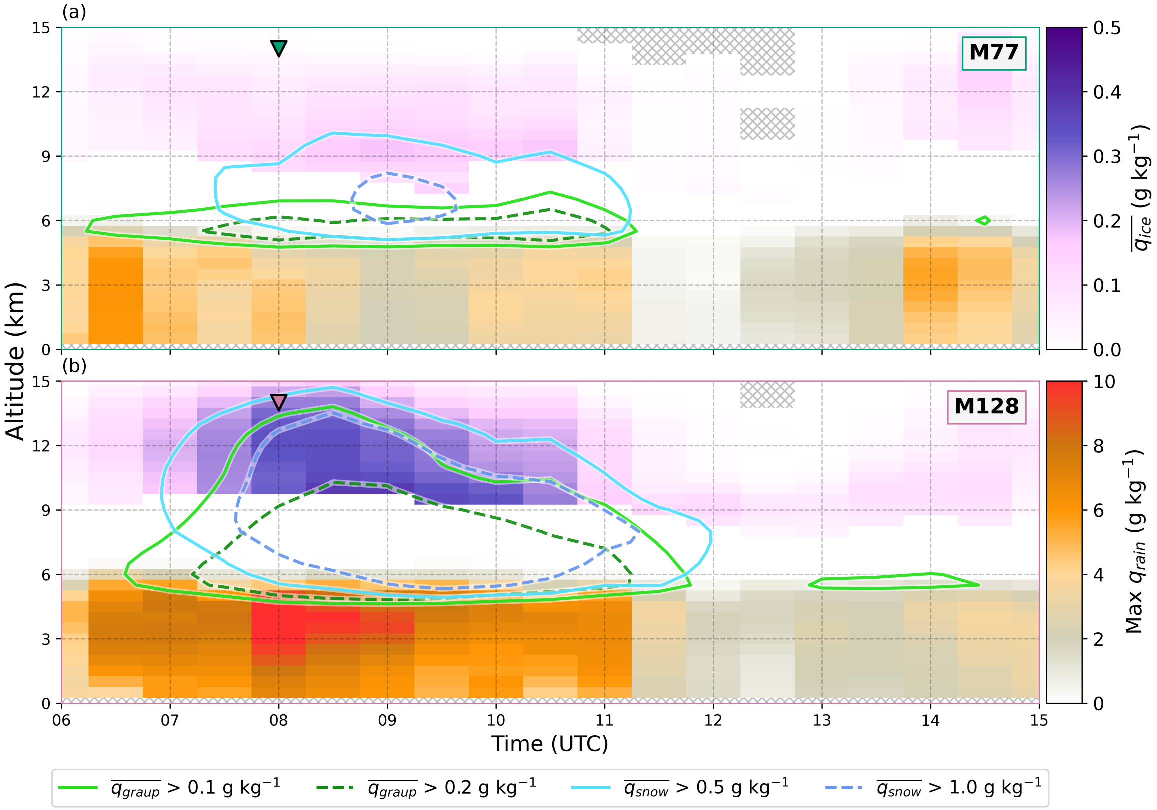

Figure 4.14: Time-height series of average ice mixing ratio (purple fill), average graupel mixing ratio (green contour), average snow mixing ratio (blue contour), and maximum rain mixing ratio (orange fill) within the coastal maximum region between 0600 - 1500 UTC 26 May 2022 for (a) M77 and (b) M128. Triangle markers indicate starting periods for R_{1hr}.

- 1500 UTC. Below the melting layer, rain is commonly observed with greater proportions of moderate and heavy rain closer to the surface. There also appears to be graupel and snow between 3.5 - 7 km ASL, with the implication being these hydrometeors melt to form the rain below. When viewed as a time-height series, we find the modal classification below the melting layer is light rain. Just before and during R_{1hr} is where moderate and heavy rainfall comprises $> 5\%$ of PID within most of the area below the melting layer. This is coincident with graupel making up $> 5\%$ of PID within and above the melting layer, implying that graupel formation contributes to greater rainfall amounts.

While S-Pol's PID cannot be compared directly to mixing ratios from M77 and M128, the presence of different hydrometeors within the models can be. In many ways, M77's mixing ratio time-height series resembles S-Pol's PID in that graupel is relatively shallow between

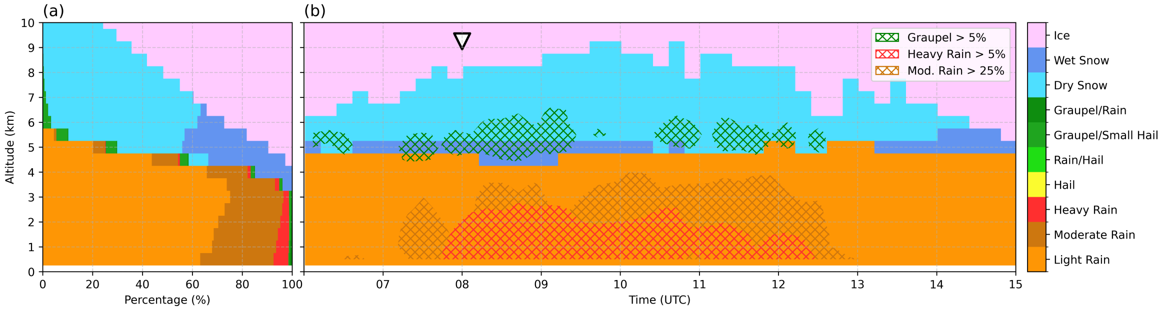

Figure 4.15: S-Pol particle identification in the coastal maximum region between 0600 - 1500 UTC 26 May 2022 as an (a) altitude relative percentage of occurrence and as a (b) time-height series of the modal classification. Additional hatched contours are added when graupel (green) or heavy rain (red) are found within 5% of the region or when moderate rain is found within 25% of the region (brown). The triangle marker indicates the starting period for R_{1hr}.

4 - 7 km ASL, it is present before and during R_{1hr} with greater depth during R_{1hr} and it's coincident with a growth in the depth of snow mixing ratio (Fig. 4.14a, 4.15b). However, M77 does not produce as much rainfall as M128 and both underestimate rain intensities and totals compared to S-Pol (Fig. 4.6). While M128 follows a similar trend as M77 in terms of graupel and snow growth leading up to and during R_{1hr}, M128 produces unrealistic graupel depth upwards of 12 km, far surpassing that maximum height where graupel is inferred from S-Pol (Fig. 4.14b, 4.15). Despite this presence of graupel throughout unrealistically large depths, M128 still cannot produce the same amount of rainfall as S-Pol suggesting there may be issues in the model's representation of rain microphysics.

The microphysics scheme used within these WRF runs is the Goddard 4ICE scheme, the scheme operationally used within CWA's operational models and often used for research case studies of rainfall in this region (Chung et al. 2020, 2026; Tsai et al. 2025). The scheme defines graupel, snow, ice, and rain using a Marshall-Palmer (M-P) distribution as follows (Marshall and Palmer 1948):

$$N(D) = N_0 e^{-\Lambda D} \tag{4.1}$$

where $N(D)$ is the number concentration, N_0 is a fixed intercept, Λ is the slope parameter, and D as the drop diameter. As N_0 is a fixed quantity, the n^{th} moment of that distribution is defined as follows:

$$M_n = \int D^n N(D) dD = \frac{n! N_0}{\Lambda^{n+1}} \tag{4.2}$$

These moments can be used to express characteristics about hydrometeor distributions within a volume. For example, fundamental characteristics of a DSD include the average size and total number of drops within a volume, more commonly expressed as the mass-weighted mean diameter, D_m, and the 0^{th} moment, M_0, respectively. These parameters can be expressed using an M-P distribution as follows:

$$D_m = M_4/M_3 = 4/\Lambda \tag{4.3}$$

$$M_0 = N_0/\Lambda \tag{4.4}$$

Similarly, the rain mixing ratio, q_r, can be expressed with proportionality to the third moment as follows:

$$q_r = \frac{\pi \rho_w}{6\rho_{air}} M_3 = \frac{\pi \rho_w}{6\rho_{air}} (\frac{3! N_0}{\Lambda^4}) = \frac{\pi \rho_w N_0}{\rho_{air} \Lambda^4} \tag{4.5}$$

With ρ_w being the density of water and ρ_{air} being the density of air. As q_r is explicitly provided by the Goddard 4ICE scheme, Λ can be determined for using q_r, and subsequently D_m and M_0, allowing for explicit representation of the model's DSD in terms of drop size and drop count. Solving for Λ returns the following:

$$\Lambda = (\frac{\pi \rho_w N_0}{\rho_{air} q_r})^{1/4} \tag{4.6}$$

Similar moments can be provided by S-Pol through the use of a double-moment normalized DSD model as detailed in Cornejo et al. (2026). Simplistically, the model uses several polarimetric variables (e.g., reflectivity, differential reflectivity, and specific attenuation) to estimate two moments of the DSD with which to model the entire DSD. Therefore, for both the WRF ensemble members and S-Pol, representations of the DSD can be made over the same region.

The number of drops, M_0, is strongly correlated with warm rain processes such as break up and collision coalescence (Cornejo et al. 2026; Lee et al. 2023). For S-Pol, we find that with the onset of R_{1hr}, the median number of drops increases within the column with a

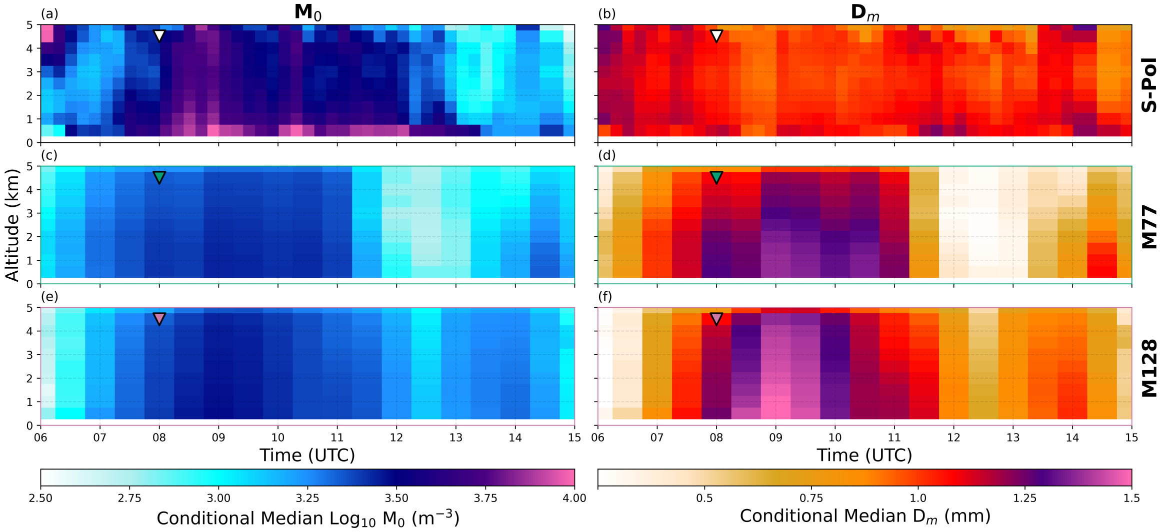

Figure 4.16: Time-height series of conditional median (a, c, e) M_0 and (b, d, f) D_m within the coastal maximum region between 0600 - 1500 UTC 26 May 2022 for (a, b) S-Pol, (c, d) M77, and (e, f) M128. Triangle markers indicate starting periods for R_{1hr}.

greater increase towards the surface implying drop multiplication processes (Fig. 4.16a). However, when viewing the model representations of M_0, we find that there are generally fewer drops at all altitudes for M77 and M128 during R_{1hr}, and the number of drops do not increase towards the surface as seen in S-Pol retrievals (Fig. 4.16c, e). Between the two members, there appears to be slightly more drops in M128 which may lead to the differences in rainfall. Despite these differences, it appears as though M77 and M128 can produce M_0 values more similar to S-Pol during non-convective periods, namely between 1300 - 1500 UTC based on Figure 4.6, potentially pointing towards the Goddard 4ICE scheme more so misrepresenting convective processes.

When considering drop growth or shrinking, D_m is used to compare the evolution of the average drop diameter. From S-Pol, D_m generally does not change much within the column during R_{1hr} with diameters near 1 mm (Fig. 4.16b). However, M77 and M128 both produce larger D_m values with a maximum near 1.5 mm for M128 (Fig. 4.16d, f). Not only do drops form larger at the surface for M77 and M128, but they are initially larger just below the melting layer as well compared to S-Pol which may imply the melting of large graupel is producing too many large drops. However, when connecting the number of drops to the average drop size, we find they are proportional within the Goddard 4ICE scheme given both rely on as follows:

$$D_m = 4M_0/N0 \tag{4.7}$$

To better visualize the relationships between size and number concentration between observations and models, the Goddard 4ICE scheme's representation of D_m and M_0 are plotted within a phase space as the black line in Figure 4.17. The median values for both M77 and M128 for all altitudes and times within the coastal maximum are added as markers on the phase space. We find that the only difference between the two members is that M128 is able to produce slightly larger drops and slightly more of them. This is indicative of greater liquid water content which may be a result of the higher precipitable water and precipitation efficiency as observed in Figure 4.7. When compared to S-Pol however, both members are underproducing drops and creating too small of drops. The median D_m and M_0 for S-Pol is higher than both M77 and M128, implying even great liquid water content values pointing to even higher precipitable water and/or precipitation efficiency amounts. However, when viewing the most common D_m and M_0 values from S-Pol (i.e., highest count in the heatmap), S-Pol tends to produce similarly sized drops as M128 ($D_m \approx 0.9$ mm), S-Pol just has more of them (Log_{10} M_0 of 3.25 m^{-3} for M128 and 3.5 m^{-3} for S-Pol). This may be a result of the Goddard 4ICE scheme's inability to break up drops (Tsai et al. 2025), a warm rain process that increases number concentration. Without this process parameterized within the Goddard 4ICE scheme, an underrepresentation of small drops leads to an underrepresentation of rainfall.

4.4 Discussion

By using an ensemble of WRF runs, a subset of six members were able to correctly place rainfall maximums along the northwest coast of Taiwan between 0700 - 1500 UTC 26 May 2022 during the PRECIP-observed IOP 1 Mei-Yu front case. While none of the members produced R_{8hr} values as high as S-Pol, some came within ~50 mm (e.g., M24 and M128). However, despite producing rainfall near the coast, M77 only produced an R_{8hr} value of 110 mm, less than half that of M24 and M128 and nearly three times lower than observed by S-Pol. Regardless of the total accumulation, all members produced high duration rainfall ($\geqslant$ 6 hours), but differed in terms of intensity. One of the key factors commonly linked to

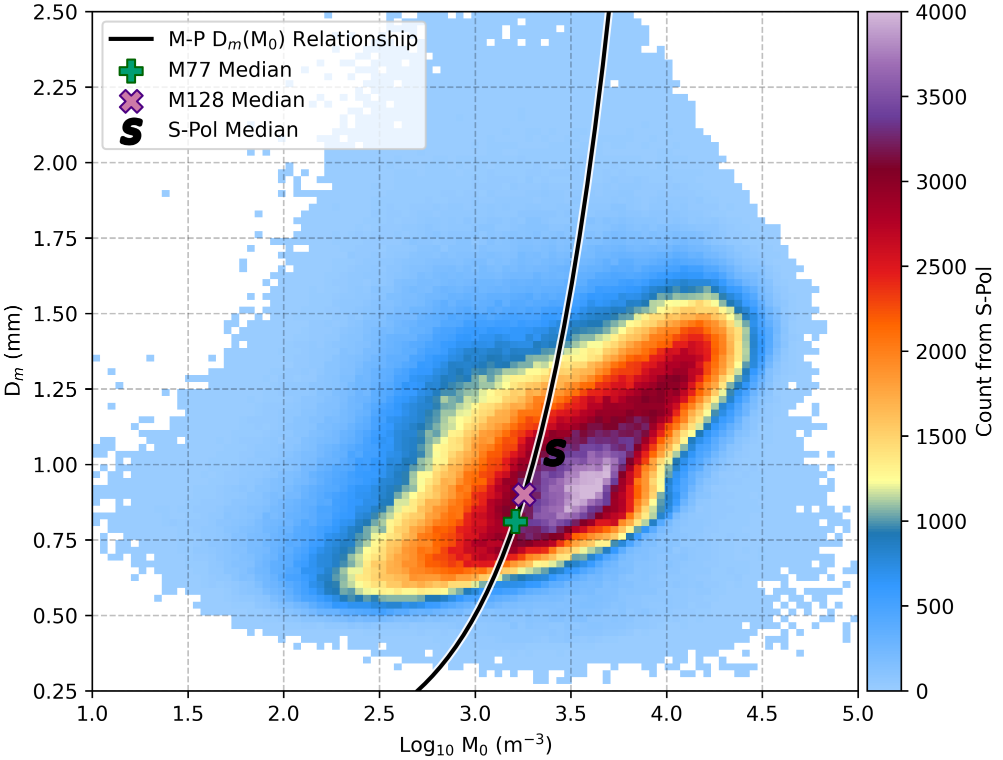

Figure 4.17: Heatmap of S-Pol M_0 and D_m values at all altitudes within the coastal maximum region between 0600 - 1500 UTC 26 May 2022 with an "S" marker for the median value. The Marshall-Palmer $D_m(M_0)$ relationship used by the Goddard 4ICE microphysics scheme is added as a solid line with markers for M77 (green plus) and M128 (pink x) median D_m and M_0 across all altitudes for the same time period and region.

enhanced Mei-Yu rainfall is moisture availability (Chien and Chiu 2023; Lien et al. 2022; Tu et al. 2020; Wang et al. 2023, 2021). While the members that produced the highest rainfall also had the highest median PW values, all members were within 5 mm of one another and exceeded three standard deviations above climatology (59 mm from Lien et al. 2022). Therefore, while more moisture is seen as key for greater rainfall intensity, overall moisture was not a missing factor across members. Instead, differences emerge when considering precipitation efficiency, particularly the ability to continuously resupply moisture during ongoing precipitation. Results suggested that precipitation rates in the members could not be sustained by local column moisture alone, indicating replenished moisture through horizontal advection into the coastal region and vertical transport that maintained condensation within the column.

When considering the factors leading to lifting of that moisture, there are a few that emerged in context of the observed multi-Doppler synthesis. While there is increased lifting associated with increased low-level vorticity, potentially by the Mei-Yu front (Fig. 4.8a), there's continued lifting and convergence in the region after the increased vorticity dissipates (Fig. 4.8, 4.9). Lifting without low-level positive vorticity is also exemplified by a few model members wherein $\mathrm{R}_{1\mathrm{hr}}$ occurs without low-level positive vorticity, indicating a separate factor may be contributing to the lifting found in Fig. 4.10. When comparing M77 and M128, some of these factors could be explored beyond the coastal maximum region. As previously noted, both members have a synoptic low-level jet present prior to $\mathrm{R}_{1\mathrm{hr}}$ based on Chen et al. (2022b)'s criteria which can supply additional moisture within the coastal maximum region to maintain a high precipitation efficiency (Fig. 4.11a, d). Downstream of this jet is a leeside vortex that forms to the northeast of Taiwan due to leeside troughing of the jet (Chen 1992; Chen et al. 2022c; Cornejo et al. 2024; Wang and Chen 2002). However, with stronger blocking in M77, indicated by more southerly flow and higher stability on the windward slopes of Taiwan, the vortex is stronger in M128 as the southwesterly monsoonal flow is more capable of rising above the terrain (Chen et al. 2007a; Chen 1992; Chen et al. 2003; Wang et al. 2005). Ensuring that the vortex is properly placed and sufficiently deep is reminiscent of Wang et al. (2021) whereby a large ensemble of Mei-Yu front simulations produced sufficient rainfall only if the leeside vortex had low enough pressure. The impact this has on rainfall is through the enhanced postfrontal winds that not only enhance convergence along the front, but keep the front within the coastal maximum region.

With weaker postfrontal flow and a stronger southerly prefrontal flow in M77 due to the barrier jet, the frontal wind shift line is actually pushed further north, similar to the cases of Cornejo et al. (2024) and Huang et al. (2026). Without strong frontal convergence, there still remains a distinct moisture gradient and some substantial rainfall in the region for M77 (Fig. 4.12a-c). This may point to some of the mechanisms by which rainfall persists in observations despite the high relative vorticity (i.e., beyond 0900 UTC in Fig. 4.8a). With the absence of a frontal wind shift, there is evidence of barrier jets providing rainfall in the prefrontal region ahead of the front. In the case of Ke et al. (2019), cold pools propagated from the main frontal system producing convective cells ahead of the front when they collided with the barrier jet, however, with no substantial rainfall observed north of the coastal maximum region in M77 (Fig. 4.12a-c), this is unlikely to be occurring. What is more likely is the convergence of the southwest flow with the barrier jet upstream of the initial blocking to form some lifting as in the case of Yeh and Chen (2003). Within their study, a synoptic low-level jet impinged on Taiwan's topography during TAMEX IOP 3, inducing a barrier jet which converges with the prevailing southwest flow. As such, the prevailing notion would be that in the absence of a strong Mei-Yu front, the coastal maximum region is an epicenter for convective activity given convergence is almost always found in the region for all members (Fig. 4.9). As the prevailing winds and subsequently the low-level shear are oriented southwesterly, it logically makes sense then that the rain will orient along the shear line, regardless of if there is frontal convergence (Chen et al. 2005; Wang et al. 2023; Xu et al. 2009). Therefore, rainfall observed may be characterized as a combination of jet convergence along the northwestern coast that may be enhanced by frontal convergence.

While the dynamical differences between the members explain much of the variability in ascent, convergence, and moisture transport, rainfall also depends on how these conditions are realized through microphysical processes. When comparing M77 and M128, their microphysical differences are not the result of different hydrometeors being present (i.e., graupel), but rather differences in concentrations and vertical extent of those hydrometeors (e.g., Fig. 4.14). Specifically, M128 has greater amounts and greater vertical extent of snow and graupel, which melt to form large drops and consequently more drops compared to M77 (Fig. 4.16). Consistent with S-Pol producing greater rainfall amounts than even M128, inferred DSDs from radar show more and larger drops compared to M128 (Fig. 4.17). However, the source and growth of these large drops within S-Pol are not the same as in the ensemble members. The Goddard 4ICE scheme has two notable drawbacks when used in Taiwan, the first being a fixed intercept, N_0 (Tao et al. 2016; Tao and Simpson 1993). By fixing this quantity, as is necessary for a single-moment microphysics scheme, the overall number of drops that can be produced, M_0, is fixed. Therefore, to achieve similar numbers of drops as observed in S-Pol, rain mixing ratio and subsequently D_m, would have to be unnaturally high (as in Fig. 4.16). This is also due to the second drawback of the Goddard 4ICE scheme, the inability to break up drops (Tao et al. 2016; Tao and Simpson 1993; Tsai et al. 2025). Thus, by excluding the processes within the microphysics scheme, the model will have a greater tendency to underproduce drops, ultimately reducing rainfall. For the Goddard 4ICE scheme to produce greater rainfall amounts, the scheme must overproduce snow and graupel, the latter of which is not recommended to be represented by an M-P distribution as this is a known drawback (Tsai et al. 2025). Within the literature, the limitations of the Goddard

4ICE scheme are currently being addressed as in Chung et al. (2026) whereby the scheme is transformed into a double-moment scheme allowing for greater diversity in N_0 and Tsai et al. (2025) whereby the M-P distribution is swapped for a Gamma distribution similarly allowing for flexibility in N_0 and adding drop break up.

4.5 Conclusions

In this study, an ensemble of high-resolution WRF simulations is analyzed in the context of radar and multi-Doppler observations from a portion of IOP 1 of the 2022 NSF-funded PRECIP field campaign to investigate the physical mechanisms, particularly at the mesoscale, that drive extreme coastal rainfall. By comparing ensemble members that all captured coastal rainfall with varying intensity with each other and with observations, we identify patterns and relationships in the model that are not directly observable, providing insight into the processes governing rainfall intensity, distribution, and persistence. A summary of the key results are as follows:

1. While members with higher precipitable water values produced the greatest 1- and 8-hr rainfall accumulations, median differences in precipitable water were small (< 5 mm) and all exceeded climatological norms. However, the highest rainfall members also exhibited moisture conversion at or above 100%, indicating that precipitation efficiency, moisture resupply and vertical advection of moisture were key drivers of rainfall intensity.
2. Convergence along the Mei-Yu front provides a primary source of lift, but precipitation is further enhanced where the orographically induced barrier jet interacts with the prevailing southwesterly prefrontal winds. Greater frontal convergence is observed when the synoptic low-level jet overcomes stability and induces deeper leeside troughing, generating stronger postfrontal winds. Members producing the most rainfall do so in regions of greatest convergence and vorticity, highlighting the role of mesoscale dynamics in modulating precipitation intensity.
3. These dynamical differences translate into microphysical contrasts. Higher rainfall members produce deeper graupel and snow layers with higher mixing ratios, as stronger moisture convergence promotes freezing aloft. Despite this, all members

> underpredict observed rainfall intensity because the microphysics scheme lacks warm-rain processes such as drop breakup and misrepresent the DSD. Graupel plays a crucial role in sustaining rainfall in the model, but its overproduction compensates for deficiencies in the DSD and warm-rain processes.

This analysis highlights the utility of both advanced multi-Doppler synthesis and microphysical inference from radars as tools for evaluating model performance in addition to the physical mechanisms only observable through models. In extending these results, future work would be to expand the number of model members used, incorporating members that displace rainfall maximums from the coastal maximum region as well as members that do not produce coastal maximums at all. By doing so, greater evaluation of the larger environment can be made such as quantifying the role of the various low-level jets and leeside troughing. Additionally, following procedures as in Cornejo et al. (2024) and Huang et al. (2026), terrain modification experiments could better determine the role of the barrier jet and leeside troughing in developing frontal convergence and/or barrier jet convergence with prefrontal flow. In a similar vein, as the Goddard 4ICE microphysics scheme did not adequately represent the microphysics observed by S-Pol, an intercomparison of microphysics schemes, including those developed by Tsai et al. (2025) and Chung et al. (2026) could better determine the microphysical controls on rainfall during this case.

Finally, this work underscores the substantial potential of multi-Doppler syntheses derived from SAMURAI for diagnosing storm dynamics in complex terrain. Even without full coverage of the coastal rainfall maximum, the retrieved kinematic fields provided critical insight into model biases. The application of a radar-based DSD model to S-Pol further enables direct comparison of microphysical characteristics within a dynamically consistent framework, opening new avenues for future research not only for this event, but for additional IOPs conducted during the PRECIP field campaign.

Chapter 5

Conclusions and Future Work

5.1 Motivation and Key Results

Extreme rainfall poses a socioeconomic challenge due to its propensity to produce floods and landslides, and can be viewed through the lens of a spectrum of both the intensity and duration of rainfall. Across these different rainfall events, there lies a variety of core ingredients that support rainfall intensity or duration including availability of moisture. Thus, by furthering our understanding of these ingredients, we can better understand extreme rainfall across varying regions and climates.

This dissertation sought to improve our understanding of rainfall intensity and duration through this ingredients-based framework using data collected during the 2022 Prediction of Rainfall Extremes Campaign in the Pacific (PRECIP). This campaign occurred between late May and early August 2022 focused over northern Taiwan with the intent of investigating these extreme rainfall ingredients and related processes. This research leveraged the dense observational network of Taiwan and several research radars deployed during PRECIP to study the controls on extreme rainfall in Taiwan across different scales. A throughline within this research is the first intensive observation period (IOP 1) which observed extreme rainfall produced during a Mei-Yu front. The dissertation was structured to scale outward in scope; from determining how best to identify and quantify extreme rainfall, to determining the microphysical processes leading to extreme rainfall, and finally, linking dynamic and thermodynamic processes to the microphysics and the rainfall associated with it, each evaluated within three chapters based on published, currently in review, and soon-to-be submitted papers. The key results of each chapter are summarized here.

Chapter 2 addressed the question: How can we best quantify extreme rainfall in regions of complex terrain using ground-based radars? Taiwan, an island covered two thirds by mountains poses a unique challenge in estimating rainfall owing to radar beam blockage and limited ground validation measurements over terrain and the adjacent ocean. As such, this chapter explored the use of specific attenuation-based rain rate retrievals, $\mathsf{R}(A_h)$, as a means to improve remotely sensed rainfall in regions of complex terrain. Attenuation itself is strongly related to rain rate at S-band frequencies, and the approach taken, the ZPHI method, has been shown to reduce the effects of partial beam blockage by terrain. This methodological chapter approaches this relatively new retrieval technique to improve it for use in the PRECIP field campaign, comparing it against more traditional methodologies. The results demonstrated that while $\mathsf{R}(A_h)$ and the newly developed $\mathsf{R}(Synth)$ perform well in estimating extreme rainfall, challenges remain in quantifying lighter rainfall due to the high amounts of urban ground clutter observed during PRECIP. Despite this challenge, the effects of partial beam blockage could be mitigated through using $\mathsf{R}(A_h)$ providing high quality rain rate retrievals blending the resolution of power-based retrievals with the skill of phase-based retrievals in heavy rainfall without the use of smoothing which reduces the highest rain rates. Additionally, incorporating $\mathsf{R}(A_h)$ into a new rain rate algorithm, $\mathsf{R}(Synth)$, further highlights that blending different rain rate estimators produces a more consistently accurate product across rainfall extremes.

Having produced a methodology by which extreme rainfall could be quantified, Chapter 3 investigated: What are the microphysical processes aloft that influence extreme rainfall, and how do these processes correspond to changes in the drop size distribution (DSD)? This chapter utilized the A_h retrieval from Chapter 2 as part of a novel DSD modeling technique applied to radar. This research was devoted to exploring the feasibility of merging different disdrometer datasets to better resolve the complete DSD toward quantifying the underlying DSD shapes in heavy rainfall in Taiwan. An outcome of this methodology was further evidence of the generalized gamma distribution's stability across different climates. This result allowed application of this DSD model to the NSF NCAR S-Pol radar dataset during IOP 1 of PRECIP to produce moments of the DSD across a range of terrain elevations in the radar domain. These modeled moments complimented the inferred microphysical processes produced using radar-derived fingerprints. A key outcome of this study was the prevalence in collision coalescence as a dominant fingerprint in both stratiform and convective echo with increases in both the number of drops and average drop size associated with the fingerprint. Additionally, inferred presence of graupel aloft was linked to enhancement in $R(A_h)$ supported by increases in both drop size and concentration below the melting level, especially in higher terrain. Therefore, this study began to unravel the microphysical links aloft to the rainfall at the surface while adapting and advancing methodologies for further DSD modeling research.

Chapter 4 scoped out further to examine: What mesoscale features promote extreme rainfall, and what are the implications this has for modeling of extreme rainfall? The study leveraged an ensemble of high-resolution numerical weather prediction model runs, multi-Doppler radar synthesis, the DSD modeling from Chapter 3, and $R(Synth)$ from Chapter 2 to compare against observations and across model members. Of the 128-member ensemble, six were chosen for their ability to reproduce a rainfall maximum in a similar location as observations during IOP 1 of PRECIP, but each member varied in terms of their accumulation with all of them underestimating compared to $R(Synth)$. The analysis revealed that while slightly higher moisture values were associated with higher rainfall amounts, it was rainfall efficiency that was more indicative of members that more closely represented observations. In a similar vein, members that were able to lift and redistribute that moisture vertically were found to produce higher rainfall values. Thus lifting sources and the ability to resupply moisture were identified as key contributors to extreme rainfall development.

While the Mei-Yu front itself was identified as one of the main lifting sources, additional lifting mechanisms were found across the members. These mechanisms include convergence of the barrier jet and the prevailing southwest flow induced by increased orographic blocking of the synoptic low-level jet. This convergence produced rainfall in lieu of strong frontal convergence in some members as enhanced stability resulted in a weaker leeside cyclone, thus weakening frontal convergence. However, in the case of stronger orographic blocking, the southerly barrier jet and weaker postfrontal winds maintains the front further north. Microphysically, these dynamic differences among model members amount to greater, albeit unrealistic, production of graupel and ice that melt and form greater rainfall amounts. When compared against the radar DSD model, it was revealed that the microphysics scheme used cannot reproduce the same number of drops at the sizes observed within the DSD model despite an overabundance of graupel in the model, revealing issues with the rain microphysics in this commonly used microphysics scheme.

Rather than viewing the preceding chapters as independent studies, their findings converge on three interrelated themes: (1) precipitation efficiency, (2) the DSD, and (3) the terrain. Within each theme, both advances and remaining uncertainties described below illuminate key directions for future research.

5.2 Efficiency in Extreme Rain

Extreme rainfall is ultimately a question of efficiency: how effectively a storm converts available moisture into surface precipitation. Across the preceding chapters, precipitation efficiency emerges not as a prescribed parameter, but as an outcome of interacting microphysical processes, storm structure, and environmental forcing. The results presented here suggest that variations in rainfall intensity and duration can be interpreted through this lens, linking radar-observed signatures to the physical mechanisms governing hydrometeor growth and fallout.

Across the six ensemble members of Chapter 4, the most intense and accumulative rainfall occurred in simulations with the highest precipitation efficiencies, underscoring efficiency as a primary control on extreme outcomes. This interpretation is consistent with the R(Synth) product, which revealed 1-hr rainfall totals exceeding the climatological extremes of precipitable water, implying sustained moisture resupply rather than static column abundance (e.g., Kim et al. 2022; Lien et al. 2022). During IOP 1, for example, moisture conversion exceeded 100%, illustrating that extreme rainfall is governed by dynamically maintained moisture throughput rather than by total column moisture alone.

In that regard, the mesoscale dynamics plays two major roles; horizontal moisture transport and lifting. To maintain the high precipitable water and subsequently, efficiency, there must be an upstream moisture source and a way to transport it. In the case of IOP 1, the prevailing moisture source was from the tropics, but the transporter was the monsoonal flow and the synoptic low-level jet (Chen et al. 1998, 2005; Chen and Yu 1988; Chen et al. 2022b; Jou and Deng 1992; Tu et al. 2019, 2020). In many ways, this echoes findings for other low-level jets globally such as the Great Plains low-level jet (Algarra et al. 2019; Higgins et al. 1997) and the South American low-level jet (Salio et al. 2007; Sasaki et al. 2022), both commonly found in climatologically drier regions in the midlatitudes compared to subtropical Taiwan. This further points to horizontal moisture fluxes being a key contributor to extreme rainfall as opposed to overall moisture content as a whole. The second role of mesoscale dynamics is lifting of moisture to either condense or freeze. In the case of

IOP 1, the primary lifting mechanism was low-level convergence along the Mei-Yu front consistent with literature (Chen 1992; Chen et al. 2008a, 2006) or by the barrier jet and the prevailing southwesterlies (Chen et al. 2005, 2022c; Ke et al. 2019; Yeh and Chen 2003). The members in Chapter 4 with the greatest rainfall totals were also those with the greatest vertical moisture fluxes magnitudes consistent with observations. As observed in Chapters 3 and 4, this moisture eventually condenses, deposits, or freezes into rain, cloud droplets, and ice, though ultimately, it all descends as liquid rain. The initial source of rain, however, is important to overall intensity and ultimately linked back to lifting. Both in Chapters 3 and 4, the presence of graupel was connected to enhanced rainfall once melted resulting in both more drops and larger drops. Graupel growth is predicated on prolonged riming through constant supply of supercooled liquid water and residence time above the melting layer, both of which are reliant on sources of lifting and/or moisture (Baschek 2005). Graupel as a means to produce heavier rainfall was key outcome of both SoWMEX/TiMREX experiments (e.g., Chang et al. 2015; Jou et al. 2011; Ruppert et al. 2013); however, this research expands on their findings by highlighting the effects graupel has on the underlying DSDs. Therefore, the resupply of moisture vertically plays a critical role in increasing rainfall intensity which enhances precipitation efficiency.

This is not to say, however, that overall moisture supply is not a crucial factor in producing extreme rainfall. As in Chapter 3, collision coalescence dominates as a prevailing warm rain process across most elevations and echo types. Evaporation played a significantly lesser role, but that may be in part due to the high baseline moisture content of Taiwan (Lien et al. 2022; Seela et al. 2024). Evaporation would act to reduce precipitation efficiency by reducing the amount of precipitation at the surface. Therefore, by maintaining higher moisture, preferably near saturation as is the case during IOP 1, evaporation does not decrease efficiency. Similarly, by keeping moisture high, condensation at lower levels drives further collision coalescence, potentially explaining as to why Dm growth for collision coalescence was greater near the surface compared to the higher portion of the warm rain depth in Chapter 3.

While this dissertation focuses on a Mei-Yu frontal case, the mechanisms highlighted, particularly the interplay between moisture transport, lift, and precipitation efficiency, are relevant across a broader spectrum of extreme rainfall events. The PRECIP 2022 campaign captured a variety of cases with differing amounts and sources of moisture, as well as varied lifting mechanisms, providing opportunities to explore how these factors influence extreme rainfall beyond the Mei-Yu front. Future studies could leverage these cases using similar diagnostic approaches to assess how changes in moisture supply or lifting processes modify precipitation efficiency. Data from radars and instruments that weren't available during IOP 1 such as Micro-Pulse DIAL LIDARs, which offer high temporal resolution moisture profiles, can be leveraged for data assimilation to improve model representation of convergence, moisture advection, and jet dynamics, key factors identified in this dissertation. Previous studies in Taiwan have shown that assimilating such datasets can substantially improve model predictions of rainfall distribution and intensity (Sun et al. 2020; Zhang et al. 2023) including events during PRECIP such as IOP 3 (Yang et al. 2024), underscoring the potential value of integrating these observations in future analyses.

5.3 Characterization of the Drop Size Distribution

If precipitation efficiency represents the system-scale outcome, then the DSD provides its microphysical foundation. Variations in DSD structure underlie the microphysical processes inherent to a storm, thereby regulating how rapidly condensate is converted to surface rainfall. Across the preceding chapters, observed and modeled differences in rainfall intensity can be traced to shifts in DSD shape and moment structure. In this sense, DSD evolution serves as the primary conduit linking storm dynamics to measurable rainfall.

A central result of this work is that the underlying shape of simulated DSDs strongly impacts rainfall evolution. Warm rain processes depend on the coexistence and interaction of drizzle and precipitation modes (e.g., Chapter 3), yet the Goddard 4ICE scheme employed in Chapter 4 constrains the DSD through fixed assumptions linking number concentration and mass-weighted mean diameter and an assumed exponential distribution. The generalized gamma distribution utilized in Chapter 3 presents a unique opportunity to evolve our ability to model microphysical changes. The double moment normalized, generalized gamma distribution presents two unique advantages compared to the Goddard 4ICE scheme. When comparing the $\hat{h}(x)$ model produced by Raupach et al. (2019) using data from the continental United States and the median $h(x)$ produced using TiMREX disdrometer data, there is little contrast. This bolstered that concept of double moment normalization being region agnostic when in previous contexts was mostly only discussed in the midlatitudes (Raupach et al. 2019). As such, by adopting double moment normalization into microphysics schemes, misrepresentation of DSDs across different climates would be reduced.

The second advantage is through double moment normalization requiring only two parameters. Using a generalized gamma distribution, the full drop size distribution could be reproduced using only the third and sixth moments (M_3 and M_6). This result suggests that a generalized gamma representation constrained by these two moments may provide a physically consistent and computationally efficient foundation for future microphysics schemes. This requires extensive knowledge of how different microphysical processes modify M_3 and M_6; however, the DSD modeling procedure paired with microphysical fingerprints provides a framework in which these relationships can be explored. Going a step further, more advanced methodology by which to infer the DSD aloft through observations can be performed with emerging utilization of S-band frequency modulated continuous wave radars which directly measure the Doppler velocity spectrum to be inverted into a DSD (Johnston et al. 2022).

Chapter 3 demonstrated and built upon the notion that representing the complete DSD, both the drizzle and precipitation modes, materially affects how microphysical structures are characterized. While $R(A_h)$ retrievals are largely proportional to rain rate and therefore relatively insensitive to full DSD shape, other polarimetric quantities, such as the Z_{dr} slope within the ZPHI algorithm, depend explicitly on higher-order DSD moments. Even with emerging efforts to reduce reliance on Z_{dr} slope (e.g., Ryzhkov et al. 2025), retrieval of A_h and polarimetric rain rates will likely continue to require assumptions about local DSD structure. Chapter 2 further showed that no single estimator, including $R(A_h)$, was sufficient across all intensities with improved stability in light rainfall achieved through blending multiple polarimetric algorithms as $R(Synth)$. However, such estimators depend on localized power-law relationships that are typically derived from disdrometer observations. Within Chapter 2, Parsivel^2 measurements were used for this purpose, yet their truncation of small drop sizes limits representation of the full DSD. When forward-simulated using a T-matrix framework, polarimetric variables derived from truncated versus complete DSDs may differ systematically albeit slightly given some polarimetric variables being more influenced by large precipitation (e.g, $Z_h \propto M_6$). Together, these findings suggest that incorporating complete DSD representations into rain rate retrieval development, particularly through T-matrix simulation of polarimetric variables, are worth exploring and may improve robustness, an area that remains largely underexplored. In doing so, however, careful consideration in future deployments of disdrometers needs to be considered as currently no single disdrometer can observe the full DSD (Thurai et al. 2017).

The processes governing extreme rainfall can be explicit as in a microphysical scheme or inferred as in polarimetric fingerprints; however, the interpretation of the effects of these processes on the DSD is not always straightforward. Polarimetric radar studies often associate collision coalescence with a reduction in number concentration accompanied by an increase in mean drop size, reflecting the aggregation of smaller drops into fewer, larger ones (Kumjian and Prat 2014; Kumjian et al. 2022). However, the DSD modeling results in Chapter 3 revealed concurrent increases in both number concentration (M_0) and mass-weighted mean diameter (D_m), suggesting a more complex evolution of the drop spectrum than the canonical interpretation implies. This complexity has implications for the representation of microphysical processes within modeling frameworks. For example, in the Goddard scheme used in Chapter 4, M_0 and D_m are intrinsically linked and drop break up is parameterized within the scheme, limiting the range of DSD evolution that can occur. Yet results from Chapter 3 indicated that breakup signatures accounted for roughly 10-20% of observed microphysical fingerprints, highlighting its potential importance in shaping the drop spectrum during extreme rainfall. These findings suggest that greater effort is needed to quantify how microphysical processes modify the full DSD and how those changes manifest in polarimetric observables. These results underscore the need for improved quantification of how warm rain processes shape the DSD and manifest in polarimetric observables, enabling more reliable interpretation of radar signatures and a deeper understanding of microphysical interactions in extreme rainfall.

In addition to warm-phase processes, ice-phase microphysics play a critical role in shaping extreme rainfall. Both observational analyses (Chapter 3) and model simulations (Chapter 4) indicate that enhanced graupel aloft can contribute to intensified surface rainfall, likely through melting-driven injection of large drops and additional liquid water into the rain layer as in Chapter 3. More broadly, ice processes including graupel, snow, and other frozen hydrometeors modulate both precipitation efficiency and the evolution of the DSD, yet they remain challenging to represent accurately in models as was evident in the Goddard 4ICE scheme. Discrepancies between radar-inferred and simulated graupel depth within Chapter 4 highlight ongoing uncertainties in the parameterization of ice microphysics, while observational limitations constrain our ability to quantify particle size distributions beyond limited in situ measurements. These gaps underscore the need for improved representation and observation of both liquid and ice hydrometeors. Achieving this would enhance radar-based interpretation of storm processes and support the development of microphysics schemes capable of reproducing realistic DSD evolution in extreme rainfall events across diverse environments.

5.4 Complex Terrain as a Modifier

Terrain is not the fundamental driver of extreme rainfall, but it modulates how rainfall processes manifest in space and time. Orography does not determine precipitation efficiency or drop size distributions in isolation; rather, it modifies airflow, moisture convergence, and storm propagation, thereby shaping the environment in which microphysical evolution unfolds. In regions such as Taiwan, orographic lifting organizes ascent and moisture transport in relatively predictable ways, often enhancing rainfall production through sustained forcing (Chen and Chen 2003; Chen et al. 1997; Chen and Li 1995). At the same time, complex terrain introduces observational challenges: beam blockage limits radar sampling and surface measurements networks of rain gauges and disdrometers sparsely populated in steep regions. Thus, terrain regulates both the physical pathways to extreme rainfall and the fidelity with which those pathways can be observed.

Terrain modifies the mechanisms that produce extreme rainfall, both directly and indirectly. In Chapter 3, for example, increasing terrain elevation was associated with greater frequency of drop breakup and the increase in rain rate when graupel was present was amplified, demonstrating a direct microphysical influence by the terrain. In Chapter 4, the primary lifting mechanism for the coastal rainfall maximum was frontal convergence rather than orographic lift, yet terrain still played an indirect role. Orographically induced barrier jets altered the position of the front, pushing it northward in members that produced less rainfall, while weaker blocking in members with greater rainfall allowed stronger upslope flow and a deeper leeside cyclone that pushed the front farther south with greater convergence. These examples highlight how terrain can amplify, redirect, or modulate the pathways through which moisture and microphysical processes translate into surface precipitation.

Complex terrain also constrains our ability to observe and validate extreme rainfall. Radar beam blockage and sparse in situ networks limit coverage in both windward and leeside regions, introducing uncertainties in microphysical, precipitation, and multi-Doppler retrievals. Chapter 2 demonstrated that attenuation retrievals can be made in regions of partial beam blockage as part of the ZPHI algorithm, mitigating some of these limitations.

Regional observational campaigns such as PRECIP and TAMEX which were focused in northern Taiwan and SoWMEX/TiMREX which were focused in the south, highlight gaps in encompassing these broader orographic phenomena such as the barrier jet which originates from blocking in southern Taiwan, yet forms in northern Taiwan (Chen et al. 2005; Chen and Chen 1995; Chen et al. 1997, 2022b; Jou et al. 2011; Ke et al. 2019; Li and Chen 1998; Yeh and Chen 2003). Fully characterizing these processes will require coordinated modeling and measurements across the entire region, improving both the evaluation of microphysics schemes and predictive understanding of extreme rainfall in complex terrain.

5.5 Concluding Thoughts and Broader Implications

Across these studies, extreme rainfall emerges as the product of interacting controls rather than any single dominant factor. Precipitation efficiency dictates how available moisture is converted into rainfall, while the DSD governs the microphysical pathways through which this conversion occurs. Terrain does not generate extreme rainfall on its own, but it persistently modifies both the physical processes and the spatial patterns in which they unfold, influencing everything from warm- and cold-rain processes to the placement of frontal convergence. Together, these findings highlight that a comprehensive understanding, accurate modeling, and effective observation of extreme rainfall require integrating efficiency, DSD evolution, and terrain to capture the full spectrum of processes controlling these events.

To expand these insights beyond a single case study, future work should consider the strategic integration of diverse observational platforms including radars, disdrometers (resolving both the drizzle and precipitation modes), LIDARS, and soundings to not only capture the temporal and spatial variability of moisture and lift, but the resulting DSDs as well. Assimilating such datasets into NWP models is critical to accurately representing convergence, mesolows, jet dynamics, and moisture transport, as highlighted in other Taiwan-based studies (Sun et al. 2020; Yang et al. 2024; Zhang et al. 2023). By applying these approaches to other rainfall regimes and geographic regions, researchers can test how variability in terrain, moisture sources, and lifting mechanisms influences extreme rainfall globally, ultimately improving prediction and hazard mitigation strategies.

Bibliography

Akaeda, K., J. Reisner, and D. Parsons, 1995: The Role of Mesoscale and Topographically Induced Circulations in Initiating a Flash Flood Observed during the TAMEX Project. *Monthly Weather Review*, **123 (6)**, 1720–1739, https://doi.org/10.1175/1520-0493(1995)123<1720:TROMAT>2.0.CO;2, URL http://journals.ametsoc.org/doi/10.1175/1520-0493(1995)123<1720:TROMAT>2.0.CO;2.

Alfieri, L., P. Claps, and F. Laio, 2010: Time-dependent <i>Z-R</i> relationships for estimating rainfall fields from radar measurements. *Natural Hazards and Earth System Sciences*, **10 (1)**, 149–158, https://doi.org/10.5194/nhess-10-149-2010, URL https://nhess.copernicus.org/articles/10/149/2010/.

Algarra, I., J. Eiras-Barca, G. Miguez-Macho, R. Nieto, and L. Gimeno, 2019: On the assessment of the moisture transport by the Great Plains low-level jet. *Earth System Dynamics*, **10 (1)**, 107–119, https://doi.org/10.5194/esd-10-107-2019, URL https://esd.copernicus.org/articles/10/107/2019/.

Atlas, D., R. C. Srivastava, and R. S. Sekhon, 1973: Doppler radar characteristics of precipitation at vertical incidence. *Reviews of Geophysics*, **11 (1)**, 1–35, https://doi.org/10.1029/RG011i001p00001, URL https://agupubs.onlinelibrary.wiley.com/doi/10.1029/RG011i001p00001.

Atlas, D., and C. W. Ulbrich, 1977: Path- and Area-Integrated Rainfall Measurement by Microwave Attenuation in the 1–3 cm Band. *J. Appl. Meteor. Climatol.*, **16**, 1322–1331, https://doi.org/10.1175/1520-0450(1977)016<1322:PAAIRM>2.0.CO;2.

Banacos, P. C., and D. M. Schultz, 2005: The Use of Moisture Flux Convergence in Forecasting Convective Initiation: Historical and Operational Perspectives. *Weather and Forecasting*, **20 (3)**, 351–366, https://doi.org/10.1175/WAF858.1, URL https://journals.ametsoc.org/doi/10.1175/WAF858.1.

Baschek, B., 2005: Influence of updrafts and embedded convection on the microphysics of riming. Ph.D. thesis, ETH Zurich, https://doi.org/10.3929/ETHZ-A-004907406, URL http://hdl.handle.net/20.500.11850/46637, artwork Size: 124 p. Medium: application/pdf Pages: 124 p.

Bell, M., 2022: nsf-lrose/lrose-topaz: lrose-topaz-20220222. Zenodo, https://doi.org/10.5281/ZENODO.6909478.

Bell, M., and H. Yu, 2023: PRECIP Radiosonde Dataset. Version 1.0. NSF NCAR Earth Observing Laboratory, URL https://data.eol.ucar.edu/dataset/621.007, artwork Size: 1953 data files, 3 ancillary/documentation files, 670 MiB Pages: 1953 data files, 3 ancillary/documentation files, 670 MiB, https://doi.org/10.26023/5SS8-D6HT-5K0N.

Bell, M. M., M. T. Montgomery, and K. A. Emanuel, 2012: Air–Sea Enthalpy and Momentum Exchange at Major Hurricane Wind Speeds Observed during CBLAST. *Journal of the Atmospheric Sciences*, **69 (11)**, 3197–3222, https://doi.org/10.1175/JAS-D-11-0276.1, URL https://journals.ametsoc.org/doi/10.1175/JAS-D-11-0276.1.

Biggerstaff, M. I., and R. A. Houze, 1991: Kinematic and Precipitation Structure of the 10–11 June 1985 Squall Line. *Monthly Weather Review*, **119 (12)**, 3034–3065, https://doi.org/10.1175/1520-0493(1991)119<3034:KAPSOT>2.0.CO;2, URL http://journals.ametsoc.org/doi/10.1175/1520-0493(1991)119<3034:KAPSOT>2.0.CO;2.

Bournas, A., and E. Baltas, 2022: Determination of the Z-R Relationship through Spatial Analysis of X-Band Weather Radar and Rain Gauge Data. *Hydrology*, **9 (8)**, 137, https://doi.org/10.3390/hydrology9080137, URL https://www.mdpi.com/2306-5338/9/8/137.

Brandes, E. A., 1977: Flow in Severe Thunderstorms Observed bu Dual-Doppler Radar. *Monthly Weather Review*, **105 (1)**, 113–120, https://doi.org/10.1175/1520-0493(1977)105<0113:FISTOB>2.0.CO;2, URL http://journals.ametsoc.org/doi/10.1175/1520-0493(1977)105<0113:FISTOB>2.0.CO;2.

Brandes, E. A., A. V. Ryzhkov, and D. S. Zrnić, 2001: An Evaluation of Radar Rainfall Estimates from Specific Differential Phase. *Journal of Atmospheric and Oceanic Technology*, **18 (3)**, 363–375, https://doi.org/10.1175/1520-0426(2001)018<0363:AEORRE>2.0.CO;2, URL http://journals.ametsoc.org/doi/10.1175/1520-0426(2001)018<0363:AEORRE>2.0.CO;2.

Brandes, E. A., G. Zhang, and J. Vivekanandan, 2002: Experiments in Rainfall Estimation with a Polarimetric Radar in a Subtropical Environment. *Journal of Applied Meteorology*, **41 (6)**, 674–685, https://doi.org/10.1175/1520-0450(2002)041<0674:EIREWA>2.0.CO;2, URL http://journals.ametsoc.org/doi/10.1175/1520-0450(2002)041<0674:EIREWA>2.0.CO;2.

Bringi, V., K. V. Mishra, M. Thurai, P. C. Kennedy, and T. H. Raupach, 2020: Retrieval of lower-order moments of the drop size distribution using CSU-CHILL X-band polarimetric radar: a case study. *Atmospheric Measurement Techniques*, **13 (9)**, 4727–4750, https://doi.org/10.5194/amt-13-4727-2020, URL https://amt.copernicus.org/articles/13/4727/2020/.

Bringi, V. N., V. Chandrasekar, N. Balakrishnan, and D. S. Zrnić, 1990: An Examination of Propagation Effects in Rainfall on Radar Measurements at Microwave Frequencies. *J. Atmos. Oceanic Technol.*, **7**, 829–840, https://doi.org/10.1175/1520-0426(1990)007<0829:AEOPEI>2.0.CO;2.

Bringi, V. N., M. Thurai, and D. Brunkow, 2008: Measurements and inferences of raindrop canting angles. *Electron. Lett.*, **44**, 1425–1426, https://doi.org/10.1049/el:20082899.

Bringi, V. N., C. R. Williams, M. Thurai, and P. T. May, 2009: Using Dual-Polarized Radar and Dual-Frequency Profiler for DSD Characterization: A Case Study from Darwin, Australia. *J. Atmos. Oceanic Technol.*, **26**, 2107–2122, https://doi.org/10.1175/2009JTECHA1258.1.

Cha, T.-Y., and M. M. Bell, 2023: Three-Dimensional Variational Multi-Doppler Wind Retrieval over Complex Terrain. *Journal of Atmospheric and Oceanic Technology*, **40 (11)**, 1381–1405, https://doi.org/10.1175/JTECH-D-23-0019.1, URL https://journals.ametsoc.org/view/journals/atot/40/11/JTECH-D-23-0019.1.xml.

Chang, P.-L., and Coauthors, 2021: An Operational Multi-Radar Multi-Sensor QPE System in Taiwan. *Bull. Amer. Meteor. Soc.*, **102**, E555–E577, https://doi.org/10.1175/BAMS-D-20-0043.1.

Chang, W.-Y., G. Lee, B. J.-D. Jou, W.-C. Lee, P.-L. Lin, and C.-K. Yu, 2020: Uncertainty in Measured Raindrop Size Distributions from Four Types of Collocated Instruments. *Remote Sensing*, **12 (7)**, 1167, https://doi.org/10.3390/rs12071167, URL https://www.mdpi.com/2072-4292/12/7/1167.

Chang, W.-Y., W.-C. Lee, and Y.-C. Liou, 2015: The Kinematic and Microphysical Characteristics and Associated Precipitation Efficiency of Subtropical Convection during SoWMEX/TiMREX. *Monthly Weather Review*, **143 (1)**, 317–340, https://doi.org/10.1175/MWR-D-14-00081.1, URL http://journals.ametsoc.org/doi/10.1175/MWR-D-14-00081.1.

Chen, C., W.-K. Tao, P.-L. Lin, G. S. Lai, S.-F. Tseng, and T.-C. C. Wang, 1998: The Intensification of the Low-Level Jet during the Development of Mesoscale Convective Systems on a Mei-Yu Front. *Monthly Weather Review*, **126 (2)**, 349–371, https://doi.org/10.1175/1520-0493(1998)126<0349:TIOTLL>2.0.CO;2, URL http://journals.ametsoc.org/doi/10.1175/1520-0493(1998)126<0349:TIOTLL>2.0.CO;2.

Chen, C.-S., W.-S. Chen, and Z. Deng, 1991: A Study of a Mountain-generated Precipitation System in Northern Taiwan during TAMEX IOP 8. *Monthly Weather Review*, **119 (11)**, 2574–2607, https://doi.org/10.1175/1520-0493(1991)119<2574:ASOAMG>2.0.CO;2, URL http://journals.ametsoc.org/doi/10.1175/1520-0493(1991)119<2574:ASOAMG>2.0.CO;2.

Chen, C.-S., and Y.-L. Chen, 2003: The Rainfall Characteristics of Taiwan. *Monthly Weather Review*, **131 (7)**, https://doi.org/10.1175/1520-0493(2003)131<1323:trcot>2.0.co;2, URL http://dx.doi.org/10.1175/1520-0493(2003)131<1323:TRCOT>2.0.CO;2.

Chen, C.-S., Y.-L. Chen, C.-L. Liu, P.-L. Lin, and W.-C. Chen, 2007a: Statistics of Heavy Rainfall Occurrences in Taiwan. *Weather and Forecasting*, **22 (5)**, https://doi.org/10.1175/waf1033.1, URL http://dx.doi.org/10.1175/WAF1033.1.

Chen, G., and Coauthors, 2019: Microphysical Characteristics of Three Convective Events with Intense Rainfall Observed by Polarimetric Radar and Disdrometer in Eastern China. *Remote Sensing*, **11 (17)**, https://doi.org/10.3390/rs11172004, URL http://dx.doi.org/10.3390/rs11172004.

Chen, G. T.-J., 1992: Mesoscale Features Observed in the Taiwan Mei-Yu Season. *J. Meteor. Soc. Japan*, **70**, 497–516, https://doi.org/10.2151/jmsj1965.70.1B_497.

Chen, G. T.-J., and I.-M. Tang, 2004: Formation and Characteristics of a Summertime Hailstorm over Northern Taiwan. *J. Meteor. Soc. Japan*, **82**, 695–709, https://doi.org/10.2151/jmsj.2004.695.

Chen, G. T.-J., C.-C. Wang, and S.-W. Chang, 2008a: A Diagnostic Case Study of Mei-yu Frontogenesis and Development of Wavelike Frontal Disturbances in the Subtropical Environment. *Monthly Weather Review*, **136 (1)**, 41–61, https://doi.org/10.1175/2007MWR1966.1, URL http://journals.ametsoc.org/doi/10.1175/2007MWR1966.1.

Chen, G. T.-J., C.-C. Wang, and D. T.-W. Lin, 2005: Characteristics of Low-Level Jets over Northern Taiwan in Mei-Yu Season and Their Relationship to Heavy Rain Events. *Monthly Weather Review*, **133 (1)**, 20–43, https://doi.org/10.1175/MWR-2813.1, URL http://journals.ametsoc.org/doi/10.1175/MWR-2813.1.

Chen, G. T.-J., C.-C. Wang, and L.-F. Lin, 2006: A Diagnostic Study of a Retreating Mei-Yu Front and the Accompanying Low-Level Jet Formation and Intensification. *Monthly Weather Review*, **134 (3)**, 874–896, https://doi.org/10.1175/MWR3099.1, URL http://journals.ametsoc.org/doi/10.1175/MWR3099.1.

Chen, G. T.-J., C.-C. Wang, and S. C.-S. Liu, 2003: Potential Vorticity Diagnostics of a Mei-Yu Front Case. *Monthly Weather Review*, **131 (11)**, 2680–2696, https://doi.org/10.1175/1520-0493(2003)131<2680:PVDOAM>2.0.CO;2, URL http://journals.ametsoc.org/doi/10.1175/1520-0493(2003)131<2680:PVDOAM>2.0.CO;2.

Chen, G. T.-J., C.-C. Wang, and A.-H. Wang, 2007b: A Case Study of Subtropical Frontogenesis during a Blocking Event. *Monthly Weather Review*, **135 (7)**, 2588–2609, https://doi.org/10.1175/MWR3412.1, URL http://journals.ametsoc.org/doi/10.1175/MWR3412.1.

Chen, G. T.-J., and C.-C. Yu, 1988: Study of Low-Level Jet and Extremely Heavy Rainfall over Northern Taiwan in the Mei-Yu Season. *Monthly Weather Review*, **116 (4)**, 884–891, https://doi.org/10.1175/1520-0493(1988)116<0884:SOLLJA>2.0.CO;2, URL http://journals.ametsoc.org/doi/10.1175/1520-0493(1988)116<0884:SOLLJA>2.0.CO;2.

Chen, J.-P., T.-C. Tsai, M.-D. Tzeng, C.-S. Liao, H.-C. Kuo, and J.-S. Hong, 2022a: Microphysical Perturbation Experiments and Ensemble Forecasts on Summertime Heavy Rainfall over Northern Taiwan. *Weather and Forecasting*, **37 (9)**, 1641–1659, https://doi.org/10.1175/WAF-D-22-0004.1, URL https://journals.ametsoc.org/view/journals/wefo/37/9/WAF-D-22-0004.1.xml.

Chen, S.-H., Y.-L. Lin, and Z. Zhao, 2008b: Effects of Unsaturated Moist Froude Number and Orographic Aspect Ratio on a Conditionally Unstable Flow over a Mesoscale Mountain. *Journal of the Meteorological Society of Japan. Ser. II*, **86 (2)**, 353–367, https://doi.org/10.2151/jmsj.86.353, URL http://www.jstage.jst.go.jp/article/jmsj/86/2/86_2_353/_article.

Chen, X. A., and Y.-L. Chen, 1995: Development of Low-Level Jets during TAMEX. *Monthly Weather Review*, **123 (6)**, 1695–1719, https://doi.org/10.1175/1520-0493(1995)123<1695:DOLLJD>2.0.CO;2, URL http://journals.ametsoc.org/doi/10.1175/1520-0493(1995)123<1695:DOLLJD>2.0.CO;2.

Chen, Y.-L., X. A. Chen, S. Chen, and Y.-H. Kuo, 1997: A Numerical Study of the Low-Level Jet during TAMEX IOP 5*. *Monthly Weather Review*, **125 (10)**, 2583–2604, https://doi.org/10.1175/1520-0493(1997)125<2583:ANSOTL>2.0.CO;2, URL http://journals.ametsoc.org/doi/10.1175/1520-0493(1997)125<2583:ANSOTL>2.0.CO;2.

Chen, Y.-L., and N. B.-F. Hui, 1990: Analysis of a Shallow Front during the Taiwan Area Mesoscale Experiment. *Monthly Weather Review*, **118 (12)**, 2649–2667, https://doi.org/10.1175/1520-0493(1990)118<2649:AOASFD>2.0.CO;2, URL http://journals.ametsoc.org/doi/10.1175/1520-0493(1990)118<2649:AOASFD>2.0.CO;2.

Chen, Y.-L., and J. Li, 1995: Characteristics of Surface Airflow and Pressure Patterns over the Island of Taiwan during TAMEX. *Monthly Weather Review*, **123 (3)**, 695–716, https://doi.org/10.1175/1520-0493(1995)123<0695:COSAAP>2.0.CO;2, URL http://journals.ametsoc.org/doi/10.1175/1520-0493(1995)123<0695:COSAAP>2.0.CO;2.

Chen, Y.-L., C.-C. Tu, F. Hsiao, C.-S. Chen, P.-L. Lin, and P.-H. Lin, 2022b: An Overview of Low-Level Jets (LLJs) and Their Roles in Heavy Rainfall over the Taiwan Area during the Early Summer Rainy Season. *Meteorology*, **1 (1)**, 64–112, https://doi.org/10.3390/meteorology1010006, URL https://www.mdpi.com/2674-0494/1/1/6.

Chen, Y.-L., C.-K. Wang, C.-C. Tu, F. Hsiao, and P.-L. Lin, 2022c: Revisiting a Mei-Yu Front Associated with Heavy Rainfall over Taiwan during 6–7 June 2003. *Atmosphere*, **13 (5)**, 644, https://doi.org/10.3390/atmos13050644, URL https://www.mdpi.com/2073-4433/13/5/644.

Chen, Y.-L., Y.-X. Zhang, and N. B.-F. Hui, 1989: Analysis of a Surface Front during the Early Summer Rainy Season over Taiwan. *Monthly Weather Review*, **117 (5)**, 909–931, https://doi.org/10.1175/1520-0493(1989)117<0909:AOASFD>2.0.CO;2, URL http://journals.ametsoc.org/doi/10.1175/1520-0493(1989)117<0909:AOASFD>2.0.CO;2.

Chien, F.-C., and Y.-C. Chiu, 2023: Factors Leading to Heavy Rainfall in Southern Taiwan in the Early Mei-Yu Season of 2020. *Monthly Weather Review*, **151 (7)**, 1885–1908, https://doi.org/10.1175/MWR-D-22-0226.1, URL https://journals.ametsoc.org/view/journals/mwre/151/7/MWR-D-22-0226.1.xml.

Cho, H.-R., and G. T. J. Chen, 1995: Mei-Yu Frontogenesis. *Journal of the Atmospheric Sciences*, **52 (11)**, 2109–2120, https://doi.org/10.1175/1520-0469(1995)052<2109:MYF>2.0.CO;2, URL http://journals.ametsoc.org/doi/10.1175/1520-0469(1995)052<2109:MYF>2.0.CO;2.

Chu, C.-M., and Y.-L. Lin, 2000: Effects of Orography on the Generation and Propagation of Mesoscale Convective Systems in a Two-Dimensional Conditionally Unstable Flow. *Journal of the Atmospheric Sciences*, **57 (23)**, 3817–3837, https://doi.org/10.1175/1520-0469(2001)057<3817:EOOOTG>2.0.CO;2, URL http://journals.ametsoc.org/doi/10.1175/1520-0469(2001)057<3817:EOOOTG>2.0.CO;2.

Chung, K.-S., H.-J. Chiu, C.-Y. Liu, and M.-Y. Lin, 2020: Satellite Observation for Evaluating Cloud Properties of the Microphysical Schemes in Weather Research and Forecasting Simulation: A Case Study of the Mei-Yu Front Precipitation System. *Remote Sensing*, **12 (18)**, 3060, https://doi.org/10.3390/rs12183060, URL https://www.mdpi.com/2072-4292/12/18/3060.

Chung, K.-S., and Coauthors, 2026: Introducing Double-Moment Warm Rain Physics into the Goddard 4ICE Microphysics Scheme. *Asia-Pacific Journal of Atmospheric Sciences*, **62 (2)**, 11, https://doi.org/10.1007/s13143-026-00430-1, URL https://link.springer.com/10.1007/s13143-026-00430-1.

Cifelli, R., V. Chandrasekar, S. Lim, P. C. Kennedy, Y. Wang, and S. A. Rutledge, 2011: A New Dual-Polarization Radar Rainfall Algorithm: Application in Colorado Precipitation Events. *J. Atmos. Oceanic Technol.*, **28**, 352–364, https://doi.org/10.1175/2010JTECHA1488.1.

Cocks, S., and Coauthors, 2019: A Prototype Quantitative Precipitation Estimation Algorithm for Operational S-Band Polarimetric Radar Utilizing Specific Attenuation and Specific Differential Phase. Part II: Performance Verification and Case Study Analysis. *J. Hydrometeor.*, **20**, 999–1014, https://doi.org/10.1175/JHM-D-18-0070.1.

Cornejo, I., K. Rasmussen, and C. C. Nam, 2023: PRECIP: PARSIVEL Disdrometer Data. Version 1.0. https://doi.org/10.26023/68DF-F1JW-8H04.

Cornejo, I. C., A. K. Rowe, M. M. Bell, and W.-Y. Chang, 2026: Modeling Rainfall Drop Size Distribution Moments using an S-Band Polarimetric Radar in Complex Terrain. Preprints, URL https://essopenarchive.org/users/1010298/articles/1370422-modeling-rainfall-drop-size-distribution-moments-using-an-s-band-polarimetric-radar-in-complex-terrain?commit=8b71a1426f5211de2f9b33c8e2a5505341b599ec, https://doi.org/10.22541/essoar.176617292.21587164/v2.

Cornejo, I. C., A. K. Rowe, M. Dixon, and U. Romatschke, 2025: Specific Attenuation-Based Rain-Rate Applicability to Varying Rainfall Intensity in Complex Terrain. *Journal of Atmospheric and Oceanic Technology*, **42 (8)**, 889–907, https://doi.org/10.1175/JTECH-D-24-0094.1, URL https://journals.ametsoc.org/view/journals/atot/42/8/JTECH-D-24-0094.1.xml.

Cornejo, I. C., A. K. Rowe, K. L. Rasmussen, and J. C. DeHart, 2024: Orographic Controls on Extreme Precipitation Associated with a Mei-Yu Front. *Mon. Wea. Rev.*, **152**, 531–551, https://doi.org/10.1175/MWR-D-23-0170.1.

Dai, F. C., and C. F. Lee, 2001: Frequency–volume relation and prediction of rainfall-induced landslides. *Engineering Geology*, **59 (3)**, 253–266, https://doi.org/10.1016/S0013-7952(00)00077-6, URL https://www.sciencedirect.com/science/article/pii/S0013795200000776.

Davis, C. A., and W.-C. Lee, 2012: Mesoscale Analysis of Heavy Rainfall Episodes from SoWMEX/TiMREX. *Journal of the Atmospheric Sciences*, **69 (2)**, 521–537, https://doi.org/10.1175/JAS-D-11-0120.1, URL https://journals.ametsoc.org/doi/10.1175/JAS-D-11-0120.1.

DeHart, J., M. Dixon, B. Javornik, M. Bell, T.-Y. Cha, A. DesRosiers, and W.-C. Lee, 2025: nsf-lrose/lrose-releases: lrose-colette-20250105. https://doi.org/10.5281/zenodo.14624762, URL https://doi.org/10.5281/zenodo.14624762, version Number: lrose-colette-20250105.

DeHart, J. C., and M. M. Bell, 2025: Quantifying the Relationships Between Dynamics and Rainfall Intensity Along the Mei-Yu Front During PRECIP 2022. *Geophysical Research Letters*, **52 (24)**, e2025GL117 992, https://doi.org/10.1029/2025GL117992, URL https://agupubs.onlinelibrary.wiley.com/doi/10.1029/2025GL117992.

Diederich, M., A. Ryzhkov, C. Simmer, P. Zhang, and S. Trömel, 2015: Use of Specific Attenuation for Rainfall Measurement at X-Band Radar Wavelengths. Part I: Radar Calibration and Partial Beam Blockage Estimation. *J. Hydrometeor.*, **16**, 487–502, https://doi.org/10.1175/JHM-D-14-0066.1.

Dixon, M., and U. Romatschke, 2022: Three-Dimensional Convective–Stratiform Echo-Type Classification and Convectivity Retrieval from Radar Reflectivity. *Journal of Atmospheric and Oceanic Technology*, **39 (11)**, https://doi.org/10.1175/jtech-d-22-0018.1, URL http://dx.doi.org/10.1175/JTECH-D-22-0018.1.

Dixon, M., U. Romatschke, and J. Hubbert, 2023: S-Pol QC1 data quality processing for PRECIP. URL https://github.com/NCAR/lrose-projects-precip/blob/main/docs/SPOL_QC1_for_PRECIP.pdf.

Dixon, M. J., J. Wilson, R. Weckworth, D. Albo, and E. Thompson, 2015: A Dual-Polarization QPE Method based on the NCAR Particle ID Algorithm Description and Preliminary Results. *37th Conf. on Radar Meteorology*, Amer. Meteor. Soc., Norman, OK, 9A.1.

Dolan, B., B. Fuchs, S. A. Rutledge, E. A. Barnes, and E. J. Thompson, 2018: Primary Modes of Global Drop Size Distributions. *Journal of the Atmospheric Sciences*, **75 (5)**, 1453–1476, https://doi.org/10.1175/JAS-D-17-0242.1, URL https://journals.ametsoc.org/doi/10.1175/JAS-D-17-0242.1.

Dolan, B., and S. A. Rutledge, 2009: A Theory-Based Hydrometeor Identification Algorithm for X-Band Polarimetric Radars. *Journal of Atmospheric and Oceanic Technology*, **26 (10)**, 2071–2088, https://doi.org/10.1175/2009JTECHA1208.1, URL http://journals.ametsoc.org/doi/10.1175/2009JTECHA1208.1.

Dolan, B., S. A. Rutledge, S. Lim, V. Chandrasekar, and M. Thurai, 2013: A Robust C-Band Hydrometeor Identification Algorithm and Application to a Long-Term Polarimetric Radar Dataset. *Journal of Applied Meteorology and Climatology*, **52 (9)**, 2162–2186, https://doi.org/10.1175/JAMC-D-12-0275.1, URL https://journals.ametsoc.org/view/journals/apme/52/9/jamc-d-12-0275.1.xml.

Doswell III, C., 1993: Flash Flood-Producing Convective Storms: Current Understanding and Research.

Doswell III, C. A., H. E. Brooks, and R. A. Maddox, 1996: Flash Flood Forecasting: An Ingredients-Based Methodology. *Weather and Forecasting*, **11 (4)**, 560–581, https://doi.org/10.1175/1520-0434(1996)011<0560:FFFAIB>2.0.CO;2, URL http://journals.ametsoc.org/doi/10.1175/1520-0434(1996)011<0560:FFFAIB>2.0.CO;2.

Dudhia, J., 1989: Numerical Study of Convection Observed during the Winter Monsoon Experiment Using a Mesoscale Two-Dimensional Model. *Journal of the Atmospheric Sciences*, **46 (20)**, 3077–3107, https://doi.org/10.1175/1520-0469(1989)046<3077:NSOCOD>2.0.CO;2, URL http://journals.ametsoc.org/doi/10.1175/1520-0469(1989)046<3077:NSOCOD>2.0.CO;2.

Dufton, D. R. L., 2016: Quantifying uncertainty in radar rainfall estimates using an X-band dual polarisation weather radar. PhD Thesis, University of Leeds.

Ellis, S., G. Meymaris, J. Hubbert, M. Dixon, G. McGehee, J. Krause, and R. Ice, 2018: Improving the Detection Probability of Low Clutter-to-Signal Ratio Ground Clutter Contamination in the WSR-88D. *34th Conf. on Env. Info. Proc. Technol.*, Amer. Meteor. Soc., Austin, TX.

Engerer, N. A., D. J. Stensrud, and M. C. Coniglio, 2008: Surface Characteristics of Observed Cold Pools. *Monthly Weather Review*, **136 (12)**, 4839–4849, https://doi.org/10.1175/2008MWR2528.1, URL http://journals.ametsoc.org/doi/10.1175/2008MWR2528.1.

Feng, Y.-C., H.-W. Hsu, T. M. Weckwerth, P.-L. Lin, Y.-C. Liou, and T.-C. C. Wang, 2021: The spatiotemporal characteristics of near-surface water vapor in a coastal region revealed from radar-derived refractivity. *Monthly Weather Review*, https://doi.org/10.1175/MWR-D-20-0425.1, URL https://journals.ametsoc.org/view/journals/mwre/aop/MWR-D-20-0425.1/MWR-D-20-0425.1.xml.

Friedrich, K., S. Higgins, F. Masters, and C. Lopez, 2013a: Articulating and Stationary PARSIVEL Disdrometer Measurements in Conditions with Strong Winds and Heavy Rainfall. *J. Atmos. Oceanic Technol.*, **30**, 2063–2080, https://doi.org/10.1175/JTECH-D-12-00254.1.

Friedrich, K., E. A. Kalina, F. J. Masters, and C. R. Lopez, 2013b: Drop-Size Distributions in Thunderstorms Measured by Optical Disdrometers during VORTEX2. *Monthly Weather Review*, **141 (4)**, 1182–1203, https://doi.org/10.1175/MWR-D-12-00116.1, URL http://journals.ametsoc.org/doi/10.1175/MWR-D-12-00116.1.

Fulton, R. A., J. P. Breidenbach, D.-J. Seo, D. A. Miller, and T. O'Bannon, 1998: The WSR-88D Rainfall Algorithm. *Weather and Forecasting*, **13 (2)**, 377–395, https://doi.org/10.1175/1520-0434(1998)013<0377:TWRA>2.0.CO;2, URL http://journals.ametsoc.org/doi/10.1175/1520-0434(1998)013<0377:TWRA>2.0.CO;2.

Gamache, J. F., and R. A. Houze, 1982: Mesoscale Air Motions Associated with a Tropical Squall Line. *Monthly Weather Review*, **110 (2)**, 118–135, https://doi.org/10.1175/1520-0493(1982)110<0118:MAMAWA>2.0.CO;2, URL http://journals.ametsoc.org/doi/10.1175/1520-0493(1982)110<0118:MAMAWA>2.0.CO;2.

Germann, U., M. Boscacci, L. Clementi, M. Gabella, A. Hering, M. Sartori, I. V. Sideris, and B. Calpini, 2022: Weather Radar in Complex Orography. *Remote Sensing*, **14 (3)**, https://doi.org/10.3390/rs14030503, URL http://dx.doi.org/10.3390/rs14030503.

Giangrande, S., R. McGraw, and L. Lei, 2013: An Application of Linear Programming to Polarimetric Radar Differential Phase Processing. *J. Atmos. Oceanic Technol.*, **30**, 1716–1729, https://doi.org/10.1175/JTECH-D-12-00147.1.

Goddard, J., and S. Cherry, 1984: The ability of dual-polarization radar (copolar linear) to predict rainfall rate and microwave attenuation. *Radio Sci.*, **19**, 201–208, https://doi.org/10.1029/RS019i001p00201.

Guan, J.-P., Y.-T. Yin, L.-F. Zhang, J.-N. Wang, and M.-Y. Zhang, 2019: Comparison Analysis of Total Precipitable Water of Satellite-Borne Microwave Radiometer Retrievals and Island Radiosondes. *Atmosphere*, **10 (7)**, 390, https://doi.org/10.3390/atmos10070390, URL https://www.mdpi.com/2073-4433/10/7/390.

Gunn, K. L. S., and T. W. R. East, 1954: The microwave properties of precipitation particles. *Quarterly Journal of the Royal Meteorological Society*, **80 (346)**, 522–545, https://doi.org/10.1002/qj.49708034603, URL https://rmets.onlinelibrary.wiley.com/doi/10.1002/qj.49708034603.

Hapuarachchi, H. a. P., Q. J. Wang, and T. C. Pagano, 2011: A review of advances in flash flood forecasting. *Hydrological Processes*, **25 (18)**, 2771–2784, https://doi.org/10.1002/hyp.8040, URL https://onlinelibrary.wiley.com/doi/full/10.1002/hyp.8040.

Hardin, J., and N. Guy, 2017: PyDSD. https://doi.org/10.5281/zenodo.9991, URL https://doi.org/10.5281/zenodo.9991, version Number: v1.0.

Helmus, J., and S. Collis, 2016: The Python ARM Radar Toolkit (Py-ART), a library for working with weather radar data in the Python programming language. *Journal of Open Research Software*, **4**, https://doi.org/10.5334/jors.119.

Henny, L., C. Thorncroft, H.-H. Hsu, and L. Bosart, 2021: Extreme Rainfall in Taiwan: Seasonal Statistics and Trends. *J. Climate*, **34**, 4711–4731, https://doi.org/10.1175/JCLI-D-20-0999.1.

Hersbach, H., and Coauthors, 2020: The ERA5 global reanalysis. *Quarterly Journal of the Royal Meteorological Society*, **146 (730)**, 1999–2049, https://doi.org/10.1002/qj.3803, URL https://rmets.onlinelibrary.wiley.com/doi/10.1002/qj.3803.

Higgins, R. W., Y. Yao, E. S. Yarosh, J. E. Janowiak, and K. C. Mo, 1997: Influence of the Great Plains Low-Level Jet on Summertime Precipitation and Moisture Transport over the Central United States. *Journal of Climate*, **10 (3)**, 481–507, https://doi.org/10.1175/1520-0442(1997)010<0481:IOTGPL>2.0.CO;2, URL http://journals.ametsoc.org/doi/10.1175/1520-0442(1997)010<0481:IOTGPL>2.0.CO;2.

Hitschfield, W., and J. Bordan, 1954: Errors Inherent in the Radar Measurement of Rainfall at Attenuating Wavelengths. *J. Atmos. Sci.*, **11**, 58–67, https://doi.org/10.1175/1520-0469(1954)011<0058:EIITRM>2.0.CO;2.

Ho, J.-Y., C.-H. Liu, W.-B. Chen, C.-H. Chang, and K. T. Lee, 2022: Using ensemble quantitative precipitation forecast for rainfall-induced shallow landslide predictions. *Geoscience Letters*, **9 (1)**, 22, https://doi.org/10.1186/s40562-022-00231-0, URL https://geoscienceletters.springeropen.com/articles/10.1186/s40562-022-00231-0.

Holloway, C. E., and J. D. Neelin, 2009: Moisture Vertical Structure, Column Water Vapor, and Tropical Deep Convection. *Journal of the Atmospheric Sciences*, **66 (6)**, 1665–1683, https://doi.org/10.1175/2008JAS2806.1, URL https://journals.ametsoc.org/doi/10.1175/2008JAS2806.1.

Hong, S.-Y., Y. Noh, and J. Dudhia, 2006: A New Vertical Diffusion Package with an Explicit Treatment of Entrainment Processes. *Monthly Weather Review*, **134 (9)**, 2318–2341, https://doi.org/10.1175/MWR3199.1, URL http://journals.ametsoc.org/doi/10.1175/MWR3199.1.

Hsiao, L.-F., and Coauthors, 2013: Ensemble forecasting of typhoon rainfall and floods over a mountainous watershed in Taiwan. *Journal of Hydrology*, **506**, 55–68, https://doi.org/10.1016/j.jhydrol.2013.08.046, URL https://linkinghub.elsevier.com/retrieve/pii/S0022169413006331.

Huang, H., K. Zhao, G. Zhang, D. Hu, and Z. Yang, 2020: Optimized raindrop size distribution retrieval and quantitative rainfall estimation from polarimetric radar. *J. Hydrol.*, **580**, 17, https://doi.org/10.1016/j.jhydrol.2019.124248.

Huang, M.-Q., P.-L. Lin, C.-C. Tu, S.-W. Hsu, and Y.-L. Chen, 2026: Effect of Low-Level Jets on the Movement of the Mei-Yu Front. *Monthly Weather Review*, e240250, https://doi.org/10.1175/MWR-D-24-0250.1, URL https://journals.ametsoc.org/view/journals/mwre/aop/MWR-D-24-0250.1/MWR-D-24-0250.1.xml.

Hubbert, J., and V. N. Bringi, 1995: An Iterative Filtering Technique for the Analysis of Copolar Differential Phase and Dual-Frequency Radar Measurements. *J. Atmos. Oceanic Technol.*, **12**, 643–648, https://doi.org/10.1175/1520-0426(1995)012<0643:AIFTFT>2.0.CO;2.

Hubbert, J. C., G. Meymaris, U. Romatschke, and M. Dixon, 2021: Using a Regression Ground Clutter Filter to Improve Weather Radar Signal Statistics: Theory and Simulations. *J. Atmos. Oceanic Technol.*, **38**, 1353–1375, https://doi.org/10.1175/JTECH-D-20-0026.1.

Jhun, J.-G., and E.-J. Lee, 2004: A New East Asian Winter Monsoon Index and Associated Characteristics of the Winter Monsoon. *Journal of Climate*, **17 (4)**, 711–726, https://doi.org/10.1175/1520-0442(2004)017<0711:ANEAWM>2.0.CO;2, URL http://journals.ametsoc.org/doi/10.1175/1520-0442(2004)017<0711:ANEAWM>2.0.CO;2.

Johnston, P. E., C. R. Williams, and A. B. White, 2022: Rain Drop Size Distributions Estimated from NOAA Snow-Level Radar Data. *Journal of Atmospheric and Oceanic Technology*, **39 (3)**, 353–366, https://doi.org/10.1175/JTECH-D-21-0049.1, URL https://journals.ametsoc.org/view/journals/atot/39/3/JTECH-D-21-0049.1.xml.

Jorgensen, D. P., and P. T. Willis, 1982: A Z-R Relationship for Hurricanes. *Journal of Applied Meteorology*, **21 (3)**, 356–366, https://doi.org/10.1175/1520-0450(1982)021<0356:AZRRFH>2.0.CO;2, URL http://journals.ametsoc.org/doi/10.1175/1520-0450(1982)021<0356:AZRRFH>2.0.CO;2.

Jou, B. J.-D., and S.-M. Deng, 1992: Structure of a Low-Level Jet and it's Role in Triggering and Organizing Moist Convection over Taiwan: A TAMEX Case Study. *Terrestrial, Atmospheric and Oceanic Sciences*, **3 (1)**, 039, https://doi.org/10.3319/TAO.1992.3.1.39(A), URL http://tao.cgu.org.tw/index.php/articles/archive/atmospheric-science/item/44.

Jou, B. J.-D., W.-C. Lee, and R. H. Johnson, 2011: An Overview Of SOWMEX/TIMREX. *The Global Monsoon System*, World Scientific, https://doi.org/10.1142/9789814343411_0018, URL http://dx.doi.org/10.1142/9789814343411_0018.

Ke, C.-Y., K.-S. Chung, T.-C. C. Wang, and Y.-C. Liou, 2019: Analysis of heavy rainfall and barrier-jet evolution during Mei-Yu season using multiple Doppler radar retrievals: a case study on 11 June 2012. *Tellus A: Dynamic Meteorology and Oceanography*, **71 (1)**, 1571 369, https://doi.org/10.1080/16000870.2019.1571369, URL https://tellusjournal.org/articles/10.1080/16000870.2019.1571369.

Ke, C.-Y., P.-J. Tsai, K.-S. Chung, Y.-L. Chen, and Y.-C. Liou, 2025: Radar Wind Retrieval, Ensemble Simulations, and Cluster Analysis of a Heavy Rainfall Event over Northern Taiwan during 1–2 June 2017. *Monthly Weather Review*, **153 (4)**, 617–635, https://doi.org/10.1175/MWR-D-24-0142.1, URL https://journals.ametsoc.org/view/journals/mwre/153/4/MWR-D-24-0142.1.xml.

Kim, S., A. Sharma, C. Wasko, and R. Nathan, 2022: Linking Total Precipitable Water to Precipitation Extremes Globally. *Earth's Future*, **10 (2)**, e2021EF002 473, https://doi.org/10.1029/2021EF002473, URL https://agupubs.onlinelibrary.wiley.com/doi/10.1029/2021EF002473.

Kruger, A., and W. F. Krajewski, 2002: Two-Dimensional Video Disdrometer: A Description. *Journal of Atmospheric and Oceanic Technology*, **19 (5)**, https://doi.org/10.1175/1520-0426(2002)019<0602:tdvdad>2.0.co;2, URL http://dx.doi.org/10.1175/1520-0426(2002)019<0602:TDVDAD>2.0.CO;2.

Kumjian, M. R., and O. P. Prat, 2014: The Impact of Raindrop Collisional Processes on the Polarimetric Radar Variables. *Journal of the Atmospheric Sciences*, **71 (8)**, https://doi.org/10.1175/jas-d-13-0357.1, URL http://dx.doi.org/10.1175/JAS-D-13-0357.1.

Kumjian, M. R., O. P. Prat, K. J. Reimel, M. van Lier-Walqui, and H. C. Morrison, 2022: Dual-Polarization Radar Fingerprints of Precipitation Physics: A Review. *Remote Sensing*, **14 (15)**, https://doi.org/10.3390/rs14153706, URL http://dx.doi.org/10.3390/rs14153706.

Kumjian, M. R., and A. V. Ryzhkov, 2012: The Impact of Size Sorting on the Polarimetric Radar Variables. *Journal of the Atmospheric Sciences*, **69 (6)**, 2042–2060, https://doi.org/10.1175/JAS-D-11-0125.1, URL https://journals.ametsoc.org/doi/10.1175/JAS-D-11-0125.1.

Kuo, Y.-H., and G. T.-J. Chen, 1990: The Taiwan Area Mesoscale Experiment (TAMEX): An Overview. *Bulletin of the American Meteorological Society*, **71 (4)**, 488–503, https://doi.org/10.1175/1520-0477(1990)071<0488:TTAMEA>2.0.CO;2, URL http://journals.ametsoc.org/doi/10.1175/1520-0477(1990)071<0488:TTAMEA>2.0.CO;2.

Ladwig, B., 2017: wrf-python. NSF National Center for Atmospheric Research, URL https://github.com/NCAR/wrf-python, artwork Size: 5 MB Pages: 5 MB, https://doi.org/10.5065/D6W094P1.

Lai, H.-W., C. A. Davis, and B. Jong-Dao Jou, 2011: A Subtropical Oceanic Mesoscale Convective Vortex Observed during SoWMEX/TiMREX. *Monthly Weather Review*, **139 (8)**, 2367–2385, https://doi.org/10.1175/2010MWR3411.1, URL https://journals.ametsoc.org/view/journals/mwre/139/8/2010mwr3411.1.xml.

Lasher-Trapp, S., S. Kumar, D. H. Moser, A. M. Blyth, J. R. French, R. C. Jackson, D. C. Leon, and D. M. Plummer, 2018: On Different Microphysical Pathways to Convective Rainfall. *Journal of Applied Meteorology and Climatology*, **57 (10)**, https://doi.org/10.1175/jamc-d-18-0041.1, URL http://dx.doi.org/10.1175/JAMC-D-18-0041.1.

Lawson, J. R., J. S. Kain, N. Yussouf, D. C. Dowell, D. M. Wheatley, K. H. Knopfmeier, and T. A. Jones, 2018: Advancing from Convection-Allowing NWP to Warn-on-Forecast: Evidence of Progress. *Weather and Forecasting*, **33 (2)**, 599–607, https://doi.org/10.1175/WAF-D-17-0145.1, URL https://journals.ametsoc.org/doi/10.1175/WAF-D-17-0145.1.

Lee, G., V. Bringi, M. Thurai, G. Lee, V. Bringi, and M. Thurai, 2023: The Retrieval of Drop Size Distribution Parameters Using a Dual-Polarimetric Radar. *Remote Sensing*, **15 (4)**, https://doi.org/10.3390/rs15041063, URL https://www.mdpi.com/2072-4292/15/4/1063, company: Multidisciplinary Digital Publishing Institute Distributor: Multidisciplinary Digital Publishing Institute Institution: Multidisciplinary Digital Publishing Institute Label: Multidisciplinary Digital Publishing Institute.

Lee, G. W., and I. Zawadzki, 2005: Variability of Drop Size Distributions: Noise and Noise Filtering in Disdrometric Data. *Journal of Applied Meteorology*, **44 (5)**, https://doi.org/10.1175/jam2222.1, URL http://dx.doi.org/10.1175/JAM2222.1.

Lee, G. W., I. Zawadzki, W. Szyrmer, D. Sempere-Torres, and R. Uijlenhoet, 2004: A General Approach to Double-Moment Normalization of Drop Size Distributions. *Journal of Applied Meteorology*, **43 (2)**, https://doi.org/10.1175/1520-0450(2004)043<0264:agatdn>2.0.co;2, URL http://dx.doi.org/10.1175/1520-0450(2004)043<0264:AGATDN>2.0.CO;2.

Lee, K. T., J.-Y. Ho, H.-M. Kao, G.-F. Lin, and T.-H. Yang, 2019: Using ensemble precipitation forecasts and a rainfall-runoff model for hourly reservoir inflow forecasting during typhoon periods. *Journal of Hydro-environment Research*, **22**, 29–37, https://doi.org/10.1016/j.jher.2018.05.002, URL https://linkinghub.elsevier.com/retrieve/pii/S1570644316302131.

Leinonen, J., 2014: High-level interface to T-matrix scattering calculations: architecture, capabilities and limitations. *Optics Express*, **22 (2)**, 1655, https://doi.org/10.1364/OE.22.001655, URL https://opg.optica.org/oe/abstract.cfm?uri=oe-22-2-1655.

Lemon, L. R., and C. A. Doswell, 1979: Severe Thunderstorm Evolution and Mesocyclone Structure as Related to Tornadogenesis. *Monthly Weather Review*, **107 (9)**, 1184–1197, https://doi.org/10.1175/1520-0493(1979)107<1184:STEAMS>2.0.CO;2, URL http://journals.ametsoc.org/doi/10.1175/1520-0493(1979)107<1184:STEAMS>2.0.CO;2.

Li, H., D. Moisseev, Y. Luo, L. Liu, Z. Ruan, L. Cui, and X. Bao, 2023: Assessing specific differential phase (K_{dp})-based quantitative precipitation estimation for the record-breaking rainfall over Zhengzhou city on 20 July 2021. *Hydro. Earth Syst. Sci.*, **27**, 1033–1046, https://doi.org/10.5194/hess-27-1033-2023.

Li, J., and Y.-L. Chen, 1998: Barrier Jets during TAMEX. *Monthly Weather Review*, **126 (4)**, 959–971, https://doi.org/10.1175/1520-0493(1998)126<0959:BJDT>2.0.CO;2, URL http://journals.ametsoc.org/doi/10.1175/1520-0493(1998)126<0959:BJDT>2.0.CO;2.

Li, J., Y.-L. Chen, and W.-C. Lee, 1997: Analysis of a Heavy Rainfall Event during TAMEX. *Monthly Weather Review*, **125 (6)**, 1060–1082, https://doi.org/10.1175/1520-0493(1997)125<1060:AOAHRE>2.0.CO;2, URL http://journals.ametsoc.org/doi/10.1175/1520-0493(1997)125<1060:AOAHRE>2.0.CO;2.

Lien, T.-Y., T.-K. Yeh, J.-S. Hong, and T.-Y. Hsiao, 2022: Variations in GPS precipitable water vapor and rainfall during the 2006–2019 Mei-yu season in Taiwan. *Advances in Space Research*, **70 (5)**, 1375–1387, https://doi.org/10.1016/j.asr.2022.05.065, URL https://linkinghub.elsevier.com/retrieve/pii/S027311772200446X.

Lim, S., W. Bang, K.-S. S. Lim, M. Thurai, and G. Lee, 2026: Improved observed full raindrop size distributions and their normalization using double and triple moments. *Atmospheric Research*, **331**, 108 675, https://doi.org/10.1016/j.atmosres.2025.108675, URL https://linkinghub.elsevier.com/retrieve/pii/S0169809525007677.

Lin, Y.-L., S. Chiao, T.-A. Wang, M. L. Kaplan, and R. P. Weglarz, 2001: Some Common Ingredients for Heavy Orographic Rainfall. *Weather and Forecasting*, **16 (6)**, https://doi.org/10.1175/1520-0434(2001)016<0633:scifho>2.0.co;2, URL http://dx.doi.org/10.1175/1520-0434(2001)016<0633:SCIFHO>2.0.CO;2.

Lu, K.-X., Y.-S. Tang, P.-F. Lin, T.-C. Chen, and P.-L. Chang, 2020: Quality control and analyses of the disdrometer network in Taiwan. *Atmos. Sci.*, **48**, 44–92, https://doi.org/10.3966/025400022020104801002.

Löffler-Mang, M., M. Kunz, and W. Schmid, 1999: On the Performance of a Low-Cost K-Band Doppler Radar for Quantitative Rain Measurements. *Journal of Atmospheric and Oceanic Technology*, **16 (3)**, https://doi.org/10.1175/1520-0426(1999)016<0379:otpoal>2.0.co;2, URL http://dx.doi.org/10.1175/1520-0426(1999)016<0379:OTPOAL>2.0.CO;2.

Maddox, R. A., 1979: A methodology for forecasting heavy convective precipitation and flash flooding. *Nat. Wea. Dig*, **4**, 30–42.

Markowski, P., and Y. Richardson, 2010: *Mesoscale Meteorology in Midlatitudes.* 1st ed., Wiley, https://doi.org/10.1002/9780470682104, URL https://onlinelibrary.wiley.com/doi/book/10.1002/9780470682104.

Marshall, J. S., and W. M. K. Palmer, 1948: THE DISTRIBUTION OF RAINDROPS WITH SIZE. *Journal of Meteorology*, **5 (4)**, 165–166, https://doi.org/10.1175/1520-0469(1948)005<0165:TDORWS>2.0.CO;2, URL http://journals.ametsoc.org/doi/10.1175/1520-0469(1948)005<0165:TDORWS>2.0.CO;2.

Matrosov, S. Y., 2005: Attenuation-Based Estimates of Rainfall Rates Aloft with Vertically Pointing Ka-Band Radars. *J. Atmos. Oceanic Technol.*, **22**, 43–54, https://doi.org/10.1175/JTECH-1677.1.

Maur, A. N. A., 2001: Statistical Tools for Drop Size Distributions: Moments and Generalized Gamma. *Journal of the Atmospheric Sciences*, **58 (4)**, https://doi.org/10.1175/1520-0469(2001)058<0407:stfdsd>2.0.co;2, URL http://dx.doi.org/10.1175/1520-0469(2001)058<0407:STFDSD>2.0.CO;2.

May, R. M., and Coauthors, 2022: MetPy: A Meteorological Python Library for Data Analysis and Visualization. *Bulletin of the American Meteorological Society*, **103 (10)**, E2273–E2284, https://doi.org/10.1175/BAMS-D-21-0125.1, URL https://journals.ametsoc.org/view/journals/bams/103/10/BAMS-D-21-0125.1.xml.

Meneghini, R., and K. Nakamura, 1990: Range Profiling of the Rain Rate by an Airborne Weather Radar. *Remote Sens. Env.*, **31**, 193–209, https://doi.org/10.1016/0034-4257(90)90089-5.

Miao, J., M. Yang, K. L. Rasmussen, M. M. Bell, H. Kuo, and T. Cha, 2025: Microphysical and Kinematical Characteristics of Merged and Isolated Convective Cells Over the Complex Terrain of the Taipei Basin. *Journal of Geophysical Research: Atmospheres*, **130 (15)**, https://doi.org/10.1029/2024jd042375, URL http://dx.doi.org/10.1029/2024JD042375.

Mlawer, E. J., S. J. Taubman, P. D. Brown, M. J. Iacono, and S. A. Clough, 1997: Radiative transfer for inhomogeneous atmospheres: RRTM, a validated correlated-k model for the longwave. *Journal of Geophysical Research: Atmospheres*, **102 (D14)**, 16 663–16 682, https://doi.org/10.1029/97JD00237, URL https://agupubs.onlinelibrary.wiley.com/doi/10.1029/97JD00237.

National Centers for Environmental Information, 2020: U.S. Billion-dollar Weather and Climate Disasters, 1980 - present (NCEI Accession 0209268). NOAA National Centers for Environmental Information, URL https://www.ncei.noaa.gov/archive/accession/0209268, https://doi.org/10.25921/STKW-7W73.

NCAR/EOL S-Pol Team, 2023: PRECIP: NCAR S-Pol radar moments data, version 1.0. UCAR/NCAR - Earth Observing Laboratory, Boulder, CO, https://doi.org/10.26023/QA4M-CDHH-MY0Z.

NCAR/EOL S-Pol Team, 2024: PRECIP: NCAR S-Pol radar moments data. Version 2.0. https://doi.org/10.26023/QA4M-CDHH-MY0Z.

Ochs, H. T., K. V. Beard, N. F. Laird, D. J. Holdridge, and D. E. Schaufelberger, 1995: Effects of Relative Humidity on the Coalescence of Small Precipitation Drops in Free Fall. *Journal of the Atmospheric Sciences*, **52 (21)**, 3673–3680, https://doi.org/10.1175/1520-0469(1995)052<3673:EORHOT>2.0.CO;2, URL http://journals.ametsoc.org/doi/10.1175/1520-0469(1995)052<3673:EORHOT>2.0.CO;2.

Passarelli, R. E. J., 1981: Autocorrelation techniques for ground clutter rejection. *20th. Conf on Radar Meteorology*, Amer. Meteor. Soc., Boston, MA.

PRECIP, 2022: PRECIP 2022 Field Campaign. URL http://precip.org/.

Pruppacher, H. R., and K. V. Beard, 1970: A wind tunnel investigation of the internal circulation and shape of water drops falling at terminal velocity in air. *Quarterly Journal of the Royal Meteorological Society*, **96 (408)**, 247–256, https://doi.org/10.1002/qj.49709640807, URL https://rmets.onlinelibrary.wiley.com/doi/10.1002/qj.49709640807.

Rao, T. N., D. N. Rao, K. Mohan, and S. Raghavan, 2001: Classification of tropical precipitating systems and associated Z - R relationships. *Journal of Geophysical Research: Atmospheres*, **106 (D16)**, 17 699–17 711, https://doi.org/10.1029/2000JD900836, URL https://agupubs.onlinelibrary.wiley.com/doi/10.1029/2000JD900836.

Raupach, T. H., and A. Berne, 2015: Correction of raindrop size distributions measured by Parsivel disdrometers, using a two-dimensional video disdrometer as a reference. *Atmos. Meas. Technol.*, **8**, 343–365, https://doi.org/10.5194/amt-8-343-2015.

Raupach, T. H., and A. Berne, 2017: Retrieval of the raindrop size distribution from polarimetric radar data using double-moment normalisation. *Atmospheric Measurement Techniques*, **10 (7)**, https://doi.org/10.5194/amt-10-2573-2017, URL http://dx.doi.org/10.5194/amt-10-2573-2017.

Raupach, T. H., M. Thurai, V. N. Bringi, and A. Berne, 2019: Reconstructing the Drizzle Mode of the Raindrop Size Distribution Using Double-Moment Normalization. *Journal of Applied Meteorology and Climatology*, **58 (1)**, 145–164, https://doi.org/10.1175/JAMC-D-18-0156.1, URL https://journals.ametsoc.org/view/journals/apme/58/1/jamc-d-18-0156.1.xml.

Ray, P. S., A. Robinson, and Y. Lin, 1991: Radar Analysis of a TAMEX Frontal System. *Monthly Weather Review*, **119 (11)**, 2519–2539, https://doi.org/10.1175/1520-0493(1991)119<2519:RAOATF>2.0.CO;2, URL http://journals.ametsoc.org/doi/10.1175/1520-0493(1991)119<2519:RAOATF>2.0.CO;2.

Ray, P. S., and K. K. Wagner, 1976: Multiple Doppler radar observations of storms. *Geophysical Research Letters*, **3 (3)**, 189–191, https://doi.org/10.1029/GL003i003p00189, URL https://agupubs.onlinelibrary.wiley.com/doi/10.1029/GL003i003p00189.

Ray, P. S., C. L. Ziegler, W. Bumgarner, and R. J. Serafin, 1980: Single- and Multiple-Doppler Radar Observations of Tornadic Storms. *Monthly Weather Review*, **108 (10)**, 1607–1625, https://doi.org/10.1175/1520-0493(1980)108<1607:SAMDRO>2.0.CO;2, URL http://journals.ametsoc.org/doi/10.1175/1520-0493(1980)108<1607:SAMDRO>2.0.CO;2.

Rivelli Zea, L., S. W. Nesbitt, A. Ladino, J. C. Hardin, and A. Varble, 2021: Raindrop Size Spectrum in Deep Convective Regions of the Americas. *Atmosphere*, **12 (8)**, 979, https://doi.org/10.3390/atmos12080979, URL https://www.mdpi.com/2073-4433/12/8/979.

Roe, G. H., 2005: Orographic Precipitation. *Annual Review of Earth and Planetary Sciences*, **33 (1)**, https://doi.org/10.1146/annurev.earth.33.092203.122541, URL http://dx.doi.org/10.1146/annurev.earth.33.092203.122541.

Rogers, R. R., and M. K. Yau, 1996: *A short course in cloud physics*. Third edition ed., No. Volume 113, International Series in Natural Philosophy, Butterworth-Heinemann, Burlington, Massachusetts.

Romatschke, U., and M. J. Dixon, 2022: Vertically Resolved Convective–Stratiform Echo-Type Identification and Convectivity Retrieval for Vertically Pointing Radars. *Journal of Atmospheric and Oceanic Technology*, **39 (11)**, https://doi.org/10.1175/jtech-d-22-0019.1, URL http://dx.doi.org/10.1175/JTECH-D-22-0019.1.

Rotunno, R., J. B. Klemp, and M. L. Weisman, 1988: A Theory for Strong, Long-Lived Squall Lines. *Journal of the Atmospheric Sciences*, **45 (3)**, 463–485, https://doi.org/10.1175/1520-0469(1988)045<0463:ATFSLL>2.0.CO;2, URL http://journals.ametsoc.org/doi/10.1175/1520-0469(1988)045<0463:ATFSLL>2.0.CO;2.

Ruppert, J. H., R. H. Johnson, and A. K. Rowe, 2013: Diurnal Circulations and Rainfall in Taiwan during SoWMEX/TiMREX (2008). *Monthly Weather Review*, **141 (11)**, 3851–3872, https://doi.org/10.1175/MWR-D-12-00301.1, URL http://journals.ametsoc.org/doi/10.1175/MWR-D-12-00301.1.

Ryu, J., H. Song, B. Sohn, and C. Liu, 2021: Global Distribution of Three Types of Drop Size Distribution Representing Heavy Rainfall From GPM/DPR Measurements. *Geophysical Research Letters*, **48 (3)**, e2020GL090 871, https://doi.org/10.1029/2020GL090871, URL https://agupubs.onlinelibrary.wiley.com/doi/10.1029/2020GL090871.

Ryzhkov, A., M. Diederich, P. Zhang, and C. Simmer, 2014: Potential Utilization of Specific Attenuation for Rainfall Estimation, Mitigation of Partial Beam Blockage, and Radar Networking. *J. Atmos. Oceanic Technol.*, **31**, 599–619, https://doi.org/10.1175/JTECH-D-13-00038.1.

Ryzhkov, A., P. Zhang, and J. Hu, 2025: Suggested Modifications for the S-Band Polarimetric Radar Rainfall Estimation Algorithm. *Journal of Hydrometeorology*, **26 (8)**, 1053–1062, https://doi.org/10.1175/JHM-D-25-0014.1, URL https://journals.ametsoc.org/view/journals/hydr/26/8/JHM-D-25-0014.1.xml.

Ryzhkov, A., and D. Zrnić, 1996: Assessment of Rainfall Measurement That Uses Specific Differential Phase. *Journal of Applied Meteorology*, **35 (11)**, 2080–2090, https://doi.org/10.1175/1520-0450(1996)035<2080:AORMTU>2.0.CO;2, URL http://journals.ametsoc.org/doi/10.1175/1520-0450(1996)035<2080:AORMTU>2.0.CO;2.

Ryzhkov, A., and D. S. Zrnić, 1995: Precipitation and Attenuation Measurements at a 10-cm Wavelength. *J. Appl. Meteor. Climatol.*, **34**, 2121–2134, https://doi.org/10.1175/1520-0450(1995)034<2120:PAAMAA>2.0.CO;2.

Ryzhkov, A., and Coauthors, 2022: Polarimetric Radar Quantitative Precipitation Estimation. *Remote Sensing*, **14 (7)**, https://doi.org/10.3390/rs14071695, URL https://www.mdpi.com/2072-4292/14/7/1695, company: Multidisciplinary Digital Publishing Institute Distributor: Multidisciplinary Digital Publishing Institute Institution: Multidisciplinary Digital Publishing Institute Label: Multidisciplinary Digital Publishing Institute.

Sachidananda, M., and D. S. Zrnić, 1985: Z_{dr} measurement considerations for a fast scan capability radar. *Radio Science*, **20 (4)**, 907–922, https://doi.org/10.1029/RS020i004p00907, URL https://agupubs.onlinelibrary.wiley.com/doi/10.1029/RS020i004p00907.

Sachidananda, M., and D. S. Zrnić, 1987: Rain Rate Estimates from Differential Polarization Measurements. *J. Atmos. Oceanic Technol.*, **4**, 588–598, https://doi.org/10.1175/1520-0426(1987)004<0588:RREFDP>2.0.CO;2.

Salio, P., M. Nicolini, and E. J. Zipser, 2007: Mesoscale Convective Systems over Southeastern South America and Their Relationship with the South American Low-Level Jet. *Monthly Weather Review*, **135 (4)**, 1290–1309, https://doi.org/10.1175/MWR3305.1, URL http://journals.ametsoc.org/doi/10.1175/MWR3305.1.

Sasaki, C. R. S., A. K. Rowe, L. A. McMurdie, and K. L. Rasmussen, 2022: New Insights into the South American Low-Level Jet from RELAMPAGO Observations. *Monthly Weather Review*, **150 (6)**, 1247–1271, https://doi.org/10.1175/MWR-D-21-0161.1, URL https://journals.ametsoc.org/view/journals/mwre/150/6/MWR-D-21-0161.1.xml.

Sauvageot, H., and J.-P. Lacaux, 1995: The Shape of Averaged Drop Size Distributions. *Journal of the Atmospheric Sciences*, **52 (8)**, 1070–1083, https://doi.org/10.1175/1520-0469(1995)052<1070:TSOADS>2.0.CO;2, URL http://journals.ametsoc.org/doi/10.1175/1520-0469(1995)052<1070:TSOADS>2.0.CO;2.

Schumacher, C., and R. A. Houze, 2003: Stratiform Rain in the Tropics as Seen by the TRMM Precipitation Radar*. *Journal of Climate*, **16 (11)**, 1739–1756, https://doi.org/10.1175/1520-0442(2003)016<1739:SRITTA>2.0.CO;2, URL http://journals.ametsoc.org/doi/10.1175/1520-0442(2003)016<1739:SRITTA>2.0.CO;2.

Schumacher, R. S., 2017: Heavy Rainfall and Flash Flooding. *Oxford Research Encyclopedia of Natural Hazard Science*, URL https://oxfordre.com/naturalhazardscience/display/10.1093/acrefore/9780199389407.001.0001/acrefore-9780199389407-e-132.

Seela, B. K., J. Janapati, P. Lin, C. Liu, and C. Tu, 2024: An Investigation on Microphysical Characteristics of Early-, Late-, and Post-Mei-yu Season Rainfall Over Taiwan. *Journal of Geophysical Research: Atmospheres*, **129 (18)**, e2024JD040 847, https://doi.org/10.1029/2024JD040847, URL https://agupubs.onlinelibrary.wiley.com/doi/10.1029/2024JD040847.

Segoni, S., L. Piciullo, and S. L. Gariano, 2018: A review of the recent literature on rainfall thresholds for landslide occurrence. *Landslides*, **15 (8)**, 1483–1501, https://doi.org/10.1007/s10346-018-0966-4, URL https://doi.org/10.1007/s10346-018-0966-4.

Seliga, T. A., and V. N. Bringi, 1976: Potential Use of Radar Differential Reflectivity Measurements at Orthogonal Polarizations for Measuring Precipitation. *Journal of Applied Meteorology*, **15 (1)**, 69–76, https://doi.org/10.1175/1520-0450(1976)015<0069:PUORDR>2.0.CO;2, URL http://journals.ametsoc.org/doi/10.1175/1520-0450(1976)015<0069:PUORDR>2.0.CO;2.

Seliga, T. A., and V. N. Bringi, 1978: Differential reflectivity and differential phase shift: Applications in radar meteorology. *Radio Science*, **13 (2)**, 271–275, https://doi.org/10.1029/RS013i002p00271, URL https://agupubs.onlinelibrary.wiley.com/doi/10.1029/RS013i002p00271.

Seo, B.-C., W. Krajewski, and A. Ryzhkov, 2020: Evaluation of the Specific Attenuation Method for Radar-Based Quantitative Precipitation Estimation: Improvements and Practical Challenges. *J. Hydrometeor.*, **21**, 1333–1347, https://doi.org/10.1175/JHM-D-20-0030.1.

Shin, K., K. Kim, J. J. Song, and G. Lee, 2023: Polarimetric Retrieval of Raindrop Size Distribution: Double-Moment Normalization Approach and Machine Learning Techniques. *Geophysical Research Letters*, **51 (1)**, https://doi.org/10.1029/2023gl106057, URL http://dx.doi.org/10.1029/2023GL106057.

Skamarock, W. C., and Coauthors, 2019: A Description of the Advanced Research WRF Model Version 4. Tech. rep., NSF National Center for Atmospheric Research. https://doi.org/10.5065/1DFH-6P97, URL https://opensky.ucar.edu/islandora/object/opensky:2898.

Smith, J. A., M. L. Baeck, A. J. Miller, A. Ryzhkov, and J. Hu, 2025: Cloudbursts of the Mid-Atlantic. *Water Resources Research*, **61 (9)**, https://doi.org/10.1029/2025wr040384, URL http://dx.doi.org/10.1029/2025WR040384.

Steiner, M., R. H. Jr, and S. Yuter, 1995: Climatological Characterization of Three-Dimensional Storm Structure from Operational Radar and Rain Gauge Data. *J. Appl. Meteor. Climatol.*, **34**, 1978–2007, https://doi.org/10.1175/1520-0450(1995)034<1978:CCOTDS>2.0.CO;2.

Steiner, M., J. Smith, S. Burges, C. Alonso, and R. Darden, 1999: Effect of bias adjustment and rain gauge data quality control on radar rainfall estimates. *Water Resour. Res.*, **35**, 2487–2503, https://doi.org/10.1029/1999WR900142.

Stout, G. E., and E. A. Mueller, 1968: Survey of Relationships Between Rainfall Rate and Radar Reflectivity in the Measurement of Precipitation. *Journal of Applied Meteorology*, **7 (3)**, 465–474, https://doi.org/10.1175/1520-0450(1968)007<0465:SORBRR>2.0.CO;2, URL http://journals.ametsoc.org/doi/10.1175/1520-0450(1968)007<0465:SORBRR>2.0.CO;2.

Sun, J., Y. Zhang, J. Ban, J.-S. Hong, and C.-Y. Lin, 2020: Impact of Combined Assimilation of Radar and Rainfall Data on Short-Term Heavy Rainfall Prediction: A Case Study. *Monthly Weather Review*, **148 (5)**, 2211–2232, https://doi.org/10.1175/MWR-D-19-0337.1, URL https://journals.ametsoc.org/view/journals/mwre/148/5/mwr-d-19-0337.1.xml.

Syl, J. v., 2001: The Shuttle Radar Topography Mission (SRTM): A Breakthrough in Remote Sensing of Topography. *Acta Astronautica*, **48**, 559–565, https://doi.org/10.1016/S0094-576500020-0.

Tam, F. I., M. Yang, and W. Lee, 2022: Polarimetric Size Sorting Signatures in the Convective Regions of Mesoscale Convective Systems in PECAN: Implications on Kinematics, Thermodynamics, and Precipitation Pathways. *Journal of Geophysical Research: Atmospheres*, **127 (10)**, https://doi.org/10.1029/2021jd035822, URL http://dx.doi.org/10.1029/2021JD035822.

Tang, Y.-S., P.-L. Chang, W.-Y. Chang, J. Zhang, L. Tang, P.-F. Lin, and C.-R. Chen, 2024: A Localized Quantitative Precipitation Estimation for S-band Polarimetric Radar in Taiwan. *J. Hydrometeor.*, **25**, 1697–1712, https://doi.org/0.1175/JHM-D-23-0205.1.

Tao, W., D. Wu, S. Lang, J. Chern, C. Peters-Lidard, A. Fridlind, and T. Matsui, 2016: High-resolution NU-WRF simulations of a deep convective-precipitation system during MC3E: Further improvements and comparisons between Goddard microphysics schemes and observations. *Journal of Geophysical Research: Atmospheres*, **121 (3)**, 1278–1305, https://doi.org/10.1002/2015JD023986, URL https://agupubs.onlinelibrary.wiley.com/doi/10.1002/2015JD023986.

Tao, W.-K., and J. Simpson, 1993: Goddard Cumulus Ensemble Model. Part I: Model Description. *Terrestrial, Atmospheric and Oceanic Sciences*, **4 (1)**, 035, https://doi.org/10.3319/TAO.1993.4.1.35(A), URL http://tao.cgu.org.tw/index.php/articles/archive/atmospheric-science/item/76.

Tao, W.-K., J. Simpson, and M. McCumber, 1989: An Ice-Water Saturation Adjustment. *Monthly Weather Review*, **117 (1)**, 231–235, https://doi.org/10.1175/1520-0493(1989)117<0231:AIWSA>2.0.CO;2, URL http://journals.ametsoc.org/doi/10.1175/1520-0493(1989)117<0231:AIWSA>2.0.CO;2.

Tao, W.-K., and Coauthors, 2011: High-Resolution Numerical Simulation of the Extreme Rainfall Associated with Typhoon Morakot. Part I: Comparing the Impact of Microphysics and PBL Parameterizations with Observations. *Terrestrial, Atmospheric and Oceanic Sciences*, **22 (6)**, 673, https://doi.org/10.3319/TAO.2011.08.26.01(TM), URL http://tao.cgu.org.tw/index.php/articles/archive/atmospheric-science/item/1044.

Testud, J., E. L. Bouar, E. Obligis, and M. Ali-Mehenni, 2000: The Rain Profiling Algorithm Applied to Polarimetric Weather Radar. *J. Atmos. Oceanic Technol.*, **17**, 332–356, https://doi.org/10.1175/1520-0426(2000)017<0332:TRPAAT>2.0.CO;2.

Thurai, M., V. Bringi, P. N. Gatlin, W. A. Petersen, and M. T. Wingo, 2019: Measurements and Modeling of the Full Rain Drop Size Distribution. *Atmosphere*, **10 (1)**, https://doi.org/10.3390/atmos10010039, URL http://dx.doi.org/10.3390/atmos10010039.

Thurai, M., V. Bringi, D. Wolff, D. Marks, C. Pabla, and P. Kennedy, 2022: Drop Size Distribution Retrievals for Light Rain and Drizzle from S-Band Polarimetric Radars. *The 5th International Electronic Conference on Atmospheric Sciences*, MDPI, ECAS 2022, https://doi.org/10.3390/ecas2022-12794, URL http://dx.doi.org/10.3390/ecas2022-12794.

Thurai, M., and V. N. Bringi, 2005: Drop Axis Ratios from a 2D Video Disdrometer. *J. Atmos. Oceanic Technol.*, **22**, 966–978, https://doi.org/10.1175/JTECH1767.1.

Thurai, M., and V. N. Bringi, 2018: Application of the Generalized Gamma Model to Represent the Full Rain Drop Size Distribution Spectra. *Journal of Applied Meteorology and Climatology*, **57 (5)**, https://doi.org/10.1175/jamc-d-17-0235.1, URL http://dx.doi.org/10.1175/jamc-d-17-0235.1.

Thurai, M., P. Gatlin, V. N. Bringi, W. Petersen, P. Kennedy, B. Notaroš, and L. Carey, 2017: Toward Completing the Raindrop Size Spectrum: Case Studies Involving 2D-Video Disdrometer, Droplet Spectrometer, and Polarimetric Radar Measurements. *Journal of Applied Meteorology and Climatology*, **56 (4)**, https://doi.org/10.1175/jamc-d-16-0304.1, URL http://dx.doi.org/10.1175/JAMC-D-16-0304.1.

Thurai, M., K. Shin, and G. Lee, 2025: Testing the Retrieval of the Rain Drop Size Distribution Moments Using X-Band Polarimetric Radar Data During a Warm Rain Event. *IEEE Transactions on Geoscience and Remote Sensing*, **63**, 1–9, https://doi.org/10.1109/tgrs.2025.3605611, URL http://dx.doi.org/10.1109/TGRS.2025.3605611.

Tokay, A., A. Kruger, and W. F. Krajewski, 2001: Comparison of Drop Size Distribution Measurements by Impact and Optical Disdrometers. *Journal of Applied Meteorology*, **40 (11)**, https://doi.org/10.1175/1520-0450(2001)040<2083:codsdm>2.0.co;2, URL http://dx.doi.org/10.1175/1520-0450(2001)040<2083:CODSDM>2.0.CO;2.

Tokay, A., and D. A. Short, 1996: Evidence from Tropical Raindrop Spectra of the Origin of Rain from Stratiform versus Convective Clouds. *Journal of Applied Meteorology*, **35 (3)**, 355–371, https://doi.org/10.1175/1520-0450(1996)035<0355:EFTRSO>2.0.CO;2, URL http://journals.ametsoc.org/doi/10.1175/1520-0450(1996)035<0355:EFTRSO>2.0.CO;2.

Tokay, A., D. Wolff, and W. Petersen, 2014: Evaluation of the New Version of the Laser-Optical Disdrometer, OTT Parsivel^2. *J. Atmos. Oceanic Technol.*, **31**, 1276–1288, https://doi.org/10.1175/JTECH-D-13-00174.1.

Trier, S. B., D. B. Parsons, and T. J. Matejka, 1990: Observations of a Subtropical Cold Front in a Region of Complex Terrain. *Monthly Weather Review*, **118 (12)**, 2449–2470, https://doi.org/10.1175/1520-0493(1990)118<2449:OOASCF>2.0.CO;2, URL http://journals.ametsoc.org/doi/10.1175/1520-0493(1990)118<2449:OOASCF>2.0.CO;2.

Tsai, T.-C., and Coauthors, 2025: Improving Global and Regional Weather Prediction Through the TCWA1 Bulk Cloud Microphysics Scheme. Preprints, URL https://essopenarchive.org/users/970964/articles/1338974-improving-global-and-regional-weather-prediction-through-the-tcwa1-bulk-cloud-microphysics-scheme?commit=e8c08c50f97b8413188fe090fa26a8bddc2551e9, https://doi.org/10.22541/essoar.175977420.00233137/v1.

Tu, C.-C., Y.-L. Chen, P.-L. Lin, and Y. Du, 2019: Characteristics of the Marine Boundary Layer Jet over the South China Sea during the Early Summer Rainy Season of Taiwan. *Monthly Weather Review*, **147 (2)**, 457–475, https://doi.org/10.1175/MWR-D-18-0230.1, URL http://journals.ametsoc.org/doi/10.1175/MWR-D-18-0230.1.

Tu, C.-C., Y.-L. Chen, P.-L. Lin, and M.-Q. Huang, 2022: Analysis and Simulations of a Heavy Rainfall Event Associated with the Passage of a Shallow Front over Northern Taiwan on 2 June 2017. *Monthly Weather Review*, **150 (3)**, 505–528, https://doi.org/10.1175/MWR-D-21-0113.1, URL https://journals.ametsoc.org/view/journals/mwre/150/3/MWR-D-21-0113.1.xml.

Tu, C.-C., Y.-L. Chen, P.-L. Lin, and P.-H. Lin, 2020: The relationship between the boundary layer moisture transport from the South China Sea and heavy rainfall over Taiwan. *Terrestrial, Atmospheric and Oceanic Sciences*, **31 (2)**, 159–176, https://doi.org/10.3319/TAO.2019.07.01.01, URL http://tao.cgu.org.tw/index.php/articles/archive/atmospheric-science/item/1682.

Ulbrich, C. W., and D. Atlas, 1998: Rainfall Microphysics and Radar Properties: Analysis Methods for Drop Size Spectra. *Journal of Applied Meteorology*, **37 (9)**, 912–923, https://doi.org/10.1175/1520-0450(1998)037<0912:RMARPA>2.0.CO;2, URL http://journals.ametsoc.org/doi/10.1175/1520-0450(1998)037<0912:RMARPA>2.0.CO;2.

United Nations Office for Disaster Risk Reduction, 2025: *Global Assessment Report on Disaster Risk Reduction 2025: Resilience Pays: Financing and Investing for our Future*. Global Assessment Report on Disaster Risk Reduction (GAR), United Nations, https://doi.org/10.18356/9789211576740, URL https://www.un-ilibrary.org/content/books/9789211576740.

van Zyl, J. J., 2001: The Shuttle Radar Topography Mission (SRTM): a breakthrough in remote sensing of topography. *Acta Astronautica*, **48 (5–12)**, https://doi.org/10.1016/s0094-5765(01)00020-0, URL http://dx.doi.org/10.1016/S0094-5765(01)00020-0.

Villarini, G., and W. F. Krajewski, 2010: Review of the Different Sources of Uncertainty in Single Polarization Radar-Based Estimates of Rainfall. *Surveys in Geophysics*, **31 (1)**, 107–129, https://doi.org/10.1007/s10712-009-9079-x, URL http://link.springer.com/10.1007/s10712-009-9079-x.

Vivekanandan, J., D. S. Zrnić, S. M. Ellis, R. Oye, A. Ryzhkov, and J. Straka, 1999: Cloud Microphysics Retrieval Using S-Band Dual-Polarization Radar Measurements. *Bull. Amer. Meteor. Soc.*, **80**, 381–388, https://doi.org/10.1175/1520-0477(1999)080<0381:CMRUSB>2.0.CO;2.

Wang, C.-C., and G. T.-J. Chen, 2002: Case Study of the Leeside Mesolow and Mesocyclone in TAMEX. *Monthly Weather Review*, **130 (11)**, 2572–2592, https://doi.org/10.1175/1520-0493(2002)130<2572:CSOTLM>2.0.CO;2, URL http://journals.ametsoc.org/doi/10.1175/1520-0493(2002)130<2572:CSOTLM>2.0.CO;2.

Wang, C.-C., G. T.-J. Chen, T.-C. Chen, and K. Tsuboki, 2005: A Numerical Study on the Effects of Taiwan Topography on a Convective Line during the Mei-Yu Season. *Monthly Weather Review*, **133 (11)**, 3217–3242, https://doi.org/10.1175/MWR3028.1, URL http://journals.ametsoc.org/doi/10.1175/MWR3028.1.

Wang, C.-C., Y.-H. Chen, Y.-Y. Lan, and W.-Y. Chang, 2023: An Evaluation of Simulated Cloud Microphysical Characteristics of Three Mei-Yu Rainfall Systems in Taiwan by a Cloud-Resolving Model Using Dual-Polarimetric Radar Observations. *Remote Sensing*, **15 (19)**, 4651, https://doi.org/10.3390/rs15194651, URL https://www.mdpi.com/2072-4292/15/19/4651.

Wang, C.-C., J. Chieh-Sheng Hsu, G. Tai-Jen Chen, and D.-I. Lee, 2014: A Study of Two Propagating Heavy-Rainfall Episodes near Taiwan during SoWMEX/TiMREX IOP-8 in June 2008. Part I: Synoptic Evolution, Episode Propagation, and Model Control Simulation. *Monthly Weather Review*, **142 (8)**, 2619–2643, https://doi.org/10.1175/MWR-D-13-00331.1, URL http://journals.ametsoc.org/doi/10.1175/MWR-D-13-00331.1.

Wang, C.-C., M.-S. Li, C.-S. Chang, P.-Y. Chuang, S.-H. Chen, and K. Tsuboki, 2021: Ensemble-based sensitivity analysis and predictability of an extreme rainfall event over northern Taiwan in the Mei-yu season: The 2 June 2017 case. *Atmospheric Research*, **259**, 105 684, https://doi.org/10.1016/j.atmosres.2021.105684, URL https://linkinghub.elsevier.com/retrieve/pii/S0169809521002362.

Wang, C.-C., G. Tai-Jen Chen, and K.-H. Ho, 2016: A Diagnostic Case Study of Mei-Yu Frontal Retreat and Associated Low Development near Taiwan. *Monthly Weather Review*, **144 (6)**, 2327–2349, https://doi.org/10.1175/MWR-D-15-0391.1, URL http://journals.ametsoc.org/doi/10.1175/MWR-D-15-0391.1.

Wang, T.-C. C., Y.-J. Lin, H. Shen, and R. W. Pasken, 1990: Characteristics of a Subtropical Squall Line Determined from TAMEX Dual-Doppler Data. Part I: Kinematic Structure. *Journal of the Atmospheric Sciences*, **47 (20)**, 2357–2381, https://doi.org/10.1175/1520-0469(1990)047<2357:COASSL>2.0.CO;2, URL http://journals.ametsoc.org/doi/10.1175/1520-0469(1990)047<2357:COASSL>2.0.CO;2.

Wang, Y., and V. Chandrasekar, 2009: Algorithm for Estimation of the Specific Differential Phase. *Journal of Atmospheric and Oceanic Technology*, **26 (12)**, 2565–2578, https://doi.org/10.1175/2009JTECHA1358.1, URL http://journals.ametsoc.org/doi/10.1175/2009JTECHA1358.1.

Wang, Y., S. Cocks, L. Tang, A. Ryzhkov, P. Zhang, J. Zhang, and K. Howard, 2019: A Prototype Quantitative Precipitation Estimation Algorithm for Operational S-Band Polarimetric Radar Utilizing Specific Attenuation and Specific Differential Phase. Part I: Algorithm Description. *J. Hydrometeor.*, **20**, 985–997, https://doi.org/10.1175/JHM-D-18-0071.1.

Weisman, M. L., and J. B. Klemp, 1984: The Structure and Classification of Numerically Simulated Convective Stormsin Directionally Varying Wind Shears. *Monthly Weather Review*, **112 (12)**, 2479–2498, https://doi.org/10.1175/1520-0493(1984)112<2479:TSACON>2.0.CO;2, URL http://journals.ametsoc.org/doi/10.1175/1520-0493(1984)112<2479:TSACON>2.0.CO;2.

Weisman, M. L., and J. B. Klemp, 1986: Characteristics of Isolated Convective Storms. *Mesoscale Meteorology and Forecasting*, P. S. Ray, Ed., American Meteorological Society, Boston, MA, 331–358, https://doi.org/10.1007/978-1-935704-20-1_15, URL http://link.springer.com/10.1007/978-1-935704-20-1_15.

Weisman, M. L., and R. Rotunno, 2004: "A Theory for Strong Long-Lived Squall Lines" Revisited. *Journal of the Atmospheric Sciences*, **61 (4)**, 361–382, https://doi.org/10.1175/1520-0469(2004)061<0361:ATFSLS>2.0.CO;2, URL http://journals.ametsoc.org/doi/10.1175/1520-0469(2004)061<0361:ATFSLS>2.0.CO;2.

Wolff, D. B., W. Petersen, A. Tokay, D. Marks, and J. Pippitt, 2019: Assessing Dual-Polarization Radar Estimates of Extreme Rainfall during Hurricane Harvey. *J. Atmos. Oceanic Technol.*, **36**, 2501–2520, https://doi.org/10.1175/JTECH-D-19-0081.1.

Wright, D. B., 2018: Rainfall Information for Global Flood Modeling. *Global Flood Hazard*, American Geophysical Union (AGU), 17–42, https://doi.org/10.1002/9781119217886.ch2, URL https://onlinelibrary.wiley.com/doi/abs/10.1002/9781119217886.ch2, section: 2 _eprint: https://agupubs.onlinelibrary.wiley.com/doi/pdf/10.1002/9781119217886.ch2.

Wu, Y., S. S. Wang, Y. Yu, C. Kung, A. Wang, S. A. Los, and W. Huang, 2019: Climatology and change of extreme precipitation events in Taiwan based on weather types. *International Journal of Climatology*, **39 (14)**, 5351–5366, https://doi.org/10.1002/joc.6159, URL https://rmets.onlinelibrary.wiley.com/doi/10.1002/joc.6159.

Xie, X., R. Evaristo, S. Troemel, P. Saavedra, C. Simmer, and A. Ryzhkov, 2016: Radar Observation of Evaporation and Implications for Quantitative Precipitation and Cooling Rate Estimation. *Journal of Atmospheric and Oceanic Technology*, **33 (8)**, https://doi.org/10.1175/jtech-d-15-0244.1, URL http://dx.doi.org/10.1175/JTECH-D-15-0244.1.

Xu, W., and E. J. Zipser, 2015: Convective intensity, vertical precipitation structures, and microphysics of two contrasting convective regimes during the 2008 TiMREX. *Journal of Geophysical Research: Atmospheres*, **120 (9)**, 4000–4016, https://doi.org/10.1002/2014JD022927, URL https://agupubs.onlinelibrary.wiley.com/doi/10.1002/2014JD022927.

Xu, W., E. J. Zipser, and C. Liu, 2009: Rainfall Characteristics and Convective Properties of Mei-Yu Precipitation Systems over South China, Taiwan, and the South China Sea. Part I: TRMM Observations. *Monthly Weather Review*, **137 (12)**, 4261–4275, https://doi.org/10.1175/2009MWR2982.1, URL http://journals.ametsoc.org/doi/10.1175/2009MWR2982.1.

Yang, M., B. J. Jou, S. Wang, J. Hong, P. Lin, J. Teng, and H. Lin, 2004: Ensemble prediction of rainfall during the 2000–2002 Mei-Yu seasons: Evaluation over the Taiwan area. *Journal of Geophysical Research: Atmospheres*, **109 (D18)**, 2003JD004 368, https://doi.org/10.1029/2003JD004368, URL https://agupubs.onlinelibrary.wiley.com/doi/10.1029/2003JD004368.

Yang, S., Y. Du, B. Han, C. Wu, and H. Kong, 2025: Microphysical Characteristics of Tropical Cyclone Choiwan (2021) Outer Rainbands Derived From Polarimetric Radar Observations on a Research Vessel. *Geophysical Research Letters*, **52 (5)**, https://doi.org/10.1029/2024gl112557, URL http://dx.doi.org/10.1029/2024GL112557.

Yang, S.-C., S.-H. Chen, L. J.-Y. Liu, H.-L. Yeh, W.-Y. Chang, K.-S. Chung, P.-L. Chang, and W.-C. Lee, 2024: Investigating the Mechanisms of an Intense Coastal Rainfall Event during TAHOPE/PRECIP-IOP3 Using a Multiscale Radar Ensemble Data Assimilation System. *Monthly Weather Review*, **152 (11)**, 2545–2567, https://doi.org/10.1175/MWR-D-24-0049.1, URL https://journals.ametsoc.org/view/journals/mwre/152/11/MWR-D-24-0049.1.xml.

Yeh, H.-C., G. T.-J. Chen, and W. T. Liu, 2002: Kinematic Characteristics of a Mei-yu Front Detected by the QuikSCAT Oceanic Winds. *Monthly Weather Review*, **130 (3)**, 700–711, https://doi.org/10.1175/1520-0493(2002)130<0700:KCOAMY>2.0.CO;2, URL http://journals.ametsoc.org/doi/10.1175/1520-0493(2002)130<0700:KCOAMY>2.0.CO;2.

Yeh, H.-C., and Y.-L. Chen, 2003: Numerical Simulations of the Barrier Jet over Northwestern Taiwan during the Mei-Yu Season. *Monthly Weather Review*, **131 (7)**, 1396–1407, https://doi.org/10.1175/1520-0493(2003)131<1396:NSOTBJ>2.0.CO;2, URL http://journals.ametsoc.org/doi/10.1175/1520-0493(2003)131<1396:NSOTBJ>2.0.CO;2.

Zawadzki, I. I., 1975: On Radar-Raingage Comparison. *Journal of Applied Meteorology (1962-1982)*, **14 (8)**, 1430–1436, URL https://www.jstor.org/stable/26177389.

Zhang, A.-S., C.-Y. Huang, S. Chen, P.-F. Zhang, D.-M. Hu, and L.-S. Xiao, 2021: Utilization of Specific Attenuation for Rainfall Estimation in Southern China. *J. Tropical Meteor.*, **27**, 48–61, https://doi.org/10.46267/j.1006-8775.2021.005.

Zhang, J., L. Tang, S. Cocks, P. Zhang, A. Ryzhkov, K. Howard, C. Langston, and B. Kaney, 2020: A Dual-Polarization Radar Synthetic QPE for Operations. https://doi.org/10.1175/JHM-D-19-0194.1, URL https://journals.ametsoc.org/view/journals/hydr/21/11/JHM-D-19-0194.1.xml.

Zhang, J., and Coauthors, 2016: Multi-Radar Multi-Sensor (MRMS) Quantitative Precipitation Estimation: Initial Operating Capabilities. *Bull. Amer. Meteor. Soc.*, **97**, 621–638, https://doi.org/10.1175/BAMS-D-14-00174.1.

Zhang, Y., 1989: *Study of Low-Level Jet during Tamex*. University of Hawai'i at Manoa.

Zhang, Y., X. Chen, and M. M. Bell, 2023: Improving Short-Term QPF Using Geostationary Satellite All-Sky Infrared Radiances: Real-Time Ensemble Data Assimilation and Forecast during the PRECIP 2020 and 2021 Experiments. *Weather and Forecasting*, **38 (4)**, 591–609, https://doi.org/10.1175/WAF-D-22-0156.1, URL https://journals.ametsoc.org/view/journals/wefo/38/4/WAF-D-22-0156.1.xml.

Zrnić, D. S., and A. Ryzhkov, 1996: Advantages of Rain Measurements Using Specific Differential Phase. *Journal of Atmospheric and Oceanic Technology*, **13 (2)**, 454–464, https://doi.org/10.1175/1520-0426(1996)013<0454:AORMUS>2.0.CO;2, URL http://journals.ametsoc.org/doi/10.1175/1520-0426(1996)013<0454:AORMUS>2.0.CO;2.